University of Alberta

Experiments Investigating Momentum Transfer, Turbulence and Air-Water Gas Transfer in a Wind Wave Tank

by

Moniz Ahmmod Mukto

A thesis submitted to the Faculty of Graduate Studies and Research
in partial fulfillment of the requirements for the degree of

Doctor of Philosophy

in

Water Resources Engineering

Department of Civil and Environmental Engineering

Spring 2011
Edmonton, Alberta

Examining Committee

Dr. Mark Loewen, Department of Civil and Environmental Engineering

Dr. Peter Steffler, Department of Civil and Environmental Engineering

Dr. Faye Hicks, Department of Civil and Environmental Engineering

Dr. Selma Guigard, Department of Civil and Environmental Engineering

Dr. Morris Flynn, Department of Mechanical Engineering

Dr. Hans Graber, Rosenstiel School of Marine and Atmospheric Science, Division of Applied Marine Physics, University of Miami

To Mahrus and Shoma,
You are my love and life.

Abstract

A series of laboratory experiments were conducted at three fetches of 4.8, 8.8 and 12.4 m, and at six wind speeds ranging from 4.1 to 9.6 m s^{-1} at each fetch in a wind-wave-current research facility. In addition, five surfactant-influenced experiments were conducted at concentrations ranging from 0.1 to 5.0 ppm at a wind speed of 7.9 m s^{-1} and a fetch of 4.8 m. The goals were to examine the momentum transfer and to characterize the turbulent flow structure beneath wind waves, and to investigate the relationship between wind waves and the gas transfer rate at the air-water interface. Digital particle image velocimetry (DPIV) was used to measure two-dimensional instantaneous velocity fields beneath the wind waves.

The friction velocities and roughness lengths of the coupled boundary layers were used to characterize the flow regime and momentum transfer. The air-side flows were found to be aerodynamically rough and the water-side flows were found to be in transition and then become hydrodynamically smooth as wind speed increased. Airflow separation from the crests of breaking waves may be responsible for making the air-side boundary layer rougher and water-side boundary layer smoother. Momentum transfer was studied by examining the partitioning of the wind stress into the viscous tangential stress and wave-induced stress. It was found that the wave steepness was the most important wind-wave property that controls the momentum transfer in the coupled boundary layers.

Two distinct layers were observed in the near-surface turbulence in

the presence of a surfactant and three layers in clean water. In the surfactant-influenced experiments, the energy dissipation rate decayed as $\zeta^{-0.3}$ in the upper layer and in the lower layer energy dissipation rate decayed as $\zeta^{-1.0}$ similar to a wall-layer. For clean experiments, the energy dissipation rate could be scaled using the depth, friction velocity, wave height and phase speed as proposed by Terray *et al.* (1996) provided that layer based friction velocities were used. In the upper layer, the near-surface turbulence was dominated by wave-induced motions and the dissipation rates decayed as $\zeta^{-0.2}$ at all fetches. Below this in the transition layer turbulence was generated by both wave-induced motions and shear currents and the dissipation rate decayed as $\zeta^{-2.0}$ at a fetch of 4.8 m. However, at fetches of 8.8 and 12.4 m, the dissipation rate decayed at two different rates; as $\zeta^{-2.0}$ in the upper region and as $\zeta^{-4.0}$ in the lower region. In the third layer, the dissipation rate decayed as $\zeta^{-1.0}$ similar to a wall-layer at a fetch of 4.8 m.

Four empirical relationships commonly used to predict the gas transfer rate were evaluated using laboratory measurements. The gas transfer rate was found to correlate most closely with the total mean square wave slope and varied linearly with this parameter. The three other parameterizations using wind speed, wind friction velocity and energy dissipation did not correlate as well.

Acknowledgements

I sincerely express gratitude to my supervisor Professor Dr. Mark Loewen for his constant supervision, support, encouragement and constructive criticism throughout the course of this research. He introduced me to a world of new measurement techniques, such as Digital Particle Image Velocimetry, Infrared (IR) Imagery etc. where, I excelled further in this field. He provided me financial support through the Canadian Foundation for Climate and Atmospheric Sciences and National Science and Engineering Research Council funds to facilitate my PhD experiments at the University of Alberta and at the Observational Science Branch, NASA, USA, to carry out research and to participate national and international conferences. I highly appreciate Dr. Peter Steffler, Dr. Faye Hicks, Dr. Selma Guigard, Dr. Morris Flynn and Dr. Hans Graber for providing me with their valuable suggestions regarding my Ph.D. thesis.

During my PhD program, I also received supportive hand and guidance from a number of people. Dr. Andrew Jessup, Dr. William Asher, Ms. Ruth Branch and Mr. Kapil Phadnis from the Applied Physics Laboratory of the University of Washington, Dr. Christopher Zappa from Lamont-Doherty Earth Observatory of Columbia University, Dr. Steven Long from NASA Air-Sea Interaction Research Facility of Wallops Flight Facility and Dr. Mohamed Atmane from this University helped me to carry out my experiments successfully. Dr. Jessup, Dr. Atmane and Mr. Phadnis helped me with IR and Environmental measurements. Dr. Asher and Ms. Branch helped me with gas transfer measurements and Dr. Asher provided me with gas transfer results and his valuable suggestions. I am also thankful to Dr. Zappa for helping me with the air-side measurements and providing me with the results.

I thankfully acknowledge the admirable work environment surrounded by faculty members, technical and administrative staff, my colleagues and friends in the water resources engineering group and in the department. I thank Mr. Perry Fedun for providing me the laboratory support at different stages of my thesis. Dr. Atmane is a great friend of mine who shared a lot of his valuable experience with me. Dr. Iran Neto and Dr. German Rojas are two of my closest friends and were partners at the coffee talks where we came up with some brilliant ideas. I gratefully cherish those moments. I also admiringly acknowledge the support I received from the Water Resources Engineering Group at Golder Associates Ltd., Calgary.

I also extend my heartfelt thanks to my parents, in-laws, family, relatives and friends for their encouragement and continuing support. Last but not the least, all of my appreciation and love goes to my wife, Shoma Tanzeeba, for her never-ending support, patience, encouragement, love and confidence in me. My unconditional love is for my son Mahrus Shayaan Mukto who made my world much meaningful and bright who came to us as a little angel during my Ph.D. studies.

I gratefully acknowledge the financial support from the University of Alberta that was awarded to me in the form of F.S. Chia Ph.D. scholarship. I also acknowledge National Science and Engineering Research Council for providing me with the research assistantship through my supervisor.

Finally, I show my sincerest gratitude and pray to almighty Allah for providing me with the strength and support I needed to make my dream come true!

Contents

List of Tables

List of Figures

Chapter 1

Introduction

1.1 Background and Motivation

When wind blows over the water surface of reservoirs, lakes or oceans, it generates a complex flow in the wind driven coupled boundary layers at the air-water interface. The characteristics of this complex flow can be studied on both sides of the interface, i.e. in the air-side boundary layer (ABL) and in the water-side boundary layer (WBL). At very low wind speeds, the flow in the WBL is only comprised of a shear current or the so-called wind drift layer since surface waves do not occur in light winds. As the wind speed increases, surface waves appear and grow, and the flow becomes much more complex due to superimposed wave-induced motions on the wind drift current. At moderate wind speeds, surface waves breaks and an even more complex flow is generated due to the fact that turbulence is superimposed on the wind drift currents and wave orbital motions (Siddiqui & Loewen, 2007).

Wind waves break over a wide variety of length scales, typically ranging from 0.1 to 100 m (Rapp & Melville, 1990). When large scale waves (wavelengths of $\sim$1 m) break, they produce a whitecap because of the significant air entrainment. When small scale waves (wavelengths of $\sim$0.1 to $\sim$1.0 m) break, they often do not entrain air because of surface tension forces prevent air entrainment (Banner & Peregrine, 1993). At short fetches

and at moderate wind speeds (i.e. 4 to 10 m s^{-1}) small scale breaking wind waves are much more wide spread than large scale breaking waves on the surface of reservoirs, lakes or oceans. These short breaking wind waves are defined as microscale breaking waves. The term 'microbreaking', now referred to as microscale wave breaking, was introduced by Banner & Phillips (1974) to describe the breaking of short wind waves without air entrainment. Microscale wave breaking is one of the key mechanisms that generate turbulence beneath the water surface and enhance mass, momentum and energy transfer across the air-water interface (Siddiqui *et al.*, 2001, 2004; Siddiqui & Loewen, 2007; Zappa *et al.*, 2001, 2004; Peirson & Banner, 2003). However, the physical processes that governs the constituent exchange at the air-water interface in the presence of these small scale wind waves are not well understood (Peirson & Banner, 2003). The central motivation of this research was to improve our understanding of the mechanisms that influence the momentum transfer, near-surface turbulence and air-water gas transfer in the coupled boundary layers.

Wind generated waves and currents are important forcing mechanisms for many physical, chemical and biological processes occurring in the near-surface waters of reservoirs, lakes, and oceans. Mixing generated by waves and currents affects the transfer of mass, momentum and energy at the air-water interface (Terray *et al.*, 1996). Accurate measurement of the near-surface flow has proven to be challenging because of the presence of fluctuating waves (Siddiqui & Loewen, 2007). Moreover, lack of control over many environmental parameters such as wind speed, temperature, humidity, and the difficulty in deploying field equipment have made field measurements daunting and prohibitively expensive (Peirson & Banner, 2003). Therefore, much of our understanding has been obtained through well-controlled laboratory experiments (Zappa *et al.*, 2004; Siddiqui & Loewen, 2007).

Many researchers have studied momentum transfer by investigating the partitioning of interfacial stresses across the air-water interface. The partitioning of interfacial stresses refers to the relative contributions of viscous tangential stress and wave-induced stress to the wind stress. The interfacial stresses play a vital role in controlling physical processes such as wind-wave growth and atmospheric circulation (Johnson *et al.*, 1998; Banner & Peirson, 1998; Bourassa, 2000; Lange *et al.*, 2004; Caulliez *et al.*, 2008). However, the physical mechanisms responsible for the momentum transfer at the air-water interface are not yet fully understood and constitute a subject of ongoing research. The surface roughness of coupled boundary layers is also an important parameter that plays a vital role in characterizing wind-wave growth. However, the variation of air-side surface roughness and its influence on wind-wave growth still continues to be the subject of ongoing debate (Donelan, 1990; Johnson *et al.*, 1998; Lange *et al.*, 2004; Drennan *et al.*, 2005). Moreover, studies on water-side surface roughness are scarce.

Natural and synthetic surfactants or surface active agents are present in natural water bodies. Surfactants are of great importance to oceanographers, limnologists and engineers because they change the physical and chemical properties of the coupled boundary layers in the air and water (Davies & Rideal, 1963). The presence of surfactants cause the air-water interface to behave similar to a rigid surface, because the surface stress is too weak to overcome the restoring force of the surfactant monolayer (Frew *et al.*, 2004). In addition, surfactants influence the propagation characteristics of waves and alter the near-surface turbulent length and velocity scales (Mass & Milgram, 1998). These effects are thought to reduce the rate of air-water gas and heat transfer (Saylor *et al.*, 2000). Therefore, the influence of surfactants on the characteristics of wind-waves, sub-surface turbulence, and the rates of momentum transfer at the air-water interface was studied while systematically

varying the surfactant concentration.

Microscale wave breaking is one of the key mechanisms that determine the structure of near-surface turbulence beneath the water surface at low to moderate wind speeds (Siddiqui & Loewen, 2007). The structure of near-surface turbulence can be described by the vertical extent and decay of the rate of dissipation of turbulent kinetic energy in the water column (Terray *et al.*, 1996; Drennan *et al.*, 1996; Siddiqui & Loewen, 2007). However, the mechanisms that control the characteristics of the near-surface turbulent structures are not fully understood. This study investigated the characteristics of the near-surface turbulent structure beneath microscale breaking waves using laboratory wind wave measurements.

Gas transfer across the air-water interface is one of the important processes in the global climate system (Wanninkhof, 1992; Asher *et al.*, 1996). The prediction of net global carbon dioxide (CO_2) uptake by the ocean or the estimation of the rate of aeration in lakes and rivers are significantly uncertain (Takahashi *et al.*, 2002; Richey *et al.*, 2002). One reason for this uncertainty lies in the inaccuracy and difficulty in measuring air-water gas fluxes directly in the field (Zappa *et al.*, 2007). Researchers have developed various empirical relationships for estimating the gas transfer rate across the air-water interface. Wind speed, wind friction velocity, wave slope and near-surface turbulence have been used as parameters in these empirical relationships (Wanninkhof, 1992; Jahne *et al.*, 1987; Frew *et al.*, 2004; Zappa *et al.*, 2007). The laboratory measurements made in this study facilitated direct comparison of various empirical relationships commonly used to parameterize the gas transfer rate.

1.2 Research Objectives and Brief Methodology

The goal of this thesis research was to improve our understanding of the mechanisms that control the momentum transfer, near-surface turbulence and air-water gas transfer in the coupled boundary layers in the presence of short wind waves through a series of controlled laboratory experiments. The specific objectives of this research were to:

1. Study the characteristics of the mean flow in the wind-driven coupled boundary layers in the presence of short wind waves.

2. Determine the effect of the surfactant concentration on the characteristics of wind-driven coupled boundary layers.

3. Examine the near-surface turbulent flow characteristics beneath microscale breaking wind waves.

4. Investigate the dependence of air-water gas transfer rate on short wind waves.

In order to achieve above objectives, a series of laboratory experiments were conducted at the Air-Sea Interaction Research Facility at NASA Goddard Space Flight Center-Wallops Flight Facility (GSFC-WFF) at Wallops Island, Virginia in April-May, 2004. Measurements were made at low to moderate wind speeds ranging from 4.1 to 9.6 m s^{-1} and at three fetches of 4.8, 8.8 and 12.4 m. Experiments were limited to wind speeds less than 10 m s^{-1} mainly because of the fact that in this study the goal was to investigate microscale breaking wind waves that break without entraining any air at wind speeds below $\sim$10 m s^{-1}. Large scale breaking waves that produce a whitecap due to significant air entrainment were beyond the scope of this study. A particle-image based wave profile measurement technique was used to obtain

accurate surface wave profiles. Digital Particle Image Velocimetry (DPIV) technique was used to measure two-dimensional velocity fields beneath the wind waves in a plane parallel to the wind and bisecting the water surface. Additional measurements were made in this experiment by several research groups. These additional measurements included water surface (skin layer) temperature, local heat transfer velocity, and bulk gas transfer velocity (Dr. W. Asher, and Dr. A. Jessup, Applied Physics Laboratory, University of Washington); bulk air temperature, humidity, mean wind velocities, and air-side boundary layer parameters (Dr. C. Zappa, Lamont-Doherty Earth Observatory, Columbia University).

1.3 Organization of the Thesis

A detail description of the experimental setup and laboratory measurements were presented in Chapter 2. The description of a particle-image based surface wave profile measurement technique was presented in Chapter 3 and measurements of the 2-D velocity fields using Digital Particle Image Velocimetry (DPIV) technique were presented in Chapter 4. Detailed discussion of the flow characteristics in the wind drift layer and the transfer of momentum across the air-water interface beneath clean water surfaces were presented in Chapter 5. The effect of a surfactant on the mean flow characteristics of the water-side boundary layer, the momentum transfer across the air-water interface and the turbulent flow characteristics were discussed in Chapter 6. An algorithm for detecting microscale-breaking waves, and the characteristics of microscale-breaking waves and non-breaking waves and its influence on the rate of turbulent kinetic energy dissipation were presented in Chapter 7. The dependence of gas transfer rate on short wind waves was investigated in Chapter 8. Conclusions and recommendations for future work were summarized in Chapter 9.

Chapter 2

The Experimental Conditions, Setup and Procedures

2.1 The Wind-Wave-Current Research Facility

A series of experiments were conducted in the Wind-Wave-Current Research Facility at the NASA Air-Sea Interaction Research Facility, Hydrospheric and Biospheric Sciences Laboratory, NASA Goddard Space Flight Center/Wallops Flight Facility, Observational Science Branch, VA, USA in April-May 2004. A sketch of the wind-wave-current research facility is shown in Figure 2.1. The facility has an overall length of 30.48 m and height of 5.05 m including a 18.29 m long, 1.22 m high and 0.91 m wide main tank section. The tank has two flow loops: the lower loop and the upper loop. The lower loop is for water circulation and the upper loop is a wind tunnel. The lower loop was filled with approximately 31 m^3 of filtered tap water to a depth of 76 cm (referred to as mean water depth) and consequently the air headspace in the wind tunnel was 46 cm. A computer controlled variable speed fan with a flow capacity of 567 m^3 min^{-1} is mounted at the upstream end of the tank that can generate wind up to 18 m s^{-1}. Water current up to 51 cm s^{-1} can be generated in either direction using a variable speed, reversible, water pump with a flow capacity of 15 m^3 min^{-1}. The water can be heated using four commercial spa

heaters and recirculated using pumps through the facility's 40.64 cm pipes. The air temperature can be cooled and humidity can be controlled at cold temperatures using a computer-controlled air-conditioning unit which has a capacity of 9x10^7 cal hr^{-1}. A 10 cm thick plastic honeycomb beach is located at the downwind end of the tank to absorb wave energy.

2.2 Experimental Conditions

Details of the experimental conditions are provided in Table 2.1. Thirty one (31) laboratory experiments were conducted in this study. These experiments were separated into two groups based on water surface cleanliness. The first group, referred to as clean experiments, included twenty-four experiments conducted using filtered tap water and the second group, referred to as surfactant-influenced experiments, included seven experiments conducted using surfactant-influenced water.

Clean experiments were sub-divided into five sets. First three sets of clean experiments were conducted at three fetches of 4.8, 8.8 and 12.4 m. These sets included 18 experiments where six experiments at each fetch were conducted at six wind speeds ranging from 4.1 to 9.6 m s^{-1}. Fourth set included five experiments where high resolution DPIV measurement were made at five wind speeds ranging from 5.4 to 9.3 m s^{-1} and at a fetch of 4.8 m. Fifth set included only one experiment conducted without any wind.

A synthetic surfactant, Triton X-100 (ACROS, Scintillation grade, CAS registry no. 9002-93-1) was added to bulk water to approximate the effects caused by phytoplankton-produced natural surfactants for the surfactant-influenced experiments (Zutic *et al.*, 1981; Botte & Mansutti, 2005). Triton X-100 has been used to model natural water surface contamination in many previous wave studies (Frew *et al.*, 1995; Milgram, 1998; Bock *et al.*, 1999; Lapham *et al.*, 2001; Liu *et al.*, 2007). Surfactant-influenced experiments

were sub-divided into two sets. First set included six experiments where concentration of Triton X-100 was varied from 0.0 to 5.0 gm m^{-3} (parts per million or ppm) at a constant wind speed of 7.9 m s^{-1} and on a fetch of 4.8 m. Second set included only one surfactant-influenced experiment conducted without any wind.

The air and water temperatures inside the tank was controlled independently. Bulk air and water temperatures, and relative humidity were measured for each experiment and are also listed in Table 2.1. The average air-water temperature difference varied from -6.0 °C to 0.1 °C. The relative humidity of air in the wind tunnel varied from 68.5% to 85.3%. For all experiments, a mean current of 6.9 cm s^{-1} was maintained in the direction parallel to the wind.

2.3 Experimental Setup and Instrumentation

A schematic of the experimental setup and instrumentation is shown in Figure 2.2. In this study, wind speed, wind velocity profile, bulk air and water temperatures, relative humidity, two-dimensional sub-surface velocity field, surface wave profile, and Lagrangian surface drift velocity were measured during each experiment. Surface tension measurements were made only for the surfactant-influenced experiments. Gas transfer measurements were made only for the clean experiments. A photograph of the experimental setup and instrumentation is shown in Figure 2.3.

2.3.1 Environmental Measurements

Wind speed and vertical profiles of wind speed were measured using two pitot tubes, one fixed and one vertically traversing, respectively. The fixed pitot tube was mounted at a height of 26 cm below the tank ceiling and the vertically traversing pitot tube was used to profile the wind speed from

a height of approximately 5 cm above the mean water depth to a height of 20 cm. The differential pressure from the pitot tubes were measured using pressure transducers (Setra model 264).

Bulk air temperature was measured using a fixed sensor (Vaisala model HMP45A), and bulk water temperature was measured using a microscale conductivity and temperature sensor (Model 125, Precision Measurement Engineering, Carlsbad, CA). Relative humidity was measured using a vertically traveling sensor (Vaisala model HMP233). Bulk air temperature, relative humidity and wind speeds were sampled at a rate of 50 Hz per channel and bulk water temperature was sampled at a rate of 750 Hz using an eight-channel A/D board (PCI-6024E model, 12 bits, National Instrument). The surface tension of the water was measured using a Cenco-du Noüy tensiometer (Model no. 70535, Central Scientific Company, Chicago, IL) only for the surfactant-influenced experiments.

2.3.2 Digital Particle Image Velocimetry Measurements

A digital particle image velocimetry (DPIV) system was used to measure the two-dimensional (2-D), sub-surface, instantaneous velocity within a given field of view parallel to the wind along the tank center plane and bisecting the water surface (See Figure 2.2). The DPIV system consisted of microscopic tracer particles, a light source, light-sheet optics, a front-surfaced mirror, a digital delay generator, a digital video camera, and a personal computer equipped with a frame grabber card and video recording software. Detail settings for the DPIV measurements are presented in Table 2.2.

Bulk water in the tank was seeded with a mixture of microscopic tracer particles. This mixture contained both Conduct-O-Fil® silver-coated hollow glass spheres (mean diameter of 15 μm; density of 1650 kg m^{-3}) and Potters

Sphericel® un-coated hollow glass spheres (mean diameter of 11 μm; density of 1,100 kg m^{-3}) manufactured by Potters Industries, Valley Forge, PA, USA.

A compact, dual-head, Nd:YAG laser system (Gemini PIV 90-30 Nd:YAG laser system, New Wave Research Inc., Fremont, CA, USA) with a maximum energy output of 90 mJ per 3-5 ns pulse width, operating at a wavelength of 532 nm with a maximum 30 Hz repetition rate was used as the light source. The laser system consisted of a rectangular metal box containing dual-heads (referred to as Nd:YAG laser head), two control panels and dual-power supply. The laser system was mounted on a metal frame located beside the wind-wave-current research facility (see Figures 2.3 and 2.4). The Nd:YAG laser head was oriented such that the longitudinal axis of the laser beam was perpendicular to the front glass of the tank. The Nd:YAG laser head was positioned at a height of approximately 133 cm above the laboratory floor, its front edge was at a distance of approximately 115 cm from the front glass of the tank, and the longitudinal axis of the laser beam was at a distance of 12.4 m from the upwind end of the tank, which was also the longest fetch for this study. Shorter fetches were created by tightly securing the bubble wraps over the water surface covering upwind end of the tank. The laser system generated pulsed, green light source with a beam diameter of approximately 4.5 mm. The percentage of laser energy used to generate pulsed laser light-sheet is provided in Table 2.2.

Two light-sheet optics were mounted on an optical bench using lens holders in front of the laser head as shown in Figure 2.5. The spherical lens (focal length of f = 1 m) was positioned at a distance of 9 cm in front of the Nd:YAG laser head and the plano-cylindrical lens (focal length of f = -19 mm) was positioned at a distance of 5 cm in front of the spherical lens. The laser beam was first passed through the spherical lens in order to reduce the beam diameter and then through the plano-cylindrical lens to transform the

laser beam into a laser-sheet. This two-lens optical combination produced a $\sim$2 mm thick laser light-sheet at the air-water interface.

A front-surfaced mirror was placed underwater above the tank bottom in a custom built mirror holder facing at an angle of approximately 45° with the horizontal plane. The front edge of the mirror holder was placed at a distance of 37 cm from the front glass of the tank. The mirror was aligned such that it deflected the laser light-sheet from the horizontal plane to a vertical plane parallel to the tank center plane and oriented along the direction of wind as shown in Figure 2.2.

A four-channel digital delay generator (model 500A, Berkeley Nucleonics, San Rafael, California) was used to control the timing and separation of the laser light pulses. For these experiments, the pulse separation time was set between 2.5 and 20.0 ms and listed in Table 2.2.

A monochrome, 2-megapixel (1,600 x 1,200 pixels), charge-coupled device (CCD), digital video camera (DS-21-02M30-SA, DALSA®, Waterloo, ON, Canada), referred to as the DPIV camera, was used to image the sub-surface flow field. The camera was mounted on the metal frame using a camera tripod head (see Figure 2.6). It was positioned below the mean water depth such that in normal DPIV resolution the vertical distance from the laboratory floor varied from 176.5 to 182.0 cm and the horizontal distance from the front glass of the tank varied from 95.5 to 114.0 cm depending on the orientation of the DPIV camera. Similarly, in high DPIV resolution the vertical distance from the laboratory floor varied from 164.0 to 172.0 cm and the horizontal distance from the front glass of the tank varied from 146.0 to 149.5 cm depending on the orientation of the DPIV camera. The orientation of the DPIV camera with respect to its longitudinal axis is listed in Table 2.2. The gain and exposure of the DPIV camera were set to 15 dB and external trigger mode, respectively. In normal DPIV resolution, the DPIV camera field of view was approximately

18.9 to 21.7 cm wide and 14.2 to 16.3 cm high producing a resolution of 0.0118 to 0.0136 cm per pixel when using a 75 mm Fujinon® camera lens depending on its horizontal distance from the front glass of the tank. Similarly, in high DPIV resolution, the DPIV camera field of view was 9.8 to 10.0 cm wide and 7.4 to 7.5 cm high producing a resolution of 0.00613 to 0.00625 cm per pixel using a 180 mm Nikon® camera lens depending on its horizontal distance from the front glass of the tank. In low resolution, the DPIV camera field of view was approximately 25.1 cm wide and 33.5 cm high producing a resolution of 0.02094 cm per pixel using a 50 mm Cosmicar® camera lens and when the camera was rotated sideways 90° anti-clockwise.

The DPIV camera was connected to a DVR Express® frame grabber card (Model CL160, IO Industries Inc., Canada) in a Pentium-IV class personal computer (hereinafter referred to as the DPIV computer) using a Camera Link® cable connection. This computer was equipped with a DVR Express® camera interface system and Video Savant 4 software (IO Industries Inc., Canada) running under Microsoft® Windows™ XP. A stripped set array of four high performance SCSI hard disks were directly connected to the frame grabber card. This setup was used to acquire and record digital video images directly from the DPIV camera to the SCSI hard disks at a rate of 30 Hz. The DPIV images were stored permanently as 8-bit gray-scale TIFF images on external hard disks without using any compression.

2.3.3 Wave Profile Measurements

It was almost impossible to accurately locate the exact position of the air-water interface in many DPIV images because of the reflected seed particles that appeared above the interface. The exact position of the interface is required to obtain reliable estimates of the near-surface velocity. Therefore, a second digital video camera (hereinafter referred to as the profile camera) identical

to the DPIV camera was used to locate the exact position of the air-water interface. This camera was used to capture digital images of the surface wave profiles where the laser light-sheet intersected the water surface.

The profile camera was also mounted on the metal frame using another camera tripod head above the DPIV camera (see Figure 2.6). It was positioned above the mean water depth such that the vertical distance from the laboratory floor varied from 219.5 to 220.5 cm and the horizontal distance from the front glass of the tank varied from 95.5 to 107.0 cm. The profile camera was oriented by looking down at an angle of 11° with respect to its longitudinal axis. In this orientation, the field of view of the profile camera was approximately 21.6 to 23.4 cm wide and 16.2 to 17.5 cm high with a resolution of 0.0135 to 0.0146 cm per pixel using a 75 mm Rainbow® camera lens depending on its horizontal distance from the front glass of the tank. The gain and exposure of the profile camera were set to 15 dB and external trigger mode, respectively.

The profile camera was connected to a DVR Express® frame grabber card (Model CL160, IO Industries Inc., Canada) in a Pentium-III class personal computer (hereinafter referred to as the profile computer) using a Camera Link® cable connection. This computer was also equipped with a DVR Express® camera interface system and Video Savant 4 software (IO Industries Inc., Canada) similar to the DPIV computer. Surface wave profile images were acquired and recorded at a rate of 30 Hz using this system. The surface wave profile images were also stored permanently as 8-bit gray-scale TIFF images on external hard disks without using any compression.

2.3.4 Infrared Measurements

The water surface temperature measurements were made using an infrared (IR) imager (FL 640 QLW, AIM Thermography systems, Heilbronn, Germany). The imager is sensitive to IR radiation in the 8-10 μm wavelength

band and has a resolution of 640 x 512 pixels with a 14-bit digital output. The IR imager was mounted on top of the tank such that the distance between the mean water depth and the imager lens was 1.24 m looking down at an incidence angle of 65 ° for all the experiments as shown in Figure 2.2. The field of view of the imager was 45 cm x 36 cm producing a resolution of 0.07 cm per pixel.

The IR imager was calibrated using a precision blackbody (Model 2004S, Santa Barbara Infrared, Santa Barbara, CA) accurate to 0.01 °C with a stability of ±0.003 °C using the procedure similar to Siddiqui *et al.* (2001). The imager was placed 2 mm away from the blackbody and the temperature of the blackbody was varied from 10 °C to 40 °C in increments of 1 °C. The imager was connected to a Microsoft® Windows™ NT based personal computer (hereinafter referred to as IR computer) that was equipped with a digital frame grabber card (Road Runner, Bitflow, Woburn, MA) and Video Savant 3.0 software (IO Industries Inc., Canada). The IR images were stored as a 12-bit digital 'Video Savant video' files at an acquisition rate of 30 Hz on external hard disks.

In order to estimate the Lagrangian surface drift velocity (U_{SL}), two circular heated patches were generated on the water surface using a carbon dioxide (CO_2) laser (Synrad, H48-2-28S, 25 W, 10 μm wavelength) and then tracked in sequences of digital images acquired using the IR imager. The pulse width of the carbon dioxide (CO_2) laser was set at 50 ms and the laser was pulsed at a frequency between 0.5 and 1.0 Hz.

2.3.5 Co-location of the DPIV and Profile Cameras and IR Imager

In order to accurately co-locate the surface wave profiles in the DPIV images a so-called co-location device, and the position of the still air-water interface were used. The co-location device was made from a rectangular metal bar in which

six small L-shaped angles of known thickness and a ruler were attached. The co-location device was mounted on a precision motorized traverse (BISLIDE computer controlled x-z traverse, Velmex Inc., Bloomfield, N.Y.) that could move in both horizontal and vertical directions within an accuracy of $\pm$ 1.8 μm per m.

Prior to each experimental run the traverse was used to position the co-location device at the still air-water interface in such a manner that the angles were visible inside the fields of view of both video cameras and the IR imager. The laser light was used to ensure horizontal alignment of the co-location device. The digital images of the angles, referred to as co-location image, were captured using both video cameras and the IR imager using a 100 W hand held lamp as a light source. The DPIV, profile and IR co-location images are shown in Figures 2.7, 2.8 and 2.9, respectively.

Similarly, the traverse was moved vertically down in the water and up in the air to capture digital images of the ruler using the DPIV and profile cameras, respectively. These images, referred to as field of view (FOV) image, are shown in Figures 2.10 and 2.11. The FOV images were used to determine the fields of view of both cameras and to obtain a conversion factor between the pixel unit and real world unit. The IR co-location image was used to determine the field of view of the IR imager.

In addition, the digital images of the still air-water interface were also captured using both video cameras by illuminating the tracer particles with the laser light-sheet. These images, referred to as still water image, are shown in Figures 2.12 and 2.13. The still water images were used to determine the position of the still air-water interface within the profile and DPIV camera field of view.

2.3.6 Synchronization of the DPIV and Profile Cameras and IR Imager

The synchronization circuit diagram is shown in Figure 2.14. To achieve simultaneous sampling of the DPIV, profile and IR images, both digital video cameras, IR imager, Nd:YAG laser and carbon dioxide (CO_2) laser were synchronized.

The DPIV computer was the primary control hub through which the synchronization process was initiated. In DPIV computer, the CL160 frame grabber card was accessed via DVR Express® Control Signal Manager interface of the Video Savant 4 software and two square wave signals, each with a frequency of 30 Hz and duty cycle of 0.5, were generated. One of the 30 Hz square wave signals was then output through a programmable TTL output line (referred to as TTL OUT1) of the CL160 frame grabber card to operate the IR imager. The other 30 HZ square wave signal was sent directly to the DPIV camera via a camera link connection to operate the DPIV camera. The same 30 Hz square wave signal was also output through another programmable TTL output line (referred to as TTL OUT0) of the CL160 frame grabber card and sent to the 'input' of a custom built divide by 2 circuit. This signal was later used to synchronize the profile camera and Nd:YAG laser.

A T-shaped BNC connector (One male and two female BNC connector) was attached to the 'input' of the divide by 2 circuit that redirected the 30 Hz square wave signal, received from TTL OUT0, in two directions. In one direction, one of the female BNC connections directed the 30 Hz signal to a programmable TTL input line (referred to as TTL IN1) of the CL160 frame grabber card installed in the profile computer, bypassing the divide by 2 circuit. In another direction, the male BNC connection sent the 30 Hz square wave signal through the divide by 2 circuit which simply divided the frequency of the 30 Hz signal by 2 and generated a 15 Hz square wave signal. The 15 Hz

square wave signal was sent to 'Ext/Gate' connection of the delay generator to synchronize the laser.

The profile computer was used as a secondary control hub to synchronize the profile camera and the carbon dioxide (CO_2) laser. The 30 Hz square wave signal, received at TTL IN1, was sent directly to the profile camera via a camera link connection by accessing the CL160 frame grabber card using the DVR Express® Control Signal Manager interface of the Video Savant 4 software. In addition, the same CL160 frame grabber card was used to generate an one (1) Hz square wave signal with a duty cycle of 0.95 to synchronize and operate the carbon dioxide (CO_2) laser.

The 15 Hz square wave signal, received at 'Ext/Gate' connection of the delay generator, was used to program four delay settings (referred to as T_1, T_2, T_3 and T_4) for the four output channels of the delay generator. A typical programming for all four delay settings using T_1, T_2, T_3 and T_4 to produce two laser light-sheet pulses with a separation time of 3 ms for 15 Hz DPIV measurement is presented in Table 2.3. The delay time set in T_1 was sent to Laser 1 Lamp Fire and delay time set in T_2 was sent to Laser 1 Q-Switch Fire. Similarly, the delay time set in T_3 was sent to Laser 2 Lamp Fire and the delay time set in T_4 was sent to Laser 2 Q-Switch Fire. The delay settings of T_1 and T_2, and T_3 and T_4 were used to generate a pair of laser light-sheet pulses at 15 Hz.

An external ON/OFF BNC trigger was connected to the DPIV computer using TTL IN0, to the profile computer using another TTL IN0, and to the IR computer using a TTL IN connection. This trigger was used to start the image acquisition in each computer. The flow chart of the external trigger sequence is shown in Figure 2.15. For each experiment, DPIV, profile and IR images were simultaneously sampled for 10 minutes that consisted of two separate five-minute experimental runs. For each five-minute experimental run, 9000

8-bit DPIV images; 9000 8-bit surface profile images and 9000 12-bit IR images were acquired.

2.3.7 Gas Transfer Measurements

The tank-averaged or bulk gas transfer velocities were measured by applying a conservative mass balance method using Helium (^3He) and Sulfur Hexafluoride (SF_6) as dual tracers for carbon dioxide (CO_2) (Asher *et al.*, 1996; Zappa *et al.*, 2004). In this technique, the tank water was first supersaturated with the tracer gases and then the decrease in their concentration over time was measured.

Gas concentrations were measured by gas chromatography using a thermal conductivity detector (Carle model 1100, Chandler Engineering Company, Tulsa, Oklahoma) for ^3He and an electron capture detector (Hewlett Packard model 5790, Hewlett Packard Company, Palo Alto, California) for SF_6. Both chromatographic measurements of gas concentration had an accuracy of $\pm 4\%$. Three water samples were collected each time at 30-minutes time interval, which were located at the upwind, middle and downwind end of the tank. The duration of each experiment was determined by the gas transfer measurement of ^3He and SF_6 that lasted between 3 and 8 hours.

2.4 Experimental Procedures

The alignment of the pulsed laser light-sheet was checked once prior conducting any experiments for this study. Please note that the Nd:YAG laser system produced a pair of laser light-sheet pulses. The alignment test of the pulsed laser light-sheet was simple. First, the light-sheet optics and the Nd:YAG laser head were positioned as described in §2.3.2. The laser energy was set to 100%. A burn paper was placed in front of the light-sheet optics at a distance of 2.0 m from the spherical lens. Then, the first laser head was pulsed continuously

for 30 seconds at a rate of 15 Hz, which burned the burn paper producing a dark gray line. Thickness of this line was measured using a precision ruler and recorded on the burn paper. Similarly, the second laser head was pulsed continuously for another 30 seconds at a rate of 15 Hz that also produced similar dark gray line overlapping the same location on the burn paper. Next, the overlapped lines were checked visually for any possible misalignment. The thickness of the overlapped lines was then measured using the same precision ruler. The laser light-sheet pulses were considered aligned if the thickness of the overlapped lines remain unchanged. Above alignment test was repeated by placing the burn paper at a distance of 2.4 m from the spherical lens.

The water surface was skimmed continuously about an hour at the beginning of each day prior to the experiments in order to remove accumulated surface contaminants. Skimming operation was performed by lowering the beach at the downwind end of the tank and draining the surface water through an opened drain valve by blowing gentle wind in the wind tunnel over the water surface. Skimming operation reduced the water volume in the tank, therefore, additional filtered tap water was filled into the tank to maintain a water depth of 76 cm. A precision ruler was used to measure water depth of still water in the tank. Moreover, biological activity in the tank was minimized by bromination of 5 ppm levels of dissolving pellets of 1-bromo-3-chloro-5,5-dimethylhydantoin (Bio-Lab Inc., Decatur, Georgia). In addition, the tank water was drained, cleaned and refilled between the groups of experiments.

The surface of the underwater mirror and front glass of the tank (at measurement location) were cleaned prior to each experiment to remove accumulated contaminants. In a few occasion, the underwater mirror was replaced prior to the experiment as the mirror got corroded due to prolonged exposure of laser light-sheet pulses. The rate of corrosion was reduced by overturning the front-surfaced mirror upside down in the mirror holder to

avoid direct contact with the tank water.

Bulk water in the tank was heated daily prior to the experiments. The air in the wind tunnel was cooled and relative humidity of air flow was controlled prior to the experiments. Air-water temperature difference was kept such that a strong thermal signature was obtained for the IR measurements.

Wind and background current were generated by setting up frequencies in a computer-controlled unit. Frequency for wind generation was varied from 19 to 32 Hz to generate wind speed ranging from 4.1 to 9.6 m s^{-1}. Wind was generated to generate surface wave in the tank. Frequency for background current generation was set to 7 Hz to generate current speed of 6.9 cm s^{-1} in the direction parallel to the wind. Background current was generated to well mix the dual tracers used for the gas transfer measurements. Generation of wind and background current was started at least an hour and 20 minutes prior to any experiment. Bulk air temperature, relative humidity and wind speeds were measured for a duration of approximately 1 to 6 hours depending on the duration of the experiments. These measurements were started at least 20 minutes prior to the DPIV, profile and IR measurements. Bulk water temperature was measured over a period of 5 to 20 minutes and started with the DPIV, profile and IR measurements.

Camera settings such as camera angle and direction, gain, frequency and exposure mode for both DPIV and profile cameras were checked prior to each experiment. Moreover, the focus of the camera lenses were checked prior to each experiment. In addition, DPIV and profile cameras were fitted with small fans so that they were not overheated while taking measurements. It was observed that the cameras were malfunctioning when got overheated.

Reflection from the laser light-sheet pulse is a serious issue when conducting any DPIV measurement. Reflection can burn CCD camera chip as well as human eye. It was therefore necessary to eliminate all reflections prior

conducting any DPIV measurement. Reflection occurred mainly due to the presence of steep surface waves and/or when air-bubbles came across the laser light-sheet, if any. In this study, reflections were eliminated by adjusting maximum energy of Nd:YAG laser using an optical attenuator, built in the first control panel. In addition, camera gain in the DPIV and profile cameras was also reduced and set to 15 dB as an added precaution. Reflections from the laser light-sheet pulses were checked prior to each experiment. In order to check the reflection on the camera lenses, following steps were followed. First, camera lenses were covered using lens caps and a piece of black card board was placed in front of the camera lenses. Then the Nd:YAG laser was set to a very low energy, such as 30% of its maximum energy. Next, laser light-sheet was pulsed for approximately five minutes during which energy was increased gradually until occurrence of any reflection was visually observed on the black card board. The highest energy at which no reflection was observed was set as the energy for that particular experiment. Moreover, the metal frame and the front glass of the tank were covered with black card boards and black polyethylene covers keeping two rectangular window open to allow for the passage of laser light-sheet and to capture DPIV and profile images using cameras. In addition, it was also observed that laser light-sheet diffused and created bright glowing environment at the measurement location when it hit the tank ceiling. Therefore, tank ceiling was covered with black felt to reduce the laser light diffusion. Please note that all experiments were conducted in a dark environment by turning all the lights off in the NASA air-sea interaction research facility.

Synchronization of DPIV and profile cameras, and IR imager was checked twice during this study, once at the beginning and once at the end of all experiments. The procedure used for synchronization test was straight forward. First, both the cameras and the IR imager were connected according

to the circuit diagram shown in Figure 2.14 to operate those at a frequency of 30 Hz and focused to take digital images of still water in the tank. Then the laser light-sheet was pulsed manually 15 times over a period of 5 minutes during which DPIV, profile and IR digital images were acquired simultaneously at a rate of 30 Hz using external trigger. Most of the captured digital images in the DPIV and profile cameras and in the IR imager appeared black except for 15 still water images for which the laser light-sheet was pulsed. Now, the frame number of the 15 acquired DPIV, profile and IR images was checked in the Video Savant software. The cameras and the imager were considered synchronized if the frame number of 15 acquired DPIV, profile and IR images matched.

The density of the microscopic tracer particles in the bulk water of the tank was checked prior to all DPIV and wave profile measurements. Please note that skimming operation reduced the number of tracer particles in the tank. In an initial test, it was found that a particle density of approximately 30 to 40 particles in a 32x32 pixels DPIV interrogation window produced optimum results. Therefore, particle density was checked prior to each experiment using two qualitative methods. In first method, average number of tracer particles in a 32x32 pixels DPIV interrogation window in 10 DPIV images were computed using a MatLab routine. In second method, velocity vectors were estimated in a 32x32 pixels DPIV interrogation window using 10 to 20 DPIV image pairs and the quality of the velocity field was checked visually. Tracer particles were added in the tank in steps as required until a particle density between 30 and 40 was obtained and velocity fields appeared satisfactory in an experienced eye.

The separation time between two frame straddling pulses was set based on velocity range and interrogation window size for various experiments. An estimate of the separation time was obtained by dividing half of the DPIV

interrogation window size with the expected maximum streamwise velocity. Estimate of the expected maximum streamwise velocity beneath wind wave at the highest wind speed was obtained from Siddiqui *et al.* (2001) (see their Figure 6). Above calculation was made with the expectation of resolving the velocity field in a 8x8 pixels DPIV interrogation window. This estimated separation time was used for the first run in most of the normal resolution DPIV measurements (see Table 2.2). Moreover, the separation time was reduced to half of the initially estimated separation time for the second run as an added precaution. Similarly, for high and low resolution DPIV measurements a separation time of 2.5 and 20.0 ms was calculated based on the same principle. However, only for few experiments the separation time was slightly varied depending on individual experimental condition. In addition, velocity vectors were estimated in a 32x32 pixels DPIV interrogation window using 10 to 20 DPIV image pairs as a part of particle density check using the estimated separation time to ensure good quality of DPIV measurements.

A particle-image based wave profile measurement technique was developed to find the location of the water surface in the wave profile images. Details of the wave profile measurement technique and its accuracy is presented in Chapter 3.

The bulk water in the tank was seeded with microscopic tracer particles that were assumed to follow the fluid flow. These tracer particles were illuminated by a pulsed laser light-sheet. The movement of these particles for a given time interval was captured on digital video image sequences. An image processing algorithm was then used to compute average displacement of particles within subregions in an image pair. Finally, the instantaneous velocity field was obtained by dividing the particle displacement by the time separation between the two laser pulses. Details of the DPIV measurements and its accuracy is presented in Chapter 4.

The infrared measurements were used to detect microscale breaking waves and to estimate Lagrangian surface drift velocity, (U_{SL}). Microscale breaking waves were detected visually in the IR images by identifying the thermal signature of warm wakes created by microscale wave breaking. Details on the detection of microscale wave breaking using infrared measurements is presented in Chapter 7.

The Lagrangian surface drift velocity, (U_{SL}) was estimated by tracking two circular heated patches that were generated at the water surface using a carbon dioxide (CO_2) laser. In order to generate two circular heated patches, the carbon dioxide (CO_2) laser beam was first split into two separate beams. These two beams produced two heated circular patches of diameter 20 mm to 30 mm at the water surface. These heated circular patches translated over the surface waves and their translations were assumed to provide a good estimate of the Lagrangian surface drift velocity. For each experiment, IR images of these heated circular patches were acquired as a 12-bit digital images with a 30 Hz acquisition rate. An image-processing algorithm similar to the one described by Atmane *et al.* (2004) was applied to the IR image sequences to track each heated patch separately and the coordinates of the centroid of the patch were was used to estimate U_{SL}. Average values of U_{SL} were computed by averaging over 300 to 600 heated patches in an experiment.

In order to calibrate the tensiometer for the surface tension measurements, surface tension of acetone (100% mole) was measured and then compared with the published results of Toryanik & Pogrebnyak (1976) at 21.7 °C and at 22.3 °C. The measured surface tension of the acetone was found 2.75 mN m^{-1} higher than the value reported by Toryanik & Pogrebnyak (1976). Therefore, all surface tension measurements were adjusted to correct for this offset. At least five water samples were collected from the tank during each experiment for the surfactant-influenced experiments. The platinum-iridium ring of the

Cenco-du Noüy tensiometer was cleaned with acetone after each measurement. The average value of the surface tension of clean water was found to be 71.7 mN m^{-1} at 22 °C and this was comparable to the value of 72.6 mN m^{-1} reported by Toryanik & Pogrebnyak (1976). The measured values of the surface tension of the surfactant-influenced experiments at five concentrations are presented in Figure 2.16. This figure shows that the surface tension (σ_T) decreases as the bulk concentration (C) of Triton X-100 increases, as expected.

SL. No.	Experiment Type	Fetch F (m)	Wind Speed U_z (m s^{-1})	Triton X-100 C (ppm)	Air Temperature T_{air} (°C)	Water Temperature T_{water} (°C)	Relative Humidity R_h (%)
1	Clean	4.8	4.1	N/A	18.9	22.8	68.8
2			5.3	N/A	20.6	23.3	76.5
3			6.1	N/A	19.8	22.8	77.4
4			6.8	N/A	22.8	24.4	75.6
5			7.9	N/A	21.5	23.8	80.3
6			9.0	N/A	20.2	22.5	83.4
7	Clean	8.8	4.2	N/A	19.2	22.8	70.4
8			5.4	N/A	21.8	22.1	71.8
9			6.2	N/A	15.6	21.7	73.8
10			7.2	N/A	19.7	21.0	77.7
11			7.9	N/A	21.9	22.2	79.4
12			9.6	N/A	19.9	21.1	81.0
13	Clean	12.4	4.1	N/A	18.4	21.9	68.5
14			5.3	N/A	18.9	23.0	76.1
15			6.2	N/A	18.9	22.0	77.9
16			6.9	N/A	20.1	22.5	80.6
17			7.9	N/A	19.9	22.6	81.6
18			9.2	N/A	19.8	21.8	83.5
19	Clean	4.8	5.4	N/A	20.7	23.7	72.9
20			6.3	N/A	21.2	24.1	79.4
21			6.8	N/A	19.7	22.6	80.1
22			8.0	N/A	21.3	23.3	81.6
23			9.3	N/A	21.2	24.0	85.3
24	Clean	N/A	No Wind	N/A	-	-	-
25	Surfactant-Influenced	4.8	7.9	0.0	22.6	22.5	76.9
26				0.1	22.3	23.9	78.6
27				0.5	21.6	23.7	82.2
28				1.0	20.9	23.4	82.7
29				3.0	20.1	21.5	77.3
30				5.0	19.5	21.4	76.0
31	Surfactant-Influenced	N/A	No Wind	5.0	21.6	22.1	74.0

Table 2.1: Details of the experimental conditions for this study. Bulk air and water temperatures, relative humidity, wind speed, surface wave profile, 2-D digital particle image velocimetry (DPIV) and infrared (IR) measurement were made for all experiments. Surface tension measurements were made only for the surfactant-influenced experiments. Gas transfer measurements were made only for the clean experiments. The parameters F, U_z, C, T_{air}, T_{water} and R_h represent wave fetch, wind speed, surfactant concentration, air temperature, water temperature and relative humidity, respectively. 'N/A' represents not applicable. The short dashed line represents that data are not available.

SL. No.	Run No.	Experiment Type	Fetch F (m)	Wind Speed U_z (m s^{-1})	DPIV Frequency (Hz)	DPIV Resolution	DPIV Camera Orientation Angle (degree)	(direction)	DPIV Camera Lens Type	FOV Hor. (cm)	Vert. (cm)	Pulse Separation Time, Δt (ms)	Laser Energy (%)
1	i ii	Clean	4.8	4.1	15	Normal	4.0	up	75 mm Fujinon	19.3	14.5	6.0 3.0	100
2	i ii			5.3			4.5	up		19.0	14.3	6.0 3.0	76
3	i ii			6.1			4.0	up		19.3	14.5	6.0 3.0	85
4	i ii			6.8			4.5	up		19.3	14.5	6.0 3.0	75
5	i ii			7.9			4.0	up		19.1	14.3	6.0 3.0	45
6	i ii			9.0			4.5	up		19.3	14.5	6.0 3.0	45
7	i ii	Clean	8.8	4.2	15	Normal	2.5	up	75 mm Fujinon	19.2	14.4	8.0 4.0	60 70
8	i ii			5.4			5.5	up		18.9	14.2	6.0 3.0	100
9	i ii			6.2			2.5	up		19.2	14.4	6.0 3.0	70
10	i ii			7.2			2.5	up		19.3	14.5	6.0 3.0	75
11	i ii			7.9			3.0	up		18.9	14.2	7.0 3.0	60
12	i ii			9.6			2.0	down		19.1	14.3	5.0 2.5	52
13	i ii	Clean	12.4	4.1	15	Normal	4.0	up	75 mm Fujinon	19.3	14.5	7.0 3.5	75
14	i ii			5.3			2.5	up		19.3	14.5	6.0 3.0	60 66
15	i ii			6.2			2.5	up		19.3	14.5	6.0 3.0	57 60
16	i ii			6.9			2.5	up		19.2	14.4	6.0 3.0	40 55
17	i ii			7.9			1.0	down		19.2	14.4	6.0 3.0	50
18	i ii			9.2			0.5	up		16.3	21.7	5.0 5.0	40
19	i ii	Clean	4.8	5.4	15	High	6.5	up	180 mm Nikon	10.0	7.5	2.5 2.5	80
20	i ii			6.3			6.0	up		10.0	7.5	2.5 2.5	100
21	i ii			6.8			5.0	up		9.8	7.4	6.0 3.0	100
22	i ii			8.0			6.5	up		10.0	7.5	2.5 2.5	60
23	i ii			9.3			6.5	up		10.0	7.5	2.5 2.5	40
24	N/A	Clean	N/A	No Wind	5	Low	1.5	down	50 mm Cosmicar	25.1	33.5	20.0	100
25	N/A	Surfactant-Influenced	4.8	7.9	15	High	6.5	up	180 mm Nikon	10.0	7.5	2.5	55
26	N/A						6.5	up		10.0	7.5	2.5	75
27	N/A						6.5	up		10.0	7.5	2.5	65
28	N/A						6.5	up		10.0	7.5	2.5	90
29	N/A						7.0	up		10.0	7.5	2.5	95
30	N/A						7.0	up		10.0	7.5	2.5	100
31	N/A	Surfactant-Influenced	N/A	No Wind	15	High	7.0	up	180 mm Nikon	10.0	7.5	5.0	100

Note:

1. Duration of individual run for experiments 1 to 23 consisted of a 5-minutes run. Duration of experiment 24 was for 15-minutes. Duration of experiments 25 to 31 consisted of a 5-minutes run.

2. In experiments 18 and 24, DPIV camera was rotated sideways 90° anti-clockwise.

Table 2.2: Detail settings for the DPIV measurements.

Separation time between two laser pulses, Δt (ms) =	3.0
DPIV or Profile Camera Frame Rate (Hz) =	30

ID	Delay Setting (sec)
T_1 setting for Laser 1: Lamp Fire	0.0150
T_2 setting for Laser 1: Q-Switch Fire	0.0002
First Laser Pulse at:	*0.0152*
T_3 setting for Laser 2: Lamp Fire	0.0180
T_4 setting for Laser 2: Q-Switch Fire	0.0182
Second Laser Pulse at:	*0.0182*

Note:

1. T_1, T_3 and T_4 were set based on same initial time
2. T_2 was set based on its own initial time
3. Laser 1 Adjustable Q-switch Delay = 0.188 ms
4. Laser 2 Adjustable Q-switch Delay = 0.194 ms
5. Delay between External Q-switch Trigger IN and Laser Pulse = 180 ns
6. Delay between External Lamp Trigger IN and Lamp Sync OUT = 9250 ns

Table 2.3: A typical delay setting for all four channels (T_1, T_2, T_3 and T_4) in the delay generator using a separation time of 3.0 ms and a camera frame rate of 30 Hz.

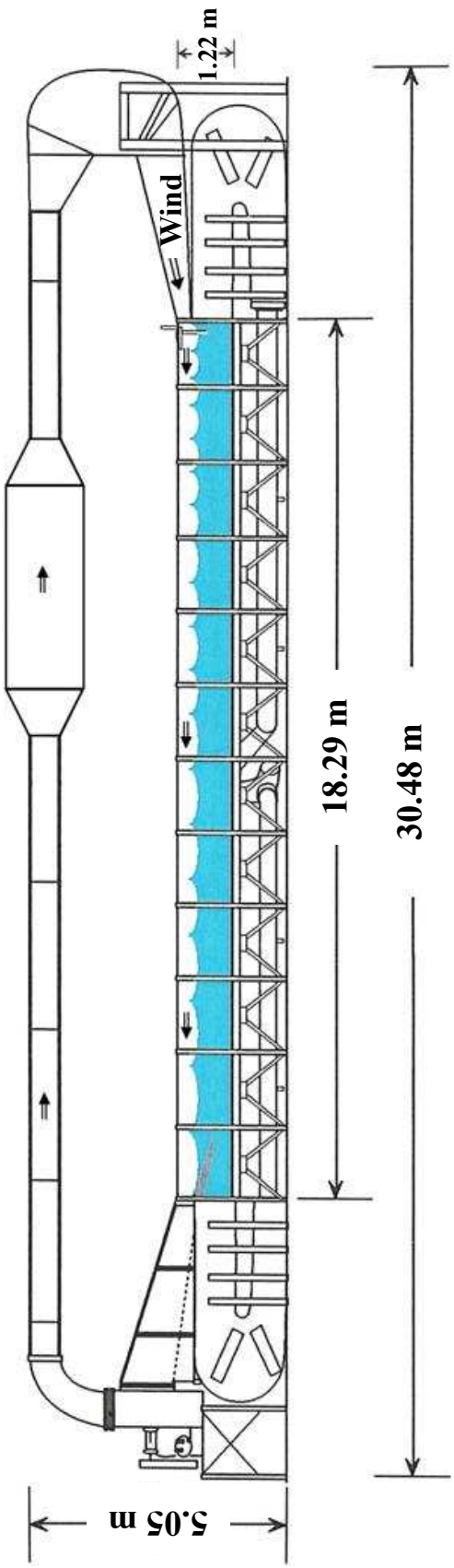

Figure 2.1: Wind-wave-current research facility.

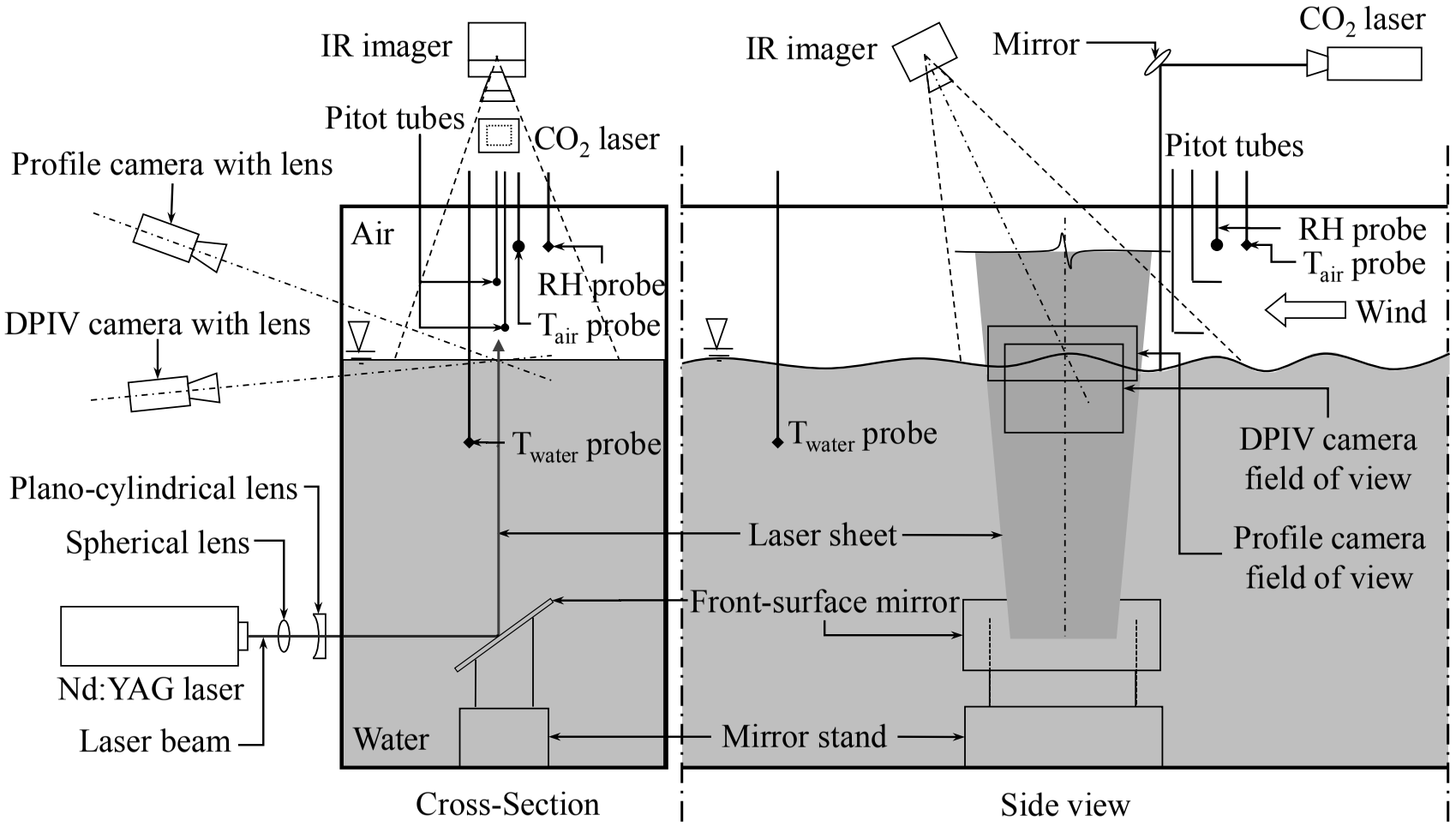

Figure 2.2: Schematic of the experimental setup and instrumentation.

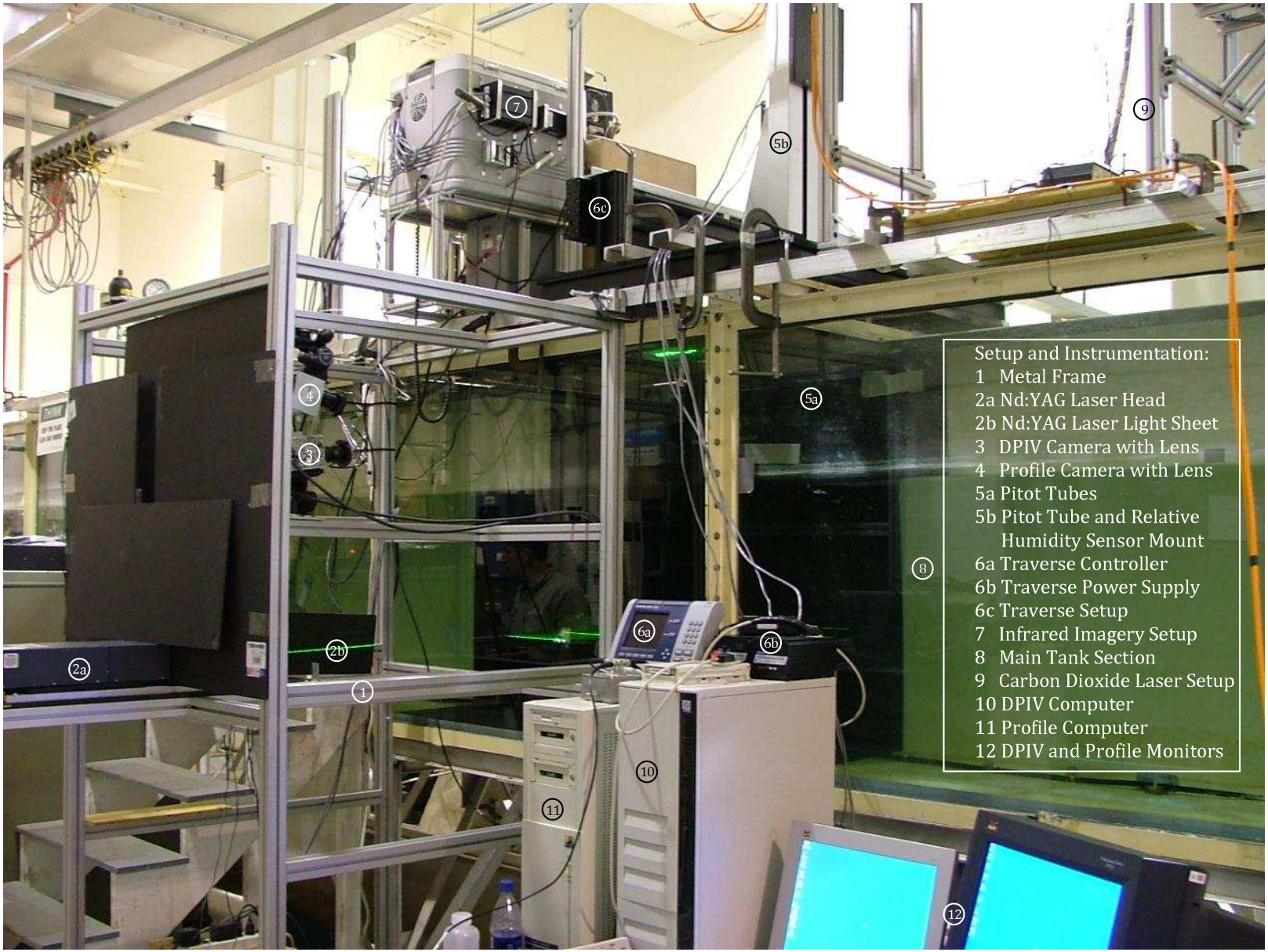

Figure 2.3: A photograph of the experimental setup and instrumentation.

Figure 2.4: A photograph of Nd:YAG laser control panels and dual-power supply.

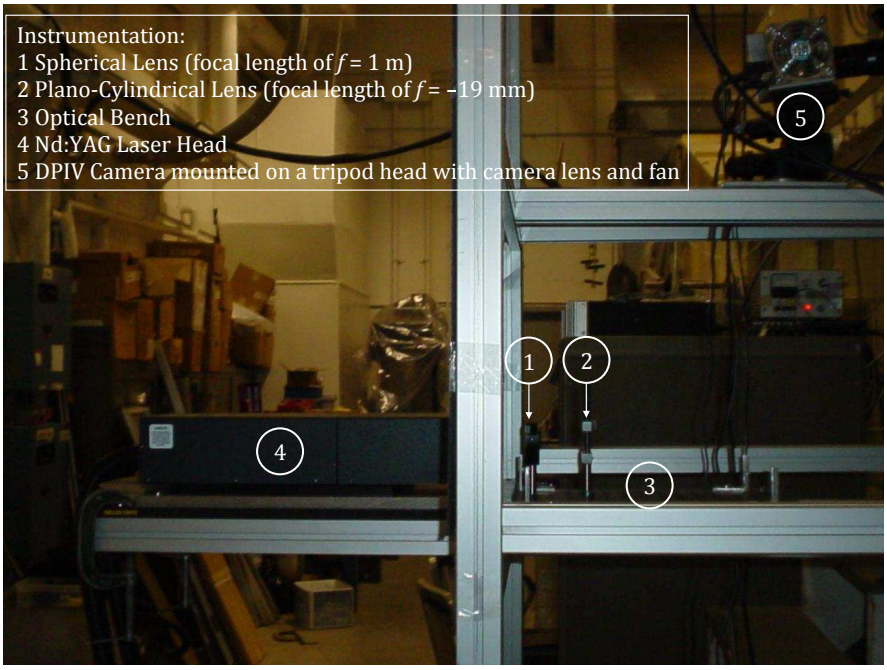

Figure 2.5: A photograph of laser light-sheet optics mounted on an optical bench. This photograph also includes Nd:YAG laser head and DPIV camera.

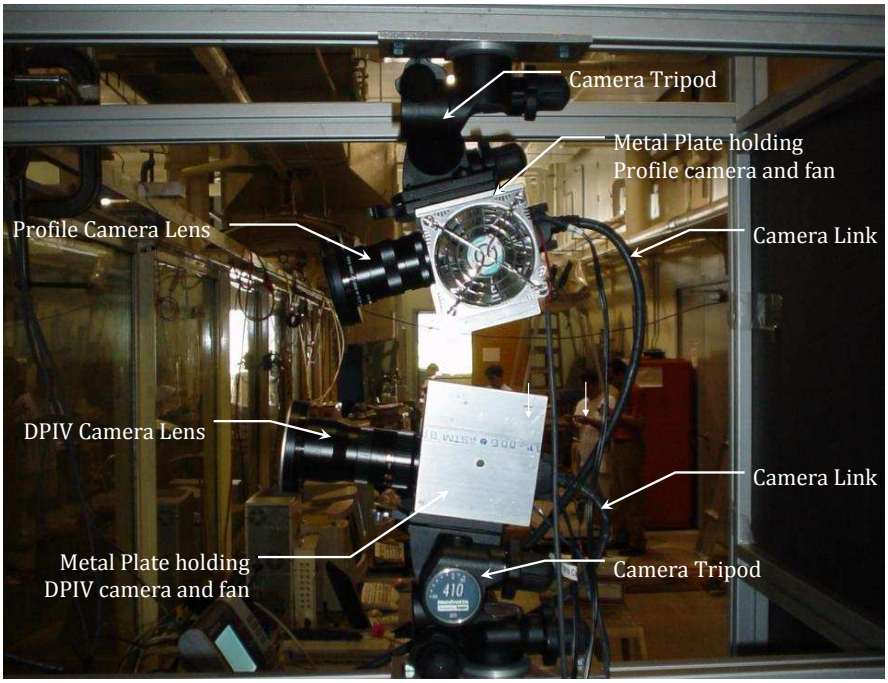

Figure 2.6: A photograph of DPIV and Profile cameras and their setup.

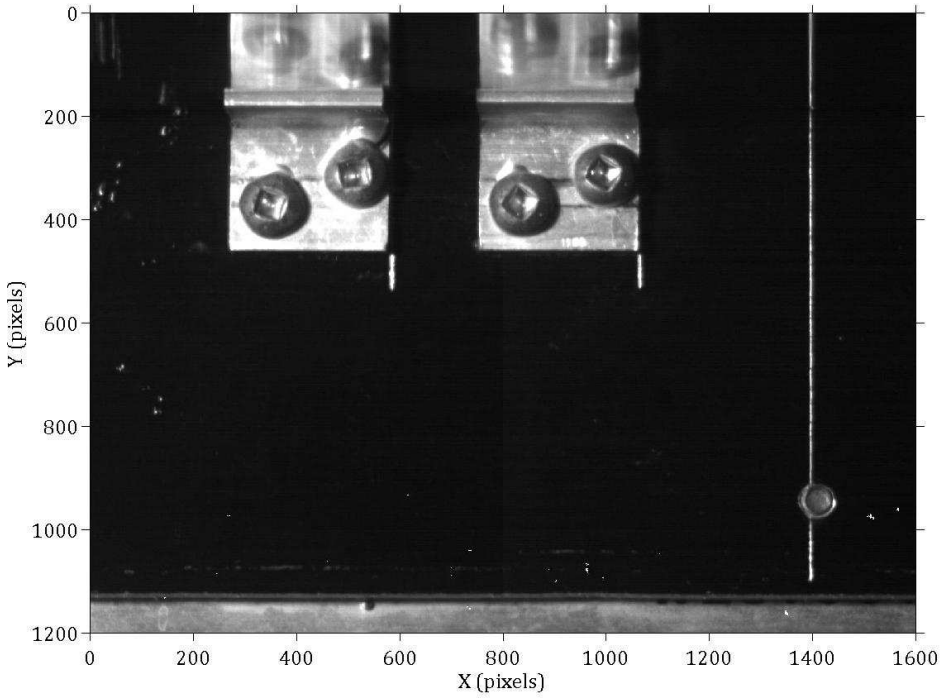

Figure 2.7: A typical DPIV co-location image.

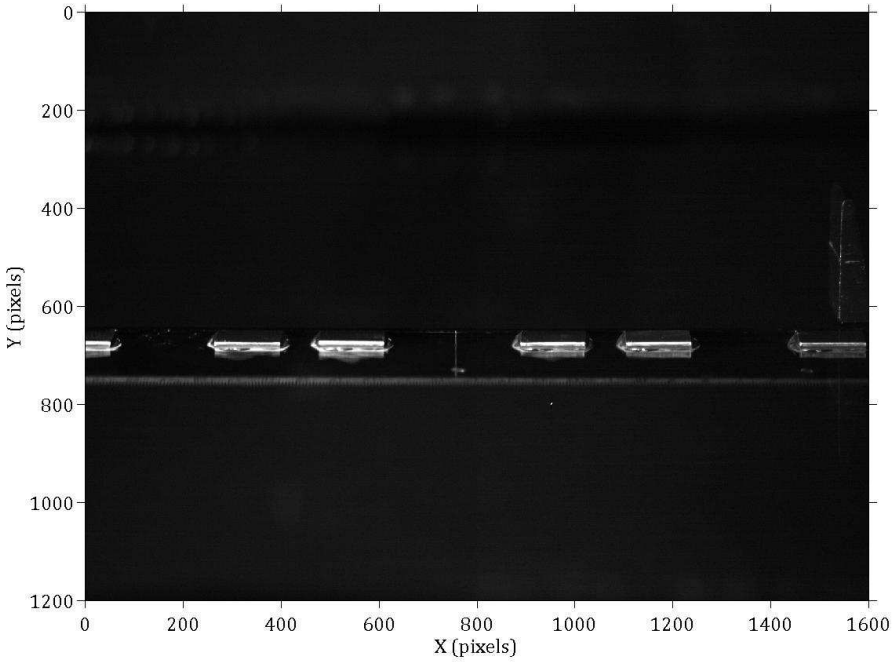

Figure 2.8: A typical profile co-location image.

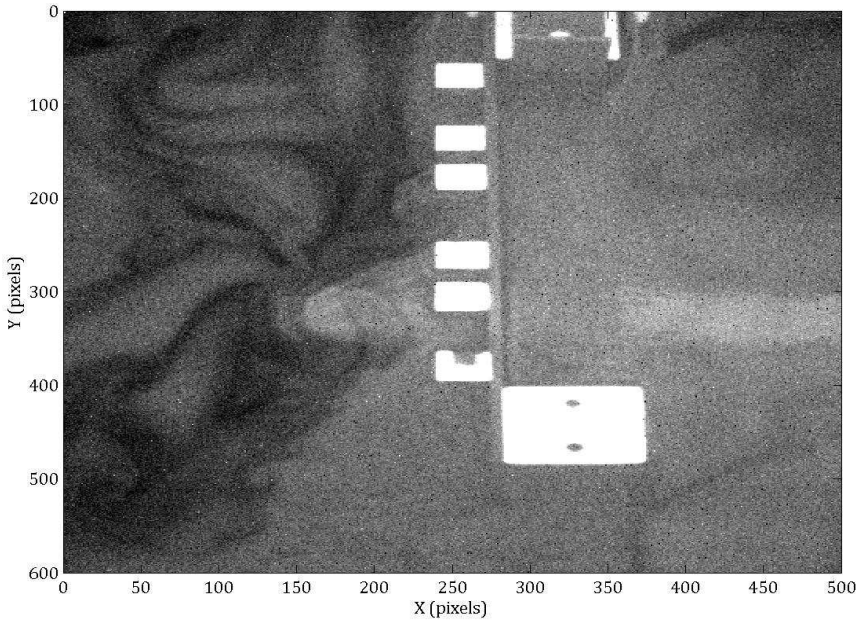

Figure 2.9: A typical IR co-location image.

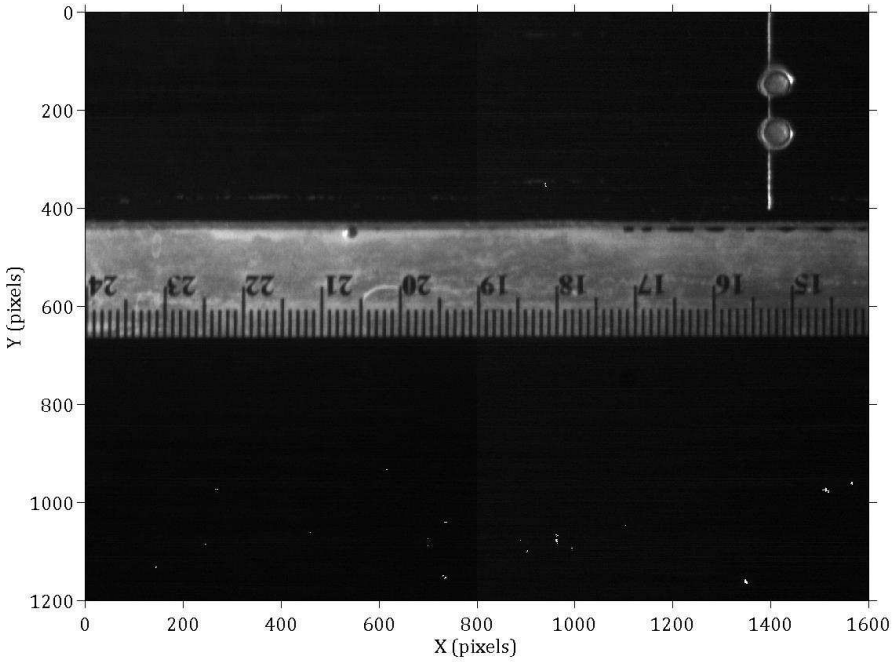

Figure 2.10: A typical DPIV FOV image.

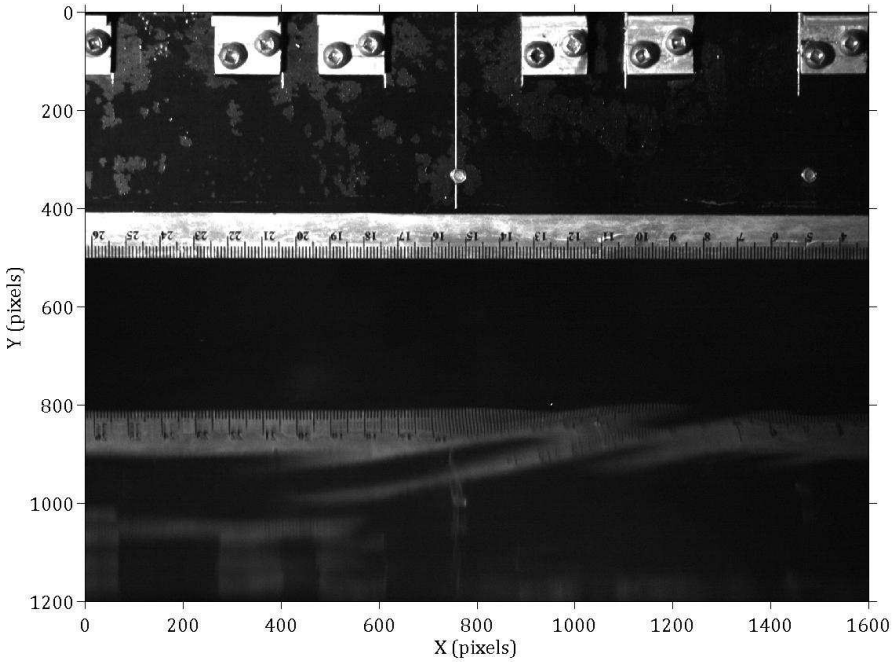

Figure 2.11: A typical profile FOV image.

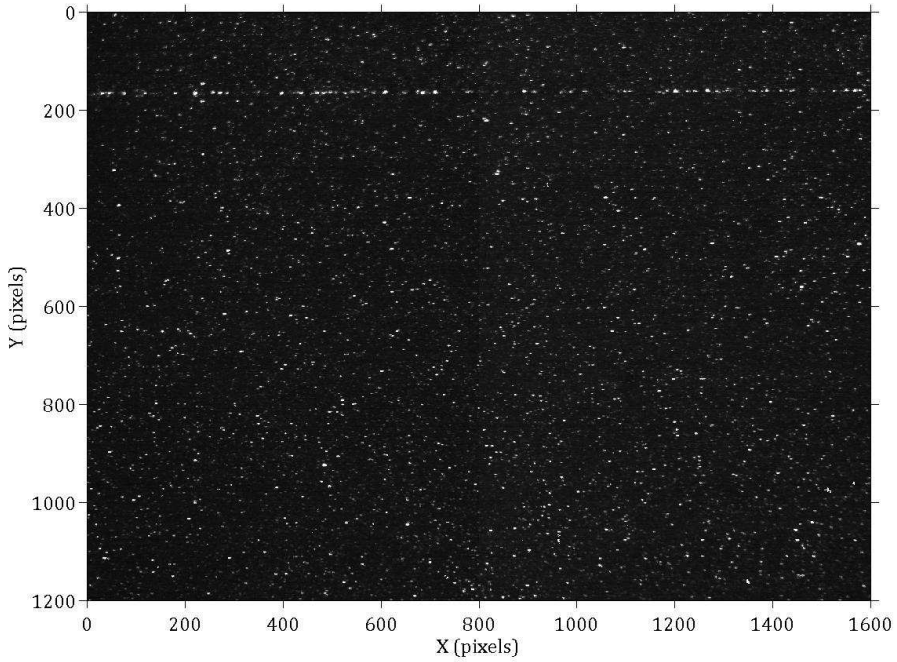

Figure 2.12: A typical DPIV still water image.

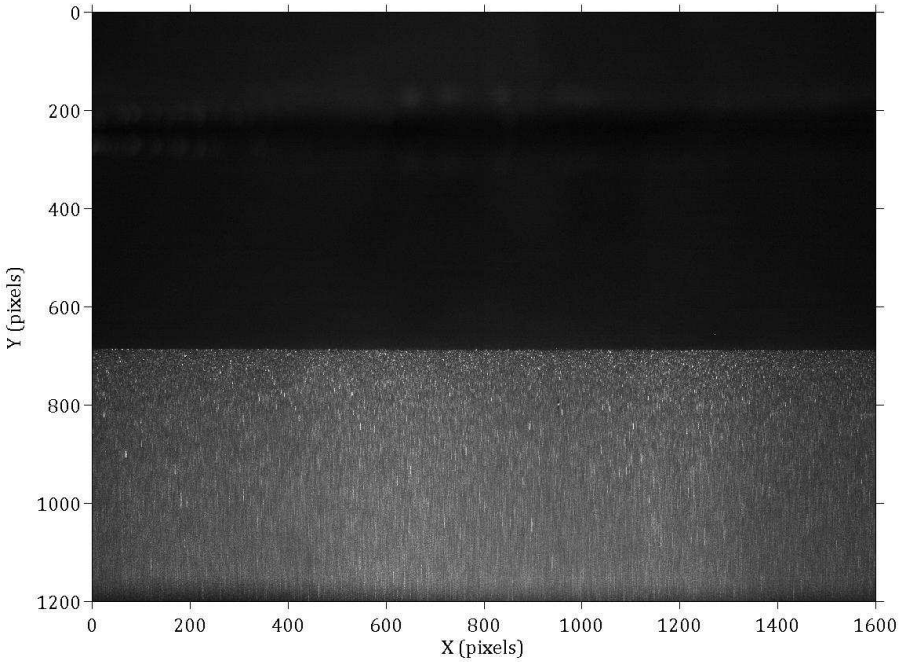

Figure 2.13: A typical profile still water image.

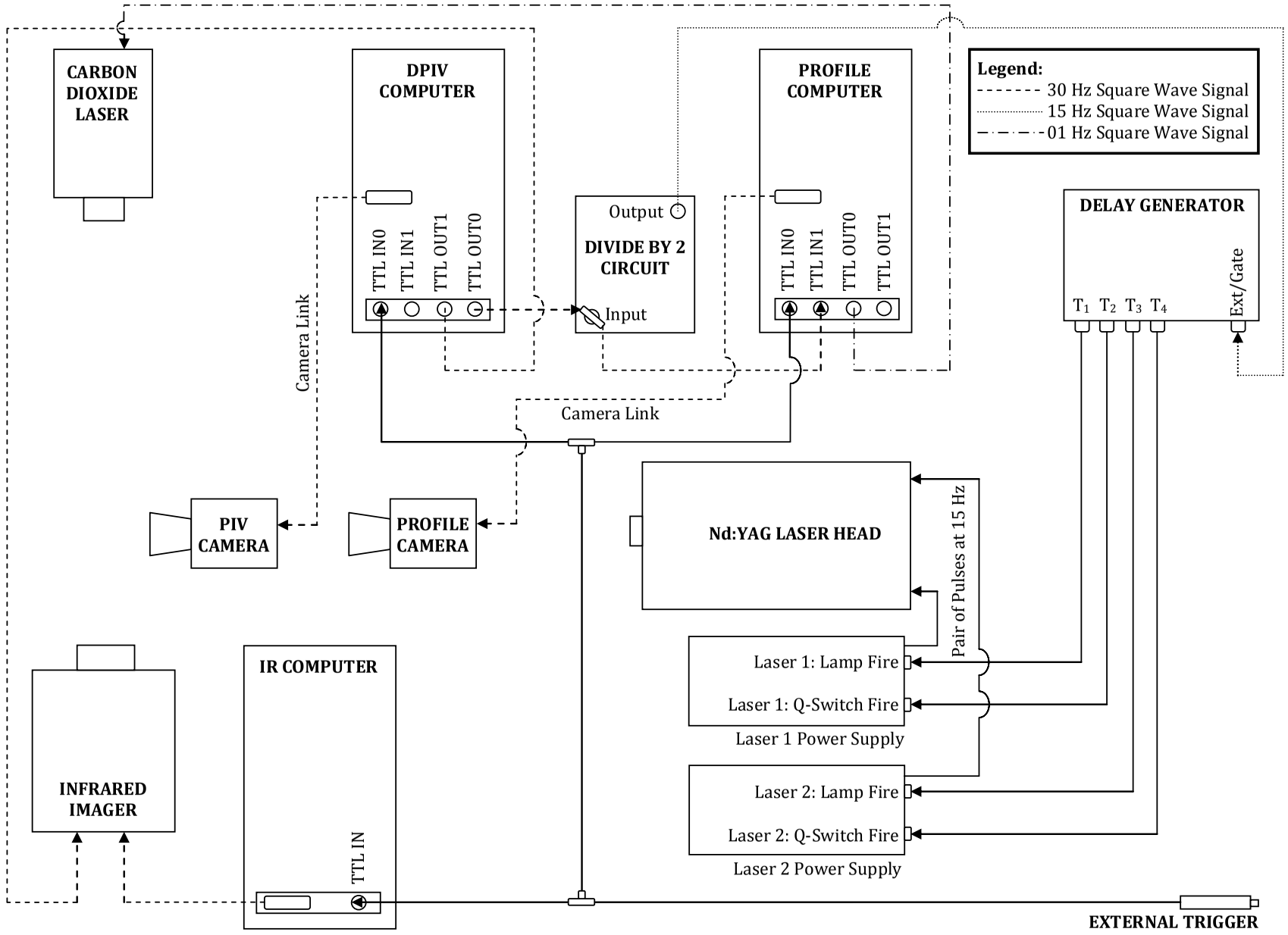

Figure 2.14: A circuit diagram showing the synchronization of the DPIV and profile cameras, IR imager, Nd-YAG laser and carbon dioxide (CO_2) laser. The 30 Hz square wave signals from the DPIV computer were used to synchronize the DPIV and profile cameras, IR imager and Nd-YAG laser. The 1 Hz square wave signal from the Profile computer was used to synchronize the carbon dioxide (CO_2) laser.

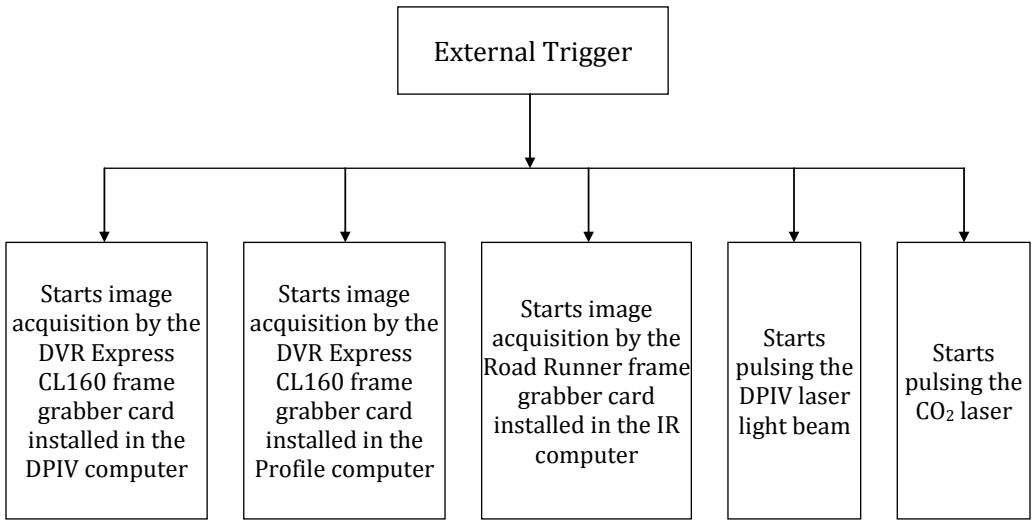

Figure 2.15: A flow chart showing the external trigger sequence. An external ON/OFF BNC trigger was used to start all five operations, simultaneously.

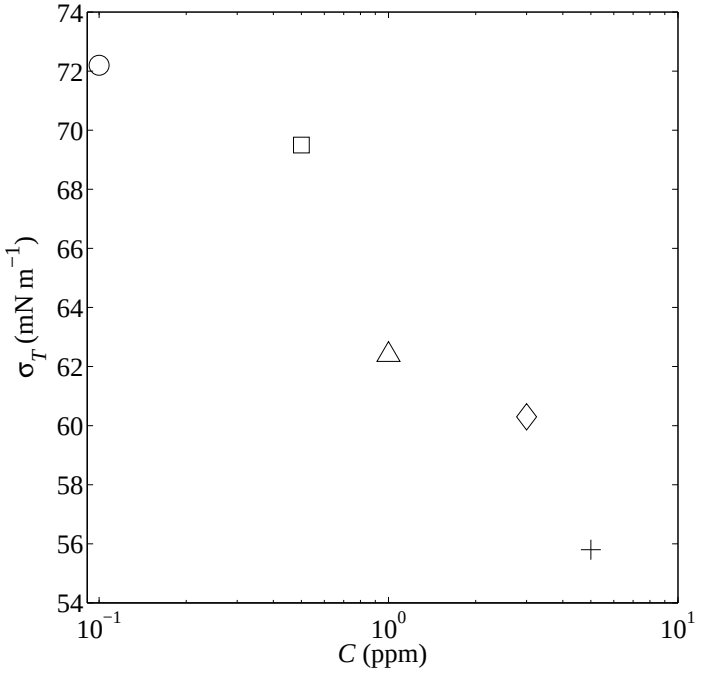

Figure 2.16: A plot of dynamic properties of water surface: surface tension, σ_T, versus surfactant concentration, C. Surface tension of clean water surface, $\sigma_T = 71.7$ mN.m^{-1}; For surfactant-influenced experiments, C (ppm): ○,= 0.1; □,= 0.5; △,= 1.0; ◇,= 3.0; +,= 5.0. All surfactant-influenced experiments were conducted at a constant wind speed of 7.9 m s^{-1} and at a fetch of 4.8 m.

Chapter 3

Development of a Particle-Image based Wave Profile Measurement Technique

3.1 Introduction

Wind generated waves and currents are important forcing mechanisms for many physical, chemical and biological processes occurring in the near-surface waters of oceans and lakes. Mixing generated by waves and currents affects the transfer of mass, momentum and energy across the air-water interface. Study of the interaction of waves and currents and their impact on the above-mentioned processes has been facilitated in recent years with the advent of sophisticated experimental techniques and instruments. For example, Digital Particle Image Velocimetry (DPIV) is a non-intrusive technique, which was used in this study to measure two-dimensional instantaneous subsurface velocity fields beneath surface waves. If velocity measurements are needed immediately beneath the fluctuating free surface, it is essential to have accurate wave profile measurements (i.e. measurements of the water surface elevation

A version of this chapter has been published. Mukto, M. A., Atmane, M. A. and Loewen, M. R. 2007. Exp. in Fluids. 42: 131-142.

that extend over a given horizontal distance) across the entire DPIV field of view. Accurate wave profile measurements are also important when computing surface wave characteristics and are required for making accurate estimates of water-side boundary layer properties beneath surface waves. Despite extensive research on the characteristics of mechanically generated surface waves and wind generated waves, accurate techniques for measuring wave profiles are still lacking.

Water surface elevations are typically measured using conventional instruments such as wire wave gauges, but single-point measurements using wire wave gauges do not capture the instantaneous spatial structure required for near-surface DPIV. Stansell & Macfarlane (2002) and Melville *et al.* (2002) used arrays of wave gauges and DPIV measurements to investigate breaking waves. However, wave gauges are intrusive and as a result, they alter the subsurface velocities if deployed near the DPIV field of view. The experimental technique presented here is non-intrusive and provides both the spatial and temporal displacement of the air-water interface without disrupting the flow field.

Particle-image based wave profile measurements require that the water be seeded with microscopic tracer particles; a light source is used to illuminate the seeded tracer particles; a video camera is used to capture images of the air-water interface from above or below the water surface, and an image-processing algorithm is used to detect the location of the air-water interface or wave profile. A typical wind wave profile image taken using a digital imaging system is shown in Figure 3.1. In this digital gray-scale image, the black portion of the image is air and the gray portion is subsurface water that was seeded with particles. Moreover, for Figure 3.1 and for the rest of the figures where applicable, the X and Y symbols denote the horizontal and vertical dimensions in pixels, respectively.

The focus of this chapter was to report on the accurate measurement of wind generated wave profiles under laboratory conditions. A particle-image based wave profile measurement technique that employs digital imagery and a new detection algorithm referred to as the 'variable threshold method' were presented. The variable threshold method was explained in §3.3 and the accuracy of the particle-image based technique was discussed in §3.4. The unique features of this technique were summarized in §3.5.

3.2 Literature Review

Peirson (1997) used a particle-image based technique to locate the position of the air-water interface by computing the mid-point between a particle and its reflection. He deployed two cameras, one looking down at an angle of 12.5° to measure wave phase and a second looking up at an angle of 7.5° that captured subsurface velocity fields. He employed a multiple pulsed single frame DPIV technique and identified particles at varying distances from the air-water interface using their subsurface reflections in the digital images from the lower camera. However, his technique did not allow him to resolve the rapid movement of the interface because his camera could only capture a surface wave profile image once every 80 ms.

Lin & Perlin (1998) used a Brewster angle imaging technique along with DPIV measurements in a free surface boundary layer investigation. However, they did not provide any information about the accuracy of their wave profile measurements. Law *et al.* (1999) used fluorescent dye instead of seed particles for wave profile measurements. They deployed one camera with two reflecting mirrors to measure wave profiles and to capture images of the seeded subsurface flow beneath the airwater interface. They evaluated the accuracy of their measurement by comparing the root mean square (r.m.s.) interface velocities obtained from their imaging technique to that obtained by a wave height

sensor. They found an uncertainty of approximately ± 5 mm s^{-1} in their r.m.s. interface velocity estimates. However, they did not quantify the spatial accuracy of their measurements.

Siddiqui *et al.* (2001) measured wave profiles using a particle-image based technique similar to the technique presented in this paper. They used a video camera looking down at an angle of 34° that captured digital images similar to the wave profile image shown in Figure 3.1. In their wave profile detection method, a constant threshold value was computed based on the average gray-scale value below the water surface. The vertical location of the water surface was identified as the first pixel that exceeded this threshold value working from the top down along each column in each wave profile image. Their method is referred to as the 'constant threshold method' in this chapter. They obtained an optimized value for the threshold by visually comparing the position of the detected wave profiles in the wave profile images as they varied the threshold value. The uncertainty in the detected wave profiles was estimated to be ± 0.3 mm.

In addition, Siddiqui *et al.* (2001) compared wave properties computed from surface wave profile data with that of the wave gauge data to validate surface wave profile measurements. They conducted a series of experiments at a fetch of 6.3 m and wind speeds of 4.5, 7.5 and 10.7 m s^{-1} in which two wave gauges were placed 1.8 cm apart and approximately 1 mm behind the plane of the laser light sheet. Wave profile images were digitized at a rate of 15 Hz and wave gauge data were also decimated to 15 Hz to produce two compatible time series. They found two essentially identical wave height spectra that were computed from the wave profile data and wave gauge data at all wind speeds. Moreover, they found that the difference in r.m.s wave height and r.m.s wave slope were less than 0.4 mm (3%) and 0.008 (8%), respectively when compared between the two measurement techniques. They concluded that

the profile images can be used to measure water surface profiles accurately. Therefore, a similar particle-image based wave profile measurement technique was developed in this study to measure wave properties.

Zarruk (2005) presented a method for measuring free surface deformation in DPIV images. He deployed a single video camera for the acquisition of DPIV images. The accuracy of his method depends on how well the free surface is illuminated by the laser sheet. He used either the location of the maximum intensity or the location of the maximum gradient in the gray-scale images to locate the air-water interface depending on the quality of the free surface illumination. When the free surface was poorly illuminated, a large number of data points were detected as outliers, which were eliminated using mathematical and statistical tools. He estimated that for well-illuminated free surfaces, the errors in locating the free surface were typically 16 pixels or 4 mm, whereas for poorly illuminated free surfaces, the typical errors were 30 pixels or 7.5 mm.

Wave profile measurements that only locate the air-water interface with an accuracy of 5 mm will not be accurate enough for detailed studies of the water-side boundary layer. In addition, small-scale surface wave features such as capillary waves will only be resolved by methods that can locate the air-water interface with an accuracy of less than a millimeter. Zarruk (2005) results illustrate the problem of trying to locate the air-water interface directly in DPIV images. In the majority of DPIV images the location of the air-water interface cannot be located accurately across the entire field of view. This is demonstrated in Figure 3.2 where a typical DPIV image is displayed in which the location of the air-water interface is ambiguous across most of the image. Therefore, two cameras are required when studying the near-surface flows generated beneath waves; one camera for making wave profile measurements and a second camera for making subsurface velocity measurements. The wave

profile detected in images gathered using the first camera (e.g. see Figure 3.1) can then be scaled and inserted into the DPIV images gathered using the second camera (e.g. see Figure 3.2). Accurate subsurface velocity fields can then be computed by applying a DPIV algorithm to the regions below the air-water interface in the DPIV images.

3.3 Wave Profile Detection

The air-water interface appears as an edge in a typical wave profile image (see Figure 3.1). Consequently, wave profile measurement is essentially the accurate detection of this edge in the digital wave profile images. Law *et al.* (1999) used dye as the tracer to detect wave profiles by locating the maximum intensity gradient in the gray-scale wave profile image. Their technique worked well because dye produces a sharp luminance contrast (i.e. a distinct continuous edge) between the air and the water and therefore, the location of the maximum intensity gradient in the wave profile image coincides with the location of the air-water interface. However, when seed particles are used as the tracer, the location of the maximum intensity gradient in the gray-scale wave profile image may not coincide precisely with the location of the air-water interface due to the non-uniform distribution of seed particles and their density. Therefore, the gradient technique employed by Law *et al.* (1999) will not perform well when seed particles are used as the tracer.

Siddiqui *et al.* (2001) used seed particles as the tracer and then applied a constant threshold value to segment the images and detect the wave profiles. However, use of this so-called constant threshold method may lead to significant errors since for a variety of reasons, wave profile images often suffer from non-uniform illumination. The profile detection algorithm presented in this paper, referred to as the variable threshold method, is an improvement over the standard constant threshold method and differs from

the standard method in two important ways. First, the variable threshold method corrects for non-uniform illumination in the wave profile images by using an optimum average image. Second, the variable threshold method corrects for the non-uniform distribution of seed particles by performing a series of morphological operations.

Generally, gray-scale values in the portion of a wave profile image that is below the water surface were spatially non-uniform (See Figure 3.1). The wave profile images were usually dimmer at the edges compared to the central region due to variations in the laser sheet intensity. The column-wise average gray-scale values are shown plotted in Figure 3.3(a), where the average gray-scale values in each of the 1,600 columns of wave profile images were computed using 3,000 wave profile images. In this figure, the spike at an average gray-scale value of approximately 65 was caused by a few pixels on the CCD chip of the camera that were stuck at pixel values between 8 and 86. The fact that average gray-scale values are 50% smaller at the edges in Figure 3.3(a) demonstrates that the illumination was non-uniform in these digital wave profile images. One way to correct for this non-uniform illumination is to use a threshold that varies spatially across the wave profile image using an average image.

Creation of an average image was simple and straightforward. First, the column-wise average of the gray-scale values of 3,000 wave profile images were computed (see Figure 3.3(a)), and this formed a one by 1,600 vector. Next, a matrix with the same size as the wave profile images (1,200 by 1,600 pixels), was generated in which each row was the column-wise average vector. The result was a 1,200 by 1,600 gray-scale average image as shown in Figure 3.3(b).

The average image can be thought of as a variable threshold created in the form of gray-scale image. When this image is subtracted from the wave profile images, it simultaneously corrects for non-uniform illumination and

applies a threshold to the images. However, it should be pointed out that the average image created as described above may not detect the most accurate wave profiles. To obtain optimal results a scaled version of the average image (i.e. the average image multiplied by a scaling factor) was applied successively to 30 wave profile images using different scaling factors. These 30 wave profile images were randomly selected from an entire experiment consisting of 9,000 or 18,000 wave profile images. The scaling factor was typically varied from 0.3 to 0.9 in increments of 0.1 and the optimum scaling factor was the value that produced the minimum random error or high frequency r.m.s. noise level in the detected wave profiles.

Computing the magnitude of the random errors in detected wave profiles is somewhat arbitrary. Inspection of detected wave profiles indicated that the random errors were associated with higher wavenumbers and therefore, an estimate of the magnitude of the random errors could be obtained by isolating these higher wavenumber signals. The detected wave profiles were examined and the wavelengths of the shortest waves that were resolved accurately by the detection algorithm were identified. The shortest detected waves had wavelengths of 10 pixels or 1.44 mm, which corresponds to a wavenumber of 0.63 radians per pixel. Two wind wave profile images are shown in Figure 3.4 with the detected wave profile plotted in each image. Examples of the shortest waves that could be accurately detected are shown labeled in both Figures 3.4(a) and 3.4(b). Based on this analysis the random noise was defined to be wave profile components with wavenumbers greater than 0.63 radians per pixel. An eighth order high pass digital Butterworth filter with a cut-off wavenumber of 0.63 radians per pixel was then used to filter the detected wave profiles. The r.m.s. of these filtered wave profiles was used as an estimate of the random errors.

The random errors computed in this manner using 30 wave profiles are

plotted in Figure 3.5 as a function of the scaling factor. The minimum errors occurred at a scaling factor of 0.6. The optimum average image was then created by multiplying the average image by the optimum scaling factor of 0.6. Next, this optimum average image was used to process all the wave profile images of an entire experiment. First the optimum average image was subtracted from each of the wave profiles images. The resulting images were then converted to binary profile images using a threshold value of zero. This operation turned pixels in the wave profile images that had gray-scale values greater than zero white and the remainder of the pixels black.

Next, a series of morphological operations were applied to the binary images, which corrected for nonuniform distribution of near-surface seed particles and removed bright reflections caused by bubbles and droplets that appeared above the air-water interface. Morphological operations are based on simple mathematical concepts from set theory and use a binary image (i.e. binary wave profile image) and a structuring element as input. For binary images, white pixels are considered as foreground and black pixels are treated as background. A structuring element is a small binary image typically defined as a three by three square matrix that acts as a mask to change the shape and form of the input binary image. A disk (i.e. 4-connected foreground) and a square (i.e. 8-connected foreground) are the two most common shapes for the structuring elements and both were used in this study. Figure 3.6(a) shows the 4-connected disk-shaped structuring element and Figure 3.6(b) shows the 8-connected square-shaped structuring element. When performing morphological operations, the center of the structuring element is translated over various pixels in the binary image and the pixels of the translated structuring element are compared mathematically with the underlying image pixel values.

The two most basic morphological operators are erosion and dilation and

more complex morphological operators are typically derived from these two basic operators. Dilation progressively enlarges the boundaries of regions containing foreground pixels and the net effect is that the sizes of white areas in the image grow while black areas or holes shrink. The erosion operator erodes the boundaries of areas containing foreground pixels and this shrinks white areas of the image and enlarges holes. Detailed descriptions of these operators can be found in numerous books on digital image processing (e.g. see Jahne (1997)). Filling, closing (i.e. dilation followed by erosion) and opening (i.e. erosion followed by dilation) were the specific morphological operations that were used in this algorithm. These operations were performed using MatLab morphological functions 'bwfill', 'imdilate', and 'imerode' that are available in the Image Processing Toolbox (MatLab version 6.5, MathWorks Inc., Natick, Massachusetts).

The filling operator first identifies the holes (i.e. a set of background pixels that are not connected to the edge of the image) in the input binary image and then, it fills the holes by changing the background pixels within the holes to foreground pixels. To identify the holes, the filling operator performs dilation on the input binary image working from the edges of the image inwards towards the center. In this way, only those background pixels that are connected to the boundary of the image are filled with foreground pixels. The remainder of the background pixels that are not connected to the boundary are left unchanged and these comprise the holes. This dilation procedure is repeated until all of the background pixels that are connected to the edge are filled. The resulting binary image is white everywhere except where there are holes. Next, the complement of this new binary image is computed in which foreground pixels are changed to background pixels and vice versa. Finally, the holes are filled by combining the complement image with the input binary image using a logical 'OR' operator. The 8-connected square-shaped structuring element

(see Figure 3.6(b)) was used when filling.

Closing is dilation followed by erosion and opening is erosion followed by dilation using the same structuring element for both operations. Closing and opening are similar to dilation and erosion, respectively. That is, closing tends to enlarge the boundaries of foreground regions and opening tends to shrink them. However, these more complex operators were used because they are better at preserving the original boundary shape. The 4-connected disk-shaped structuring element (see Figure 3.6(a)) was used when closing and opening operations were performed. The disk-shaped structuring element closely resembled the shape of a particle-image and this helped to preserve the concave or convex shaped boundaries at the air-water interface.

The exact sequence of the morphological operations used to process the wave profile images was filling, closing, opening and filling. The effect of these operations on a typical input binary wave profile image is illustrated in Figure 3.7. Displayed in Figure 3.7(a) is a magnified view of the wave crest region of the original input binary image. In this image, numerous holes are visible just beneath the air-water interface. These holes were caused by the non-uniform distribution of near-surface seed particles. In addition to the holes the non-uniform seed distribution also produces an air-water interface that is rather jagged in places. Also visible in the image are a number of small white spots just above the air-water interface. These spots were caused by laser light that was reflected from small water droplets. The source of these droplets was likely splashing associated with wave breaking or possibly the spray produced by air bubbles bursting at the water surface. The purpose of the morphological operations was to fill the holes, remove the spots above the interface and to reduce the jaggedness of the interface prior to edge detection.

The effect of the filling operation performed with the 8-connected square-structuring element is seen by comparing Figures 3.7(a) and 3.7(b).

In Figure 3.7(b) it can be seen that the filling operation has filled all of the holes in the image. After filling, closing was performed on the modified binary image using the 4-connected disk shaped structuring element. The subtle effect of the closing operation is shown in Figure 3.7(c). The closing operation smoothes the boundary slightly by filling some of the jagged features located at the interface. Next, an opening operation using the 4-connected disk shaped structuring element was performed. The image produced by this operation is displayed in Figure 3.7(d) and it is evident that the primary effect of opening was the removal of all of the white spots above the interface. Finally, a second filling operation was performed as a safeguard to ensure that all holes were completely filled.

Next, a gradient technique was used to detect the position of the air-water interface in the output binary image. After the morphological operations were performed, the air-water interface formed a sharp edge in the output binary image, see Figure 3.7(d). The sharp edge was detected using the first derivative. The first derivative or gradient was computed in the vertical direction (i.e. along each column) in each binary image. The ordinate or vertical location of the maximum gradient in each column was computed and this was the detected location of the air-water interface. Note that the maximum gradient is always one for these binary images. A wave profile detected in this manner is shown plotted on top of the original wave profile image in Figure 3.8.

The morphological operations were not always 100% effective at removing bright reflections and patches that appeared above the air-water interface. Sometimes these bright patches remained above the free surface and caused spikes in the wave profile data. An example of a spike produced by a water droplet is shown in Figure 3.9(a). These spikes were detected and then corrected using a standard despiking technique. In the despiking algorithm,

spikes were detected by applying a threshold to the absolute value of the local slope of the wave profile and the spikes were then corrected using cubic spline interpolation. The slope threshold was set at a value between 10 and 30 pixels per pixel using a trial and error procedure for each experiment. The despiking algorithm was applied to the profile plotted in Figure 3.9(a) and the resulting despiked profile is plotted in Figure 3.9(b). A schematic illustrating all of the computational steps used in the variable threshold method is presented in Figure 3.10.

3.4 Results and Discussion

The accuracy of the particle-image based wave profile measurement technique was assessed in three different ways. First, the magnitudes of the errors were estimated using simulated wave profiles, real still water profiles and real wind wave profiles. Second, the effect of the morphological operations on the accuracy of the technique was determined using simulated binary and real wind wave profile images. Third, a comparison was made between the variable and the constant threshold method to evaluate the accuracy of the variable threshold method using real wind wave profile images.

The errors associated with the technique can be separated into quantization errors, D.C. offsets and all other types of errors. The magnitude of these other errors depends on a variety of experimental conditions including non-uniform illumination, non-uniform distribution of near-surface seed particles and camera noise. Quantization errors occur when the digital video camera digitizes each wave profile image. That is, the exact vertical location of the air-water interface is rounded to the nearest pixel when the image is digitized and this produces a quantization or round-off error. The magnitude of the quantization error was estimated by computing the r.m.s. difference between 'exact' (i.e. real-valued) simulated wave profiles and simulated profiles that

have been 'digitized' by rounding them to the nearest integer.

Exact simulated wave profiles were created by generating wave profiles using the following equation,

$$\eta_{i,m}(x) = a_i \sin(k_i x + \phi_m) \tag{3.1}$$

where, $\eta_{i,m}(x)$ is the surface displacement in pixels, a_i is the wave amplitude in pixels, k_i is the wavenumber in radians per pixel, x is the horizontal dimension in pixels, and ϕ_m is the random phase in radians. For simplicity, the wave slope, $a_i k_i$, was kept constant and set equal to 2.5 in the simulated wave profiles. This slope corresponds to the steepest wave slope found in the detected wave profiles. That is, waves with wavelengths of 10 pixels or 1.44 mm and amplitudes of four pixels or 0.58 mm. This very large wave slope ($a_i k_i = 2.5$) was chosen for this simulation because it was assumed that the steeper wave slopes would produce higher errors (i.e., this produces a conservative estimate of the errors). Thirty-two wavenumbers were selected in the range 0.02-2.5 radians per pixel, which corresponds to wavelengths from 320 (46 mm) to 2.5 (0.36 mm) pixels. Note that wavelength shorter than 2.5 pixels or 0.36 mm with slopes of $a_i k_i = 2.5$ will have amplitudes less than one pixel that cannot be resolved digitally. The 32 wave components were each used to generate 100 simulated wave profiles each with a different random phase, ϕ_m (i.e. subscript m varied from one to 100). This produced a total of 3,200 unique simulated wave profiles each 1,600 pixels in length. These 3,200 simulated wave profiles were used to compute the magnitude of the quantization error by computing the r.m.s. difference between the exact and rounded integer-valued simulated wave profiles. The average r.m.s. quantization error was found to be ± 0.29 pixels or ± 0.04 mm.

D.C. offset is a bias error, which may arise in the course of wave profile detection because of incorrect threshold selection or by improper use of

morphological operations. To assess the magnitude of the D.C. offset and true r.m.s. errors associated with our wave profile detection algorithm ten real still water images with known water surface elevations were used. It was assumed that the magnitude of the D.C. offset in detected real wind wave profiles would be comparable with the D.C. offset computed for the detected still water profiles. The 'exact' location of the air-water interface in the still water images was determined by fitting a straight line to a number of points found manually using the pointing device. Then, the still water profile was detected using the variable threshold method. The profile was detected eight times in each still water image using an average image scaled by factors ranging from 0.5 to 1.2. These still water profiles were then compared with the 'exact' profile by computing the D.C. offset for each detected still water profile. Here, D.C. offset is defined as the mean difference between the 'exact' profile and detected still water profile. In addition, high frequency r.m.s. noise levels and true r.m.s. noise levels were also computed for each detected still water profile. High frequency r.m.s. noise levels were estimated as described previously by applying a high pass filter. True r.m.s. noise levels were computed using the 'exact' still water profiles. In Figure 3.11, the D.C. offsets and high frequency r.m.s. noise levels are plotted as a function of the scaling factor for one still water image. The data in this figure is typical and it shows that the minimum value of the D.C. offset and high frequency r.m.s. noise level occur at the same scaling factor of 0.7 (i.e., the optimum scaling factor). This demonstrates that detecting the wave profiles with the optimum scaling factor minimizes both the D.C. offset and the r.m.s. errors. Note that in Figure 3.11 the magnitude of the minimum D.C. offset was -0.0382 pixels or -0.005 mm considerably smaller than the minimum high frequency r.m.s. error which was 0.4133 pixels or 0.06 mm.

It is interesting to observe that the D.C. offset is large and negative (i.e.,

the detected profile is above the true location) when the scaling factor is 0.5. As the scaling factor increases the D.C. offset decreases rapidly and is slightly less than zero at a scaling factor of 0.7 and then becomes positive (i.e., the detected profile is below the true location) as the scaling factor increases. The mean absolute bias error was found to be 0.07 pixels or 0.01 mm using profiles detected in ten still water images. For these detected still water profiles, the average high frequency r.m.s. error was estimated to be 0.42 pixels or 0.06 mm. The average value of the true r.m.s. error for these profiles was found to be 0.88 pixels or 0.13 mm which is approximately a factor of two larger than the high frequency r.m.s. error. The correlation coefficient between the high frequency r.m.s. error and the true r.m.s. error was 0.70. This indicates that reasonable estimates of the true r.m.s. error can be made when detecting real wind wave profiles by computing the high frequency r.m.s. error and then simply multiplying by a factor of two. This is important because when detecting real wind wave profiles there are no other practical ways to estimate the r.m.s. error because the true location of the wind wave profile is unknown.

To estimate the magnitude of all other types of errors, 3,200 real wind wave profiles were detected in wave profile images using the variable threshold method. The high frequency noise levels were computed as described previously by applying a high pass filter to the detected profiles. For these real wind wave profiles, the average high frequency r.m.s. error was found to be ± 0.43 pixels (± 0.06 mm), which includes the quantization error. Therefore, the magnitude of all other types of errors, excluding quantization errors, was found to be ± 0.32 pixels (± 0.05 mm). This translates into an average true r.m.s. error of ± 0.64 pixels (± 0.09 mm). Note that the average true r.m.s. error for these real wind wave profiles should be similar to that of the still water profiles because the high frequency r.m.s. errors were comparable.

The morphological operations alter the detected wave profiles in a manner

similar to a low pass filter. The first step in quantifying this effect was to create 3,200 simulated binary profile images using the profiles created using Equation (3.1). The binary profile images were used because the only errors incurred when processing these types of images will be caused by the morphological operations. The variable threshold algorithm was then used to detect the profiles in these 3,200 binary images. The percentage difference between wavenumber spectra of the integer-valued simulated wave profiles and the detected wave profiles was computed. The percentage error (i.e. difference) in the wavenumber spectrum of the detected profiles is shown plotted in Figure 3.12. This figure shows that the morphological operations do not significantly alter waves with wavenumbers less than approximately 0.3 radians per pixel or wavelengths longer than 21 pixels or 3 mm. For a wavenumber of 0.63 radians per pixel or a wavelength of 10 pixels or 1.44 mm, the morphological operations caused an error of approximately 22% in the wavenumber spectrum. Note that a 22% error in the wavenumber spectrum corresponds to a 10% r.m.s. error in the wave amplitude. The positive percentage errors in Figure 3.12 confirm that the morphological operations act as a low pass filter as this operation reduced the wave amplitudes in the detected profiles.

Real wind wave profile images were used to quantify the benefits of using the morphological operations. The average high frequency r.m.s. errors computed before and after the application of the morphological operations using real wind wave profiles were found to be ± 2.03 pixels (± 0.29 mm) and ± 0.43 pixels (± 0.06 mm), respectively. Therefore, the morphological operations reduced the random errors approximately by a factor of five when detecting real wind wave profiles. However, because the morphological operations act like a low-pass filter they do reduce the amplitudes of waves shorter than 10 pixels or 1.44 mm by 10% or more.

The accuracy of the variable threshold method was compared to the accuracy of the constant threshold method by applying these two methods to 9,000 real wind wave profile images. In Figures 3.13(a) and 3.13(b), wave profiles detected at a wind speed of 9.3 m s^{-1} and a fetch of 4.8 m using the constant and variable threshold methods are compared. The wind wave profile detected using the constant threshold method (Figure 3.13(a)) is clearly less accurate compared to the wave profile detected using the variable threshold method (Figure 3.13(b)). Figure 3.13 also shows that the variable threshold method was better at detecting the small-scale features in the profiles such as the capillary waves that were formed and riding on the forward face of the wind wave. In addition, because the constant threshold method does not correct for non-uniform illumination, the detected wave profile in Figure 3.13(a) has large random errors near the edges of the image. Finally, the average high frequency r.m.s. error (i.e. noise level) in the profiles detected using the variable threshold and constant threshold methods at this wind speed and fetch were ± 0.43 pixels (± 0.06 mm) and ± 1.45 pixels (± 0.21 mm) respectively. Therefore, the variable threshold method reduced the error by a factor of approximately 3.5 compared to the constant threshold method.

The variable threshold method was applied to the profile images gathered at all wind speeds ranging from approximately 4.1 to 9.6 m s^{-1} and at all the three fetches. The average high frequency r.m.s. errors in the detected real wind wave profiles for all these experimental runs were found to vary from ± 0.36 (± 0.05 mm) to ± 0.57 (± 0.08 mm) pixels. This corresponds to average true r.m.s. errors that varied from approximately ± 0.7 (± 0.1 mm) to ± 1.1 (± 0.16 mm) pixels. It should be noted that the variable threshold method occasionally failed to accurately detect the wind wave profile in a particular image. These failures typically occurred when an energetic breaking wave was in the field of view of the camera. These energetic breaking events

may generate spray, entrain air or create a free surface geometry that is too tortuous. The algorithm then fails because the air-water interface no longer coincides with a single distinct edge in the image. The number of failures increased with wind speed and fetch because more of these energetic breaking waves tended to occur at longer fetches and higher wind speeds. The total percentage of failures was always less than 1% in any experimental run.

3.5 Conclusion

A particle-image based wave profile measurement technique was developed to measure wave profiles in digital monochrome images. The algorithm presented here, referred to as the variable threshold method, corrected for non-uniform illumination and non-uniform distribution of near-surface seed particles. The technique accurately detected wind generated waves as short as 10 pixels (1.44 mm) in wavelength. Simulated and real wind wave profiles and real still water profiles were used to assess the accuracy of the measurement technique. The average r.m.s. quantization error was estimated to be ± 0.29 pixels (± 0.04 mm), the bias error or D.C. offset was found to be negligible and the magnitude of all other types of high frequency errors was estimated to be ± 0.32 pixels (± 0.05 mm). True r.m.s. error was found to be a factor of two larger than the high frequency r.m.s. error. Although the morphological operations used to correct for non-uniform distribution of near-surface seed particles effectively low-pass filter waves shorter than 10 pixels (1.44 mm), they improved the accuracy of the detected wave profiles by up to a factor of five. The variable threshold method and the constant threshold method were compared using real wind wave profile images. This comparison demonstrated that the variable threshold method was approximately 3.5 times more accurate than the constant threshold method and had true r.m.s. error that varied from approximately ± 0.7 (± 0.1 mm) to ± 1.1 (± 0.16 mm) pixels.

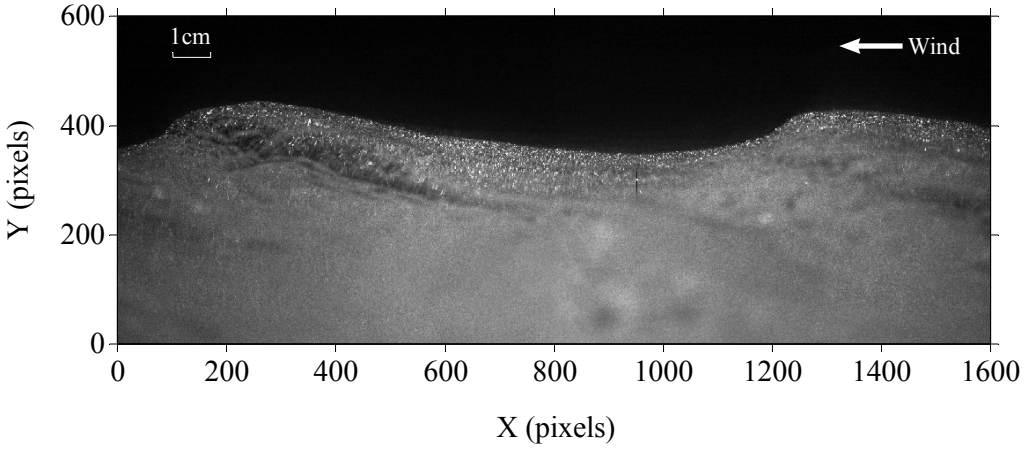

Figure 3.1: A typical digital wind wave profile image.

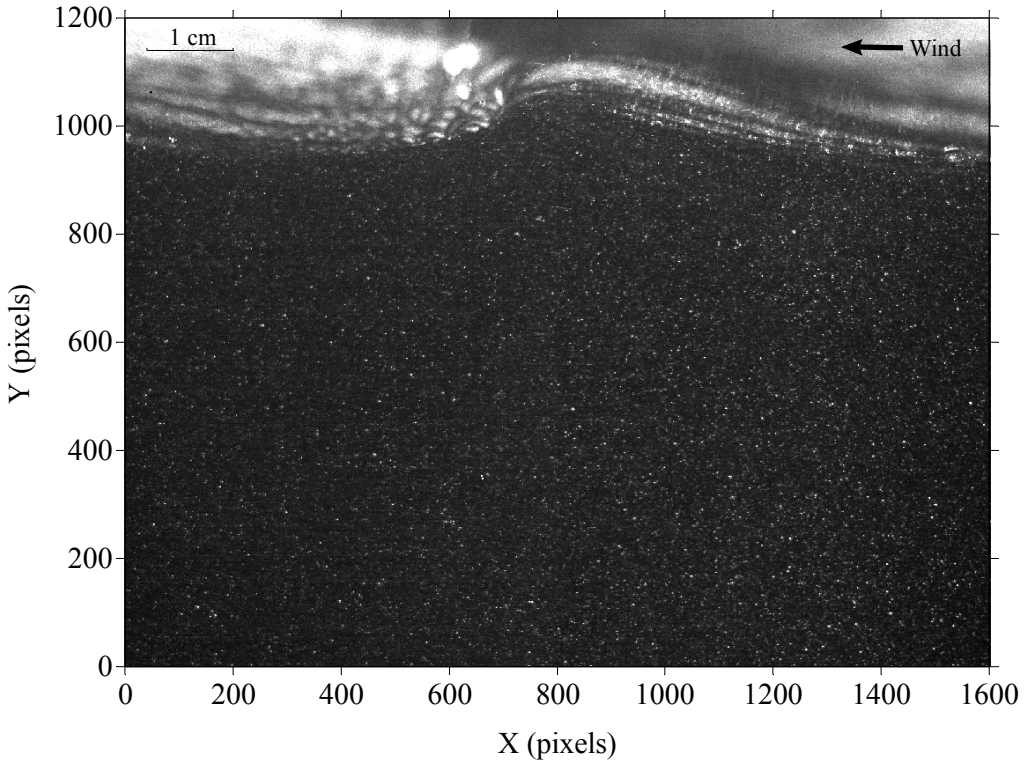

Figure 3.2: A typical DPIV image.

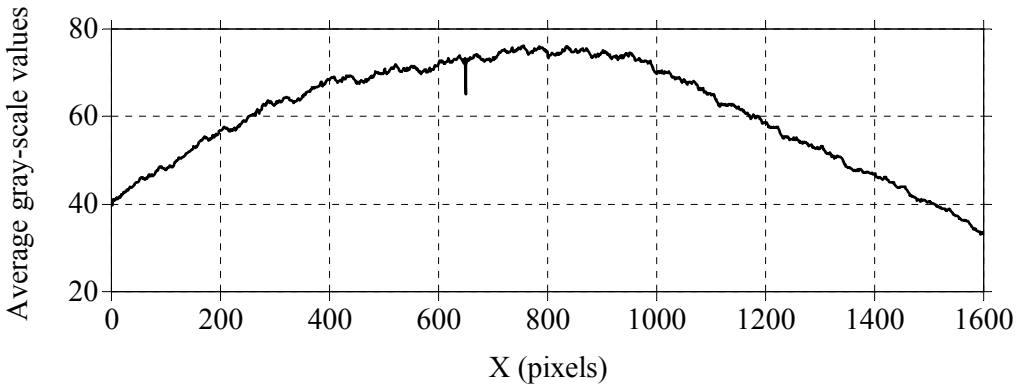

(a)

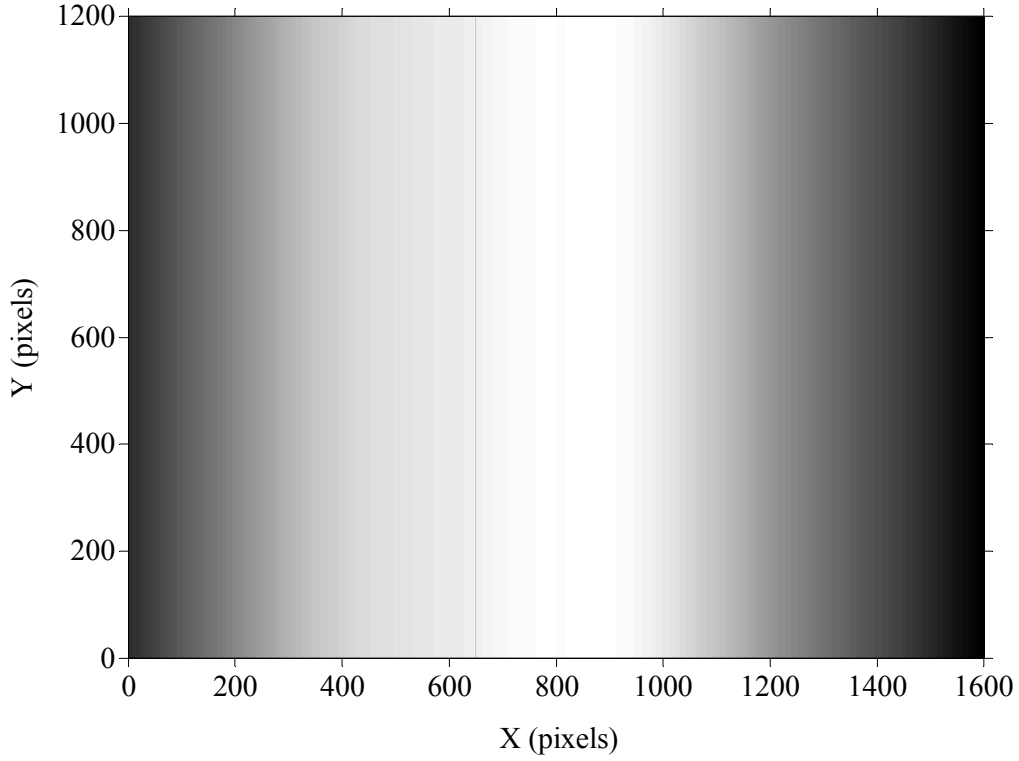

(b)

Figure 3.3: Top plot (a) shows column-wise average of the gray-scale values obtained using 3,000 wind wave profile images illustrating the non-uniform illumination. The bottom plot (b) shows a typical 1,200 by 1,600 pixel average image.

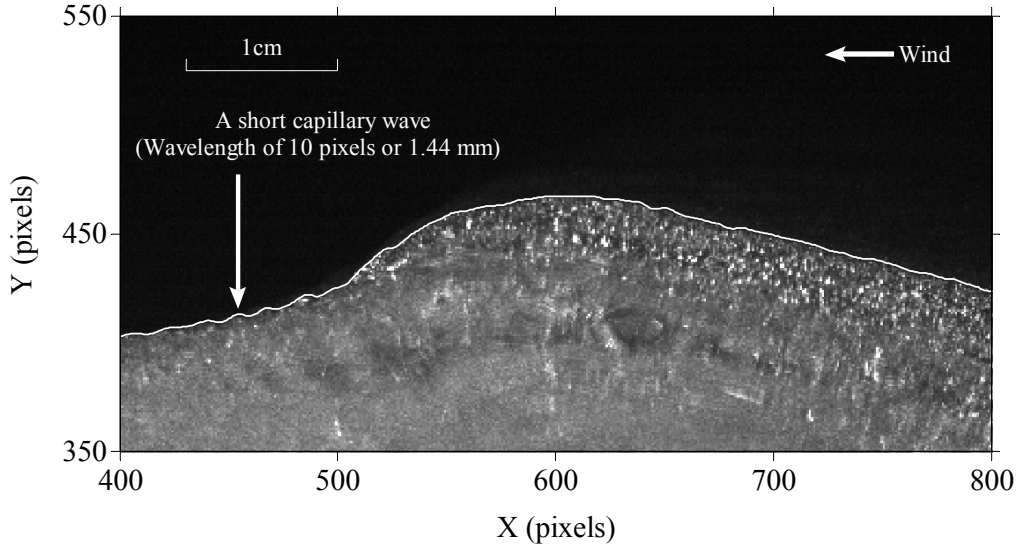

(a)

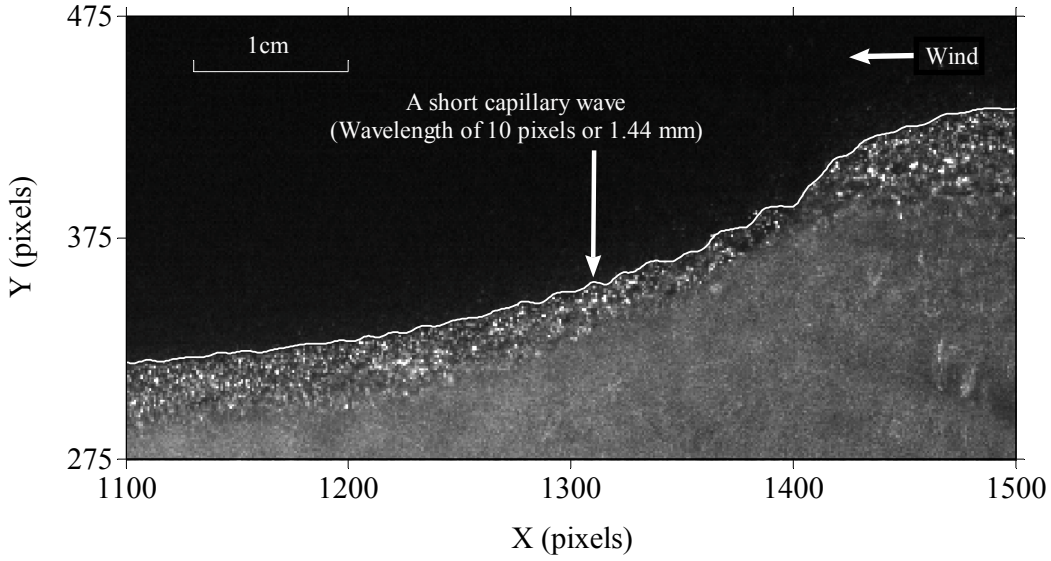

(b)

Figure 3.4: Wind wave profile images (a) and (b) showing the shortest wavelength capillary waves that are accurately detected using the variable threshold method.

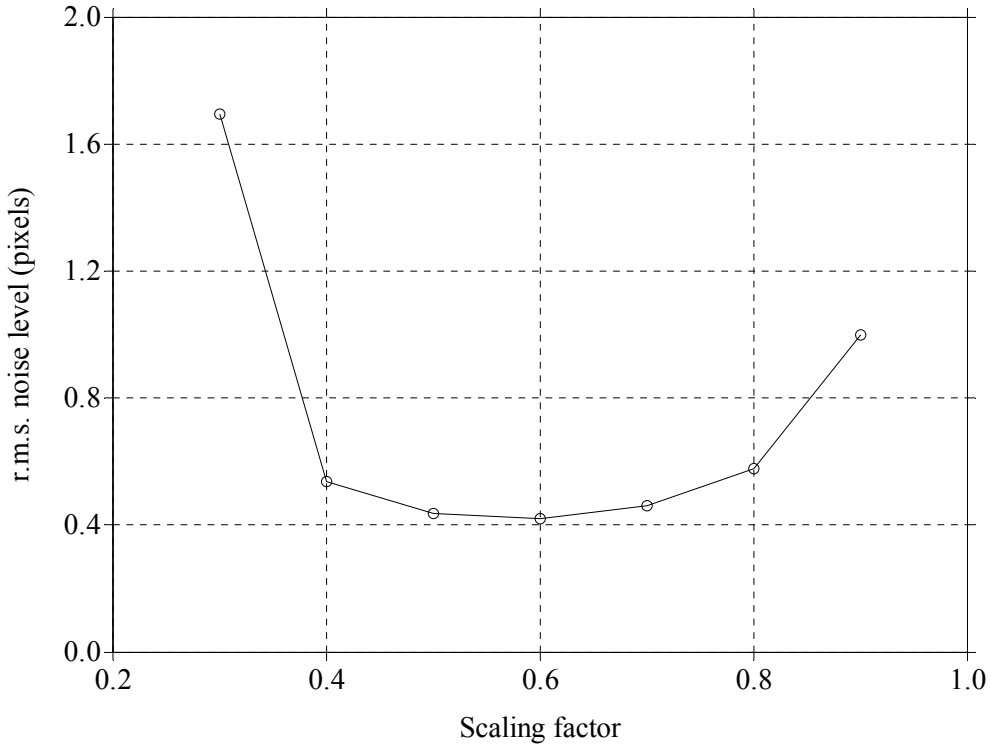

Figure 3.5: The random errors or noise level computed from 30 wave profiles detected using the variable threshold method plotted as a function of the scaling factor.

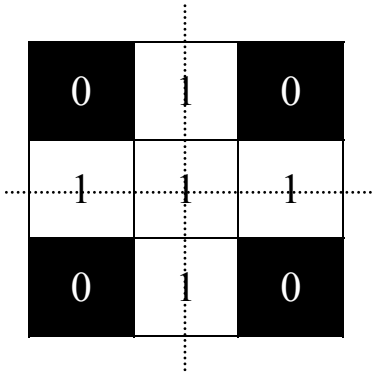

(a)

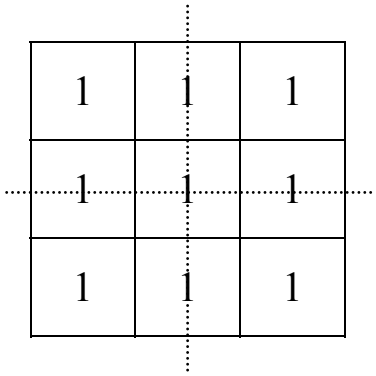

(b)

Figure 3.6: (a) A three by three disk shaped structuring element with 4-connected foreground. (b) A three by three square structuring element with 8-connected foreground.

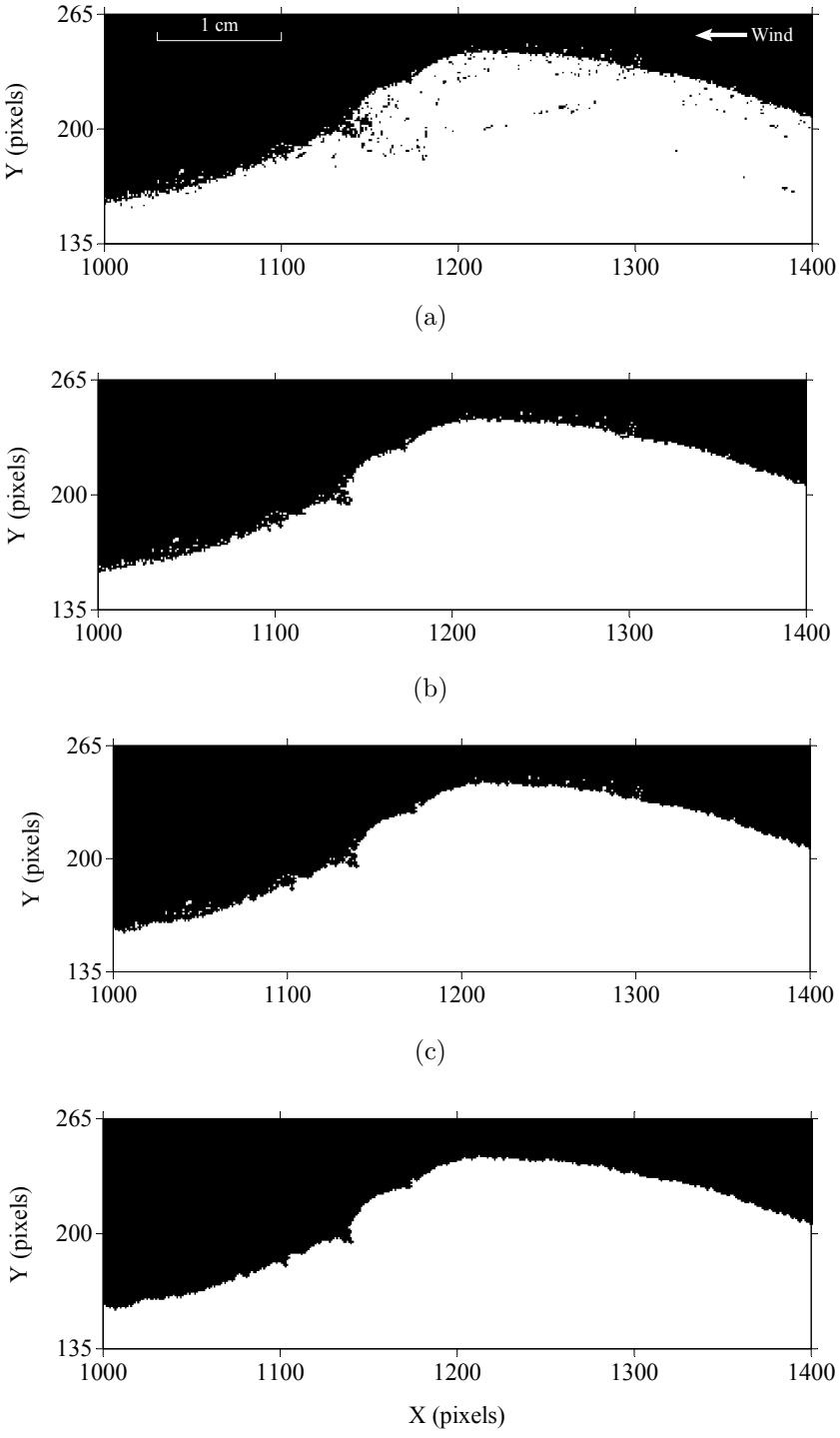

Figure 3.7: Image sequence (a) to (d) illustrating the effect of morphological operations on a binary wave profile image; (a) original binary wave profile image, (b) binary image after filling, (c) binary image after closing, and (d) binary image after opening.

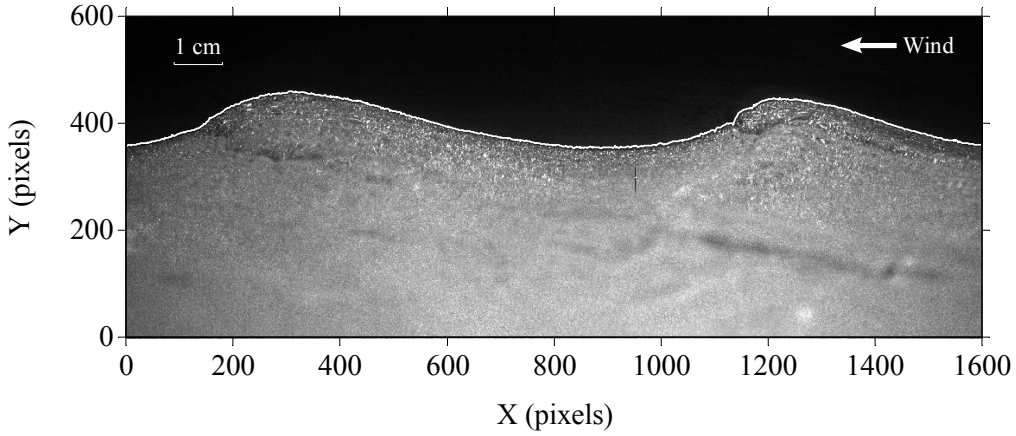

Figure 3.8: A wind wave profile image with a detected wave profile at the air-water interface.

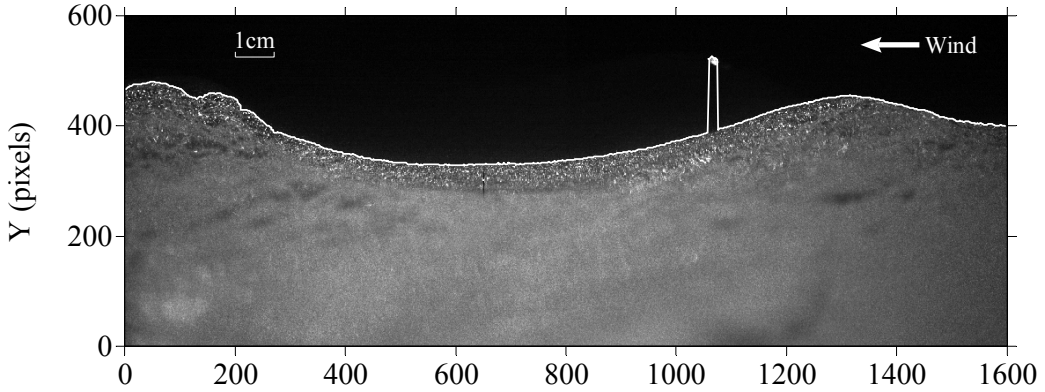

(a)

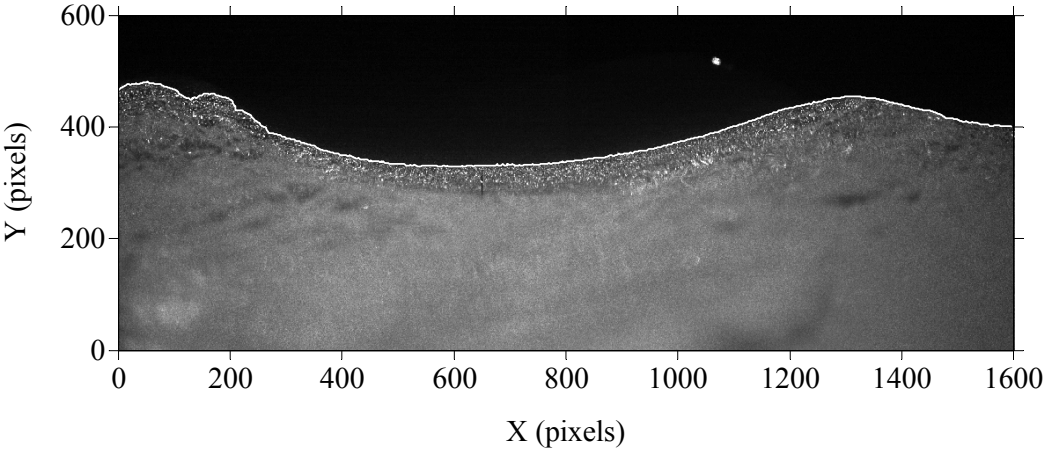

(b)

Figure 3.9: (a) A wind wave profile image with a detected wave profile that includes a spike. (b) The same wave profile image after it has been despiked.

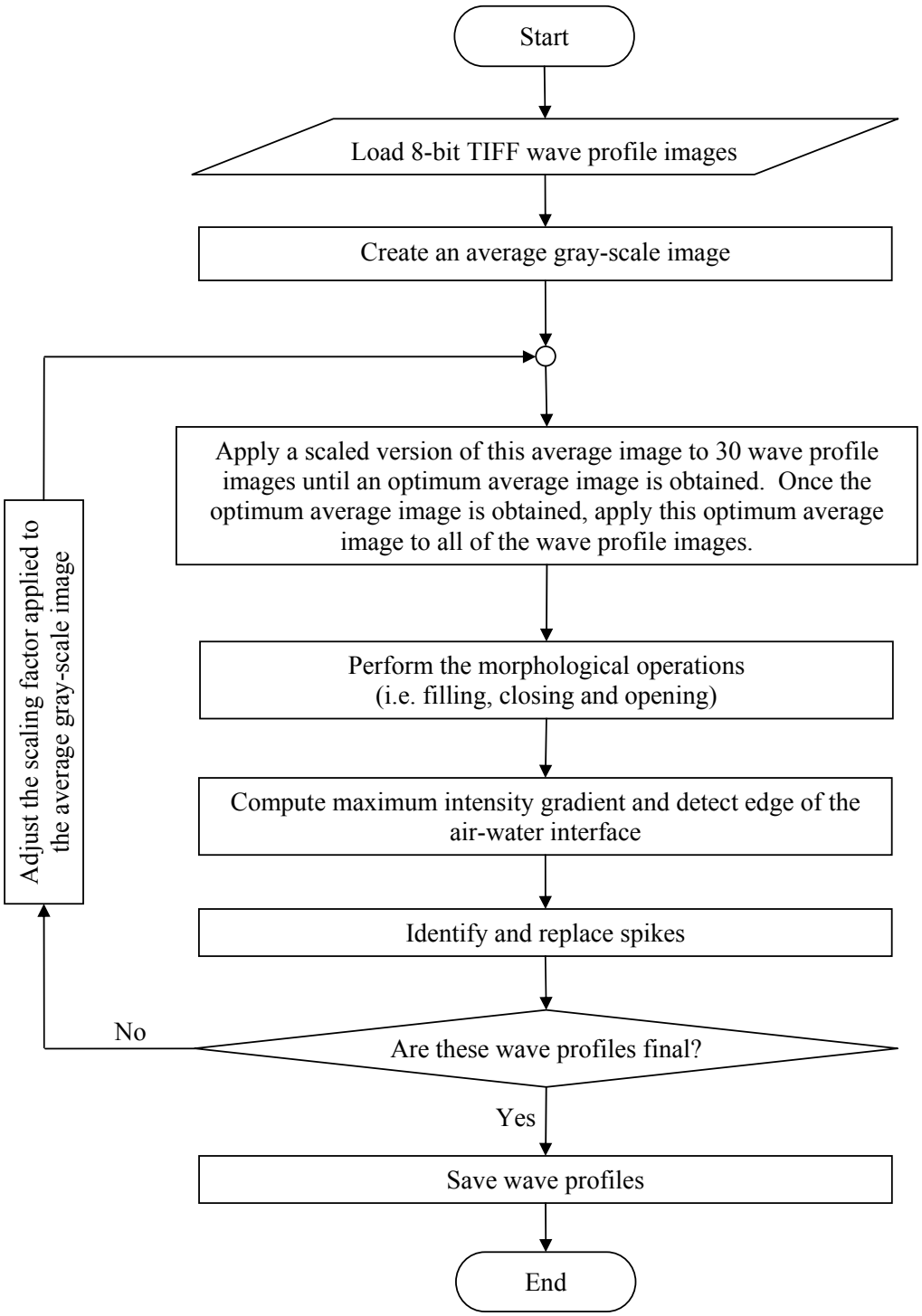

Figure 3.10: Flowchart illustrating the computational steps used in the variable threshold method.

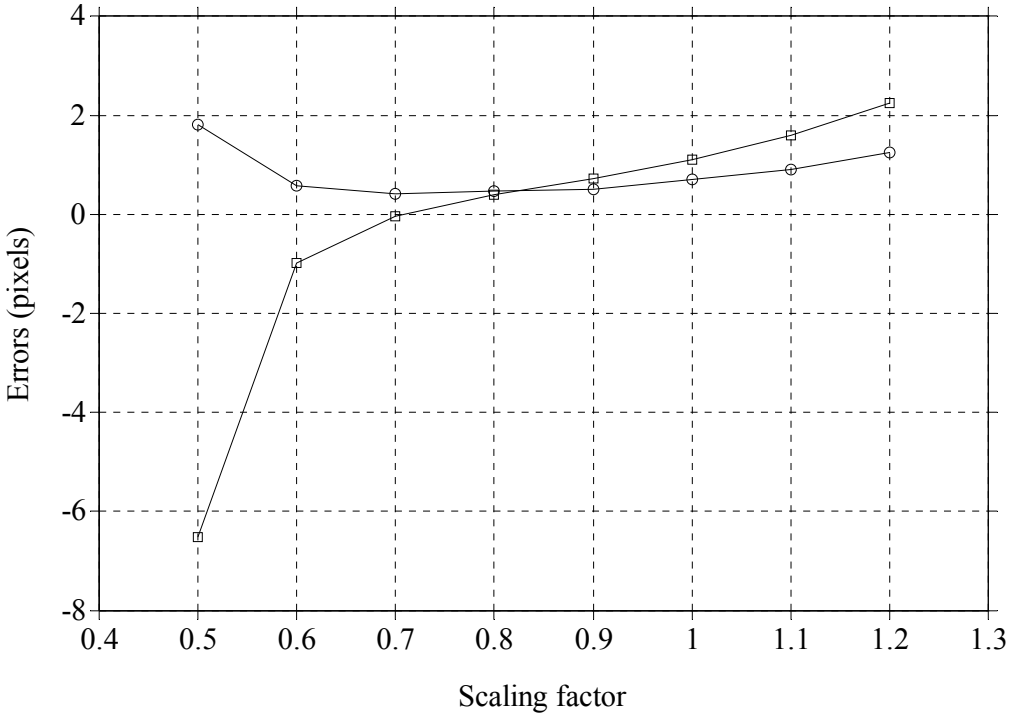

Figure 3.11: The D.C. offset or bias error (open squares) and high frequency r.m.s. error (open circles) computed from a still water profile plotted as a function of the scaling factor.

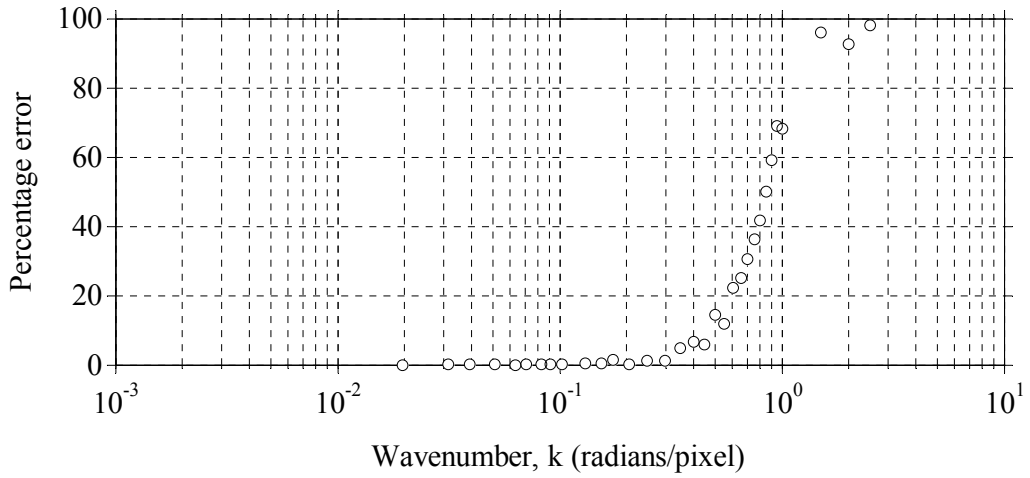

Figure 3.12: Percentage error in the wavenumber spectrum computed using 3,200 wave profiles detected using the variable threshold method in simulated binary images. This is the error caused by the morphological operations.

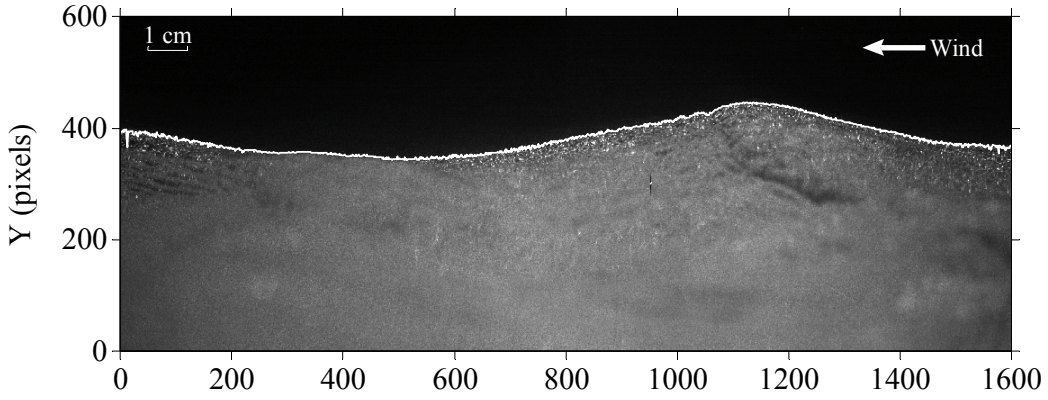

(a)

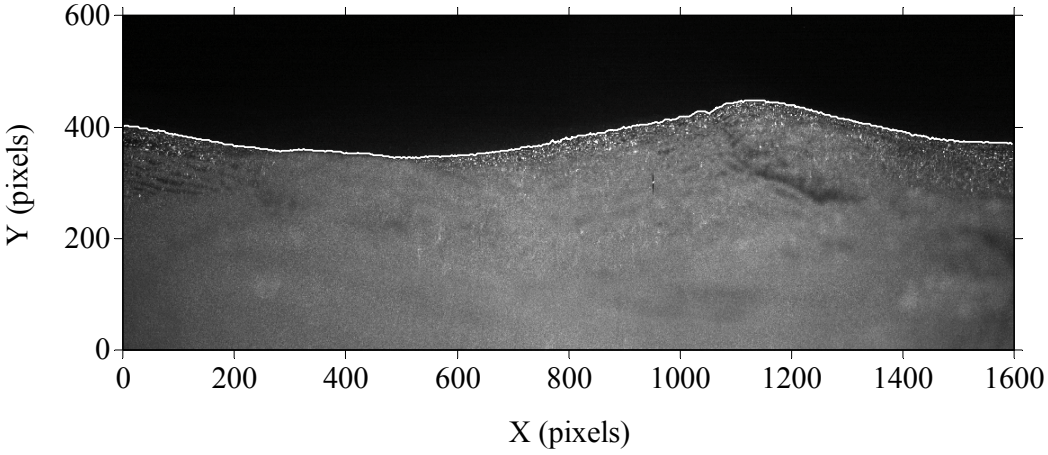

(b)

Figure 3.13: Comparison of wave profiles detected in the same wave profile image using two different methods: (a) the constant threshold method, (b) the variable threshold method.

Chapter 4

Estimation of Near-Surface Velocity Beneath Complex Air-Water Interface using DPIV

4.1 Introduction

Digital particle image velocimetry (DPIV) is a non-intrusive measurement technique to obtain two or three-dimensional instantaneous velocity fields (Keane & Adrian, 1990; Adrian, 1991; Willert & Gharib, 1991). The raw DPIV data includes thousands of singly exposed digital images referred to as DPIV images. Typically 9000 DPIV images are recorded from a five-minute experimental run when a 15-Hz laser light pulse is used as a light source. The DPIV images are processed to estimate velocity fields using a sophisticated image processing algorithm, referred to as the DPIV algorithm. Figure 4.1 shows a typical DPIV image that was acquired in this study at a wind speed of 7.9 m s^{-1} and a fetch of 4.8 m. An air-water interface, also referred to as surface wave profile and delineated as a white line, is shown in this figure.

In this study it was necessary to make velocity measurements very close to the water surface. These measurements were very challenging due to the fact that the measurements were made beneath short wind waves and these waves generate a complex air-water interface when they break. As a

result, a DPIV algorithm was developed in this study that can accurately estimate near-surface velocity fields beneath the complex air-water interface in a wave-following Eulerian coordinate system. The accuracy of the DPIV algorithm was first assessed in a fixed Eulerian coordinate system using standard synthetic image sequences without the air-water interface. Next, the accuracy of near-surface velocity estimates was assessed in detail using a simple horizontal air-water interface. Finally, the accuracy of the DPIV algorithm was assessed in a wave-following Eulerian coordinate system using a triangular wave form to simulate an air-water interface.

This chapter was organized as follows. Following the introduction in §4.1 and literature review in §4.2, the DPIV algorithm was presented in §4.3. The vorticity and dissipation estimation procedures using grid transformation were described in §4.4. The accuracy of the DPIV algorithm was presented in §4.5 using standard synthetic image sequences. Finally, the conclusions were summarized in §4.6.

4.2 Literature Review

Okamoto *et al.* (2000) developed a set of standard synthetic image sequences in order to evaluate the accuracy of DPIV algorithms. The standard image sequences were developed as part of the PIV standard project (PIV-STD) by the Visualization Society of Japan (Okamoto *et al.*, 2000) based on the velocity field of a planar wall-jet (Tsubokura *et al.*, 1997). The standard synthetic image sequences are distributed via the website http://www.vsj.or.jp/piv as part of a collaboration with the Visualization Society of Japan.

Quenot & Okamoto (2000) evaluated the performance of an optical flow technique referred to as Orthogonal Dynamic Programming (ODP) using the standard synthetic image sequences. They found that the accuracy of their algorithm was within 2-3% for the recovery of the two-components of the

velocity field using the standard image sequences.

Thomas *et al.* (2005) developed a two-stage DPIV algorithm to estimate velocity fields in which the global motion was first estimated followed by a local motion estimation. They concluded that the standard synthetic image sequences from the PIV-STD project could be used effectively to check the accuracy of their algorithm.

It has become an industry standard in the DPIV research community to make use of synthetic images to check the accuracy of DPIV or PTV (Particle Tracking Velocimetry) algorithm. For example, three PIV challenges were organized in three years 2003, 2005 and 2008, respectively, where synthetic images as well as real images from the experiments were used to check the accuracy and robustness of various PIV and PTV algorithms worldwide (Stanislas *et al.*, 2003, 2005, 2008).

4.3 DPIV Algorithm

A cross-correlation based multi-pass multi-grid DPIV algorithm was developed in this study that combines a number of recent improvements available in the literature. The DPIV algorithm was based on the following four processing steps:

1. Pre-processing of DPIV images;
2. Image interrogation using a FFT-based cross-correlation algorithm;
3. Detection and removal of spurious vectors; and,
4. Implementation of a multi-pass and multi-grid procedure.

Details of the processing steps were described in the following sections.

4.3.1 Pre-Processing of DPIV Images

The objective of this step was to improve the quality of the DPIV images by removing background noise from the DPIV images prior to performing any image interrogation. Sources of background noise in DPIV images are manifold, such as, camera sensor noise, and bright glow and reflection from the laser light (Honkanen & Nobach, 2005). Background noise can cause self correlation and produces bias error towards zero displacement (Honkanen & Nobach, 2005). Researchers have included image pre-processing step in their algorithms to improve the quality of the DPIV images and computed velocities (Cowen & Monismith, 1997; Westerweel, 1997; Honkanen & Nobach, 2005).

In this study, background noise was removed in three steps. First, a digital image was acquired prior to each DPIV experiment by keeping the camera lens cover on, which was referred to as the background image. This background image was used to capture camera sensor noise such as stuck pixels. This background image was then subtracted from the entire set of DPIV images acquired in an experiment. The gray-scale values in the regions of those stuck pixels were replaced by the median gray-scale value of the corresponding DPIV image. Second, each DPIV image was folded within a gray-scale value ranging from 0 to 200 and a smoothing filter was applied using a 5 x 5 Gaussian mask. Note that the gray-scale value in the acquired DPIV images varied from 0 to 255. This folding and smoothing operation partially removed the non-uniform illumination between the DPIV image pair. Third, an average image, which had the same dimensions as the DPIV image (i.e. 1600 x 1200 pixels), was created in which the gray-scale value in each pixel was obtained by averaging the gray-scale values of the neighboring 5 x 5 pixels obtained from the corresponding DPIV image. The average image was then subtracted from the corresponding DPIV image.

4.3.2 Image Interrogation using a FFT-based Cross-Correlation Algorithm

The image interrogation was performed by applying a FFT-based cross-correlation algorithm between an interrogation window and a search window. The size of the search window was double the size of the interrogation window to eliminate the loss of pairs problem that typically occurs due to large in-plane motion. The performance of this algorithm has been evaluated previously by many researchers (Adrian, 1988, 1991; Keane & Adrian, 1990; Fincham & Spedding, 1997; Westerweel, 1997, 2000; Gui *et al.*, 2000, 2001). In addition, a three-point Gaussian fit was used for the interpolation of the cross-correlation peak as suggested by Willert & Gharib (1991).

A Gaussian window mask was applied to the interrogation and search windows prior to performing any image interrogation as suggested by Gui *et al.* (2001). A DPIV image pair may be described by gray intensity distributions $f(i,j)$ and $g(i,j)$ in a fixed interrogation window size of M x N pixels, the evaluation functions of the masked correlation interrogation algorithm can be written as,

$$\phi_{fg}(m,n) = \frac{\sum[w(i,j)\cdot f(i,j) \times w(i-m,j-n)\cdot f(i-m,j-n)]}{\sqrt{\sum[w(i,j)\cdot f(i,j)]^2 \times \sum[w(i-m,j-n)\cdot f(i-m,j-n)]^2}} \tag{4.1}$$

where, the window mask $w(i,j)$ is given as a Gaussian (exponential) function:

$$w(i,j) = \exp^{-2\left(\frac{(i-\frac{M}{2})^2}{(\frac{M}{2})^2}+\frac{(j-\frac{N}{2})^2}{(\frac{N}{2})^2}\right)} \tag{4.2}$$

According to Gui *et al.* (2001), the Gaussian window mask is only effective when the particle image displacement is relatively small (less than 5 pixels with a 32 x 32 pixels interrogation window). Therefore, the window masking technique is particularly beneficial when the window offset technique is applied within the DPIV algorithm (Gui *et al.*, 2001). The benefit of using the window masking technique is that it can reduce the evaluation bias and gradient

of the evaluation bias thus reducing measurement uncertainty (Gui *et al.*, 2001). An evaluation bias occurs due to the fact that the DPIV velocity estimates typically tend to be smaller than the true values when a FFT-based cross-correlation algorithm is used for image interrogation (Gui *et al.*, 2000).

The displacement fields were computed over an irregular grid, and then distributed on a regular grid by means of Adaptive Gaussian Window (AGW) interpolation (Agui & Jimenez, 1987). This procedure applied a smoothing effect to the displacement field that helped reducing the undesired oscillation caused by the multi-pass multi-grid DPIV algorithm (Raffel *et al.*, 2007).

4.3.3 Detection and Removal of Spurious Vectors

In a multi-pass multi-grid DPIV algorithm, such as this one, data validation at the end of each image interrogation step is crucial. Otherwise, erroneous displacement vectors will propagate into subsequent passes.

In this algorithm, spurious vectors were detected using a normalized median test as described by Westerweel & Scarano (2005). One of the advantages of this technique is the use of a single universal threshold (typically a value of 2) that can be applied to a variety of flow conditions without having any a priori knowledge of the flow characteristics such as turbulence level. Moreover, the use of a normalized median test makes the implementation of multi-pass multi-grid DPIV algorithm more straightforward. The detected spurious vectors were replaced using the AGW interpolation method described by Agui & Jimenez (1987).

4.3.4 Implementation of a Multi-Pass and Multi-Grid Procedure

Scarano & Riethmuller (1999, 2000) proposed an algorithm where the particle displacements were predicted and corrected by means of an iterative procedure.

The multi-pass multi-grid algorithm developed in this study was modeled after the DPIV algorithm of Scarano & Riethmuller (1999, 2000). In a multi-pass procedure, image interrogation was applied to a relatively coarse grid satisfying the basic interrogation criteria of one-quarter rule in the first pass as suggested by Scarano & Riethmuller (1999). Estimated displacement fields were validated using the procedure described by Westerweel & Scarano (2005) and then used as a predictor displacement field in the subsequent pass following Scarano & Riethmuller (1999, 2000). In a multi-grid procedure, the coarse grids were refined into finer grids by dividing the grid size into half (Scarano & Riethmuller, 1999, 2000). Typically, the multi-grid procedure is implemented simultaneously in every pass in a multi-pass and multi-grid DPIV algorithm. In this study, the predictor displacement fields were distributed onto the finer grids by using a more accurate AGW interpolation scheme (Agui & Jimenez, 1987) instead of using a simple bilinear interpolation scheme as proposed by Scarano & Riethmuller (1999).

In the second pass, the DPIV image pair was deformed based on the predictor displacement field such that both images compensate for half of the displacement resulting in a second-order accurate estimate of the displacement (Scarano, 2002). The DPIV image pair may be deformed using either a discrete (Scarano & Riethmuller, 1999) or a sub-pixel window offset technique (Scarano & Riethmuller, 2000) based on the predictor displacement fields. The DPIV algorithm developed in this study included both window offset techniques. A discrete window offset technique is straight forward, whereas, in a sub-pixel window offset technique, the interrogation and search windows are deformed within the accuracy of a fraction of a pixel. The gray-scale values are not available at sub-pixel locations within a discrete DPIV image, and therefore, a two-dimensional Cardinal function with a Whittaker reconstruction image interpolation scheme was implemented to retrieve gray-scale values at a

sub-pixel image locations (Hall, 1979),

$$R(x,y) = \sum\sum f(i,j) \times \frac{\sin[\pi(i-x)]}{\pi(i-x)} \frac{\sin[\pi(i-y)]}{\pi(i-y)} \tag{4.3}$$

where, $R(x,y)$ is the gray-scale value retrieved at a sub-pixel image location from the discrete image array $f(i,j)$. However, Equation (4.3) can not be applied directly as the *sinc* function continues to infinity. Therefore, a limited number of neighboring pixels need to be considered that will result in a truncated-sinc filter kernel. The response of the truncated-sinc can be improved by multiplying the truncated-sinc function by a 1-D Blackman window (Niblack, 1986):

$$w(i) = 0.42 - 0.5\cos(\frac{2\pi i}{M}) + 0.08\cos(\frac{4\pi i}{M}) \tag{4.4}$$

In the second pass, the image interrogation was performed on a finer grid using the same FFT-based cross-correlation algorithm and a refined displacement field was obtained. The refined displacement field was then validated again following the steps described in §4.3.3. The refined displacement field can either be used as a predictor displacement field in the third pass or can be used as the final displacement field if a convergence criterion is satisfied. In this study, the multi-pass multi-grid procedure ended after a pre-defined number of iterations (typically 2 passes) was performed.

In this study, an initial interrogation window size of 64 x 64 pixels with a 50% overlap between the interrogation windows was used in the first pass and a finer interrogation window size of 32 x 32 pixels with a 50% overlap was used in the second pass that produced a grid difference of 16 pixel. Interrogation windows smaller than 32 x 32 pixels were not used in the image interrogation since it was not practical to estimate velocity fields in a finer resolution using the DPIV images acquired in this study.

4.4 Vorticity and Dissipation Estimation

The vorticity, ω_y was computed as follows,

$$\omega_y = \frac{\partial w}{\partial x} - \frac{\partial u}{\partial z} \tag{4.5}$$

where, ω_y is the vorticity component normal to the planar velocity field.

Doron *et al.* (2001) compared the accuracy of five different methods to estimate the turbulent kinetic energy dissipation rate. The methods were 'line fit in the inertial range', 'integral of the dissipation spectrum', 'locally axisymmetric turbulence', 'energy flux across equilibrium range', and the 'direct' estimate of the dissipation. They found that the 'direct' method was the most accurate method. The 'direct' method uses the velocity gradients directly obtained from the DPIV measurements and the continuity equation to estimate ε using the following equation,

$$\varepsilon = 3\nu_w \left\{ \overline{\left(\frac{\partial u'}{\partial x}\right)^2} + \overline{\left(\frac{\partial w'}{\partial z}\right)^2} + \overline{\left(\frac{\partial u'}{\partial z}\right)^2} + \overline{\left(\frac{\partial w'}{\partial x}\right)^2} + 2\overline{\left(\frac{\partial u'}{\partial z}\frac{\partial w'}{\partial x}\right)} + \frac{2}{3}\overline{\left(\frac{\partial u'}{\partial x}\frac{\partial w'}{\partial z}\right)} \right\} \tag{4.6}$$

where u' and w' are the streamwise and vertical turbulent velocities, ν_w is the kinematic viscosity of water and the overbar denotes time-averaged values.

In the wave-following Eulerian coordinate system (ξ, ζ), the origin is always set at the air-water interface, where the positive ξ axis points horizontally and the negative ζ axis points downwards parallel to the gravity vector. The velocity gradients required to compute ω_y and ε in the xz plane were computed by performing the following grid transformation:

$$\frac{\partial u}{\partial x} = \frac{1}{|J|\left[\frac{\partial u}{\partial \xi}\frac{\partial z}{\partial \zeta} - \frac{\partial u}{\partial \zeta}\frac{\partial z}{\partial \xi}\right]} \tag{4.7}$$

$$\frac{\partial w}{\partial x} = \frac{1}{|J|\left[\frac{\partial w}{\partial \xi}\frac{\partial z}{\partial \zeta} - \frac{\partial w}{\partial \zeta}\frac{\partial z}{\partial \xi}\right]} \tag{4.8}$$

$$\frac{\partial u}{\partial z} = \frac{1}{|J|\left[\frac{\partial u}{\partial \zeta}\frac{\partial x}{\partial \xi} - \frac{\partial u}{\partial \xi}\frac{\partial x}{\partial \zeta}\right]} \tag{4.9}$$

$$\frac{\partial w}{\partial z} = \frac{1}{|J| \left[\frac{\partial w}{\partial \zeta} \frac{\partial x}{\partial \xi} - \frac{\partial w}{\partial \xi} \frac{\partial x}{\partial \zeta} \right]} \tag{4.10}$$

where, J is the Jacobian matrix defined by,

$$J = \begin{bmatrix} \frac{\partial x}{\partial \xi} & \frac{\partial z}{\partial \xi} \\ \frac{\partial x}{\partial \zeta} & \frac{\partial z}{\partial \zeta} \end{bmatrix} \tag{4.11}$$

The streamwise (u) and vertical (w) velocity components can be replaced with $u^{'}$ and $w^{'}$ in the above velocity gradient computation to estimate dissipation using Equation (4.6).

Velocity gradients were computed by applying a finite difference technique to the neighboring velocity estimates and by performing the grid transformation as shown above. Velocity gradients were computed using a 2nd-order accurate central difference technique except for the near-surface grid points where a 1st-order accurate forward difference technique was used.

4.5 Accuracy

Accuracy of the estimated displacement fields was evaluated in three steps. First, the accuracy of the DPIV algorithm was assessed in a fixed Eulerian coordinate system using standard synthetic image sequences without the air-water interface. Second, the near-surface accuracy of the algorithm was assessed using a simple horizontal air-water interface. Third, the accuracy of the algorithm was assessed in a wave-following Eulerian coordinate system using a triangular wave form that simulated the air-water interface.

4.5.1 Standard Synthetic Image Sequences

The performance of the DPIV algorithm was assessed using a set of eight standard synthetic image sequences. Each image sequence includes a set of four synthetic images of known displacement distribution generated to test the performance of the DPIV algorithm. Okamoto *et al.* (2000) used the

velocity field of a planar wall-jet to generate a reference image sequence (image sequence #1) that included a set of four synthetic images. The velocity field of a planar wall-jet, referred to as the reference velocity field, that impinges on the wall with a jet Reynolds number of 6000 was simulated by Tsubokura *et al.* (1997) using a Large-Eddy-Simulation (LES) technique. Okamoto *et al.* (2000) generated the reference image sequence by adjusting a set of parameters in such a manner that the reference image sequence should ideally represent the reference velocity field. Figure 4.2 shows the first image of the reference image sequence (Figure 4.2(a)), and the reference velocity field (Figure 4.2(b)).

In addition, Okamoto *et al.* (2000) generated seven other image sequences using the same reference velocity field where average synthetic translation, seeding density, particle size and laser light sheet thickness were varied. All standard synthetic images were provided in both bitmap and raw image format and the size of each synthetic image was 256 x 256 pixels covering an actual area of 100 mm x 100 mm. Details of the parameters used to generate these standard synthetic image sequences can be found in Okamoto *et al.* (2000). A brief description of the parameters used to generate the standard synthetic image sequence was described below:

- Reference image sequence/image sequence #1: this was the reference image sequence for the 2-D wall shear flow for which parameters were set as follows:
  - the time interval between an image pair was set to 33 ms,
  - the average synthetic translation was 7.39 pixels/interval (i.e. in-plane velocity),
  - the number of particles was 4000,
  - the average particle diameter was 5 pixels and the standard deviation of particle diameter was 1.4 pixels,

  - the laser light sheet thickness was set to 20.0 mm which defined the scale of the out-of-plane velocity, and,
  - the average out-of-plane velocity per laser light thickness was 0.017 per interval (out-of-plane velocity is defined as the fraction of the particles leaving and entering the light sheet per interval). The seven other image sequences differed from the reference image sequence by only one parameter as described below.

- Image sequence #2: in this image sequence the average synthetic translation was increased to 22.4 pixels/interval and the corresponding time interval and average out-of-plane velocity were 100 ms and 0.06 per interval, respectively;

- Image sequence #3: in this image sequence the average synthetic translation was reduced to 2.24 pixels/interval and the corresponding time interval and average out-of-plane vorticity were 10 ms and 0.006 per interval, respectively;

- Image sequence #4: in this image sequence the number of particles was increased to 10000;

- Image sequence #5: in this image sequence the number of particles was reduced to 1000;

- Image sequence #6: in this image sequence the standard deviation of particle diameter was set to 0.0, which represented uniform particle diameter;

- Image sequence #7: in this image sequence the average particle diameter was increased to 10 and the corresponding standard deviation of particle diameter was set to 4.0; and,

- Image sequence #8: in this image sequence the laser light sheet thickness was made 2.0 mm, which was 10 times thinner than that of the reference image sequence of 20.0 mm.

4.5.2 Performance Measure

A commonly used statistical measure, the root mean square error ($RMSE$) was used as one of the performance measures. It is defined as,

$$RMSE = \sqrt{\frac{1}{N}\sum_{i=1}^{N}|p_i - o_i|^2} \tag{4.12}$$

where, p_i is the predicted data, o_i is the ground truth data, and N is the total number of data.

Another performance measure, referred to as the degree of agreement (d_1), was proposed by Wilmott *et al.* (1985). It is defined as,

$$d_1 = 1 - \frac{\sum_{i=1}^{N}|p_i - o_i|}{\sum_{i=1}^{N}(|p_i - \bar{o}| + |o_i - \bar{o}|)} \tag{4.13}$$

where, $\bar{o}$ is the mean of the ground truth data defined as,

$$\bar{o} = \frac{\sum_{i=1}^{N} o_i}{N} \tag{4.14}$$

The $RMSE$, is a measure of the average difference between the predicted and ground truth data, whereas, the degree of agreement, d_1, depicts the degree to which the predicted data matches with the ground truth data. The value of d_1 varies between 0 and 1, 1 being the perfect match and vice-versa. Thomas *et al.* (2005) also used Equations (4.12) and (4.13) as performance measures to check the accuracy of their DPIV algorithm.

4.5.3 Accuracy in a Fixed Eulerian Coordinate System

The standard synthetic image sequences were grouped into four broad categories to assess the accuracy of the DPIV algorithm in a fixed Eulerian

coordinate system without the air-water interface. The results obtained in this study were compared to the results presented by Thomas *et al.* (2005) because they also used the standard synthetic image sequences to evaluate the performance of their DPIV algorithm. Note that 100% of the velocity vectors (i.e. 1024 velocity vectors) were recovered from the image sequences to compare with the reference vector field. Four types of comparisons were made:

1. Synthetic Translation: Image sequences #1, 2 and 3 were grouped into this category in which synthetic translations were varied from 2.24 to 22.4 pixel/interval.

2. Seeding Density: Image sequences #1, 4 and 5 were grouped into this category in which the number of particles in each image was varied from 1000 to 10000.

3. Particle Size: Image sequences #1, 6 and 7 were grouped into this category in which the average particle diameter was varied between 5.0 and 10.0 pixels and the standard deviation of particle diameter was varied between 0.0 and 4.0 pixel, where, the zero value represented a uniform particle diameter.

4. Laser Light Sheet Thickness: Image sequences #1 and 8 were grouped into this category in which the laser light sheet thickness was varied between 2.0 and 20.0 mm.

Table 4.1 displays the accuracy of the estimated displacement vectors for varying synthetic translations. It was found that the $RMSE$ of the estimated displacement field was 0.30, 0.63 and 5.85 pixel and d_1 was 0.89, 0.95 and 0.85 for average synthetic translations of 2.24, 7.39 and 22.4 pixel/interval, respectively. The most accurate estimated displacement field was observed

for image sequence #1. Thomas *et al.* (2005) found that the $RMSE$ was 0.25, 0.51 and 11.89 pixel and d_1 was 0.87, 0.93 and 0.58 for average synthetic translations of 2.24, 7.39 and 22.4 pixel/interval, respectively.

Table 4.2 displays the accuracy of the estimated displacement fields for varying seeding densities. It was found that the $RMSE$ of the estimated displacement field was 0.84, 0.63 and 0.81 pixel and d_1 was 0.92, 0.95 and 0.93 for seeding densities of 15, 62 and 156, respectively. It was observed that both too low and too high seeding densities were not desirable for DPIV experiment and the optimal seeding density lied somewhere in between 1000 and 10000 particles in this case. It was evident from these results that the reference image sequence produced the optimal results. Thomas *et al.* (2005) found that the $RMSE$ was 0.56, 0.52 and 0.44 pixel and d_1 was 0.93, 0.93 and 0.94 for seeding densities of 15, 62 and 156, respectively.

Table 4.3 displays the accuracy of the estimated displacement fields for varying particle sizes. It was found that the $RMSE$ of the estimated displacement field increased from 0.63 to 0.89 pixel, and d_1 decreased from 0.95 to 0.91 as larger particle size (diameter of 10 pixels) was used compared to the smaller particle size (diameter of 5 pixels). Moreover, it was found that the $RMSE$ of the estimated displacement field increased from 0.63 to 0.76 pixel, and d_1 decreased from 0.95 to 0.93 when the uniform particle diameter was used. Thomas *et al.* (2005) reported better performance with the larger particle diameter as they found that the $RMSE$ decreased from 0.52 to 0.44 pixel and d_1 slightly increased from 0.93 to 0.94 as the particle average diameter was doubled. In addition, they did not observe any change in the results when uniform particle diameter was used.

Table 4.4 displays the accuracy of the estimated displacement fields for varying laser light sheet thicknesses. It was found that the $RMSE$ of the estimated displacement field increased from 0.63 to 0.78 pixel, and d_1 decreased

from 0.95 to 0.93 when a thinner laser light sheet thickness was used. Thomas *et al.* (2005) found insignificant effect due to change in laser light sheet thickness as $RMSE$ increased marginally from 0.52 to 0.54 and no change was observed for d_1 as the laser light sheet thickness was reduced.

4.5.4 Near-Surface Accuracy

Figure 4.3(a) shows an example of a hypothetical DPIV image in which velocity fields are estimated in a fixed Eulerian coordinate system. The velocity grid points are shown at the center of the interrogation regions that are referenced to a fixed Eulerian coordinate system. An air-water interface is also shown in this figure as a solid black line. The distance between two velocity grid points was assumed to be 16 pixels. In order to estimate the near-surface velocity field beneath the air-water interface in a fixed Eulerian coordinate system, the gray-scale values above the interface are assumed to be converted to the median gray-scale value in the DPIV image pair. Two major drawbacks are associated with this image interrogation technique. First, the vertical distance between the first velocity grid points below the interface and the position of the air-water interface (i.e. the water surface) varies from 1 to 15 pixels as shown in Figure 4.3(a). As a result, the velocity data are computed at unequal distances from the interface, i.e., $d_1 \neq d_2 \neq d_3 \neq d_4$. Second, Figure 4.3(a) also shows that the contributing area in each interrogation window just below the interface varies depending on the position of the air-water interface, i.e., $A_1 \neq A_2 \neq A_3 \neq A_4$. Therefore, a DPIV algorithm that estimates velocity fields in a fixed Eulerian coordinate system would be susceptible to two additional sources of errors when used to estimate near-surface velocities. Figure 4.3(b) shows the same hypothetical DPIV image in which velocity fields are estimated in a wave-following Eulerian coordinate system. In this figure, velocity fields were estimated equidistant (8 pixels) from the water surface. Moreover, the

contributing area in each interrogation window is always 100% of the area in the interrogation window. Therefore, the estimated velocity fields in a wave-following Eulerian coordinate system should eliminate the two sources of DPIV errors that occurred when using a fixed Eulerian coordinate system beneath a wavy air-water interface.

The near-surface accuracy of both types of algorithms can be compared in a systematic manner. It was demonstrated in Figure 4.3(a) that the contributing area in each interrogation window near the surface was smaller than the actual interrogation window size of 16 x 16 pixels. Therefore, it was argued that a systematic reduction of the area in the interrogation window near the air-water interface would produce increased errors. In order to assess this hypothesis, a simple horizontal air-water interface was used. Four cases with the horizontal air-water interface placed arbitrarily at a depth of 100 pixel below the top of the image were tested:

- Case 1: In this case 100% of the contributing area in each interrogation window was used for image interrogation.
- Case 2: The area in each interrogation window was reduced by 25% by converting the gray-scale value of the top quarter in each area into the median gray-scale value.
- Case 3: The area in each interrogation window was reduced by 50%.
- Case 4: The area in each interrogation window was reduced by 75%.

Table 4.5 displays the accuracy of the estimated near-surface displacement at a distance of 8 pixels for all four test cases. It was found that the $RMSE$ of estimated displacement fields increased from 0.43 to 2.84, a factor of 6.6, as the contributing area in each interrogation window was reduced from 100% to 25%. In addition, the degree of agreement (d_1) was reduced from 0.94

to 0.73. This simple analysis demonstrated that the wave-following Eulerian coordinate DPIV algorithm produced near-surface velocity estimates that were up to a factor of 6.6 times more accurate than a fixed Eulerian coordinate DPIV algorithm.

4.5.5 Accuracy Using a Wave-Following Eulerian Coordinate System Beneath a Wavy Interface

The accuracy of the DPIV algorithm using a wave-following Eulerian coordinate system was assessed using the standard synthetic images of the image sequence # 1 in which a triangular wave form was used to simulate the air-water interface. The triangular wave form was generated with a specified wavelength, λ and amplitude, a. The wavelength was set equal to 256 pixel, which was the horizontal dimension of a standard synthetic image and the amplitude was set equal to 64 pixel, which was multiple of 8 pixel. A triangular wave form was used because it was simple to implement and a multiple of 8 pixels was used for the amplitude because the estimated vector fields beneath the triangular interface will then coincide with the reference vector fields. The triangular wave form had a wave steepness of $ak = 1.57$ radians. The triangular wave form is shown in Figure 4.4 inserted onto the first image in the image sequence # 1. The recovered vector fields are also shown in the same figure.

Table 4.6 lists values of $RMSE$ and d_1 for the estimated displacement fields at various depths below the triangular interface. It was found that the $RMSE$ of the displacement was 0.46, 0.40 and 0.33 pixels at depths of 8, 16 and 24 pixels, respectively. The degree of agreement (d_1) was approximately equal to 0.94.

4.6 Conclusion

A multi-pass multi-grid DPIV algorithm was developed in this study to estimate the near-surface instantaneous velocity fields beneath complex air-water interface. One of the unique features of the developed DPIV algorithm is that the algorithm can be used to estimate the near-surface instantaneous velocity fields in a wave-following Eulerian coordinate system. The DPIV algorithm was developed based on a FFT-based cross-correlation algorithm that included several recent improvements published in the DPIV literature. The improvements in the DPIV algorithm included image pre-processing technique for removal of background noise, Gaussian window masking for reduction of evaluation bias, a three point Gaussian peak interpolation, as well as discrete and sub-pixel window offset technique for image interrogation. The DPIV algorithm was implemented following a multi-pass multi-grid procedure. A superior Adaptive Gaussian Window interpolation technique was used to distribute the estimated displacement fields from irregular grids to regular grids as well as to smooth the predictor displacement field into finer grids. In addition, use of a normalized median test for data validation made the multi-pass procedure more robust.

The accuracy of the algorithm was evaluated using standard synthetic image sequences obtained from the STD-PIV project for which ground truth velocity vectors were available. The accuracy of the DPIV algorithm was assessed by comparing the estimated velocity vectors with the ground truth velocity vectors and with the published result of Thomas *et al.* (2005). Performance of the DPIV algorithm was assessed in both fixed and wave-following Eulerian coordinate systems with and without the air-water interface.

The accuracy of the developed DPIV algorithm was assessed for three

scenarios. First, the accuracy of the developed algorithm was assessed in a fixed Eulerian coordinate system using standard synthetic image sequences in the absence of a free surface where synthetic translation, seeding density, particle size, and laser light thickness were varied. The root mean square error and the degree of agreement between the estimated displacement field and ground truth displacement field were found to vary from 0.3 to 5.85 pixel and from 85 to 95%, respectively. The accuracy of the developed DPIV algorithm was found to be comparable to that of the Thomas *et al.* (2005), who also used the same set of synthetic image sequences for image interrogation. Next, the near-surface accuracy of the developed algorithm was assessed by implementing the algorithm in a fixed and wave-following Eulerian coordinate systems using a simple horizontal air-water interface. It was found that the wave-following Eulerian coordinate DPIV algorithm produced near-surface velocity estimates that were up to a factor of 6.6 times more accurate than a fixed Eulerian coordinate DPIV algorithm. Finally, a triangular air-water interface was used to assess the near-surface accuracy of the developed DPIV algorithm in a wave-following Eulerian coordinate system. The near-surface accuracy of the estimated displacement fields for the top three rows was found to be in good agreement (approximately 94 to 95%) with the ground truth velocity vectors. For this scenario, the root mean square error of the estimated displacement fields for the first, second and third row was approximately 0.46, 0.40 and 0.33 pixel, respectively.

Image Sequence	Δt (ms)	Average Synthetic Translation (pixel/interval)	*RMSE* of Displacement (pixel)	d_1
#3	10	2.24	0.30	0.89
#1	33	7.39	0.63	0.95
#2	100	22.4	5.85	0.85

Table 4.1: Accuracy of the estimated displacement fields for varying average synthetic translations. Where, $RMSE$ is the root mean square error and d_1 is the degree of agreement. Δt is the time interval between two laser pulses.

Image Sequence	Number of particles	Seeding density (Number per 32 x 32 pixels window)	*RMSE* of Displacement (pixel)	d_1
#5	1000	15	0.84	0.92
#1	4000	62	0.63	0.95
#4	10000	156	0.81	0.93

Table 4.2: Accuracy of the estimated displacement fields for varying seeding densities. Where, $RMSE$ is the root mean square error and d_1 is the degree of agreement.

Image Sequence	Particle average diameter (pixel)	Standard deviation of particle diameter (pixel)	*RMSE* of Displacement (pixel)	d_1
#1	5.0	1.4	0.63	0.95
#6	5.0	0.0	0.76	0.93
#7	10.0	4.0	0.89	0.91

Table 4.3: Accuracy of the estimated displacement fields for varying particle sizes. Where, $RMSE$ is the root mean square error and d_1 is the degree of agreement.

Image Sequence	Laser light sheet thickness (mm)	*RMSE* of Displacement (pixel)	d_1
#1	20	0.63	0.95
#8	2	0.78	0.93

Table 4.4: Accuracy of the estimated displacement fields for varying laser light sheet thicknesses. Where, $RMSE$ is the root mean square error and d_1 is the degree of agreement.

Data Location	Distance from surface profile (pixel)	Contributing area of each interrogation window (pixel^2) (% of Area)	*RMSE* of Displacement (pixel)	d_1
Top row	8	256 (100%)	0.43	0.94
Top row	8	192 (75%)	0.56	0.93
Top row	8	128 (50%)	1.77	0.84
Top row	8	64 (25%)	2.84	0.73

Table 4.5: Near-surface accuracy of the estimated displacement fields for varying contributing area in interrogation window using a simple horizontal air-water interface. Where, $RMSE$ is the root mean square error and d_1 is the degree of agreement.

Data Location	Distance from surface profile (pixel)	No of data	*RMSE* of Displacement (pixel)	d_1
Top row	8	32	0.46	0.94
Second row	16	32	0.40	0.94
Third row	24	32	0.33	0.95

Table 4.6: Near-surface accuracy of the estimated displacement fields for top three rows beneath a triangular wave form simulated as an air-water interface. Where, $RMSE$ is the root mean square error and d_1 is the degree of agreement.

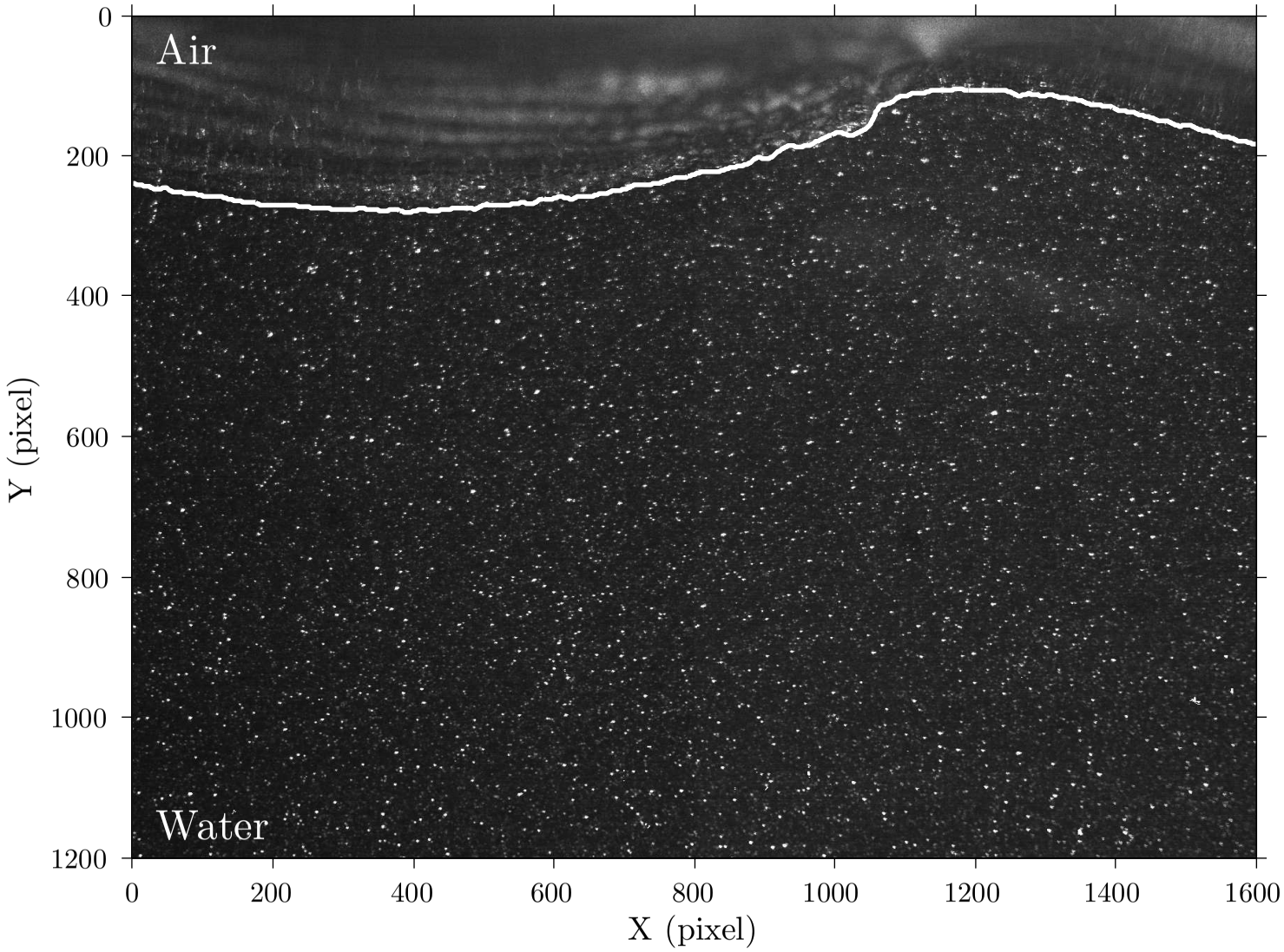

Figure 4.1: A typical DPIV image acquired at a wind speed of 7.9 m s^{-1} and at a fetch of 4.8 m. A surface wave profile, delineated as a white line, is also shown in this figure.

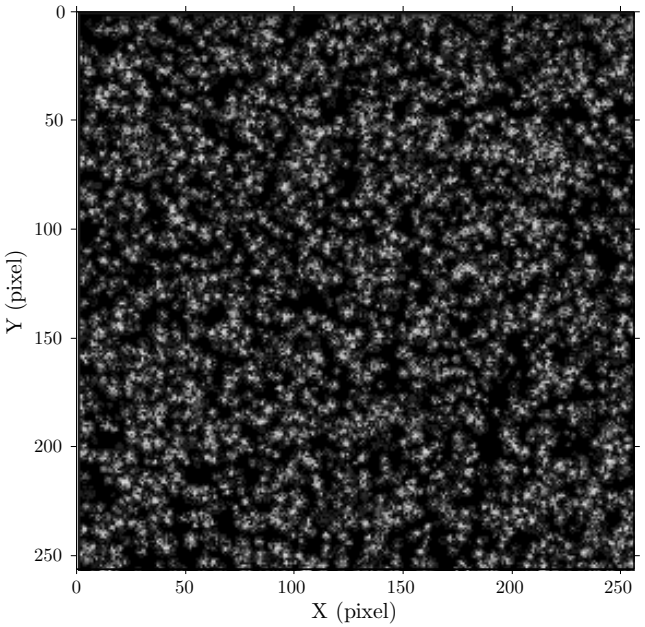

(a)

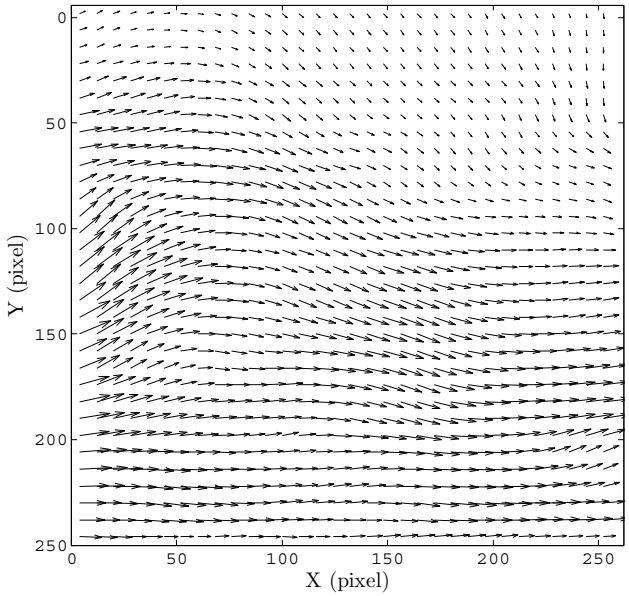

(b)

Figure 4.2: Plots of the reference image sequence and reference velocity fields: (a) first image of a set of four synthetic images; (b) velocity fields of a planar wall-jet.

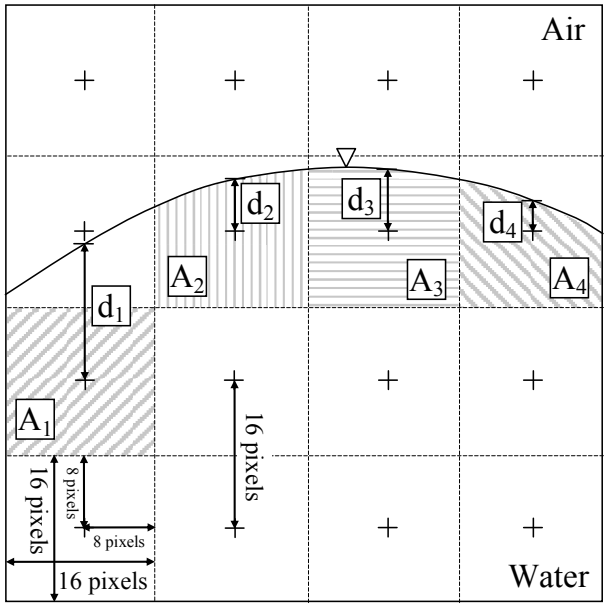

(a)

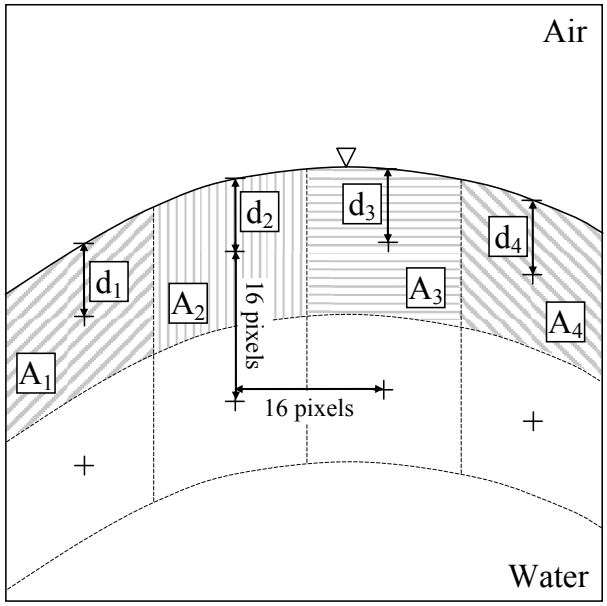

(b)

Figure 4.3: Plots of hypothetical DPIV images with air-water interface inserted onto the images: (a) velocity grid points in a fixed Eulerian coordinate system; (b) velocity grid points in a wave-following Eulerian coordinate system.

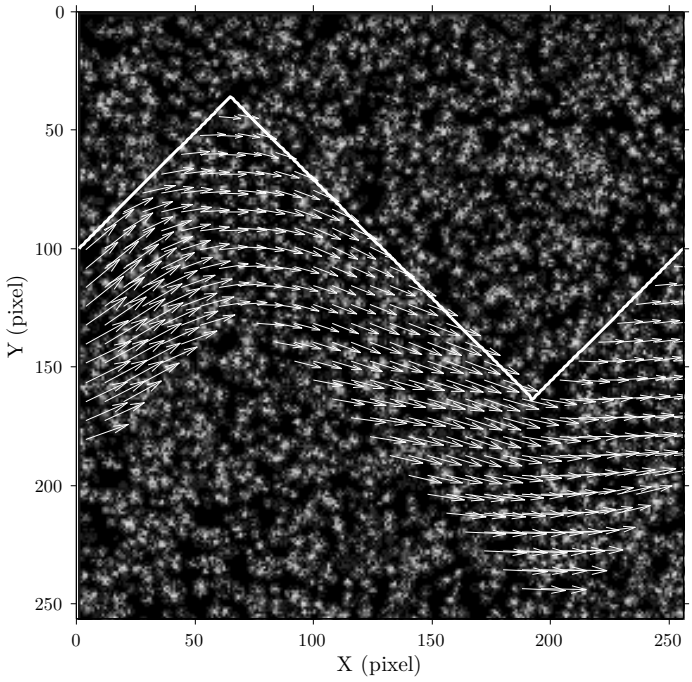

Figure 4.4: A plot of recovered displacement fields superimposed onto the first image of the reference image sequence beneath a triangular wave form simulated as an air-water interface.

Chapter 5

Dependence of Surface Roughness and Interfacial Stresses on the Properties of Very Young Wind-Waves

5.1 Introduction

When wind blows moderately over a water surface of reservoirs, lakes or oceans, it enhances the exchange of gas, momentum and heat across the air-water interface. The wind-driven transfer of momentum in the coupled boundary layers, i.e. from the air-side boundary layer (ABL) to the water-side boundary layer (WBL), is very important to many physical, chemical and biological processes. Many researchers have studied momentum transfer by investigating the partitioning of interfacial stresses across the air-water interface. The partitioning of interfacial stresses refers to the relative contributions of viscous tangential stress (τ_t) and wave-induced stress (τ_w) to the wind stress (τ_a). The interfacial stresses play a vital role in controlling physical processes such as wind-wave growth and atmospheric circulation (Johnson *et al.*, 1998; Banner & Peirson, 1998; Bourassa, 2000; Lange *et al.*, 2004; Caulliez *et al.*, 2008). However, the physical mechanisms responsible for the momentum transfer at the air-water interface are not yet fully understood and constitute a subject

of ongoing research.

The surface roughness of coupled boundary layers is also an important parameter that plays a vital role in characterizing the wind-wave growth. Researchers have studied the air-side surface roughness represented by the aerodynamic roughness length, z_{oa} and showed that z_{oa} depends on the wind friction velocity, u_{*a}; the gravitational acceleration, g; and wind-wave properties such as the wave steepness and wave age. However, the variation of z_{oa} and its influence on wind-wave growth still continues to be the subject of ongoing debate (Donelan, 1990; Johnson *et al.*, 1998; Lange *et al.*, 2004; Drennan *et al.*, 2005). Moreover, studies of water-side surface roughness represented by hydrodynamic roughness length, z_{ot} are scarce. Therefore, the dependence of the surface roughness and interfacial stresses on wind-wave properties was examined in this chapter using laboratory measurements. The development of a particle-image based wave profile measurement technique (Mukto *et al.*, 2007) and accurate near surface velocity measurements beneath the wind-waves using Digital Particle Image Velocimetry (DPIV) has advanced the study of the characteristics of these coupled boundary layers.

This chapter is organized as follows. Following the introduction in §5.1 and literature review in §5.2, the non-dimensional functional relationships between surface roughnesses, interfacial stresses and wind-wave properties are developed in §5.3. Wind-wave properties and the characteristics of the mean flow are presented in §5.4. Laboratory evidence showing the dependence of surface roughnesses and interfacial stresses on wind-wave properties are discussed in §5.5 and conclusions are drawn in §5.6.

5.2 Literature Review

5.2.1 The surface roughness in coupled boundary layers

Charnock (1955) first suggested that z_{oa} is a function of u_{*a} and g, and expressed the aerodynamic Charnock parameter as, $\alpha^a_{Ch} = z_{oa}/(u^2_{*a}/g)$. For mature (i.e. well-developed or nearly-developed) ocean waves, he proposed that α^a_{Ch} is a constant (Charnock, 1955) and that it is equal to 0.012 (Charnock, 1958). Smith (1980, 1988) also suggested that α^a_{Ch} is constant but equal to 0.011. Wu (1980) supported Charnock's concept of a constant value for α^a_{Ch} and based on field data he proposed a value of α^a_{Ch} equal to 0.0185. He argued that the scatter found in the Charnock's parameter was caused by intrinsic errors in the drag coefficient measurements and curve fitting method.

Over the last 40 years, there has been a great deal of debate concerning the constancy of the Charnock parameter. Recent measurements and model studies have provided strong evidence of its dependency on the wind-wave growth. Unfortunately, no theoretical basis had been established yet to explain the functional dependency of α^a_{Ch} on the wave field and most of the proposed functional relationships were derived based on dimensional arguments. As a result, no universally accepted functional relationship is currently accepted for z_{oa} and this is due to a combination of factors. First, large scatter in most of the field and laboratory data sets produced large uncertainty in many of the derived relationships (Johnson *et al.*, 1998; Lange *et al.*, 2004). Second, combined use of the field and laboratory data sets lead to misinterpretation and called into question of many proposed functional relationships (Wu, 1980; Donelan *et al.*, 1993).

Kitaikorodskii & Volkov (1965) first postulated that z_{oa} varied with wave height. Manton (1971) suggested that the wave slope rather than the wave height determines the magnitude of the surface roughness since the surface

waves are essentially sinusoidal. Hsu (1974) then suggested that z_{oa} varied with wind-wave properties. He collected 19 sets of field and laboratory data under neutral or near-neutral atmospheric stability conditions and proposed a relationship between z_{oa}, u_{*a}, H and c_p such that $z_{oa}/H = 1/[2\pi(c_p/u_{*a})^2]$ (where, H is the characteristic wave height, c_p is the wave phase speed at the peak of the spectrum, and c_p/u_{*a} is the wave age). He obtained this relationship by fitting a regression line using the mean value of each data set. Alternatively, he proposed that z_{oa} could also vary with the dominant wave steepness, H/λ_d such that $gz_{oa}/u_{*a}^2 \propto H/\lambda_d$ (where, λ_d is the dominant wavelength). However, his ideas did not receive much attention at that time for the following reasons. First, Hsu (1974) combined field and laboratory data to obtain the wave dependent functional relationship for z_{oa}. Wu (1980) and Donelan (1990) cautioned that the combined use of the field and laboratory data to obtain a wave dependent functional relationship for z_{oa} may lead to erroneous conclusion as waves in the wind-wave tanks and field are very different in nature. Second, for only three of the nineteen data sets did Hsu (1974) explicitly defined the type of wave height and phase speed he used. Third, Wu (1980) argued that Hsu (1974) used data sets that were mostly collected under fully developed waves for which α_{Ch}^a may be assumed to be a constant.

A number of researchers have tried to develop a universally accepted wave dependent functional relationship for z_{oa} similar to the relationship proposed by Hsu (1974). The two most widely used wave dependent functional relationships for the dimensionless aerodynamic roughness length, α_n, may be written in the following forms,

$$\alpha_n = c_1(wave\ age)^{c_2} \tag{5.1}$$

$$\alpha_n = c_3(wave\ slope\ or\ steepness)^{c_4} \tag{5.2}$$

where, α_n may be defined as $z_{oa}/(u_{*a}^2/g)$ (i.e. the well-known aerodynamic Charnock parameter, α_{Ch}^a), z_{oa}/H or $z_{oa}u_{*a}/\nu_a$ (i.e. the aerodynamic roughness Reynolds number, where, ν_a is the kinematic viscosity of air). The wave age is defined as either c_p/u_{*a} or c_p/U_z, wave slope and steepness are defined as S_{rms} (i.e. the r.m.s wave slope) and H/λ_d, respectively. The characteristic wave height is defined as H_s (i.e. the significant wave height) or H_{rms} (i.e. the root-mean-square (r.m.s) wave height), and U_z is the wind speed at an arbitrary height, z. In oceans or lakes, z is usually measured at 10-m height above the mean water level. Many researchers have proposed wave dependent functional relationships in the form of Equations (5.1) and (5.2) based on measurements and model studies. A short description of these studies is presented below and the functional relationship(s) they proposed for z_{oa} are listed in Table 5.1. Donelan (1990), Toba *et al.* (1990), Maat *et al.* (1991), Smith *et al.* (1992), Donelan *et al.* (1993), Anctil & Donelan (1996), Johnson *et al.* (1998) and Drennan *et al.* (2003) presented wave age dependent functional relationships for z_{oa} similar to Equation (5.1). Anctil & Donelan (1996) and Taylor & Yelland (2001) proposed wave slope or wave steepness dependent functional relationships for z_{oa} similar to Equation (5.2). Nordeng (1991), Makin & Kudryavtsev (2002), Moon *et al.* (2004) and Caulliez *et al.* (2008) used mathematical models to develop functional relationships for α_{Ch}^a.

Donelan (1990) investigated the dependence of z_{oa}/H_{rms} on the wave age using laboratory wind-wave tank data (Donelan, 1979) and field data from Lake Ontario (Donelan, 1982). For the laboratory data, the wave age (defined as c_p/u_{*a}) varied from 1 to 5 and for field data it varied from 4 to 29. He found that z_{oa}/H_{rms} decreased with an increase of any of the three forms of the wave age (i.e. c_p/U_{10}, $c_p/U_{\lambda/2}$, and c_p/u_{*a}) using both the field and laboratory data (see Table 5.1).

Toba *et al.* (1990) analyzed field data collected during storm events at

an oil producing platform in Bass Strait, Australia along with some other representative field and laboratory data. They combined field and laboratory data and proposed a wave age dependent relationship for α_{Ch}^{a} in which α_{Ch}^{a} increased with increasing wave age. However, their findings are subject to controversy due to their use of both laboratory and field data.

Maat *et al.* (1991) proposed another wave age dependent functional relationship for z_{oa} derived using the 1986 HEXMAX (Humidity Exchange over the Sea Main Experiment) field data, which was carried out in the North Sea near the Dutch coast (see Table 5.1). They used measurements that were taken on a platform using a sonic anemometer and a waverider buoy. Out of a total of 57 data sets, only 33 data sets were collected when a pure wind sea state existed. They excluded the data sets that had multiple-peaked wave spectra or when swell dominated. For their field data, the value of c_p/u_{*a} varied from 7 to 45, and the value of α_{Ch}^{a} varied from 0.005 to 0.1. Using dimensional analysis they found that α_{Ch}^{a} may be a function of c_p/u_{*a}, and using HEXMAX data they showed that α_{Ch}^{a} was inversely proportional to c_p/u_{*a} (see Table 5.1).

Smith *et al.* (1992) also used the same 33 sets of sonic anemometer data from the 1986 HEXMAX field data in addition to another 18 sets of pressure anemometer data to obtain a wave age dependent functional relationship for z_{oa} (see Table 5.1). They also used only pure wind sea data, however, the major difference between their study and the study of Maat *et al.* (1991) was the correction for flow distortion caused by the tower that they applied to their data. For their data, the value of c_p/u_{*a} varied from 10 to 30, and the value of α_{Ch}^{a} varied from 0.005 to 0.015. They obtained two different wave age dependent functional relationships for z_{oa}. Their first relationship was similar to the relationship obtained by Maat *et al.* (1991) but with a different value of c_1 (see Table 5.1). Their second relationship was similar to the second field

relationship proposed by Donelan (1990), however, with a different value of c_2.

Keller *et al.* (1992) conducted wind-wave tank measurements with variable wind speeds up to 13 m s^{-1} at a fetch of 16.3 m. In their laboratory experiments, the wave age was varied from 0.8 to 1.3, which indicates the waves were very young. They did not look for any relationship between α_{Ch}^a and c_p/u_{*a}. However, Makin & Kudryavtsev (2002) reanalyzed their data and found that α_{Ch}^a increased with increasing c_p/u_{*a}.

Donelan *et al.* (1993) confirmed the wave age dependency of z_{oa} using field data from Lake Ontario, HEXMAX and the North Atlantic. They found that z_{oa}/H_{rms} decreased with increasing c_p/U_{10} except for the case where swell dominated. However, they were unsuccessful in finding a relationship between z_{oa}/H_{rms} and c_p/u_{*a} as did Donelan (1990). Anctil & Donelan (1996) conducted field measurements of shoaling waves in Lake Ontario. They showed that z_{oa}/H_{rms} depended on both c_p/U_{10} and S_{rms}. Similar to Donelan *et al.* (1993) they found that z_{oa}/H_{rms} decreased with increasing c_p/U_{10}, whereas, z_{oa}/H_{rms} increased with increasing S_{rms}. In addition, they found that a multiple regression using both c_p/U_{10} and S_{rms} produced the best prediction of z_{oa}/H_{rms}.

Johnson *et al.* (1998) used RASEX (Risø Air-Sea Exchange) field data and field data compiled by Donelan *et al.* (1993) to obtain a relationship between α_{Ch}^a and c_p/u_{*a}. RASEX took place at an offshore wind turbine site in the Danish Baltic Sea in 1994 and the wave age varied from 7 to 26. The uncertainty involved in computing u_{*a} made it difficult for them to obtain any wave age dependent functional relationship for α_{Ch}^a. To minimize this problem they combined the data from different sites and found that α_{Ch}^a decreased with increasing c_p/u_{*a}. The functional relationship they obtained between α_{Ch}^a and c_p/u_{*a} is presented in Table 5.1.

Taylor & Yelland (2001) presented a dominant wave steepness (H_s/λ_d)

based functional relationship for z_{oa}/H_s using HEXMAX, RASEX and Lake Ontario field data. They found that z_{oa}/H_s increased with increasing H_s/λ_d. For their data, the value of H_s/λ_d varied from 0.02 to 0.05.

Drennan *et al.* (2003) used five different field data-sets with wave ages from 5 to 33 for pure wind seas in deep water and for fully rough flow conditions to obtain a wave age dependent functional relationship for z_{oa}. They found that z_{oa}/H_{rms} decreased with increasing c_p/u_{*a}. They also presented a functional relationship between α^a_{Ch} and c_p/u_{*a} in which they showed a decreasing trend in α^a_{Ch} with increasing values of c_p/u_{*a} which was consistent with Johnson *et al.* (1998).

Lange *et al.* (2004) used field data that were gathered at Rødsand in the Danish Baltic Sea, and they found a decreasing trend in α^a_{Ch} with increasing values of c_p/u_{*a} which was similar to Johnson *et al.* (1998) and Drennan *et al.* (2003). For their field data, c_p/u_{*a} varied from 10 to 25, and α^a_{Ch} varied from 0.001 to 1.

Drennan *et al.* (2005) tested the applicability of Equations (5.1) and (5.2) using eight field data sets, which represented a wide variety of field conditions. For their field data, c_p/u_{*a} varied from 7 to 50, and H_s/λ_d varied from 0.001 to 0.07. They found that in mixed sea conditions Equation (5.2) performed better and for underdeveloped young wind seas Equation (5.1) performed better. For swell-dominated conditions with relatively high wave steepness Equation (5.2) performed better.

Caulliez *et al.* (2008) carried out experiments in a large wind wave tank where they took measurements at three fetches of 6, 13 and 26 m for wind speeds ranging from 2.5 to 13 m s^{-1}. In their measurements, c_p/u_{*a} varied from 1.9 to 5.6, and significant dominant wave steepness varied from 0.058 to 0.34. They found that $z_{oa}u_{*a}/\nu_a$ increased as the significant dominant wave steepness increased or c_p/u_{*a} decreased.

Nordeng (1991) developed relationships for the wave age dependent z_{oa} using two theoretical approaches. First, he combined a roughness length model given by Kitaigorodskii (1973) with Phillips spectrum (Phillips, 1977) and a wave age dependent Phillips coefficient (Janssen, 1989) to obtain a wave age dependent model for α^a_{Ch}. This model also depended on the von Kármán constant, κ. This model predicted that α^a_{Ch} increased with increasing wave age up to $c_p/u_{*a} \simeq 5$ and that it reached a maximum value of 0.018 and then decreased with increasing wave age up to $c_p/u_{*a} = 20$ ($\kappa = 0.4$ for all these analysis). Second, he computed α^a_{Ch} employing a model developed using the total wind stress, which includes both the turbulent stress and the wave-induced stress. This model also predicted similar trends with wave age, however, the maximum predicted value for α^a_{Ch} was 0.085 at $c_p/u_{*a} \simeq 10$ and $U_{10} = 10$ m s^{-1}.

Makin & Kudryavtsev (2002) developed a wind-over-waves coupled model to investigate the impact of airflow separation from the dominant breaking waves. They found that α^a_{Ch} increased with increasing wave age for $c_p/u_{*a} < 2$ and for $c_p/u_{*a} > 2$ they did not find a well-defined relationship. Moreover, they observed that as the steepness of the dominant waves increased, the breaking probability as well as the separation stress also increased.

In a recent model study, Moon *et al.* (2004) examined the effect of surface waves on air-water momentum exchange over developing and young waves by combining ocean wave models and a wave boundary layer model. For fully developed waves (i.e. $c_p/u_{*a} > 10$), they estimated that the value of α^a_{Ch} was approximately between 0.01 and 0.02. For young waves (i.e. $c_p/u_{*a} < 10$) and for wind speeds higher than 30 m s^{-1} they found that α^a_{Ch} increased with increasing wave age.

It is evident from these previous measurements and model studies that α^a_{Ch} is dependent mainly on the wave age. In the field when $c_p/u_{*a} > 5.0$;

α^a_{Ch} was found to decrease as c_p/u_{*a} increased. However, for very young laboratory waves for which $c_p/u_{*a} < 5.0$; α^a_{Ch} was found to increase as c_p/u_{*a} increased. All of the field studies also found that other dimensionless forms of z_{oa} (i.e. z_{oa}/H_{rms} or z_{oa}/H_s) decreased with increasing wave age and increased with increasing wave slope or steepness although many different functional relationships were proposed.

Although the wave dependence of α^a_{Ch} has been studied extensively for the last few decades, there have only been a couple of studies (Bye, 1988; Bourassa, 2000) that investigated the hydrodynamic Charnock parameter, α^w_{Ch} (defined as $\alpha^w_{Ch} = z_{ot}/(u^2_{*t}/g)$, where, z_{ot} is the hydrodynamic roughness length, and u_{*t} is the water-side or tangential friction velocity). Bye (1988) estimated that the value of α^w_{Ch} was of order unity based on a theoretical argument. He estimated α^w_{Ch} by scaling with the wind friction velocity. Bourassa (2000) developed a shear stress model for the WBL and reanalyzed the data of Bye (1965) and Churchill & Pade (1980, 1981). He found that the value of α^w_{Ch} was of the order of 850 with an uncertainty factor of 2.6. Bourassa (2000) also reanalyzed the value of α^w_{Ch} using the data presented by Bye (1988) and found that the value of α^w_{Ch} varied between 350 and 1200. Moreover, Bourassa (2000) indicated that the value of α^w_{Ch} might also depend on wind-wave properties such as c_p/u_{*a}.

5.2.2 Stress Partitioning

When wind blows over the water surface, interfacial stresses are developed due to wind forcing. The stress that develops in the ABL far above the water surface is called the wind stress or total stress expressed as $\tau_a = \rho_a u^2_{*a}$, where ρ_a is the density of air. In a stable ABL, close to the water surface, the wind stress is expressed as the sum of viscous tangential stress (τ_t) and waveform drag or wave-induced stress (τ_w) contributions such that $\tau_a = \tau_t + \tau_w$ (see for

example Stewart, 1961; Mitsuyasu, 1985; Wu, 1987; Banner, 1990; Melville, 1996; Bourassa, 2000; Veron *et al.*, 2007). The viscous tangential stress is expressed as $\tau_t = \rho_w u_{*t}^2$, where ρ_w is the density of water. Before the onset of the wind waves, τ_a generated by the light wind is equal to τ_t in the water (Banner & Peirson, 1998). As the wind forcing increases, the wave field develops and τ_a is then partitioned into τ_t and τ_w. The relative magnitudes of τ_t and τ_w required to balance τ_a is still a subject of ongoing research. It was determined from recent measurements and model studies that τ_a is mostly supported by τ_w at moderate to high wind speeds (Peirson, 1997; Banner & Peirson, 1998; Bourassa, 2000; Veron *et al.*, 2007; Caulliez *et al.*, 2008). It should be noted that for hydrodynamically smooth flow τ_t/τ_a tends towards one, for hydrodynamically fully rough flow the waveform drag or wave-induced stress is much higher than the viscous tangential stress and τ_t/τ_a becomes very small in the range between 0.2 and 0.3, and for transitional flow τ_t/τ_a falls in between.

In the field or laboratory, estimates of τ_a are typically obtained from measurements of u_{*a} made using either the eddy correlation method or mean profile based methods (Tseng *et al.*, 1992). Measurements of τ_t can be made on either side of the air-water interface. The water side tangential stress is typically computed from the tangential friction velocity (u_{*t}) in a similar manner as τ_a using sub-surface mean velocity profiles. Peirson (1997) and Banner & Peirson (1998) measured the tangential friction velocity in the water using a viscous sublayer profile method (Foss *et al.*, 2007) and Siddiqui & Loewen (2007) measured water-side tangential friction velocities using a logarithmic profile method referred to as the Clauser method (Clauser, 1956).

There have been a number of field and laboratory studies that investigated the partitioning of stresses at the air-water interface expressed either as τ_t/τ_a or τ_w/τ_a. Stewart (1961) used measurements of U_z, H, wave period (T) and

duration (t) from Groen & Dorrestein (1958) to compute the partitioning of stress in the form of τ_w/τ_a. He suggested that at least 20% of τ_a was partitioned into τ_w. He also noted that this estimate was actually a lower limit because he was not able to estimate the momentum flux that was lost to the drift current because of wave-dissipation mechanisms. Manton (1971) theoretically derived an equation for the ratio τ_w/τ_a such that, $\tau_w/\tau_a = (3c/16C_D)(c_p/U_z)(1 - c_p/U_z)$, where, C_D is the drag coefficient and c is a constant obtained from measurements. Using $c \simeq 1.3\times10^{-2}$, $C_D \simeq 1.2\times10^{-3}$ and taking $(c_p/U_z) = 0.5$, he estimated that the maximum value of the stress ratio would be $\tau_w/\tau_a \simeq 0.52$. Therefore, Manton (1971) concluded that over 50% of τ_a was transferred to the WBL in the form of wave drag. Wu (1968, 1975) made measurements of wind profiles, surface and near-surface wind drift currents and waves in a wind-wave tank and found that the value of τ_w/τ_a varied from $\approx$0.2 to 0.3 at various wind speeds. Phillips (1977) estimated that in the open ocean the magnitude of τ_w/τ_a was approximately equal to 0.23. Snyder *et al.* (1981) used field data to determine τ_w by measuring air pressure fluctuations over ocean waves and τ_a using a sonic anemometer. They found that the value of τ_w/τ_a was approximately equal to 0.57. Hsu *et al.* (1982) used laboratory wind-wave data and estimated that the magnitude of τ_w/τ_a varied from 0.4 to 0.6. Therefore, the results of Manton (1971), Snyder *et al.* (1981) and Hsu *et al.* (1982) support the hypothesis that more than 50% of the wind stress, τ_a is supported by τ_w.

Mitsuyasu (1985) used the data from Mitsuyasu & Honda (1982) and derived the following relationship $\tau_w/\tau_a = 2.2\times10^2(H_s/\lambda_d)^2$. This relationship predicts that τ_w increases as the waves became steeper and that it becomes equal to τ_a at $H_s/\lambda_d = 0.07$. Moreover, they argued that although a large fraction of τ_a was initially supported by the waves, that, most of the momentum associated with τ_w was lost due to wave breaking and only a small

fraction (i.e. approximately 5%) was advected away by the wind-waves.

Peirson (1997) and Banner & Peirson (1998) used Particle Image Velocimetry (PIV) to study the properties of the WBL beneath laboratory wind-waves. They measured τ_t/τ_a at three fetches of 0.13, 2.45 and 4.35 m for various wind speeds. At the shortest fetch, in the absence of any wind-waves, they found that τ_t equalled τ_a. However, at the longest fetch of 4.35 m, they found that the ratio of τ_t/τ_a decreased from 0.63 at 4.7 m s^{-1} to 0.3 at 8.1 m s^{-1}. Bourassa (2000) reanalyzed two sets of near surface current data (Bye, 1965; Churchill & Pade, 1980, 1981) and estimated values of τ_t. He found that the magnitude of τ_t/τ_a was approximately equal to 1.0 at a wind speed of 5 m s^{-1} and then it decreased rapidly to a value of 0.15 to 0.3 as the wind speed increased to 10 m s^{-1}.

Veron *et al.* (2007) conducted experiments in the large wind-wave-current tank at the Air-Sea Interaction Laboratory, University of Delaware. They collected two-dimensional velocity fields in the airflow above the surface waves using PIV for four 10-m equivalent wind speeds varying from 5.7 to 14.9 m s^{-1} at a fetch of 21.1 m. Their data exhibited strong evidence of airflow separation over short wind-waves. They observed that τ_t is highest at the wave crest and then dropped abruptly and collapsed to a value equal to approximately zero once the airflow separation occurred on the leeward face of the wave. They also observed that τ_t re-generated past the wave trough on the windward side of the wind-waves.

Caulliez *et al.* (2008) modified the wind-over-waves coupled model used by Makin & Kudryavtsev (2002) to predict τ_a, τ_t, τ_w and airflow separation stress for various wind speeds at fetches of 6, 13, and 26 m. They found that τ_t/τ_a strongly depends on wind speed and weakly depends on fetch. Their model predicted that τ_t is the significant contributor to τ_a for a 10-m equivalent wind speed below 6 m s^{-1} at all three fetches and as the wind speed increased τ_t/τ_a

decreased rapidly before vanishing at wind speeds higher than 11 m s^{-1}.

5.3 Dimensional Analysis

5.3.1 Functional dependence of the surface roughness

Charnock (1955) proposed that z_{oa} should depend on u_{*a} and g. In addition, if it is assumed that z_{oa} depends on the wave field then H and λ_d should be included in the dimensional analysis. A functional relationship for z_{oa} can then be written as,

$$z_{oa} = f_1(u_{*a},\ g,\ H,\ \lambda_d) \tag{5.3}$$

where, f_1 is a function of its arguments u_{*a}, g, H and λ_d. In this study, the characteristic wave height was taken either as the significant wave height, H_s, or as the r.m.s. wave height, H_{rms}. The mean horizontal wind speed at height z, U_z and the wave fetch, F were not included in the dimensional analysis because of the fact that the effect of these two variables is implicitly included in the variables u_{*a}, H and λ_d.

Performing dimensional analysis with H and u_{*a} as repeating variables, the following three dimensionless groups can be formed,

$$\frac{z_{oa}}{H} = \phi_1\left(\frac{H}{\lambda_d},\ \frac{u_{*a}}{\sqrt{gH}}\right) \tag{5.4}$$

where, $u_{*a}/\sqrt{gH}$ is a form of Froude number. The deep water dispersion relationship gives $\lambda_d \propto c_p^2/g$. Now, combining H/λ_d and $u_{*a}/\sqrt{gH}$ and substituting for λ_d, it can be shown that,

$$\frac{z_{oa}}{H} = \varphi_1\left(\frac{H}{\lambda_d},\ \frac{c_p}{u_{*a}}\right) \tag{5.5}$$

Moreover, combining z_{oa}/H and $u_{*a}/\sqrt{gH}$, Equation (5.5) can then be rearranged into the following form,

$$\frac{gz_{oa}}{u_{*a}^2} = \psi_1\left(\frac{H}{\lambda_d},\ \frac{c_p}{u_{*a}}\right) \tag{5.6}$$

where the left hand side (i.e. gz_{oa}/u_{*a}^2) is defined as the aerodynamic Charnock parameter, α_{Ch}^a.

This dimensional analysis shows that Equations (5.5) and (5.6) apply to the majority of the relationships listed in Table 5.1. Therefore, the validity of Equations (5.5) and (5.6) was explored in this study using laboratory wind-wave measurements.

5.3.2 Functional dependence of the interfacial stresses

If the tangential friction velocity, u_{*t} is considered the dependent variable and it is assumed that u_{*t} depends on u_{*a}, z_{oa}, z_{ot}, H and λ_d, the functional relationship of u_{*t} can then be written as,

$$u_{*t} = f_2(\ u_{*a},\ z_{oa},\ z_{ot},\ H,\ \lambda_d) \tag{5.7}$$

Using dimensional analysis and taking H and u_{*a} as the repeating variables, the following four dimensionless groups can be formed,

$$\frac{u_{*t}}{u_{*a}} = \phi_2 \left(\frac{H}{\lambda_d},\ \frac{z_{ot}}{H},\ \frac{z_{oa}}{H} \right) \tag{5.8}$$

The ratio u_{*t}/u_{*a} can also be written in the form of a stress ratio, i.e. $\tau_t/\tau_a = \rho_w u_{*t}^2/\rho_a u_{*a}^2$, since the ratio of ρ_w/ρ_a is approximately constant and is assumed to be equal to 837 in this study. Using the stress ratio, Equation (5.8) can be written in the following form,

$$\frac{\tau_t}{\tau_a} = \frac{\rho_w u_{*t}^2}{\rho_a u_{*a}^2} = \psi_2 \left(\frac{H}{\lambda_d},\ \frac{z_{ot}}{H},\ \frac{z_{oa}}{H} \right) \tag{5.9}$$

5.4 Results

5.4.1 Wind-wave properties

Table 5.2 lists the following wind-wave properties for four sets of laboratory experiments; the root-mean-square (r.m.s.) wave height (H_{rms}), significant

wave height (H_s), dominant wavelength (λ_d), mean-square wave slope ($\langle S^2 \rangle$), dominant apparent wave frequency (f_d) and wave phase speed (c_p). H_{rms}, H_s, λ_d and $\langle S^2 \rangle$ were computed using the wave profile data. The dominant apparent wave frequency and c_p were computed from λ_d using the deep-water linear dispersion relationship. Mukto *et al.* (2007) used a particle-image based wave profile measurement technique to measure surface wave profiles and found that the morphological operations performed on the wave profile image did not significantly alter the detection of surface waves with wavelengths longer than $\sim$3 mm (i.e. only less than 2% error occurred in the wavenumber spectrum) and did not have any affect on wavelengths longer than $\sim$9 mm. Therefore, for computation of $\langle S^2 \rangle$, the surface wave profiles were smoothed using a low-pass filter with a cut-off wavelength of 3 mm. However, for computation of λ_d, the surface wave profiles were smoothed using a low-pass filter with a cut-off wavelength of 9 mm. The standard error of the mean in H_{rms}, H_s, λ_d, $\langle S^2 \rangle$, c_p and f_d at a 4.8 m fetch was found to be $\pm$0.007 cm, $\pm$0.012 cm, $\pm$0.107 cm, $\pm$0.001, $\pm$0.169 cm s^{-1} and $\pm$0.01 Hz, respectively.

In Figure 5.1, wave height frequency spectra computed from the wave profile data are shown plotted at a fetch of 8.8 m and at six different wind speeds ranging from 4.2 to 9.6 m s^{-1}. Note that the Nyquist frequency of these time series is only 7.5 Hz and this causes the spectra at low wind speed to be cut-off. However, the shapes and magnitudes of the spectra are observed to be reasonable. Similar results were also obtained at fetches of 4.8 and 12.4 m. The ratio of mean water depth, d to wavelength, λ_d varied from 3.4 to 17 confirming that the wind-waves in this study were deep water waves. The wave fields that were generated in this study at varying fetches and wind speeds were all found contain microscale breaking waves. The data in Table 5.2 shows that the waves became larger in amplitude, grew longer and steeper, and traveled faster as the wind speed increased from 4.0 to 9.6 m s^{-1} at all three fetches.

At 4.8 m fetch, H_{rms} increased from 0.12 to 0.88 cm, H_s increased from 0.18 to 1.3 cm, λ_d increased from 4.5 to 13.4 cm, $\langle S^2 \rangle$ increased from 0.019 to 0.063, c_p increased from 26.4 to 45.8 cm s^{-1} and f_d decreased from 8.5 to 4.4 Hz as wind speed increased from 4.1 to 9.3 m s^{-1}. At longer fetches, H_{rms}, H_s, λ_d, $\langle S^2 \rangle$ and c_p increased and f_d decreased compared to the shortest fetch.

5.4.2 Surface drift velocity

The surface drift velocity, U_s, is defined as $U_s = U_{SL} - U_{Stokes}$, where, U_{SL} is the Lagrangian surface drift velocity, and U_{Stokes} is the Stokes drift velocity (Kenyon, 1969; Wu, 1975; Cheung & Street, 1988). The Stokes drift velocity, U_{Stokes} is given by,

$$U_{Stokes} = \int \frac{2\sigma^3 F(\sigma)}{g} d\sigma \tag{5.10}$$

where, σ is the intrinsic wave frequency in rad s^{-1}, and $F(\sigma)$ is the frequency spectrum of the surface displacement (Bye, 1967). The intrinsic wave frequencies were computed by solving the following equation (Kundu & Cohen, 2002) for σ,

$$\omega = \sigma + U_{SL} k \tag{5.11}$$

where, ω is the apparent wave frequency (rad s^{-1}) and the wavenumber, k is given by $k = \sigma^2/g$ using the deep-water linear dispersion relation. To obtain U_{Stokes}, the integration in Equation (5.10) was performed over the entire frequency spectrum. The values of U_{SL}, U_{Stokes} and U_s are presented in Table 5.3. The data in Table 5.3 shows that U_{SL} and U_s values increased with increasing U_z, however, no definite relationship was observed with fetch. In the case of U_{Stokes}, the values of U_{Stokes} increased both with increasing U_z and F.

5.4.3 Wind friction velocity and roughness length

In the laboratory, u_{*a} was determined from vertical profiles of the mean horizontal wind speed, U_z. The profiles followed a log-linear velocity distributions expressed as,

$$U(z) - U_s = \frac{u_{*a}}{\kappa}\left[ln\left(\frac{z}{z_{oa}}\right) + f\left(\frac{z}{L_M}\right)\right] \tag{5.12}$$

where, κ is the von Kármán constant (assumed to be 0.4) and $f()$ is a function of its arguments z and the Monin-Obukhov length, L_M. The function $f(z/L_M)$ was determined in an iterative fashion using the gradient flux technique (McGillis *et al.*, 2001*b*; Zappa *et al.*, 2003). The wind friction velocity and z_{oa} were determined from the slope and intercept of Equation (5.12).

The values of u_{*a}, z_{oa} and the aerodynamic roughness Reynolds number, z_{oa}^{+} are listed in Table 5.3. Results from four sets of experiments are listed in Table 5.3. This includes the normal and high resolution DPIV data at 4.8 m fetch and the normal resolution DPIV data at 8.8 and 12.4 m fetch. The values of u_{*a} were found to vary from 8.9 to 54.8 cm s^{-1} and the values of z_{oa} ranged from 332 to 556 μm. The standard error of the mean of u_{*a} and z_{oa} at 4.8 m fetch were estimated to be $\pm$2.4 cm s^{-1} and $\pm$30 μm, respectively.

A comparison of the two sets of u_{*a} values measured at 4.8 m fetch raised the suspicion that u_{*a} values measured during the normal resolution DPIV measurement were underestimated. All of the u_{*a} data listed in Table 5.3 are plotted versus wind speed, U_z, in Figure 5.2. The solid line represents the best-fit regression line fitted to the data taken during the high resolution DPIV measurement at a fetch of 4.8 m and normal resolution DPIV measurement at fetches 8.8 and 12.4 m. Two dotted lines represent the upper and lower bound of the 99% confidence limits of the regression line. It was observed in Figure 5.2 that u_{*a} data obtained during the normal resolution DPIV measurement at a fetch of 4.8 m fell outside the lower bound of the 99% confidence limit. In

addition, in a few cases u_{*a} data measured at a fetch of 4.8 m during the normal resolution DPIV measurement produced τ_t/τ_a values greater than one. It should be noted that τ_t is a component of τ_a and should always be less than or equal to τ_a. Therefore, the u_{*a} data measured at a fetch of 4.8 m during the normal resolution DPIV measurement were not used any further in this study. Figure 5.2 shows that u_{*a} increases with increasing U_z, however, no definite trend is observed with varying fetch.

In Figure 5.3, z_{oa} is plotted versus U_z. This plot shows that on average z_{oa} data measured at a fetch of 4.8 m are lowest and average values at fetches 8.8 and 12.4 m are progressively larger. In general, z_{oa} values exhibit a similar trend with U_z for all three fetches. That is z_{oa} data are constant up to a certain wind speed and then abruptly increase. At fetch of 4.8 m, z_{oa} is equal to $\sim$350 μm up to 8.0 m s^{-1} and then increases abruptly to a value of 450 μm at 9.3 m s^{-1}. At fetch of 8.8 m, z_{oa} is equal to $\sim$350 μm up to a wind speed of 5.5 m s^{-1} then it increases abruptly to 450 μm and remains at this value up to a wind speed 8.0 m s^{-1} and then increases to 550 μm at 9.6 m s^{-1} (ignoring the low value at 8.0 m s^{-1}). At a fetch of 12.4 m, z_{oa} is constant at $\sim$450 μm for wind speeds up to 8.0 m s^{-1} and then it increases to 550 μm at 9.2 m s^{-1}.

The aerodynamic roughness Reynolds number, z_{oa}^+, is expressed as $z_{oa}^+ = u_{*a}z_{oa}/\nu_a$, where, ν_a is the kinematic viscosity of air. Conventionally, the airflow is considered aerodynamically smooth if $z_{oa}^+ < 0.11$ and fully rough if $z_{oa}^+ > 2.3$ (Donelan, 1990). Table 5.3 lists the values of z_{oa}^+ and their range is between 4.26 and 19.35 at various wind speeds and fetches indicating that the airflows were aerodynamically rough. In Figure 5.4 a plot of z_{oa}^+ versus U_z shows that as the wind speed increased from 4.0 to 8.0 m s^{-1}, z_{oa}^+ increased gradually from $\sim$4 to $\sim$10 and then it jumped from $\sim$10 to $\sim$20 when the wind speed increased from $\sim$8 to $\sim$9.5 m s^{-1} at all fetches.

5.4.4 DPIV mean velocity

The instantaneous velocity fields were extracted from the DPIV images in a wave-following Eulerian coordinate system (Siddiqui & Loewen, 2007). In this coordinate system (ξ, ζ), the origin is always at the air-water interface where the positive ξ axis points horizontally and the negative ζ axis points downwards parallel to the gravity vector. The horizontal and vertical spacing between velocity grid points was 2 mm for normal resolution DPIV measurements at fetches of 4.8, 8.8 and 12.4 m and 1 mm for the high resolution DPIV measurement at a fetch of 4.8 m. Therefore, the first grid point was located either at 2 mm or 1 mm below the air-water interface depending on the spatial resolution of the DPIV measurements. The mean velocity components were obtained by time-averaging 10-minutes of instantaneous velocity data at a given grid point in the wave-following coordinate system. Therefore, a total of 9000 samples (i.e. 10-minutes of data sampled at a rate of 15 Hz) were used to compute the average velocity at each grid point. Profiles of the streamwise component of the mean velocity, U at different wind speeds and three fetches of 4.8, 8.8 and 12.4 m from the low resolution DPIV runs are shown plotted in Figures 5.5, 5.6 and 5.7, respectively. The mean vertical velocity was found to be essentially zero for all four sets of experiments (not shown here) indicating that there were no significant systematic errors in the velocity measurements. Figures 5.5 to 5.7 show that U increases with increasing U_z at all fetches, however, no definite trend is observed for the velocity profiles as the fetch is varied from 4.8 to 12.4 m. It should be noted that it was not possible to obtain profiles of U for $U_z = 9.6$ m s^{-1} at 8.8 m fetch and for $U_z = 7.9$ and 9.2 m s^{-1} at 12.4 m fetch due to so-called 'trough effect'. The trough effect occurred when a wave trough in the cross-stream direction in front of the DPIV field of view obstructed the camera view. As a result, it was not possible to compute

accurate velocity field in the trough affected region.

5.4.5 Water-side friction velocity and roughness length

A log-layer was observed in the measured streamwise mean velocity profile (see Figure 5.8) and therefore, the log-layer was described well by the following equation,

$$\frac{U_s - U}{u_{*t}} = \frac{1}{\kappa} ln \left(\frac{\zeta}{z_{ot}} \right) \tag{5.13}$$

In Equation (5.13), U, U_s and ζ are measured quantities, κ is assumed to be 0.4, and the two unknowns are u_{*t} and z_{ot}. Estimates of u_{*t} and z_{ot} were obtained from Equation (5.13) using the Clauser method as described in Foss *et al.* (2007) and Siddiqui & Loewen (2007). The average value of correlation coefficient was greater than 0.99 when the velocity data in the log-layer (see Figures 5.5 to 5.7) were fitted to Equation (5.13). The Clauser method was applied to the velocity data in the range between $\zeta^+ = (\zeta u_{*t}/\nu_w)$ equal to 100 and 300 in this study. It should be noted that the estimates of u_{*t} do not depend on U_s but the estimates of z_{ot} are heavily dependent on U_s. Therefore, accurate measurements of U_s are required in order to obtain accurate z_{ot} estimates. Estimates of u_{*t} and z_{ot} are listed in Table 5.3. The values of u_{*t} varied from 0.448 to 0.933 cm s^{-1} and the values of z_{ot} ranged from 3 to 493 μm. The standard error of the mean for u_{*t} and z_{ot} was estimated to be $\pm$0.017 cm s^{-1} and $\pm$10 μm, respectively.

It is important to note that u_{*t} estimated using Equation (5.13) (i.e. the Clauser method) may not necessarily be equal to the viscous or tangential friction velocity. To verify that u_{*t} estimated using Equation (5.13) is an accurate estimate of the viscous friction velocity (u_{*v}), viscous friction velocities were estimated using an independent method (i.e. viscous sublayer

profile method) using the following equation,

$$u_{*v} = \sqrt{\frac{\tau_v}{\rho_w}} \tag{5.14}$$

where, the water-side viscous tangential stress (τ_v) was assumed to be given by,

$$\tau_v = \mu_w \left(\frac{U_s - U_1}{\Delta\zeta} \right) \tag{5.15}$$

where, μ_w is the dynamic viscosity of the water, U_1 is the streamwise mean velocity 1.0 mm below the water surface (at the first grid point), and then $\Delta\zeta$ is equal to 1.0 mm. Note that only velocity data obtained from the high resolution DPIV measurements at fetch of 4.8 m was used in Equation (5.15) because the remainder of the velocity data was lower resolution and the first grid point was 2.0 mm below the surface.

Estimates of u_{*t} and u_{*v} computed using Clauser's method and the viscous sublayer profile method, respectively, are compared in Table 5.4 at five wind speeds and a fetch of 4.8 m. It was found that the estimates of u_{*t} were on average $\sim$10% smaller than the estimates of u_{*v}. The close agreement between the estimates of the viscous and tangential friction velocity confirmed that the Clauser method provided accurate estimates of the viscous or tangential friction velocity.

One concern associated with the computation of viscous tangential stress was that the estimates of τ_v were obtained using U_1 values that might be measured outside the viscous sublayer at non-dimensional depths (ζ^+) ranging from 7.5 to 11, where, $\zeta^+ = \zeta u_{*t}/\nu_w$ is the standard wall coordinate. According to the "law of the wall", the non-dimensional viscous sub-layer thickness should be equal to 5, which is smaller than our estimated values of 7.5 to 11. Is it possible that a thicker viscous sub-layer develops on either side of the air-water interface due to wind-waves? It is well-known that the presence of deformable fluctuating surface waves can control the structure and dynamics of

the coupled boundary layers (Janssen, 1989; Peirson, 1997; Banner & Peirson, 1998; Janssen, 1999; Siddiqui & Loewen, 2007; Veron *et al.*, 2007). Peirson (1997) and Banner & Peirson (1998) estimated tangential friction velocities using velocity data within the top 1.0 mm beneath the water surface and found that the non-dimensional viscous sub-layer thickness was extended up to $z^+ \simeq 7$. So, it can be argued based on their laboratory measurement that the viscous sublayer thickness beneath a wind driven water surface can be much larger than the conventional wall layer estimates. If this is true than the measurement of U_1 at a depth of 1.0 mm could possibly at the edge of the viscous sublayer. However, it is also possible that the small % difference between u_{*v} and u_{*t} (see Table 5.4) is due to the fact that $\delta_v = 5u_{*t}/\nu_w$ and in fact $\zeta = 1.0$ mm is just outside the viscous sublayer.

The variations of u_{*t} with U_z for all four sets of experiments at various wind speeds and all three fetches are shown in Figure 5.9. This plot shows that u_{*t} increases with increasing U_z and decreases with increasing F. In Figure 5.10, z_{ot} is plotted versus U_z and z_{ot} values are found to decrease with U_z. Moreover, at a given U_z, z_{ot} tends to decrease as fetch increases.

The hydrodynamic roughness Reynolds number is expressed as $z_{ot}^+ = z_{ot}u_{*t}/\nu_w$. Table 5.3 lists the values of z_{ot}^+ and they are found to vary between 0.02 and 2.97. These z_{ot}^+ values indicate that the flow in the WBL was typically in transition between the smooth and rough regimes. In Figure 5.11 a plot of z_{ot}^+ versus U_z shows that the flow tends to become smooth as the wind speed or fetch increases. At a fetch of 4.8 m, this plot shows that all the hydrodynamic flows were in the transition regime at all wind speeds. At a fetch of 8.8 m, Figure 5.11 shows that the hydrodynamic flows are in the transition regime for wind speeds ranging from 5.4 to 7.2 m s^{-1} and then it became smooth at a wind speed of 7.9 m s^{-1}. At a fetch of 12.4 m, the hydrodynamic flows were in the transition regime as the wind speed varied between 4.0 and 5.3 m s^{-1}

and that it became smooth at wind speeds greater than 6.0 m s^{-1}.

5.4.6 Velocity defect law

The streamwise mean velocity profiles can be represented in the form of velocity defect law in universal wall coordinates,

$$u^+ = \frac{U_s - U(\zeta)}{u_{*t}} \text{ and, } \zeta^+ = \frac{\zeta u_{*t}}{\nu_w} \tag{5.16}$$

where, u^+ and ζ^+ are the non-dimensional velocity and depth respectively (Cheung & Street, 1988). Three layers are typically defined for a boundary layer over a smooth solid wall (Kundu & Cohen, 2002). A viscous sublayer adjacent to the smooth wall at $\zeta^+ < 5$ and in this layer $u^+ = \zeta^+$; a logarithmic layer, in which the velocity varies logarithmically with depth for $30 < \zeta^+ < 300$; and a buffer layer for $5 < \zeta^+ < 30$ where the velocity profile is neither linear nor logarithmic. In this study, we found that a logarithmic layer existed in the region $100 < \zeta^+ < 300$ and a buffer layer existed for $\zeta^+ < 100$.

Figures 5.12, 5.13 and 5.14 show the streamwise mean velocity profiles at three fetches of 4.8, 8.8 and 12.4 m, respectively, plotted in the form of a velocity defect law in wall coordinates. The dark solid and dashed-dotted straight lines represent the law of the wall for a turbulent boundary layer with a zero pressure gradient over smooth and rough walls respectively (Schlichting & Gersten, 2000). At 4.8 m fetch, the non-dimensional velocity profiles at three low wind speeds (4.1 to 6.1 m s^{-1}) fell between the smooth and rough wall boundary lines confirming that the flow was in the transitional regime. At three other higher wind speeds (6.8 to 9.0 m s^{-1}), the flow was in between smooth and transitional regime. At 8.8 m fetch, the non-dimensional velocity profiles were hydrodynamically in transitional flow regime except for the highest wind speed when the flow was found to be in the smooth regime. At 12.4 m fetch, the non-dimensional velocity profile at the lowest wind speed

was in transitional flow regime and the flow at remaining three other higher wind speeds was in transitional to smooth flow regime.

5.5 Wind-Wave Dependent Roughness and Interfacial Stresses

5.5.1 Wind-wave dependent roughness

One of the main focuses of this chapter was to examine the constancy of α^a_{Ch} by investigating its relationship with wind-wave properties such as c_p/u_{*a} and H_s/λ_d as discussed in §5.3. In Figure 5.15, α^a_{Ch} is plotted versus c_p/u_{*a} at various wind speeds for all three fetches. In Figure 5.15, the data clearly shows that α^a_{Ch} increases as c_p/u_{*a} increases. An exponential equation fitted to the observed data gives the following relationship,

$$\frac{gz_{oa}}{u^2_{*a}} = 0.0055 \exp\left(1.4\frac{c_p}{u_{*a}}\right) \qquad r = 0.73 \tag{5.17}$$

where, r is the Pearson product-moment correlation coefficient (Rodgers & Nicewander, 1988).

The increasing trend of α^a_{Ch} with c_p/u_{*a} as presented in Figure 5.15 is similar to the increasing trend found by Keller *et al.* (1992) using laboratory wind-wave data and model predictions by Makin & Kudryavtsev (2002) (both data are plotted in Figure 5.15). The model by Makin & Kudryavtsev (2002) predicted that for very young waves (i.e. $c_p/u_{*a} < 2$) α^a_{Ch} increased with increasing c_p/u_{*a} and for $c_p/u_{*a} > 2$ it is not well-defined. The wave age for our observed data varied from 0.84 to 2.58 indicating that these are very young wind-waves as $c_p/u_{*a} < 5$ (Phillips, 1977). The conclusion from Figure 5.15 is that α^a_{Ch} is not constant and increases with increasing c_p/u_{*a} when $c_p/u_{*a} < 5$.

Figure 5.16 shows the variation of α^a_{Ch} with dominant wave steepness (H_s/λ_d). A regression line fitted to the data in Figure 5.16 gives the following

relationship,

$$\frac{gz_{oa}}{u_{*a}^2} = 6 \times 10^{-5}(H_s/\lambda_d)^{-2.6} \qquad r = 0.60 \tag{5.18}$$

This equation and the data in Figure 5.16 demonstrate that α_{Ch}^a decreases as H_s/λ_d increases. The data in Figure 5.16 also support the hypothesis that α_{Ch}^a is not constant and varies with wind-wave properties. Moreover, based on a comparison of r values for Equations (5.17) and (5.18), it can be concluded that α_{Ch}^a is correlated more closely with c_p/u_{*a} than with H_s/λ_d.

Other forms of the dimensionless z_{oa} (i.e. z_{oa}/H_{rms} or z_{oa}/H_s) as represented by Equation (5.5) are examined next. First, a plot of z_{oa}/H_{rms} versus c_p/u_{*a} is presented in Figure 5.17. In Figure 5.17, it is evident that z_{oa}/H_{rms} increases with increasing c_p/u_{*a} at all fetches. Moreover, for a given c_p/u_{*a}, z_{oa}/H_{rms} decreased with increasing fetch. In Table 5.1, the relationships given by Donelan (1990) and Drennan *et al.* (2003) predicted that z_{oa}/H_{rms} decreased with increasing c_p/u_{*a}. They observed an opposite trend because their relationships were obtained using field observation of older waves. Donelan (1990) field data correspond to wave ages from 4 to 29 and Drennan *et al.* (2003) wave ages ranged from 5 to 33. So, it should be noted that wave age plays a significant role in determining the dependence of α_{Ch}^a with wind-wave properties.

In Figure 5.18, z_{oa}/H_s is plotted against H_s/λ_d similar to Figure 3(d) by Taylor & Yelland (2001). It is found that z_{oa}/H_s decreases as H_s/λ_d increases and a regression line fitted to the data gives the following relationship,

$$\frac{z_{oa}}{H_s} = 1.2 \times 10^{-4} \left(\frac{H_s}{\lambda_d}\right)^{-2.33} \qquad r = 0.90 \tag{5.19}$$

The correlation between z_{oa}/H_s and H_s/λ_d is much stronger than the correlation between α_{Ch}^a and H_s/λ_d. Taylor & Yelland (2001) presented a relationship similar to Equation (5.19), however, their relationship exhibited the opposite trend as their relationship was obtained from data with wave ages

ranging from 7 to 33. It is important to note that H_s/λ_d alone can explain 90% of the variability in z_{oa}/H_s and therefore, Equation (5.19) can be used to predict z_{oa}. Moreover, Equation (5.19) also confirms that z_{oa} depends on wind-wave properties such as H_s/λ_d.

The functional dependence of z_{oa} was further investigated by plotting the aerodynamic roughness Reynolds number ($z_{oa}^+ = z_{oa}u_{*a}/\nu_a$) versus H_s/λ_d in Figure 5.19. The trend in Figure 5.19 demonstrates that as H_s/λ_d increases, z_{oa}^+ also increases indicating that the flow in the ABL became rougher as the waves grew steeper. A regression line fitted to the data in Figure 5.19 gives the following relationship,

$$\frac{z_{oa}u_{*a}}{\nu_a} = 2210\,(H_s/\lambda_d)^{2.23} \qquad r = 0.88 \tag{5.20}$$

The high value of the correlation coefficient indicates that the data are described well by Equation (5.20) and that z_{oa}^+ is primarily a function of H_s/λ_d for these very young waves. In addition, extrapolating Equation (5.20) it was found that when H_s/λ_d is less than $\sim$0.046, the ABL becomes aerodynamically smooth. Caulliez *et al.* (2008) investigated the dependence of z_{oa}^+ on significant dominant wave steepness. The significant wave steepness of the dominant waves was estimated directly from the frequency spectrum of the time derivative of the water surface height signals and c_p. They found that z_{oa}^+ and the significant dominant wave steepness were related by a power law similar to the Equation (5.20). They argued that z_{oa}^+ is mainly controlled by airflow momentum flux to the dominant waves.

Similarly, the functional dependence of dimensionless forms of z_{ot} on wind-wave properties is examined in Figures 5.20, 5.21 and 5.22. First, it should be noted that no significant correlation was observed between α_{Ch}^w and c_p/u_{*a} when a figure similar to Figure 5.15 is plotted (not shown here). Values of α_{Ch}^w were found to vary between 1 and 100, whereas, Bourassa (2000) found

the values of α_{Ch}^{w} ranged between 350 and 1200. In Figure 5.20 a plot of α_{Ch}^{w} versus H_s/λ_d shows that α_{Ch}^{w} decreases as H_s/λ_d increases. A regression line fitted to the observed data gives the following relationship,

$$\frac{gz_{ot}}{u_{*t}^2} = 10^{-4}\left(H_s/\lambda_d\right)^{-4.36} \qquad r = 0.59 \tag{5.21}$$

A plot of z_{ot}/H_{rms} versus c_p/u_{*a} (not shown here) demonstrated that z_{ot}/H_{rms} and c_p/u_{*a} were not correlated. However, another dimensionless form of z_{ot}, i.e. z_{ot}/H_s is plotted versus H_s/λ_d in Figure 5.21. It is found that z_{ot}/H_s decreases as H_s/λ_d increases. A regression line fitted to the data presented in Figure 5.21 gives the following relationship,

$$\frac{z_{ot}}{H_s} = 4 \times 10^{-11}\left(\frac{H_s}{\lambda_d}\right)^{-7.29} \qquad r = 0.81 \tag{5.22}$$

Comparing Pearson's r value it was found that the correlation between z_{ot}/H_s and H_s/λ_d was much stronger than the correlation between α_{Ch}^{w} and H_s/λ_d.

Figure 5.22 shows the variation of the hydrodynamic roughness Reynolds number, $z_{ot}^{+} = z_{ot}u_{*t}/\nu_w$ with H_s/λ_d. This figure demonstrates that the sub-surface flow in the WBL became smoother as the waves became steeper. The functional relationship between z_{ot}^{+} and H_s/λ_d is given by the following regression equation,

$$\frac{z_{ot}u_{*t}}{\nu_w} = 2 \times 10^{-6}\left(H_s/\lambda_d\right)^{-4.56} \qquad r = 0.64 \tag{5.23}$$

The data presented in Figure 5.22 and Equation (5.23) show that z_{ot}^{+} decreases very rapidly with increasing H_s/λ_d.

5.5.2 Wind-wave dependent interfacial stresses and its partitioning

The values of the interfacial stresses (τ_t and τ_a) in the coupled boundary layers for six wind speeds and three fetches are listed in Table 5.3. The ratio of τ_t/τ_a quantifies the partitioning of τ_a into its components (i.e. τ_t and τ_w) at the

air-water interface. In Figure 5.23, τ_t/τ_a is plotted versus U_z at all three fetches. This plot clearly shows the dependence of τ_t/τ_a on both the wind speed and the fetch. It is observed that τ_t/τ_a decreases as fetch increases from 4.8 to 12.4 m and as U_z increases from 4.0 m s^{-1} to 9.6 m s^{-1}. At a fetch of 4.8 m, τ_t/τ_a decreased rapidly from $\sim$1.0 to $\sim$0.25 as U_z increased from 5.4 to 9.3 m s^{-1}. This variation of τ_t/τ_a with U_z is similar to the trend observed by Banner & Peirson (1998). Moreover, for the two other data sets at the longer fetches, τ_t/τ_a first decreased rapidly from $\sim$0.7 at 4.0 m s^{-1} to $\sim$0.2 at 6.0 m s^{-1} and then remained approximately constant at $\sim$0.2 to 9.6 m s^{-1}. This trend of τ_t/τ_a with U_z is very similar to the findings of Bourassa (2000).

Caulliez *et al.* (2008) present model predictions of τ_t/τ_a that were similar to the trends in Figure 5.23. However, they did not find a strong fetch dependence with τ_t/τ_a. They found that at fetches of 6, 13 and 26 m τ_t/τ_a decreased from $\sim$1.0 to $\sim$0.6 as U_{10} (i.e. a 10-m equivalent wind speed) increased from 2.5 to 6.0 m s^{-1}. As U_{10} goes from 6 to 11 m s^{-1}, τ_t/τ_a decreases rapidly from $\sim$0.6 to $\sim$0.2 and then vanishes at wind speeds higher than 11 m s^{-1}.

The dimensional analysis presented in §5.3 indicated that τ_t/τ_a should depend on the dominant wave steepness, H_s/λ_d and the ratio of roughness lengths, z_{ot}/z_{oa}. In Figure 5.24, τ_t/τ_a is plotted versus H_s/λ_d and the data show that τ_t/τ_a decreased as H_s/λ_d increased. A regression line fitted to the data presented in Figure 5.24 gives the following relationship,

$$\frac{\tau_t}{\tau_a} = 8.4 \times 10^{-5} \left(\frac{H_s}{\lambda_d} \right)^{-3.34} \qquad r = 0.88 \tag{5.24}$$

This plot reveals that a larger fraction of τ_a is partitioned into τ_w as the wind waves become steeper. For these short wind waves, τ_t/τ_a decreased from $\sim$1.0 to $\sim$0.2 as H_s/λ_d increased from 0.06 to 0.1. The strong correlation between τ_t/τ_a and H_s/λ_d suggests that the stress partitioning can be parameterized using wave steepness for these young wind waves.

In Figure 5.25, τ_t/τ_a is plotted as a function of z_{ot}/z_{oa}. An exponential line fitted to the data in Figure 5.25 gives the following relationship,

$$\left|\frac{\tau_t}{\tau_a}\right|_{\sim 0.2}^{\sim 1.0} = 0.21 \exp\left(3.8 \frac{z_{ot}}{z_{oa}}\right) \qquad r = 0.85 \tag{5.25}$$

One of the most striking observations from Figure 5.25 and Equation (5.25) is that τ_t/τ_a decreases exponentially as z_{ot}/z_{oa} decreases and that τ_t/τ_a becomes constant at a value of $\sim$0.2 for z_{ot}/z_{oa} values equal to or less than $\sim$0.06. It is also interesting to observe from Figure 5.25 and Equation (5.25) that when τ_t/τ_a is equal to $\sim$1.0, z_{ot}/z_{oa} is equal to $\sim$0.5. This indicates that at a very low wind speed $\tau_t \sim \tau_a$ and that the water-side roughness length is approximately equal to half of the air-side roughness length.

A number of conclusions were drawn based on the relationship obtained from Figure 5.25 and Equation (5.25). First, this relationship helps explaining the physical mechanism responsible for making the ABL rougher and WBL smoother. It was shown in Table 5.3 that z_{oa} increased and z_{ot} decreased at all fetches as wind speed increased. Moreover, it was shown in Figure 5.23 that τ_t/τ_a decreased at all fetches as wind speed increased. It is evident that as the wind speed increased τ_t/τ_a decreased, z_{oa} increased and z_{ot} decreased at all fetches. Caulliez *et al.* (2008) showed that the stress induced by airflow separation at the crests of breaking wind waves increased and τ_t/τ_a decreased concomitantly as the wind speed increased at all fetches. This implies that as the wind forcing became stronger, the airflow separation from the breaking wind waves became severe causing more agitation in the air-side boundary layer and less agitation in the water-side boundary layer. As a result, z_{oa} increased and z_{ot} decreased making the air-side boundary layer rougher and the water-side boundary layer smoother. Therefore, it is argued that the physical mechanism mainly responsible for the reduction of roughness length in the WBL is due to the airflow separation at the leeward side of the breaking

wind waves as discussed by Makin & Kudryavtsev (2002), Veron *et al.* (2007) and Caulliez *et al.* (2008).

Secondly, Phillips (1977) and Banner & Peirson (1998) argued that when wind blows above an ocean surface at moderate to high wind speeds, airflow in the air-side boundary layer is better described as being in the transition regime, considering the influence of τ_t even during the highest wind speeds. The findings presented in this chapter could also be interpreted similar to the results of Phillips (1977) and Banner & Peirson (1998) that airflow in the air-side boundary layer was typically in transition regime and never became fully rough as τ_t/τ_a was never less than ($\sim$0.2) even at the highest wind speeds. However, the aerodynamic roughness Reynolds number presented in §5.4.3 showed that the airflows were aerodynamically in fully rough regime.

Finally, the strong correlation between τ_t/τ_a and z_{ot}/z_{oa} suggested that z_{ot}/z_{oa} should also be correlated with H_s/λ_d. A power law fitted to the data gives the following relationship,

$$\frac{z_{ot}}{z_{oa}} = 3.92 \times 10^{-10} \left(\frac{H_s}{\lambda_d}\right)^{-7.65} \qquad r = 0.83 \tag{5.26}$$

5.6 Conclusions

This study reports on a series of laboratory experiments investigating the dependence of surface roughness and interfacial stresses on wind-wave properties. Velocity measurements in the coupled air-water boundary layers and measurements of wind-wave properties were made at various wind speeds ranging from 4.0 to 9.6 m s^{-1} and at three fetches of 4.8, 8.8 and 12.4 m. Roughness lengths and friction velocities in the coupled boundary layers were computed using air-side and water-side velocity measurements.

The measurement of wind-wave properties showed that the height, length, slope and phase speed of waves increased with increasing wind speed and fetch

as expected. For very young laboratory wind-waves, it was verified that the wave age and wave steepness are the two most important wind-wave properties that control the momentum transfer in the coupled boundary layers. In this study, the wave age was found to vary between 0.84 and 2.58 and the wave steepness was found to vary between 0.04 and 0.12.

It was established that the water-side friction velocity calculated using Clauser's method is an accurate estimate of the tangential or viscous friction velocity. Moreover, it was argued that the non-dimensional viscous sub-layer thickness is larger than the conventional wall layer estimate.

For very young laboratory wind-waves investigated in this study the aerodynamic and hydrodynamic Charnock parameters were found to vary with wind-wave properties. It was found that the aerodynamic Charnock parameter is most closely correlated with wave age and that the aerodynamic Charnock parameter increases with increasing wave age. Similar trends were observed in the laboratory wind-wave experiments by Keller *et al.* (1992) and the model prediction by Makin & Kudryavtsev (2002). The aerodynamic Charnock parameter was found to be weakly correlated with wave steepness. However, another form of the dimensionless aerodynamic roughness length (i.e. z_{oa}/H_{rms}) was found to correlate closely with the wave steepness. In the case of the hydrodynamic Charnock parameter, it was found to be weakly correlated with wave steepness and did not correlate significantly with wave age. The hydrodynamic Charnock parameter decreased as the wave steepness increased but the correlation was rather weak. It was also observed that the ratio of the hydrodynamic roughness length to wave height correlated closely with wave steepness. It was concluded that the aerodynamic roughness Reynolds number was closely correlated with the wave steepness but that the hydrodynamic roughness Reynolds number showed weak correlation with wave steepness.

Momentum transfer at the air-water interface was studied by examining

the partitioning of wind stress into its component viscous tangential stress for the very young laboratory wind-waves. It was determined that the momentum transfer across the air-water interface depends on the wind speed, fetch, and wind-wave properties. It was observed that the ratio of the tangential stress to wind stress is strongly correlated with wave steepness and the ratio of roughness lengths. Based on our measurements of interfacial stresses and roughness lengths in the coupled boundary layers, and model studies by Caulliez *et al.* (2008) it was argued that the airflow separation from the crests of breaking waves could be responsible for making the air-side boundary layer rougher and water-side boundary layer smoother. Moreover, it was concluded that airflow above wind-waves is in a state of fully rough regime for moderate to high wind speed. In addition, it was shown that the estimate of surface roughness could be obtained by using wave steepness.

Wave age dependent functional relationships for the aerodynamic roughness

$\alpha_n = c_1(wave\ age)^{c_2}$

Researcher(s)	Data type	α_n	*wave age*	c_1	c_2
Charnock (1955)	Field;	gz_{oa}/u_{*a}^2	–	Constant	0
Toba *et al.* (1990)	Field & Lab. Bass Strait & others	gz_{oa}/u_{*a}^2	c_p/u_{*a}	0.02	0.5
Maat *et al.* (1991)	Field; HEXMAX	gz_{oa}/u_{*a}^2	c_p/u_{*a}	0.8	-1.0
Smith *et al.* (1992)	Field; HEXMAX	gz_{oa}/u_{*a}^2	c_p/u_{*a}	0.48	-1.0
Johnson *et al.* (1998)	Field; RASEX & Donelan *et al.* (1993)	gz_{oa}/u_{*a}^2	c_p/u_{*a}	1.89	-1.59
Drennan *et al.* (2003)	Field; HEXMAX WAVES, FETCH AGILE & SWADE	gz_{oa}/u_{*a}^2	c_p/u_{*a}	1.7	-1.7
Donelan (1990)	Field; Lake Ontario, 1982	z_{oa}/H_{rms}	c_p/u_{*a}	1.84	-2.53
	Same as above	z_{oa}/H_{rms}	c_p/U_{10}	5.53×10^{-4}	-2.66
	Laboratory; Wave tank, 1979	z_{oa}/H_{rms}	c_p/u_{*a}	0.205	-2.18
	Same as above	z_{oa}/H_{rms}	c_p/U_{10}	9.76×10^{-6}	-3.48
Smith *et al.* (1992)	Field; HEXMAX	z_{oa}/H_{rms}	c_p/U_{10}	5.32×10^{-4}	-3.53
Donelan *et al.* (1993)	Field; HEXMAX & Lake Ontario, 1982	z_{oa}/H_{rms}	c_p/U_{10}	6.7×10^{-4}	-2.6
Anctil & Donelan (1996)	Field; Lake Ontario, 1996	z_{oa}/H_{rms}	c_p/U_{10}	3.7×10^{-4}	-3.22
Drennan *et al.* (2003)	Field; HEXMAX WAVES, FETCH AGILE & SWADE	z_{oa}/H_{rms}	c_p/u_{*a}	13.4	-3.4

Wave slope or steepness dependent functional relationships for the aerodynamic roughness

$\alpha_n = c_3(wave\ slope\ or\ steepness)^{c_4}$

Researcher(s)	Data type	α_n	*wave slope/ steepness*	c_3	c_4
Anctil & Donelan (1996)	Field; Lake Ontario, 1996	z_{oa}/H_{rms}	S_{rms}	2550	6.76
Taylor & Yelland (2001)	Field; RASEX HEXMAX & Lake Ontario, 1996	z_{oa}/H_s	H_s/λ_d	1200	4.5

Mathematical model based functional relationships for the aerodynamic roughness

$\alpha_{Ch}^a = f(wave\ age\ or\ drag\ coefficient)$

Researcher	Model type	α_{Ch}^a	Functional form
Nordeng (1991)	Mathematical model-1	gz_{oa}/u_{*a}^2	$0.11(c_p/u_{*a})^{-3/4}\,\phi_1\,(c_p/u_{*a})$
where, $\phi_1^2 = 1 - \exp(-2\kappa c_p/u_{*a})[1 + (2\kappa c_p/u_{*a}) + 1/2(2\kappa c_p/u_{*a})^2 + 1/6(2\kappa c_p/u_{*a})^3]$			
Nordeng (1991)	Mathematical model-2	gz_{oa}/u_{*a}^2	$10\exp(-\kappa\sqrt{C_D})g/(C_D U_{10}^2)$ where, $C_D = [\kappa/\ln(10/z_{oa})]^2$

Table 5.1: Wave dependent functional relationships for the aerodynamic roughness length

Parameter	$F = 4.8$ m (Normal DPIV resolution)						$F = 4.8$ m (High DPIV resolution)					
U_z (m s^{-1})	4.1	5.3	6.1	6.8	7.9	9.0	-	5.4	6.3	6.8	8.0	9.3
H_{rms} (cm)	0.12	0.23	0.35	0.47	0.66	0.80	-	0.24	0.38	0.50	0.69	0.88
H_s (cm)	0.18	0.35	0.52	0.69	0.97	1.18	-	0.36	0.56	0.74	1.03	1.30
λ_d (cm)	4.5	5.6	7.2	8.6	10.8	12.5	-	5.8	7.4	8.8	11.4	13.4
$\langle S^2 \rangle$	0.019	0.039	0.046	0.047	0.054	0.060	-	0.038	0.050	0.053	0.057	0.063
c_p (cm s^{-1})	26.4	29.6	33.5	36.6	41.1	44.2	-	30.1	34.0	37.1	42.2	45.8
f_d (Hz)	8.5	7.3	6.1	5.5	4.7	4.4	-	7.1	5.9	5.5	4.6	4.2
T_{air}(°C)	18.9	20.6	19.8	22.8	21.5	20.2	-	20.7	21.2	19.7	21.3	21.2
T_{water}(°C)	22.8	23.3	22.8	24.4	23.8	22.5	-	23.7	24.1	22.6	23.3	24.0
Parameter	$F = 8.8$ m (Normal DPIV resolution)						$F = 12.4$ m (Normal DPIV resolution)					
U_z (m s^{-1})	4.2	5.4	6.1	7.2	7.9	9.6	4.0	5.3	6.2	6.9	7.9	9.2
H_{rms} (cm)	0.27	0.53	0.75	0.96	1.08	1.38	0.56	0.95	1.15	1.33	1.61	1.91
H_s (cm)	0.41	0.78	1.11	1.41	1.59	2.04	0.83	1.41	1.70	1.97	2.38	2.81
λ_d (cm)	6.9	10.0	12.8	15.3	16.7	19.1	11.9	16.4	18.7	19.9	22.1	23.7
$\langle S^2 \rangle$	0.029	0.044	0.048	0.054	0.061	0.078	0.033	0.041	0.048	0.056	0.070	0.092
c_p (cm s^{-1})	32.9	39.5	44.6	48.8	51.0	54.6	43.2	50.5	54.1	55.8	58.7	60.8
f_d (Hz)	6.1	4.8	4.2	3.8	3.5	3.0	4.2	3.4	3.1	2.8	2.7	2.6
T_{air}(°C)	19.2	21.8	15.6	19.7	21.9	19.9	18.4	18.9	18.9	20.1	19.9	19.8
T_{water}(°C)	22.8	22.1	21.7	21.0	22.2	21.1	21.9	23.0	22.0	22.5	22.6	21.8

Table 5.2: Summary of wind-wave properties at different experimental conditions. F is the wave fetch; U_z, wind speed in the wave tank; H_{rms}, the r.m.s. wave height; H_s, the significant wave height; λ_d, the dominant wavelength; $\langle S^2 \rangle$, the mean-square wave slope; (c_p), the wave phase speed; f_d, the dominant apparent wave frequency. T_{air}, the bulk air temperature; T_{water}, the bulk water temperature. Short dashed line represents that data are either missing due to computational limitations or not available.

Parameter	$F = 4.8$ m (Normal DPIV resolution)						$F = 4.8$ m (High DPIV resolution)					
U_z (m s^{-1})	4.1	5.3	6.1	6.8	7.9	9.0	-	5.4	6.3	6.8	8.0	9.3
U_{SL} (cm s^{-1})	16.84	20.40	23.61	26.90	30.15	33.85	-	20.11	23.31	26.68	29.75	32.77
U_{Stokes} (cm s^{-1})	0.15	0.47	0.85	1.14	1.57	1.76	-	0.50	0.92	1.23	1.64	1.97
U_s (cm s^{-1})	16.69	19.93	22.76	25.76	28.58	32.09	-	19.61	22.39	25.45	28.11	30.80
u_{*a} (cm s^{-1})	8.9	17.5	22.9	28.8	32.7	40.9	-	20.4	28.5	32.9	44.5	54.8
z_{oa} (μm)	-	-	-	-	-	-	-	344	346	346	351	454
z_{oa}^+	-	-	-	-	-	-	-	4.67	6.53	7.61	10.31	16.45
τ_a (Pa)	-	-	-	-	-	-	-	0.050	0.097	0.129	0.235	0.356
u_{*t} (cm s^{-1})	0.645	0.725	0.796	0.733	0.841	0.933	-	0.754	0.781	0.809	0.833	0.902
z_{ot} (μm)	164	108	79	14	13	14	-	164	77	30	20	15
z_{ot}^+	1.12	0.84	0.66	0.11	0.12	0.14	-	1.34	0.65	0.25	0.18	0.15
τ_t (Pa)	0.042	0.052	0.063	0.053	0.070	0.087	-	0.057	0.061	0.065	0.069	0.081
c_p/u_{*a}	2.97	1.70	1.46	1.27	1.26	1.08	-	1.47	1.19	1.13	0.95	0.84
Parameter	$F = 8.8$ m (Normal DPIV resolution)						$F = 12.4$ m (Normal DPIV resolution)					
U_z (m s^{-1})	4.2	5.4	6.1	7.2	7.9	9.6	4.0	5.3	6.2	6.9	7.9	9.2
U_{SL} (cm s^{-1})	15.73	22.20	24.52	26.13	31.06	35.62	16.46	20.39	22.55	24.33	27.93	29.64
U_{Stokes} (cm s^{-1})	0.72	1.36	1.87	2.28	2.24	2.63	1.35	2.24	2.43	2.71	3.08	3.62
U_s (cm s^{-1})	15.01	20.84	22.65	23.85	28.82	32.99	15.11	18.15	20.12	21.62	24.85	26.02
u_{*a} (cm s^{-1})	18.4	30.2	36.0	42.4	44.9	52.8	16.7	27.9	30.1	35.0	37.2	50.6
z_{oa} (μm)	345	349	451	457	379	550	438	450	461	464	458	556
z_{oa}^+	4.26	6.94	11.12	12.95	11.19	19.35	4.93	8.44	9.29	10.83	11.36	18.79
τ_a (Pa)	0.040	0.109	0.155	0.215	0.240	0.333	0.033	0.093	0.108	0.146	0.165	0.306
u_{*t} (cm s^{-1})	0.572	0.646	0.618	0.645	0.693	-	0.448	0.460	0.526	0.529	-	-
z_{ot} (μm)	493	47	20	29	3	-	130	25	17	6	-	-
z_{ot}^+	2.97	0.32	0.13	0.19	0.02	-	0.60	0.12	0.09	0.03	-	-
τ_t (Pa)	0.033	0.042	0.038	0.041	0.048	-	0.020	0.021	0.028	0.028	-	-
c_p/u_{*a}	1.79	1.31	1.24	1.15	1.14	1.03	2.58	1.81	1.80	1.59	1.58	1.20

Table 5.3: Measurements of air- and water-side mean flow properties at different experimental conditions. F is the wave fetch; U_z, wind speed in the wave tank; U_{SL}, the Lagrangian surface drift velocity; U_{Stokes}, the Stokes drift velocity; U_s, the surface drift velocity; u_{*a}, wind friction velocity; z_{oa}, aerodynamic roughness length; z_{oa}^+, aerodynamic roughness Reynolds number; τ_a, wind stress; u_{*t}, water-side or tangential friction velocity; z_{ot}, hydrodynamic roughness length; z_{ot}^+, hydrodynamic roughness Reynolds number; τ_t, water-side or tangential stress; c_p/u_{*a}, wave age. The short dashed line represents that data are either missing due to computational limitations or not available.

F (m)	U_z (m s^{-1})	u_{*t} (cm s^{-1})	u_{*v} (cm s^{-1})	ζ^+	Difference %
	5.4	0.75	0.69	7.5	9
	6.3	0.78	0.80	8.7	-2
4.8	6.8	0.81	0.95	9.9	-16
	8.0	0.83	0.94	10.1	-12
	9.3	0.90	1.01	11.0	-11

Table 5.4: Comparison between the estimates of u_{*t} and u_{*v} computed using two mean profile based methods. The u_{*t} values were computed using Clauser method and the u_{*v} values were computed using viscous sublayer profile method. Here, $\zeta^+ = \zeta u_{*t}/\nu_w$, and Difference (%) $= (u_{*t} - u_{*v})/u_{*v} \times 100$

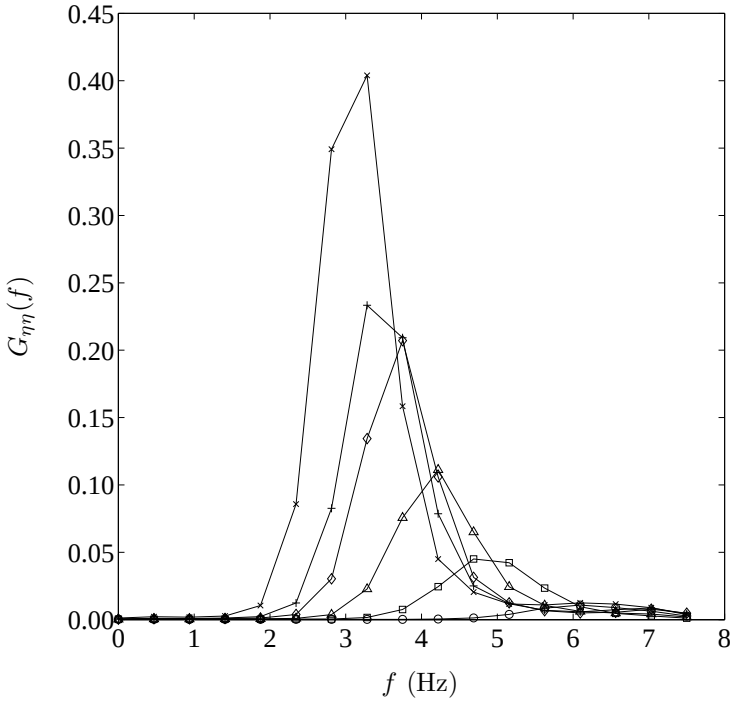

Figure 5.1: Frequency spectra computed from wave profile data at a fetch of 8.8 m and at six different wind speeds, U_z (m s^{-1}): ○,= 4.2; □,= 5.4; △,= 6.1; ◇,= 7.2; +,= 7.9; and ×,= 9.6.

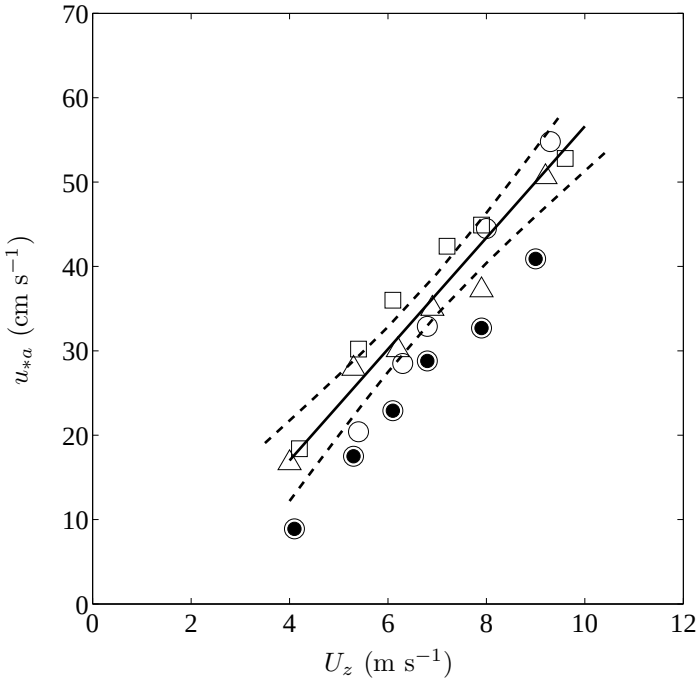

Figure 5.2: A plot of wind friction velocity, u_{*a}, versus wind speed, U_z at three fetches; ○,= 4.8 m (Circles with a solid dot represent u_{*a} measurements taken during normal resolution DPIV measurement); □,= 8.8 m; and △,= 12.4 m. The solid straight line is the best fit regression line fitted to the u_{*a} values at a fetch of 4.8 m during high resolution DPIV measurement, and at fetches of 8.8 and 12.4 m during normal resolution DPIV measurements. The dashed lines show upper and lower bound of the 99% confidence limits.

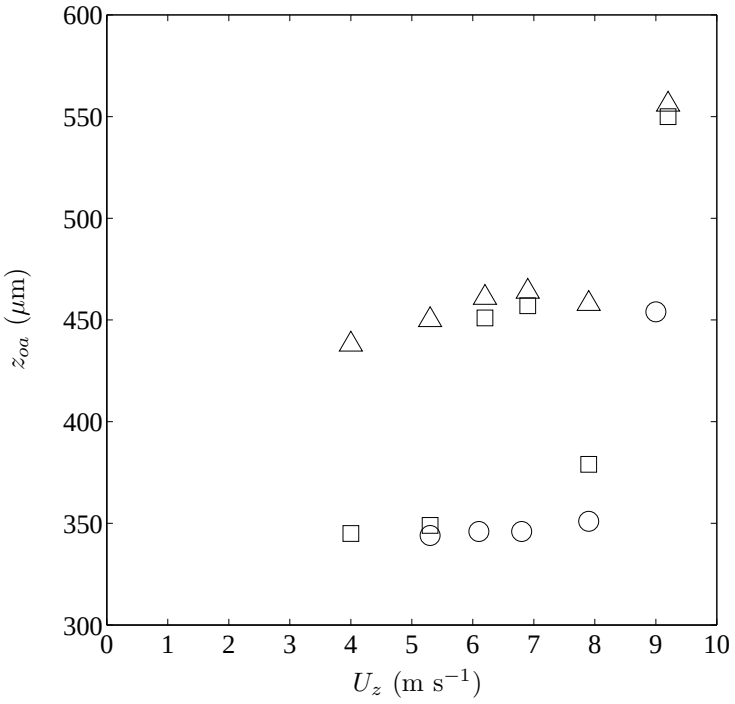

Figure 5.3: A plot of aerodynamic roughness length, z_{oa}, versus wind speed, U_z at three fetches; ○,= 4.8 m; □,= 8.8 m; and △,= 12.4 m.

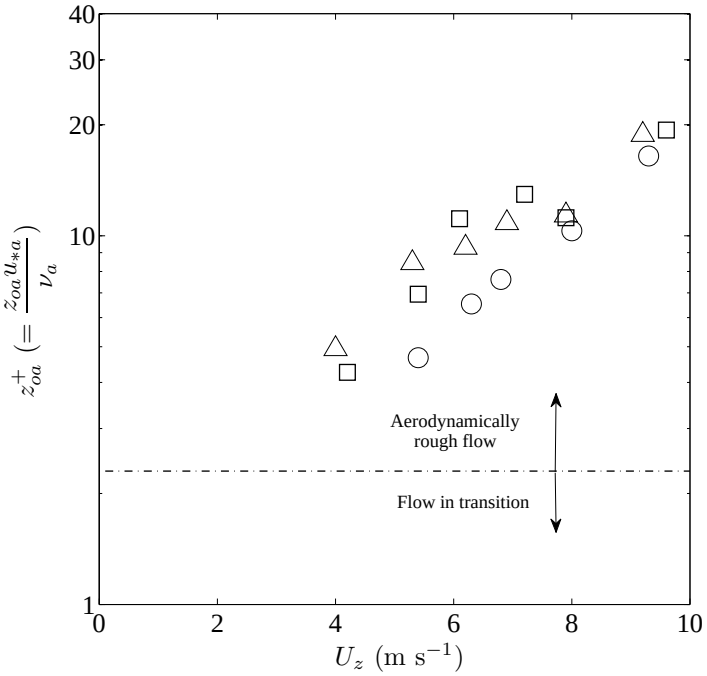

Figure 5.4: A plot of aerodynamic roughness Reynolds number, $z_{oa}u_{*a}/\nu_a$, versus wind speed, U_z at three fetches, ○,= 4.8 m; □,= 8.8 m; and △,= 12.4 m.

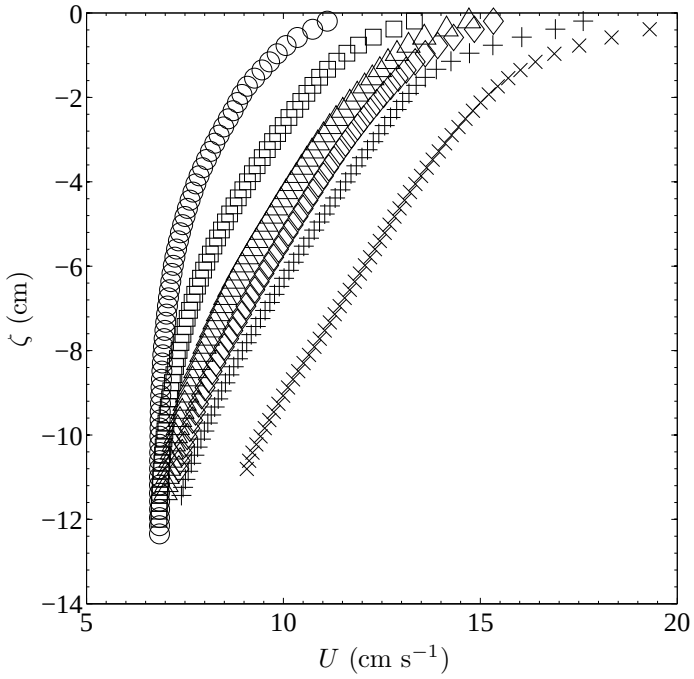

Figure 5.5: A plot of streamwise mean velocity, U versus vertical distance from the interface, ζ in the wave-following coordinate system. For 4.8 m fetch at six different wind speeds, U_z (m s^{-1}): ○,= 4.1; □,= 5.3; △,= 6.1; ◇,= 6.8; +,= 7.9; and ×,= 9.0. The mean velocity at a given depth was obtained by time-averaging 10-minutes of data and spatially averaging over the width of the DPIV field of view.

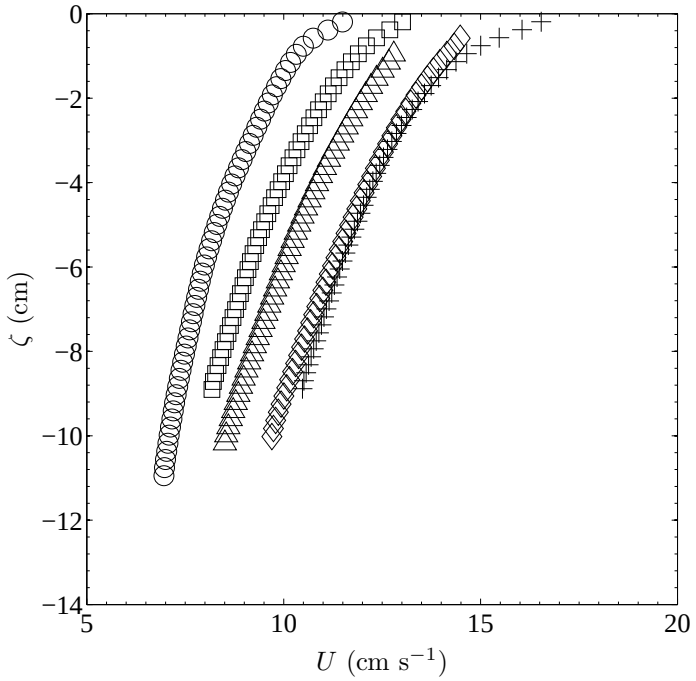

Figure 5.6: A plot of streamwise mean velocity, U versus vertical distance from the interface, ζ in the wave-following coordinate system. For 8.8 m fetch at five different wind speeds, U_z (m s^{-1}): ○,= 4.2; □,= 5.4; △,= 6.1; ◇,= 7.2; and +,= 7.9. The mean velocity at a given depth was obtained by time-averaging 10-minutes of data and spatially averaging over the width of the DPIV field of view.

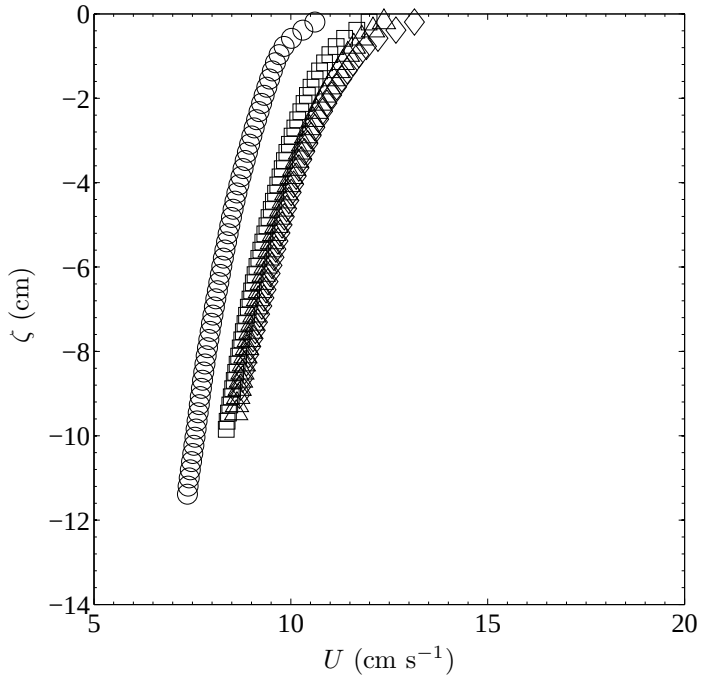

Figure 5.7: A plot of streamwise mean velocity, U versus vertical distance from the interface, ζ in the wave-following coordinate system. For 12.4 m fetch at four different wind speeds, U_z (m s^{-1}): ○,= 4.0; □,= 5.3; △,= 6.2; and ◊,= 6.9. The mean velocity at a given depth was obtained by time-averaging 10-minutes of data and spatially averaging over the width of DPIV field of view.

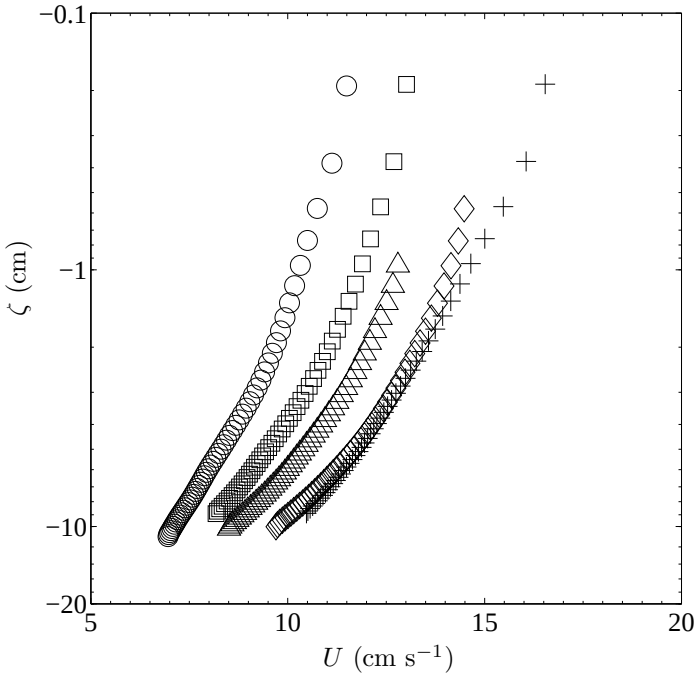

Figure 5.8: A plot of streamwise mean velocity, U versus vertical distance from the interface, ζ in a semi-logarithmic scale. For 8.8 m fetch at five different wind speeds, U_z (m s^{-1}): ○,= 4.2; □,= 5.4; △,= 6.1; ◇,= 7.2; and +,= 7.9. The mean velocity at a given depth was obtained by time-averaging 10-minutes of data and spatially averaging over the width of DPIV field of view.

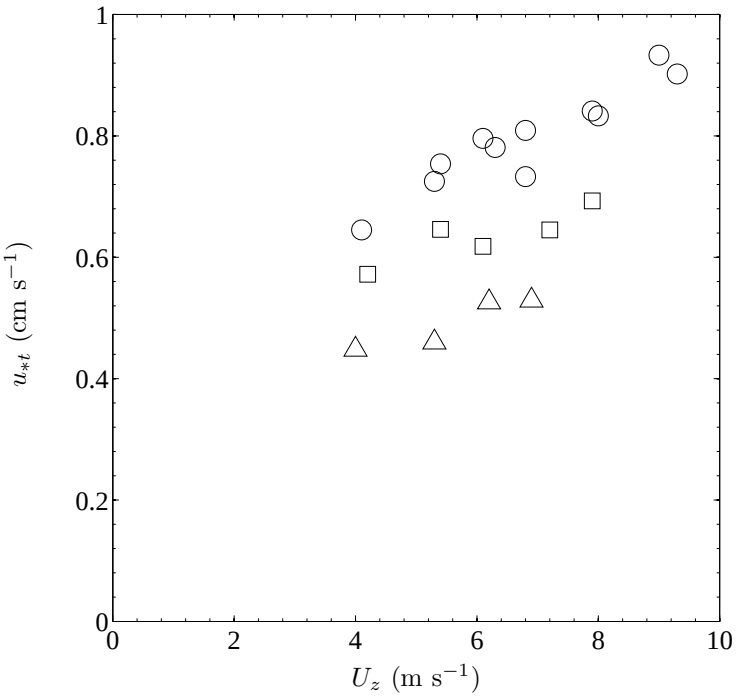

Figure 5.9: A plot of water-side friction velocity, u_{*t}, versus wind speed, U_z at three fetches; ○,= 4.8 m; □,= 8.8 m; and △,= 12.4 m.

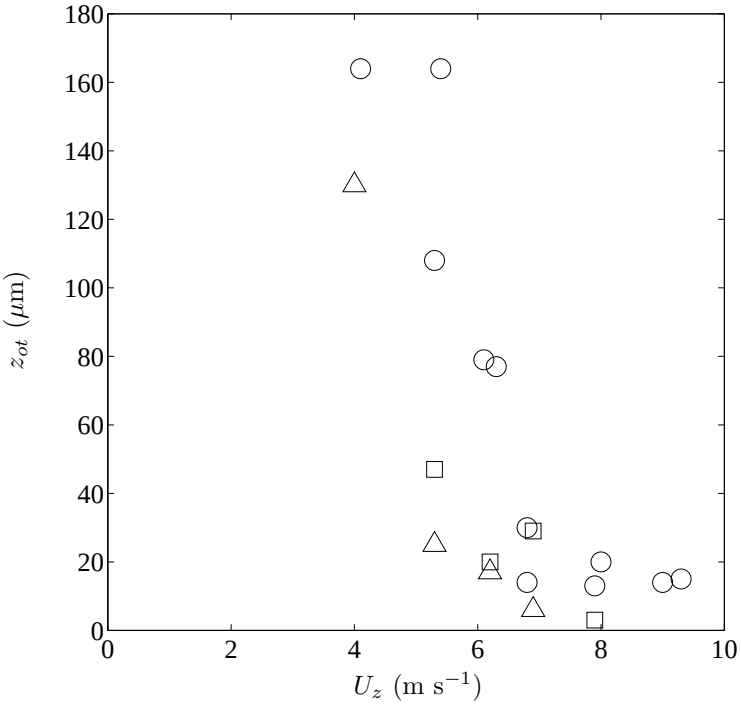

Figure 5.10: A plot of hydrodynamic roughness length, z_{ot}, versus wind speed, U_z at three fetches; ○,= 4.8 m; □,= 8.8 m and △,= 12.4 m. An outlier of magnitude 493 μm at U_z = 4.2 m s^{-1} and F = 8.8 m was eliminated using Peirce's criterion (Ross, 2003).

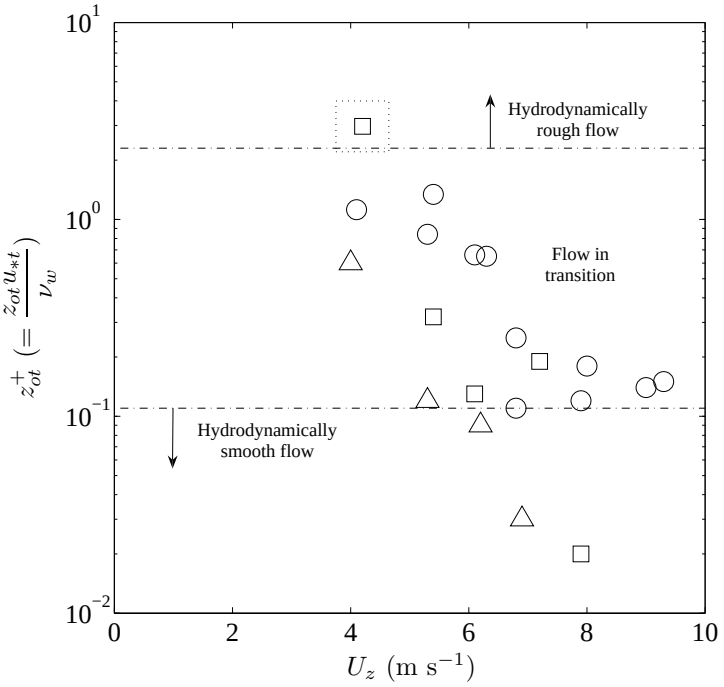

Figure 5.11: A plot of hydrodynamic roughness Reynolds number, $z_{ot}u_{*t}/\nu_w$, versus wind speed, U_z at three fetches; ○,= 4.8 m; □,= 8.8 m; and △,= 12.4 m. An outlier inside the dotted square box was eliminated using Peirce's criterion (Ross, 2003).

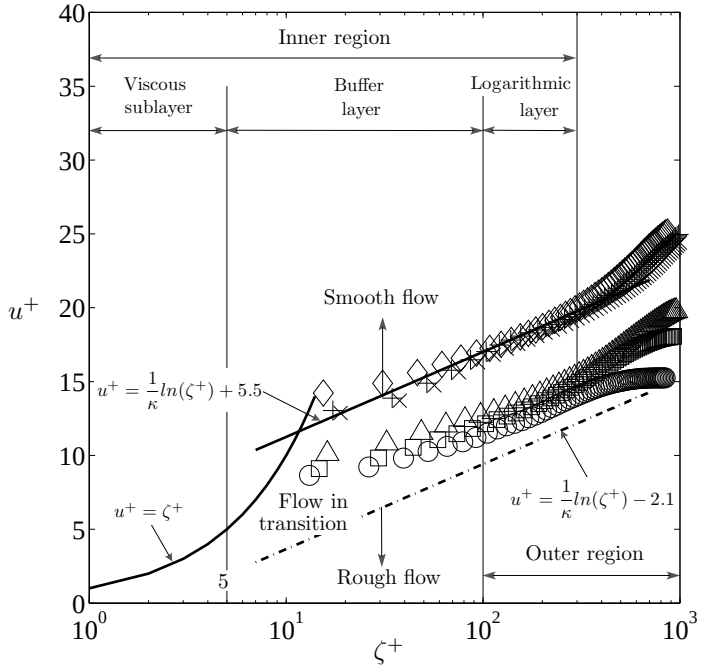

Figure 5.12: The streamwise mean velocity plotted in the form of a velocity defect law in wall coordinates. $u^+ = (U_s - U)/u_{*t}$ and $\zeta^+ = \zeta u_{*t}/\nu_w$. For 4.8 m fetch at six different wind speeds, U_z (m s^{-1}): ○,= 4.1; □,= 5.3; △,= 6.1; ◊,= 6.8; +,= 7.9; and ×,= 9.0.

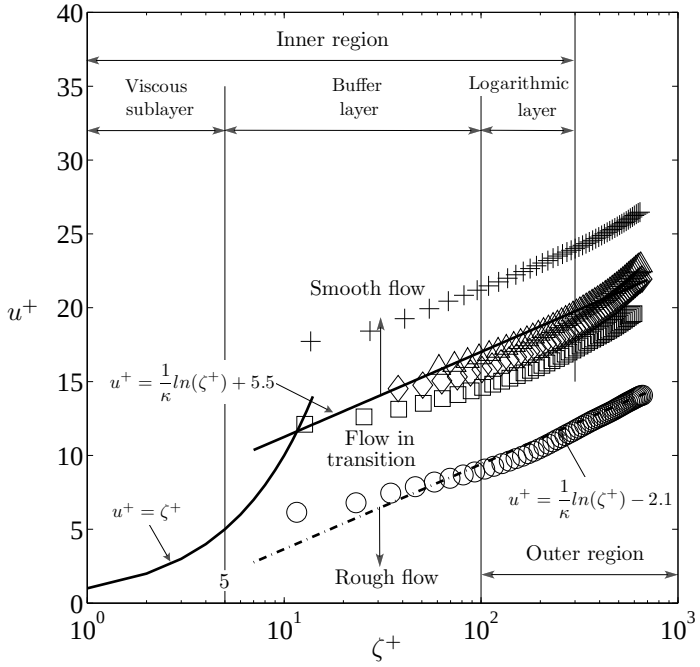

Figure 5.13: The streamwise mean velocity plotted in the form of a velocity defect law in wall coordinates. $u^+ = (U_s - U)/u_{*t}$ and $\zeta^+ = \zeta u_{*t}/\nu_w$. For 8.8 m fetch at five different wind speeds, U_z (m s^{-1}): ○,= 4.2; □,= 5.4; △,= 6.1; ◊,= 7.2; and +,= 7.9.

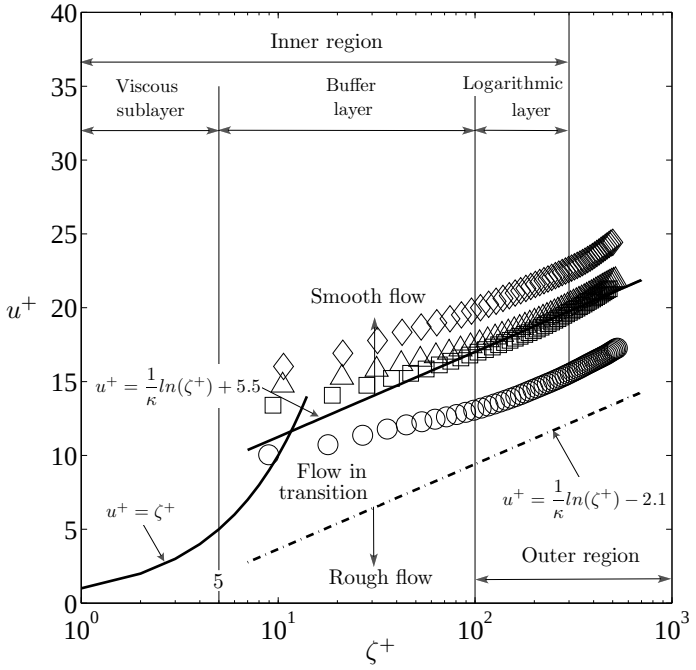

Figure 5.14: The streamwise mean velocity plotted in the form of a velocity defect law in wall coordinates. $u^+ = (U_s - U)/u_{*t}$ and $\zeta^+ = \zeta u_{*t}/\nu_w$. For 12.4 m fetch at four different wind speeds, U_z (m s^{-1}): ○,= 4.0; □,= 5.3; △,= 6.2; and ◊,= 6.9.

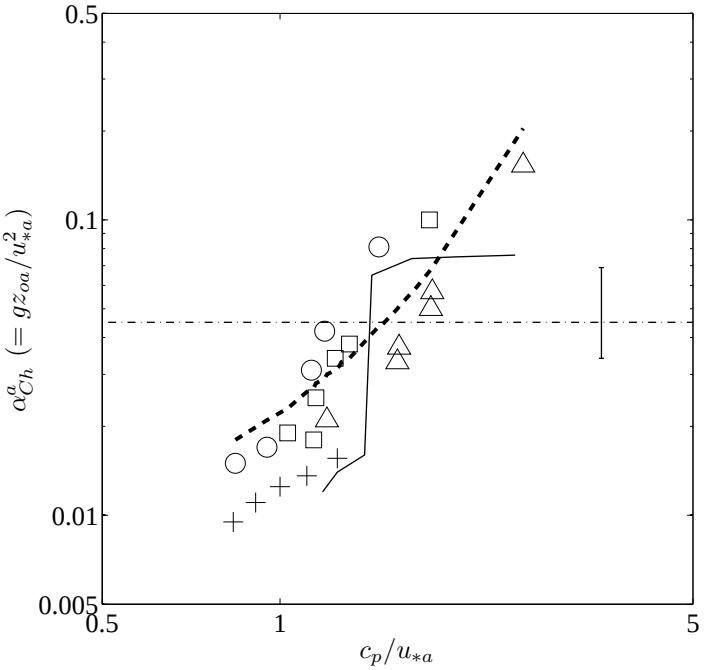

Figure 5.15: A plot of aerodynamic Charnock parameter, α^a_{Ch}, versus wave age, c_p/u_{*a} at three fetches; ○,= 4.8 m; □,= 8.8 m; and △,= 12.4 m. The dash-dotted line represents the average value of $\alpha^a_{Ch} = 0.045$. The vertical bar shows the error band associated with the mean value of α^a_{Ch} (Johnson *et al.*, 1998). The dashed line is the best-fit exponential line (Equation (5.17)) for the observed data ($r = 0.73$). The solid line shows the predicted values of α^a_{Ch} using model study by Makin & Kudryavtsev (2002). The '+' symbol represents the laboratory data obtained from Keller *et al.* (1992).

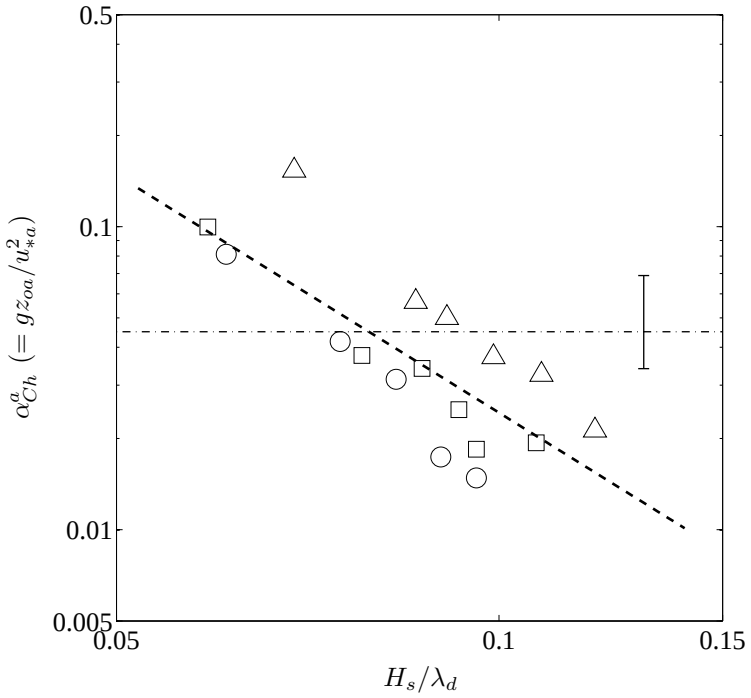

Figure 5.16: A plot of aerodynamic Charnock parameter, α^a_{Ch} versus dominant wave steepness, H_s/λ_d at three fetches; ○,= 4.8 m; □,= 8.8 m; and △,= 12.4 m. The dash-dotted line represents the average value of $\alpha^a_{Ch} = 0.045$. The vertical bar shows the error band associated with the mean value of α^a_{Ch} (Johnson *et al.*, 1998). The dashed line is the best-fit regression line (Equation (5.18)) for the observed data ($r = 0.60$).

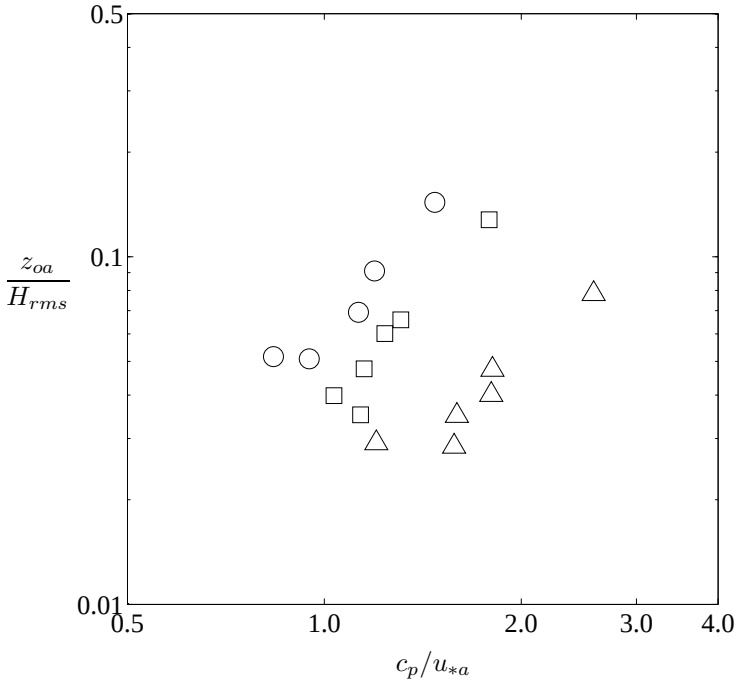

Figure 5.17: A plot of dimensionless aerodynamic roughness length, z_{oa}/H_{rms}, versus wave age, c_p/u_{*a} at three fetches; ○,= 4.8 m; □,= 8.8 m; and △,= 12.4 m.

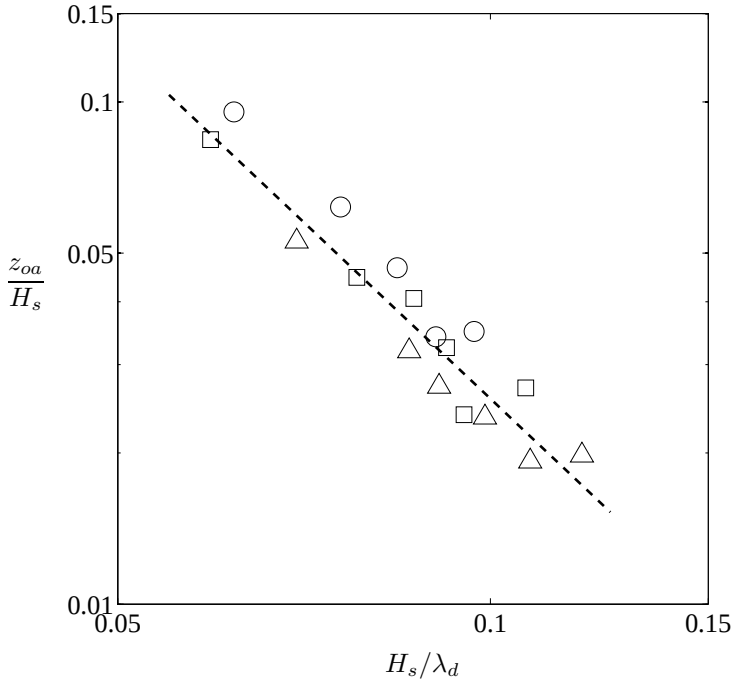

Figure 5.18: A plot of dimensionless aerodynamic roughness length, z_{oa}/H_s versus dominant wave steepness, H_s/λ_d at three fetches; ○,= 4.8 m; □,= 8.8 m; and △,= 12.4 m. The dashed line is the best-fit regression line (Equation (5.19)) for the observed data ($r = 0.90$).

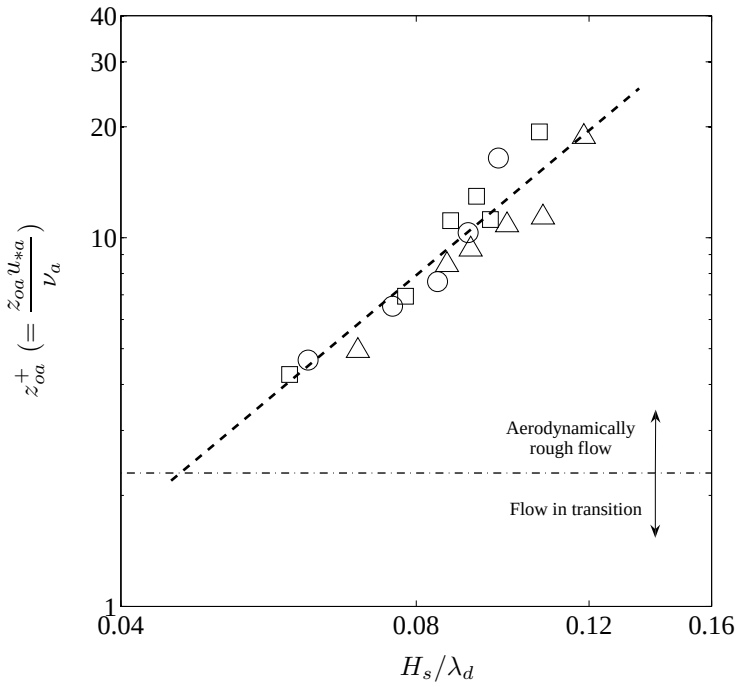

Figure 5.19: A plot of aerodynamic roughness Reynolds number, $z_{oa}u_{*a}/\nu_a$ versus dominant wave steepness, H_s/λ_d at three fetches; ○,= 4.8 m; □,= 8.8 m and △,= 12.4 m. The dashed line is the best-fit regression line (Equation (5.20)) for the observed data ($r = 0.88$).

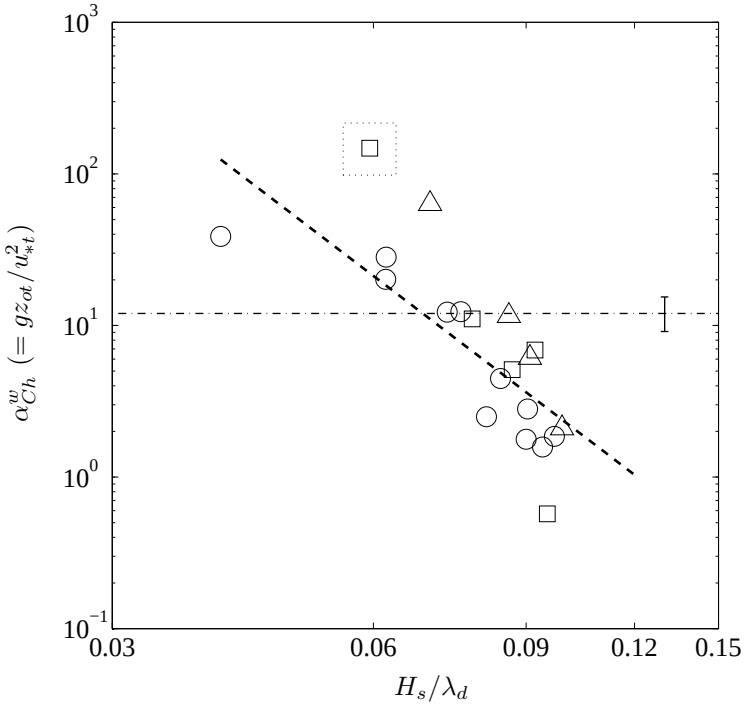

Figure 5.20: A plot of hydrodynamic Charnock parameter, α^w_{Ch} versus dominant wave steepness, H_s/λ_d at three fetches; ○,= 4.8 m; □,= 8.8 m and △,= 12.4 m. An outlier inside the dotted square box was eliminated using Peirce's criterion (Ross, 2003). The dash-dotted line represents the average value of $\alpha^w_{Ch} = 12.0$. The vertical bar shows the error band associated with the mean value of α^w_{Ch} (Johnson *et al.*, 1998). The dashed line was the best-fit regression line (Equation (5.21)) for the observed data ($r = 0.59$).

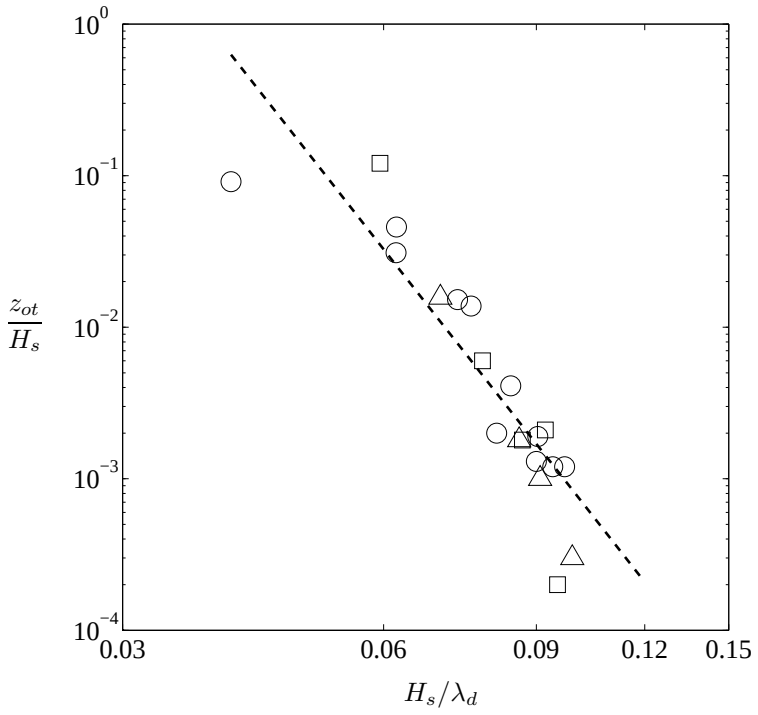

Figure 5.21: A plot of dimensionless hydrodynamic roughness length, z_{ot}/H_s versus dominant wave steepness, H_s/λ_d at three fetches; ○,= 4.8 m; □,= 8.8 m; and △,= 12.4 m. The dashed line is the best-fit regression line (Equation (5.22)) for the observed data ($r = 0.81$).

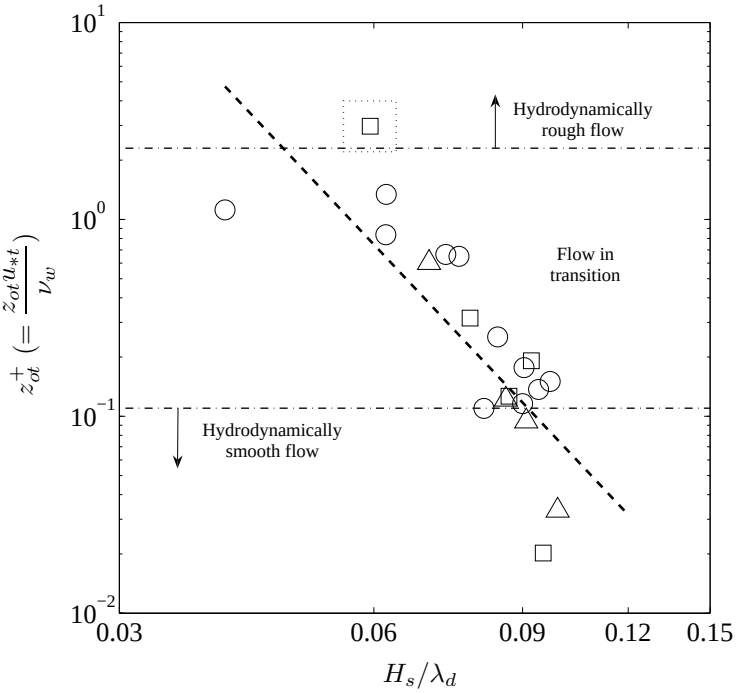

Figure 5.22: A plot of hydrodynamic roughness Reynolds number, $z_{ot}u_{*t}/\nu_w$ versus dominant wave steepness, H_s/λ_d at three fetches; ○,= 4.8 m; □,= 8.8 m and △,= 12.4 m. The dashed line is the best-fit regression line (Equation (5.23)) for the observed data ($r = 0.64$).

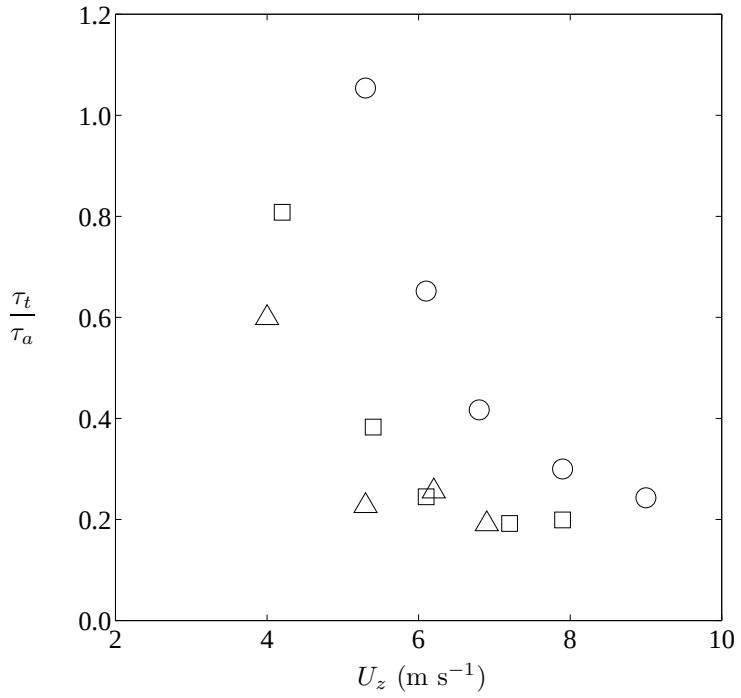

Figure 5.23: A plot of the ratio of the water-side tangential stress, τ_t to the wind stress, τ_a versus wind speed, U_z at three fetches; ○,= 4.8 m; □,= 8.8 m and △,= 12.4 m.

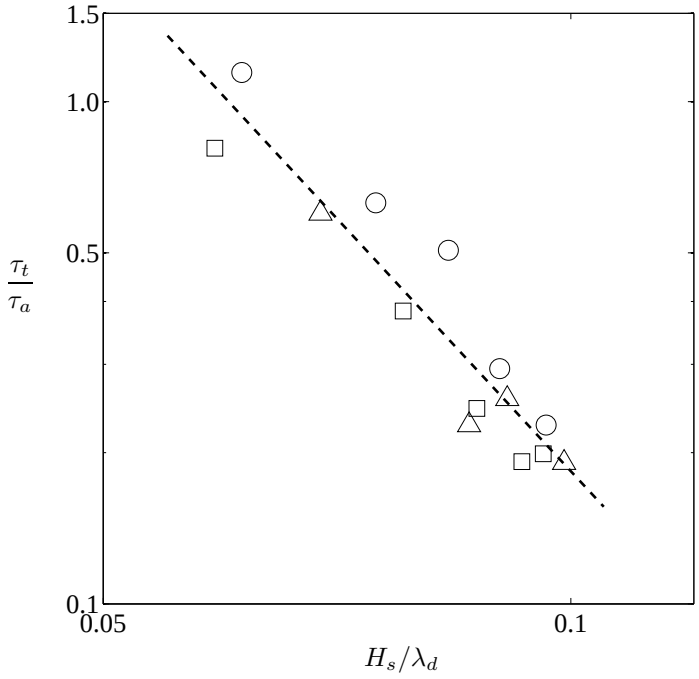

Figure 5.24: A plot of the stress ratio, τ_t/τ_a versus dominant wave steepness, H_s/λ_d at three fetches; ○,= 4.8 m; □,= 8.8 m and △,= 12.4 m. The dashed line is the best-fit regression line (Equation (5.24)) for the observed data ($r = 0.88$).

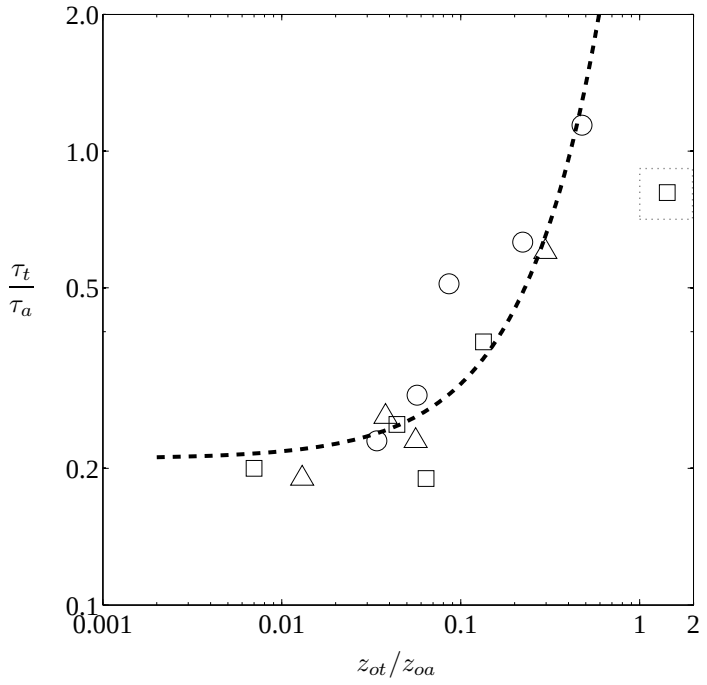

Figure 5.25: A plot of stress ratio, τ_t/τ_a versus roughness length ratio, z_{ot}/z_{oa} at three fetches; ○,= 4.8 m; □,= 8.8 m and △,= 12.4 m. An outlier inside the dotted square box was eliminated using Peirce's criterion (Ross, 2003). The dashed line is the best-fit exponential line (Equation (5.25)) for the observed data ($r = 0.85$).

Chapter 6

Effect of Surfactant on Wind-Driven Coupled Boundary Layers

6.1 Introduction

Surfactants or surface active agents are naturally and synthetically present in reservoirs, lakes and oceans. Sources and diversity of these surfactants, which contaminate water surfaces are numerous (see for example Wilson & Collier, 1972; Zutic *et al.*, 1981; Botte & Mansutti, 2005). In the ocean, the main source of natural surfactants is marine organisms, that is phytoplankton that exude them as their metabolic byproducts (Zutic *et al.*, 1981). Presence of surfactants in natural water bodies are of great importance to scientists, limnologists and engineers because they change the physical and chemical properties of the coupled boundary layers in the air and water (Davies & Rideal, 1963). Surfactants typically reduce the surface tension in proportion to their concentration at the free surface. Thus when the surfactant concentration varies along a free surface, surface tension gradients occur and these produce shear stresses, thus altering the boundary condition (Lang & Gharib, 2000). Surfactants are important to the dynamics of free-surface flows because their presence influences the behavior of the near-surface turbulence (Lang

& Gharib, 2000). Specifically, in reservoirs, lakes and oceans, surfactants influence the characteristics of wind-waves and sub-surface flow, and alter the rates of mass, momentum and energy transfer across the air-water interface (Frew *et al.*, 2004). Accurate predictions of these transport processes are important for global weather and ocean circulation models (Cane *et al.*, 1997).

The main objective of this chapter was to improve our understanding of the water-side boundary layer beneath surfactant-influenced water surfaces under varying surfactant concentrations. Therefore, a series of experiments in a laboratory wind-wave tank were conducted under the varying surfactant-influenced water surfaces. Triton X-100 was used as a synthetic surfactant and surfactant concentration was varied from 0 to 5 ppm at a wind speed of 7.9 ms^{-1} and a fetch of 4.8 m. The specific focus of this chapter was to investigate the influence of surfactant concentrations on mean flow characteristics of the water-side boundary layer (WBL), the partitioning of the wind stress into tangential and wave-induced components and the near-surface turbulence. One of the particular interest was to compare the degree to which the water-side boundary layers formed beneath surfactant-influenced water surfaces resemble the boundary layer formed adjacent to solid wall.

The remainder of this chapter was organized as follows. Following the introduction in §6.1 the literature review was presented in §6.2. A new wave-dependent dissipation scaling model was proposed in §6.3. The results on wind-wave and mean flow characteristics were presented in §6.4. Stress partitioning across the air-water interface were investigated in §6.5. Near-surface turbulence under the influence of varying surfactant concentrations was examined and discussed in §6.6 and conclusions were drawn in §6.7.

6.2 Literature Review

6.2.1 Wind-Wave Characteristics

Franklin (1774; cited by Miles, 1966) was one of the researchers who attempted to explain the surface wave damping phenomenon based on his observations, however, Reynolds (1880; cited by Miles, 1966) and Aitken (1883; cited by Miles, 1966) were the first to provide satisfactory explanations of the observed wave damping. Later, Keulegan (1951) and Van-Dorn (1953) observed that the addition of a surfactant to clean water prevented noticeable wave formation for wind speeds up to 12 m s^{-1}. Levich (1962, first Russian edition was published in 1952) examined the capillary-gravity wave damping due to surfactants based on physicochemical hydrodynamics. Miles (1966) concluded that viscous dissipation of wave energy near the air-water interface was responsible for the majority of the observed small-scale wave damping. Gottifredi & Jameson (1970) investigated the characteristics of wind generated short capillary-gravity waves in a laboratory wind-water tunnel in the presence of a surfactant. They found that the surfactant reduced the growth rate of short wind-waves by a factor of four compared to the growth rate in clean water.

Recently, laboratory (Frew *et al.*, 1995; Milgram, 1998; Bock *et al.*, 1999; Lapham *et al.*, 2001) and field (Frew *et al.*, 2004) studies have been conducted to investigate the effect of surfactants on small-scale wave damping. Frew *et al.* (1995) studied wave damping by measuring the propagation characteristics (i.e. wave amplitude and phase) of mechanically generated wave packets at a frequency of 28 Hz. They observed enhanced wave damping due to presence of the surfactant Triton X-100. Milgram (1998) conducted a study in a laboratory wave tank to determine the effect of turbulence on wave decay in the presence of synthetic (i.e. insoluble oleyl alcohol and soluble Triton X-100)

and natural surfactants. He concluded that the presence of a surfactant or turbulence had an effect on the wave decay rate. Bock *et al.* (1999) performed laboratory experiments in two circular wind-wave tanks in the presence of the surfactant Triton X-100 and found that small-scale wind-waves (wavenumber above 100 rad m^{-1}) were significantly damped, whereas, longer gravity waves (wavenumber below 12 rad m^{-1}) were hardly affected. Lapham *et al.* (2001) used an optical technique to measure the characteristics of gravity-capillary water waves in the presence of the surfactant Triton X-100. They found that the linear wave phase speed and damping agreed well with the existing theory. Frew *et al.* (2004) made field measurements in coastal and offshore waters south of Cape Cod, New England to study the influence of wind stress, small-scale waves, and surfactants on air-water gas transfer at wind speed less than 10 m s^{-1}. They observed that high wave number waves were heavily damped in the presence of natural surfactants. Liu *et al.* (2007) studied the dynamics of longitudinal surface waves in a large water tank under the influence of surfactants. They used three soluble synthetic surfactants in their studies and found that the longitudinal waves were highly damped in the presence of a surfactant.

6.2.2 Stress Partitioning at the Air-Water Interface

The partitioning of the total wind stress, τ_a into wave-induced stress, τ_w and water-side viscous or tangential stress, τ_t in the air-side boundary layer (ABL) is an important physical process that occurs at the air-water interface (Wu, 1987; Melville, 1996). Stewart (1961) studied stress partitioning and showed that a significant portion of τ_a was partitioned into τ_w. Wu (1968, 1975) made measurements of wind profiles, surface and near-surface wind drift currents and waves in a wind-wave tank and found that τ_w was approximately 0.2 to 0.3 of τ_a for wind speeds up to approximately 13 m s^{-1}. Phillips (1977) estimated

that the ratio of τ_w/τ_a was approximately 0.23 in the open ocean. Using field measurements, Snyder *et al.* (1981) found that the ratio of τ_w/τ_a varied from approximately 0.3 at 4 m s^{-1} to 0.8 at 7 m s^{-1}. Hsu *et al.* (1981, 1982) conducted wind-wave tank experiments and estimated that the ratio τ_w/τ_a varied from 0.4 to 0.6. Mitsuyasu (1985) derived an expression of τ_w/τ_a for the regular monochromatic waves such that $\tau_w/\tau_a = 2.2\times10^2(H/\lambda)^2$, where, H is the wave height and λ is the wavelength. With the help of this expression, he concluded that τ_w increased as the waves got steeper and became equal to τ_a at $H/\lambda = 0.07$. For wind-waves, he showed that only 5% of τ_a was supported by the wind-waves. He argued that although a large fraction of τ_a was initially supported by the waves, nevertheless, most of τ_w were lost due to wave breaking and only a small fraction was transported away by the wind-waves. Wu (1987) concluded that the ratio of τ_w/τ_a varied with the non-dimensional fetch, gF/U_{10}^2, where, g is the gravitational constant, F is the fetch and U_{10} is the wind speed measured at 10 m height above the mean sea level.

Banner & Peirson (1998) used particle image velocimetry (PIV) to study the characteristics of the water-side boundary layer (WBL) beneath laboratory wind-waves. They measured the ratio of τ_t/τ_a at fetches of 0.13, 2.45 and 4.35 m for various wind speeds. At the shortest fetch, in the absence of any background wind-waves, they found that τ_t equalled τ_a. However, at the longest fetch of 4.35 m, they found that the ratio of τ_t/τ_a decreased from approximately 0.63 at $\sim$4.7 m s^{-1} to 0.3 at $\sim$8.1 m s^{-1}. In order to obtain an accurate estimate of τ_t, Bourassa (2000) derived an expression for τ_t and reanalyzed two sets of near surface current data (Bye, 1965; Churchill & Pade, 1980, 1981). He found that the ratio of τ_t/τ_a was approximately 1.0 at a wind speed of 5 m s^{-1} and then the ratio decreased rapidly to a smaller fraction of 0.3 and 0.15 as the wind speed increased from 6 m s^{-1} to 10 m s^{-1}. The

laboratory and field measurements described above indicated that the ratio of either τ_w/τ_a or τ_t/τ_a was a function of wind speed, U_z and fetch, F.

6.2.3 Turbulence beneath Wind-Waves

The assessment of the turbulent kinetic energy dissipation rate, ε in the WBL is necessary to describe many physical and biochemical processes occurring in the upper layer of oceans and lakes (Siddiqui & Loewen, 2007). The values of ε could be used to investigate the resemblance of the flows in the WBL to the flows that occur in boundary layers adjacent to solid walls (i.e. wall-layers) (Siddiqui & Loewen, 2007) and to support the fact that near-surface turbulence can enhance as a result of wave breaking or wave-turbulence interactions (Kitaigorodskii *et al.*, 1983; Agrawal *et al.*, 1992; Anis & Moum, 1995; Terray *et al.*, 1996; Soloviev & Lukas, 2003; Gemmrich & Farmer, 2004; Siddiqui & Loewen, 2007).

Csanady (1984) provided observational evidence that the flows in the WBL were analogous to the flows in the wall-layers. Soloviev *et al.* (1988) made small-scale turbulence measurements in the upper 10 m of the Atlantic Ocean for wind speeds (at 10 m height) ranging from 1.9 m s^{-1} to 6.5 m s^{-1}. Their measurements of ε supported the wall-layer analogy proposed by Csanady (1984). A large number of recent studies provided growing evidence that the breaking of small-scale waves and wave-turbulence interaction play a significant role in enhancing the near-surface turbulence (Kitaigorodskii *et al.*, 1983; Agrawal *et al.*, 1992; Anis & Moum, 1995; Terray *et al.*, 1996; Soloviev & Lukas, 2003; Gemmrich & Farmer, 2004; Siddiqui & Loewen, 2007). Natural and anthropogenic surfactants are often present on the surface of oceans and lakes (Frew *et al.*, 2004). Presence of these surfactants influences the behavior of the near-surface turbulence (Lang and Gharib 2000). Specifically, surfactants affect near-surface turbulence length and velocity scales as they

reduce near surface dissipation rates (Frew et al. 1995).

Kitaigorodskii *et al.* (1983) used a miniature drag sphere to measure velocities beneath wind-waves in the Lake Ontario. They observed much higher values of ε in the upper 1 m layer than predicted by the wall-layer theory. They argued that the source of this additional turbulent energy was either wave breaking or wave-turbulence interactions. Agrawal *et al.* (1992) also reported the occurrence of enhanced dissipation beneath the wind-waves that was observed during the field measurements in the Lake Ontario. They concluded that ε was enhanced by at least one or two order of magnitude relative to the predictions of wall-layer theory close to the air-water interface and they attributed this enhanced dissipation to wave breaking. Anis & Moum (1995) measured velocity profiles using microstructure profilers in the upper oceanic boundary layer under various atmospheric and sea conditions. Depending on the forcing conditions, they found that some of their measured ε followed the wall-layer theory, whereas, other measurements exhibited enhanced ε and decayed exponentially with depth, z.

Elkamash (2005) studied the characteristics of the near-surface turbulence generated beneath short wind waves under clean and surfactant-influenced water surfaces. They used 1 ppm of Triton X-100 in a laboratory wind-wave tank and conducted experiments at five different wind speeds ranging from 3.8 to 9.6 m s^{-1} and at a fetch of 5.5 m. They found that the ratio of the energy dissipation rate in surfactant-influenced water to that in clean water decreased from 1.0 to 0.70 as the wind speed increased from 3.8 to 9.6 m s^{-1}. Moreover, they concluded that the rate of energy dissipation was found to be proportional to ζ^{-1}, which agrees with the wall-layer theory. Here, ζ is the vertical distance from surface in a wave-following coordinate system.

Numerous studies showed that short waves get damped in the presence of surfactants. In addition, several studies provided growing evidence that

τ_a is partitioned into τ_w and τ_t in the WBL and near-surface dissipation is enhanced under the influence of strong wind forcing. However, investigation on stress partitioning and the characteristics of the near-surface turbulence under surfactant-influenced water surface are still lacking. Although the small-scale breaking waves and wave-turbulence interaction enhances the near-surface turbulence, presence of surfactants was found to significantly reduce the near-surface dissipation rates. Therefore, it was speculated that under weak wind forcing or under the strong surfactant-influenced water surface the sub-surface WBL may resemble wall-layer. Therefore, the effect of surface contamination on the characteristics of the coupled boundary layers was studied under varying surfactant concentrations. Wave characteristics, stress partitioning and near-surface turbulence were the measured parameters that were studied beneath the surfactant-influenced water surfaces.

6.3 Development of a Wave-Dependent Dissipation Scaling Model

A new wave-dependent dissipation scaling model was proposed based on dimensional analysis. In the proposed scaling model, ε was assumed to be function of depth ζ, wave parameters H_s, c_p, mean flow property u_* and gravitational acceleration g. Here, g was intended to account for the presence of surface gravity waves at the interface. Therefore, ε can be represented by the following function,

$$\varepsilon = f(\zeta,\ H_s,\ c_p,\ u_*,\ g) \tag{6.1}$$

Using dimensional analysis and choosing H_s and u_* as two repeating variables, the following four non-dimensional groups can be formed,

$$\frac{\varepsilon H_s}{u_*^3} = \phi\left(\frac{\zeta}{H_s},\ \frac{c_p}{u_*},\ \frac{gH_s}{u_*^2}\right) \tag{6.2}$$

where, ϕ is a function of its arguments.

To obtain a functional relationship for ε that would include the effect of all the variables mentioned above, c_p/u_* and gH_s/u_*^2 were combined with $\varepsilon H_s/u_*^3$ and following functional form was obtained,

$$\frac{\varepsilon c_p}{g u_*^2} = \varphi\left(\frac{\zeta}{H_s}\right) \tag{6.3}$$

where, φ is a function of its arguments.

6.4 Results

6.4.1 Wind-wave characteristics

Table 6.1 lists the wind-wave characteristics for the six experiments conducted at a fetch of 4.8 m and at a wind speed of 7.9 m s^{-1}. Wind-wave characteristics included the root-mean-square (r.m.s.) wave height (H_{rms}), significant wave height (H_s), mean-square wave slope ($\langle S^2 \rangle$), dominant apparent wave frequency (f_d), dominant wavelength (λ_d) and wave phase speed (c_p). The bulk air temperature (T_{air}) and bulk water temperature (T_{water}) were included as environmental parameters. All wind-wave characteristics were computed using the wave profile data. To compute the wave slopes, the surface wave profiles were smoothed using a low-pass filter with a cut-off wavelength of 3 mm. So, this means that $\langle S^2 \rangle$ were computed for waves with wavenumber, $k < 2094$ rad m^{-1}. For the dominant wavelength computation, the wave profiles were low-pass filtered with a cut-off wavelength of 9 mm. The measured values of λ_d and the deep-water linear dispersion relationship were used to compute f_d and c_p.

It is evident from Table 6.1 that the effect of the surfactant on wave height and wave slope was significant. The waves were severely damped (i.e. H_s was reduced by a factor of 2.2) at the highest concentration compared to clean water. Moreover, the waves became smoother (i.e. a reduction of 3.7

for $\langle S^2 \rangle$) at the highest concentration compared to clean water. Moreover, it is interesting to note that λ_d and c_p decreased slightly while the f_d increased slightly with increasing C. Therefore, the presence of the surfactant in the tank water altered the characteristics of the wind-waves, making them significantly smaller in amplitude.

6.4.2 Wind friction velocity and roughness length

The wind friction velocity (u_{*a}) and aerodynamic roughness length (z_{oa}) are determined as the slope and intercept of Equation (5.12). The values of the wind friction velocity, u_{*a} and aerodynamic roughness length, z_{oa} are listed in Table 6.2. In Figure 6.1, the variation of u_{*a} is plotted as a function of surfactant concentration, C. This figure shows that the magnitude of u_{*a} decreased drastically as C was increased from 0 to 5 ppm. Moreover, the wind stresses, τ_a (defined by $\tau_a = \rho_a u_{*a}^2$, where, ρ_a is the air density) were computed using these u_{*a} values and were listed in Table 6.2. The τ_a values decreased by a factor of 2.7 as C increased from 0 to 5 ppm demonstrating the fact that at a constant wind speed the τ_a can be reduced dramatically in the presence of a surfactant.

The aerodynamic roughness Reynolds number, z_{oa}^+, is defined as $z_{oa}^+ = u_{*a} z_{oa} / \nu_a$, where, ν_a is the kinematic viscosity of air. The flow in the ABL becomes aerodynamically smooth when $z_{oa}^+ < 0.11$ and the flow becomes fully rough if $z_{oa}^+ > 2.3$ (Donelan, 1990). The values of z_{oa}^+ that were listed in Table 6.2 decreased from 10.2 to 6.28 as C increased from 0 to 5 ppm. This shows that the flow did become less rough as C was increased, although the flow stayed on the fully rough regime. Elkamash (2005) found a value for $z_{oa}^+ = 8.82$ at a comparable wind speed of $U_z = 8.16$ m s^{-1} and C=1.0 ppm, which shows good agreement with our result of $z_{oa}^+ = 8.6$ at C=1.0 ppm.

6.4.3 Surface drift velocity

The surface drift velocity, U_s, is defined as $U_s = U_{SL} - U_{Stokes}$, where, U_{SL} is the Lagrangian surface drift velocity, and U_{Stokes} is the Stokes drift velocity (Kenyon, 1969; Wu, 1975; Cheung & Street, 1988). The Stokes drift velocity, U_{Stokes} is given by,

$$U_{Stokes} = \int \frac{2\sigma^3 F(\sigma)}{g} d\sigma \tag{6.4}$$

where, g is the gravitational constant, σ is the intrinsic wave frequency in rad s^{-1}, and $F(\sigma)$ is the frequency spectrum of the surface displacement (Bye, 1967). The intrinsic wave frequencies were computed by solving the following equation for σ,

$$\omega = \sigma + U_{SL}k \tag{6.5}$$

where, $\omega = 2\pi f_d$ in rad s^{-1} and wavenumber, k is substituted by $k = \sigma^2/g$ using the deep-water linear dispersion relation (Kundu & Cohen, 2002). To obtain U_{Stokes}, the integration in Equation (6.4) was performed over the entire frequency spectrum. The values of U_{SL}, U_{Stokes} and U_s are presented in Table 6.2. The data in Table 6.2 show that U_{Stokes} was reduced significantly when C was increased and at 5 ppm it was reduced by about a factor of six compared to clean water. This reduction was a result of the increased damping of the wind-waves. The surface drift velocity increased by a factor of 1.3 as C increased from 0 to 5 ppm.

Keulegan (1951) and Fitzgerald (1964) found that the ratio of the surface drift velocity to the wind speed, U_s/U_z was approximately 0.03 for wind speeds greater than 2 m s^{-1} for clean experiment. Gottifredi & Jameson (1970) reported that with a surfactant concentration of $\sim$1 ppm, this ratio increased substantially to a value of 0.046. They argued that this 50% increase in U_s/U_z compared to the clean experiment could be attributed to the surface tension gradient at the interface. It was found that U_s increased with increasing C

and that U_s/U_z increased from 0.034 to 0.045 as C increased from 0 to 5 ppm at a constant wind speed.

The ratio of the surface drift velocity to the wind friction velocity, U_s/u_{*a} was plotted in Figure 6.2 as a function of surfactant concentration, C. This plot shows that U_s/u_{*a} increased almost linearly with wind speed from approximately 0.6 to approximately 1.4 as C increased from 0 to 5 ppm. Wu (1975) reported that U_s/u_{*a} varied between 0.4 and 0.7 in his laboratory study. However, he did not observe any systematic variation with wind speed and proposed that $U_s/u_{*a} \cong 0.53$. Peirson & Banner (2003) measured U_s at different phases of microscale breaking waves in the laboratory and found that U_s/u_{*a} increased from 0.23 ± 0.02 in the trough to 0.33 ± 0.07 at the crest.

6.4.4 DPIV mean velocity

The instantaneous velocity fields were extracted from the DPIV images in a wave-following Eulerian coordinate system. In this coordinate system, the origin (ξ, ζ) is always at the air-water interface where the positive ξ axis points horizontally and the negative ζ axis points downwards parallel to the gravity vector. The horizontal and vertical spacing between velocity grid points was 1 mm. Therefore, the first grid point was located exactly 1 mm below the air-water interface. The mean velocity components were obtained by time-averaging 5 minutes of instantaneous velocity data at a given grid point in the wave-following coordinate system. Therefore, a total of 4500 samples (i.e. five-minutes of data sampled at a rate of 15 Hz) were used to compute the average velocity at each grid point. Profiles of the streamwise component of the mean velocity, U at all six surfactant concentrations are shown plotted in Figure 6.3. The mean vertical velocity was found to be essentially zero (not shown here) for all experimental conditions indicating that there were no significant systematic errors in the velocity measurements. Figure 6.3 shows

that the profiles of U can be described by dividing the profiles in two distinctive zones. At depths less than approximately 3 mm the magnitude of U increased nearly monotonically with increasing C. At greater depths the magnitude of U tended to decrease with increasing C.

6.4.5 Water-side friction velocity and roughness length

A log-layer was observed in the measured streamwise mean velocity profile and therefore the log-layer was described by the following equation,

$$\frac{U_s - U(\zeta)}{u_{*t}} = \frac{1}{\kappa} ln \left(\frac{\zeta}{z_{ot}} \right) \tag{6.6}$$

where, U_s is the Eulerian surface drift velocity, $U(\zeta)$ is the measured streamwise mean velocity, u_{*t} is the water-side friction velocity, z_{ot} is the hydrodynamic roughness length, and κ is the von Kármán constant. The von Kármán constant was assumed to be 0.4.

In Equation (6.6), $U(\zeta)$ and U_s were measured quantities and the two unknowns were u_{*t} and z_{ot}. A least squares regression procedure similar to the one described by Siddiqui & Loewen (2007) was used to estimate u_{*t} and z_{ot} from Equation (6.6). The average value of the correlation coefficient was greater than 0.99 when the streamwise velocity data were fitted to Equation (6.6) confirming that a log-layer existed in the $U(\zeta)$ profile. However, it should be noted that estimates of u_{*t} do not depend on U_s but estimates of z_{ot} are heavily dependent on U_s. Therefore, accurate measurements of U_s were required in order to obtain accurate z_{ot} estimates. Siddiqui & Loewen (2007) pointed out that a 5% error in U_s could generate an error of up to 200% in z_{ot}. Estimates of u_{*t} and z_{ot} are listed in Table 6.2. The values of u_{*t} varied from 0.787 to 0.930 cm s^{-1} and the values of z_{ot} ranged from 0.3 to 23.2 μm. The values of z_{ot} decreased rapidly from 23.2 μm at $C = 0$ to approximately 1.0 μm for $C \geq 0.5$ ppm. The non-dimensional roughness length, z_{ot}^{+} (computed

as $z_{ot}^{+} = u_{*t} z_{ot}/\nu_w$, where, ν_w is the kinematic viscosity of water) varied from 0.003 to 0.194 and is shown plotted versus concentration in Figure 6.4. For $C \leq 0.1$ ppm, the water-side boundary layer was in the transitional regime as the values of z_{ot}^{+} were between the smooth (i.e. $z_{ot}^{+} < 0.11$) and rough (i.e. $z_{ot}^{+} > 2.3$) limits (Donelan, 1990). For $C \geq 0.5$ ppm, the water-side boundary layer was found to be hydrodynamically smooth since $z_{ot}^{+} < 0.11$. This data shows evidence that the flow regime in the water-side boundary layer tended to become smoother similar to the trend observed for the air-side boundary layer as the surfactant concentration increased.

6.4.6 Velocity defect law

The streamwise mean velocity profiles can be represented in the form of velocity defect law in universal wall coordinates,

$$u^{+} = \frac{U_s - U(\zeta)}{u_{*t}} \text{ and, } \zeta^{+} = \frac{\zeta u_{*t}}{\nu_w} \tag{6.7}$$

where, u^{+} and ζ^{+} are the non-dimensional velocity and depth respectively (Cheung & Street, 1988). Three layers are typically defined for a boundary layer over a smooth solid wall (Kundu & Cohen, 2002). A viscous sublayer adjacent to the smooth wall at $\zeta^{+} < 5$ and in this layer $u^{+} = \zeta^{+}$; a logarithmic layer, in which the velocity varies logarithmically with depth for $30 < \zeta^{+} < 300$; and a buffer layer for $5 < \zeta^{+} < 30$ where the velocity profile is neither linear nor logarithmic. In this study, a logarithmic layer was found to exist in the range $100 < \zeta^{+} < 300$ and a buffer layer existed for $\zeta^{+} < 100$. The thickness of the viscous sublayer can be estimated using the relation, $\delta_\nu = 5\nu_w/u_{*t}$ and δ_ν was found to vary from 0.53 mm to 0.6 mm. Unfortunately, the position of the first grid point in the DPIV measurements was at 1 mm, therefore, it was not possible to directly confirm the existence of the viscous sublayer in the water-side boundary layer.

Figure 6.5 shows the streamwise mean velocity profiles for the five experiments plotted in the form of a velocity defect law in wall coordinates. The dark solid and dashed-dotted straight lines represent the law of the wall for a turbulent boundary layer with a zero pressure gradient over smooth and rough walls, respectively (Schlichting & Gersten, 2000). For $C \leq 0.1$ ppm, the non-dimensional velocity profiles fall between the smooth and rough wall boundary lines confirming that the flow was in the transitional regime. For $C \geq 0.5$ ppm, the non-dimensional velocity profiles were found to be in the hydrodynamically smooth regime. One notable feature of the non-dimensional velocity profiles is that they are not monotonic in there vertical position in Figure 6.5. However, the vertical position of the non-dimensional velocity profiles on the plot is consistent with the z_{ot}^{+} values presented in Table 6.2. Siddiqui & Loewen (2007) argued that the non-monotonic behavior of these velocity profiles was likely due to the uncertainties involved in the estimation of u_{*t} and z_{ot}.

6.5 Stress Partitioning Across the Air-Water Interface

Partitioning of the wind stress, τ_a can be examined using either the wave-induced stress, τ_w or the tangential stress, τ_t, that is, we can use either the ratio τ_t/τ_a or $\tau_w/\tau_a = 1 - \tau_t/\tau_a$. In Figure 6.6, the stress ratio, τ_t/τ_a is plotted versus surfactant concentration, C. It can be seen that τ_t/τ_a increases from approximately 0.3 to one as C increases from 0 to 5 ppm. For $C = 0$, approximately 30% of τ_a was transferred to τ_t while the remaining 70% was transferred to τ_w. Therefore, for $C \leq 1$ ppm, a large fraction of τ_a was transferred to τ_w due to the presence of strong waves. At $C = 3$ ppm, τ_a was nearly equally partitioned between τ_t and τ_w. Whereas, at $C = 5$ ppm, the wind-waves were severely damped and all of τ_a was transferred to τ_t. It is

evident from Figure 6.6 that the presence of a surfactant on the water surface can dramatically increase τ_a transferred through τ_t. Moreover, as the surface became smoother with the addition of surfactant, more and more wind energy was imparted into near surface current which caused the Eulerian surface drift velocity to increase (see Table 6.2).

The variation of τ_t/τ_a with C can also be examined in terms of wind-wave characteristics. Wind-waves can be described using the wave height, wavelength and wave slope. The wave height and wavelength can be combined into the wave steepness, ak, where, a is the r.m.s. wave amplitude and k is the wave number. Figure 6.7 and 6.8 show the variation of the stress ratio, τ_t/τ_a, with the mean square wave slope, $\langle S^2 \rangle$, and square of the wave steepness, $(ak)^2$, respectively. The trend observed in both the figures is very similar. As C decreased both $\langle S^2 \rangle$ and $(ak)^2$ increased and the water surface became rougher. As the water surface roughened, τ_t decreased and τ_w increased.

Mitsuyasu (1985) derived a relationship between τ_w/τ_a and wave steepness, which can be rewritten in the following form,

$$\frac{\tau_t}{\tau_a} = 1 - 22.3\,(ak)^2 \tag{6.8}$$

In Figure 6.8, Equation (6.8) is compared with the observed τ_t/τ_a. It was found that Equation (6.8) underestimates the observed τ_t/τ_a at low slopes $(ak)^2 \simeq 0.01$ and at high slopes $(ak)^2 > 0.03$. Moreover, the r.m.s. difference between the values of τ_t/τ_a predicted by Equation (6.8) and the observed τ_t/τ_a was found to be 0.15.

6.6 Near-Surface Turbulence in the WBL

Doron *et al.* (2001) compared the accuracy of five different methods to estimate the turbulent kinetic energy dissipation rate. The methods were 'line fit in the

inertial range', 'integral of the dissipation spectrum', 'locally axisymmetric turbulence', 'energy flux across equilibrium range', and the 'direct' estimate of the dissipation. They found that the 'direct' method was the most accurate method. The 'direct' method uses the velocity gradients directly obtained from the DPIV measurements and the continuity equation to estimate ε using the following equation,

$$\varepsilon = 3\nu_w \left\{ \overline{\left(\frac{\partial u'}{\partial x}\right)^2} + \overline{\left(\frac{\partial w'}{\partial z}\right)^2} + \overline{\left(\frac{\partial u'}{\partial z}\right)^2} + \overline{\left(\frac{\partial w'}{\partial x}\right)^2} + 2\overline{\left(\frac{\partial u'}{\partial z}\frac{\partial w'}{\partial x}\right)} + \frac{2}{3}\overline{\left(\frac{\partial u'}{\partial x}\frac{\partial w'}{\partial z}\right)} \right\} \tag{6.9}$$

where $u^{'}$ and $w^{'}$ are the streamwise and vertical turbulent velocities, ν_w is the kinematic viscosity of water and the overbar denotes time-averaged values.

In a wind drift layer, the instantaneous velocity field can be decomposed into three components using the following equation,

$$u(x,t) = U + \tilde{u}(x,t) + u^{'}(x,t) \tag{6.10}$$

where U, $\tilde{u}$ and $u^{'}$ are the mean, wave-induced and turbulent components of the velocity, respectively (Benilov *et al.*, 1974). The mean velocity component was obtained by time averaging the instantaneous velocities that were estimated directly from the DPIV measurements in a wave following coordinate system. When the mean velocity component was subtracted from the instantaneous velocities, the resulting velocities were comprised of the wave-turbulent velocity components (u_{wt} and w_{wt}). Several decomposition methods were developed in the past to separate the wave-induced and turbulent velocity components and all of these methods assumed that the waves were two-dimensional and non-dispersive (see Cheung & Street, 1988; Jiang *et al.*, 1990; Thais & Magnaudet, 1995). These assumptions were questionable for the laboratory wind-wave data obtained in this study and therefore, wave-turbulent velocity components were not decomposed applying any of these methods.

Siddiqui & Loewen (2007) used the 'direct' method to estimate ε using the gradients of u_{wt} and w_{wt} in Equation (6.9). They compared the estimated values of ε with values computed using other methods and concluded that u_{wt} and w_{wt} can be used reliably in Equation (6.9) to get accurate estimate of ε. The primary reason for this was that the wave-induced velocity gradients were typically a factor of 2.5 times smaller than the corresponding turbulent velocity gradients beneath the short wind-waves generated by a similar wind speed range of 4.5 to 11.0 m s^{-1} (Siddiqui & Loewen, 2007). Therefore, in this study u_{wt} and w_{wt} were used in Equation (6.9) to obtain reliable estimates of ε.

Figure 6.9 shows vertical profiles of ε for the six experiments. The data presented here encompasses wave ages from $1 \leq c_p/u_{*a} \leq 1.6$ and therefore these waves were defined as very young since $c_p/u_{*a} < 5$ (Phillips, 1977). As C increased, ε decreased monotonically and the reduction was most significant near the surface. At a depth of 2 mm below the surface, ε was reduced by a factor of 2.7 for $C = 5$ ppm compared to the clean experiment.

Soloviev *et al.* (1988) (hereinafter referred to as S88) proposed the following dimensionless relationship for fully developed wind-waves,

$$\frac{\varepsilon\kappa\zeta}{u_{*t}^3} = \chi\left(\frac{g\zeta}{u_{*t}^2}\right) \tag{6.11}$$

where, χ is a universal function of the argument $g\zeta/u_{*t}^2$. In Figure 6.10, the rate of energy dissipation is shown plotted using the wall layer scaling given in Equation (6.11) for all six experiments. A vertical dashed line plotted at $\varepsilon\kappa\zeta/u_{*t}^3 = 1$ in Figure 6.10 is for an unstratified constant stress shear flow near a rigid wall (Lumley & Panofsky, 1964). For $C \leq 1$ ppm, the data presented in Figure 6.10 collapse into a relatively narrow band close to the constant stress layer prediction line. The profiles at the two highest concentrations (i.e. $C \geq 3.0$ ppm) have lower dimensionless dissipation values.

Moreover, it is evident from Figure 6.10 that the dimensionless dissipation rates are smaller for the surfactant-influenced experiments as compared to the clean experiment. This shows that the presence of higher concentrations of surfactant significantly reduces the dissipation rate of turbulent kinetic energy. However, the trend observed in the non-dimensional dissipation profiles is not monotonic with C. This non-monotonic behavior of the energy dissipation rates is the direct result of the non-monotonic variation of u_{*t} with C (see Table 6.2).

The proposed new dissipation scaling model was tested using our observed data under surfactant-influenced water surface. The proposed model for normalized ε is given by the following relationship,

$$\frac{\varepsilon c_p}{g u_{*t}^2} = \phi\left(\frac{\zeta}{H_s}\right) \tag{6.12}$$

Figure 6.11 shows the plot of normalized energy dissipation profiles, $\varepsilon c_p/gu_{*t}^2$ versus the normalized depth, ζ/H_s for all the six experiments. This new scaling for ε which included local gravity, wave and water-side mean flow characteristics seemed to work well for our observed data as they collapsed well along the two distinct regions such that $\varepsilon = \zeta^{-0.3}$ in the upper layer up to $\zeta/H_s = 0.6$ and $\varepsilon = \zeta^{-1}$ for the lower layer. This figure confirms that the total dissipation under short wind waves varies with the wave characteristics (i.e. H_s and c_p), mean flow characteristics (i.e. u_{*t}), gravity (g) and depth (ζ). Moreover, it was also revealed that near the surface up to a depth of $0.6H_s$, the rate of total dissipation is almost constant and at higher depths it resemblance the wall-layer theory.

Figure 6.12 shows a plot of the depth-averaged rate of energy dissipation, $\langle\varepsilon\rangle$, (averaged over the top $0.6H_s$ layer) versus the mean square wave slope, $\langle S^2\rangle$. Similar to Siddiqui & Loewen (2007), this plot shows that $\langle\varepsilon\rangle$ increased with increasing $\langle S^2\rangle$ as C decreased. Moreover, $\langle\varepsilon\rangle$ was reduced by a factor

of approximately three at the highest concentration compared to the clean experiment.

6.7 Conclusions

In this study, the characteristics of coupled boundary layers formed at a wind-driven air-water interface were investigated under clean and surfactant-influenced conditions. The synthetic surfactant Triton X-100 in concentrations from 0 to 5 ppm was added to filtered tap water to model surfactant-influenced water surfaces. All experiments were conducted at a fetch of 4.8 m and at a constant wind speed of 7.9 m s^{-1}. As expected, the presence of the surfactant made the waves significantly smaller in amplitude and flatter. The significant wave height and mean square wave slope were reduced by a factor of 2.2 and 3.7, respectively as the concentration was increased from 0 to 5 ppm. However, the effect of surfactant on wavelength was insignificant. The wind stress was found to decrease by a factor of 2.7 as concentration increased from 0 to 5 ppm. This shows a clear evidence that the wind stress can reduce significantly with the increase in surface contamination although the wind speed remains constant. The air-side boundary layer was found to be aerodynamically rough at all concentrations, however, it became less rougher as the surfactant concentration increased. The water-side boundary layer was found to be in the transition regime at concentration less or equal to 0.1 ppm and became hydrodynamically smooth at concentration greater or equal to 0.5 ppm beneath these short-fetch wind waves. The roughness lengths in both the air-side boundary layer and water-side boundary layer were found to decrease as the surfactant concentration was increased. The surface drift velocity was increased by a factor of 1.3 as the concentration increased from 0 to 5 ppm.

The stress partitioning was examined by computing the ratio of the

water-side tangential stress to the wind stress. This stress partitioning ratio increased from approximately 0.3 to 1 as the surfactant concentration increased from 0 to 5 ppm. The stress partitioning ratio was observed to increase with decreasing wave slope or wave steepness as the surfactant concentration was increased. The rate of dissipation of turbulent kinetic energy decreased monotonically and the reduction was most significant near the surface. At a concentration of 5 ppm the surfactant reduced ε by a factor of 2.7 compared to the clean experiment. A new wave-dependent dissipation scaling model is proposed and verified using the observed data for dissipation rate, where, dissipation rate is normalized using the gravitational acceleration, the wave phase speed, water-side friction velocity, the significant wave height and the depth. We found that there are two distinct layers; an upper layer where dissipation rate decays as $\zeta^{-0.3}$ and a lower layer where dissipation rate decays as ζ^{-1}. Therefore, the rate of dissipation of turbulent kinetic energy beneath the surface up to a depth of approximately 0.6 times the significant wave height was found to be significantly smaller than would occur in a comparable wall-layer. However, at higher depths, dissipation rate resemblance wall-layer theory. The depth-averaged energy dissipation rate decreased as the mean square wave slope decreased and as the surfactant concentration increased. Moreover, the depth-averaged dissipation rate was reduced by approximately a factor of three at the highest concentration compared to the clean experiment.

C (ppm)	0.0	0.1	0.5	1.0	3.0	5.0
T_{air}(°C)	22.6	22.3	21.6	20.9	20.1	19.5
T_{water}(°C)	22.5	23.9	23.7	23.4	21.5	21.4
H_{rms} (cm)	0.71	0.66	0.60	0.54	0.41	0.32
H_s (cm)	1.05	0.98	0.89	0.80	0.61	0.4
$\langle S^2 \rangle$	0.055	0.050	0.042	0.034	0.021	0.015
f_d (Hz)	3.71	3.72	3.73	3.74	3.77	3.77
λ_d (cm)	11.3	11.30	11.20	11.17	10.98	10.98
c_p (cm s^{-1})	42.07	42.00	41.81	41.75	41.40	41.40

Table 6.1: Summary of environmental parameters and wave characteristics for different experimental conditions. C, Triton X-100 concentrations; T_{air}, the bulk air temperature; T_{water}, the bulk water temperature; H_{rms}, the r.m.s. wave height; H_s, the significant wave height; $\langle S^2 \rangle$, the mean-square wave slope; f_d, the dominant apparent wave frequency; λ_d, the dominant wavelength; and (c_p), the wave phase speed.

C (ppm)	0.0	0.1	0.5	1.0	3.0	5.0
U_{SL} (cm s^{-1})	29.1	30.65	33.08	32.30	35.54	36.14
U_{Stokes} (cm s^{-1})	2.03	1.58	1.24	1.01	0.55	0.32
U_s (cm s^{-1})	27.05	29.07	31.84	31.29	34.99	35.82
u_{*a} (cm s^{-1})	43.48	44.04	40.18	37.11	31.80	26.34
z_{oa} (μm)	358	351	354	350	347	357
z_{oa}^+	10.20	10.16	9.39	8.60	7.35	6.28
τ_a (Pa)	0.225	0.230	0.192	0.164	0.121	0.083
u_{*t} (cm s^{-1})	0.798	0.866	0.791	0.787	0.812	0.930
z_{ot} (μm)	23.2	14.4	1.4	1.9	0.3	0.8
z_{ot}^+	0.194	0.134	0.012	0.016	0.003	0.008
τ_t (Pa)	0.063	0.075	0.062	0.062	0.066	0.086

Table 6.2: Measurement of surface velocity; wind and water-side friction velocity, roughness length, roughness Reynolds number and interfacial stresses at different experimental conditions. C, Triton X-100 concentrations; U_{SL}, the Lagrangian surface drift velocity; U_{Stokes}, the Stokes drift velocity; U_s, the surface drift velocity; u_{*a}, wind friction velocity; z_{oa}, aerodynamic roughness length; z_{oa}^+, aerodynamic roughness Reynolds number; τ_a, wind stress; u_{*t}, water-side friction velocity; z_{ot}, hydrodynamic roughness length; z_{ot}^+, hydrodynamic roughness Reynolds number; τ_t, water-side tangential stress.

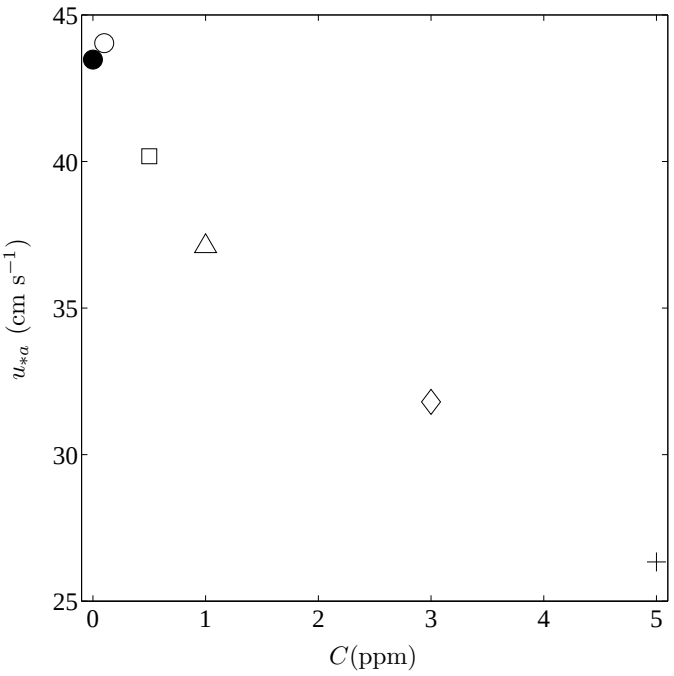

Figure 6.1: Variation of wind friction velocity, u_{*a}, as a function of surfactant concentration, C. For clean experiment, C: ●,= 0 ppm. For surfactant-influenced experiments, C (ppm): ○,= 0.1; □,= 0.5; △,= 1.0; ◊,= 3.0; +,= 5.0. Experiments were conducted at a wind speed of 7.9 m s^{-1} and a fetch of 4.8 m.

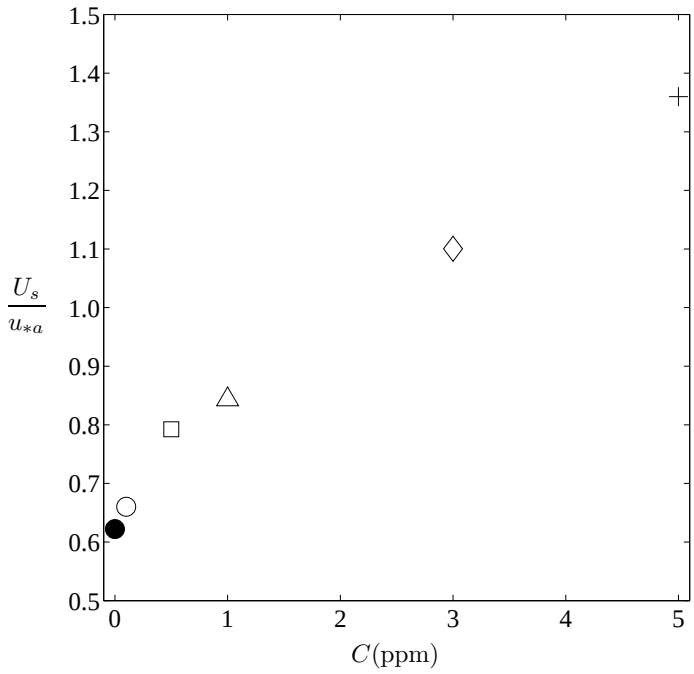

Figure 6.2: Ratio of surface velocity, U_s, to wind friction velocity, u_{*a}, versus surfactant concentration, C, for all six experiments. For clean experiment, C: ●,= 0 ppm. For surfactant-influenced experiments, C (ppm): ○,= 0.1; □,= 0.5; △,= 1.0; ◊,= 3.0; +,= 5.0. Experiments were conducted at a wind speed of 7.9 m s^{-1} and a fetch of 4.8 m.

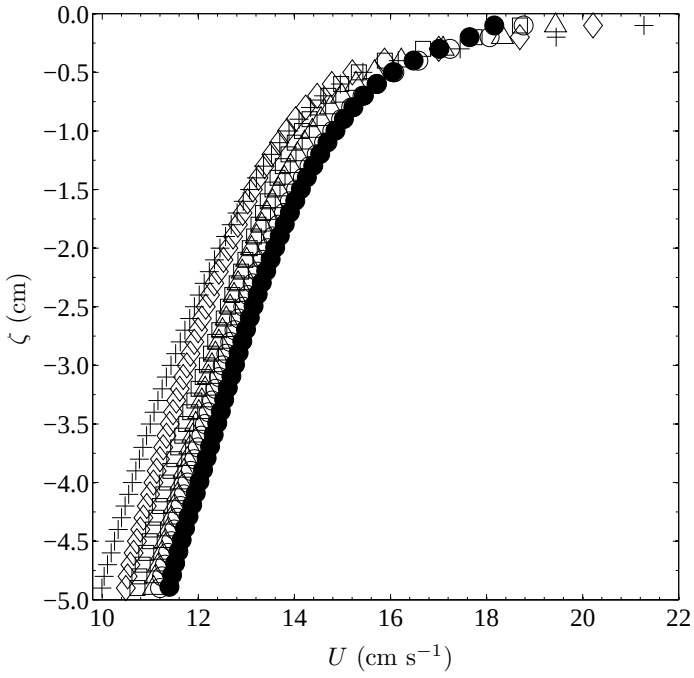

Figure 6.3: A plot of streamwise mean velocity, U versus vertical distance from the interface, ζ in the wave-following coordinate system. For clean experiment, C: ●,= 0 ppm. For surfactant-influenced experiments, C (ppm): ○,= 0.1; □,= 0.5; △,= 1.0; ◇,= 3.0; +,= 5.0. Experiments were conducted at a wind speed of 7.9 m s^{-1} and a fetch of 4.8 m. The mean velocity at a given depth was obtained by time-averaging 5-minutes of data and spatially averaging over the width of the DPIV field of view.

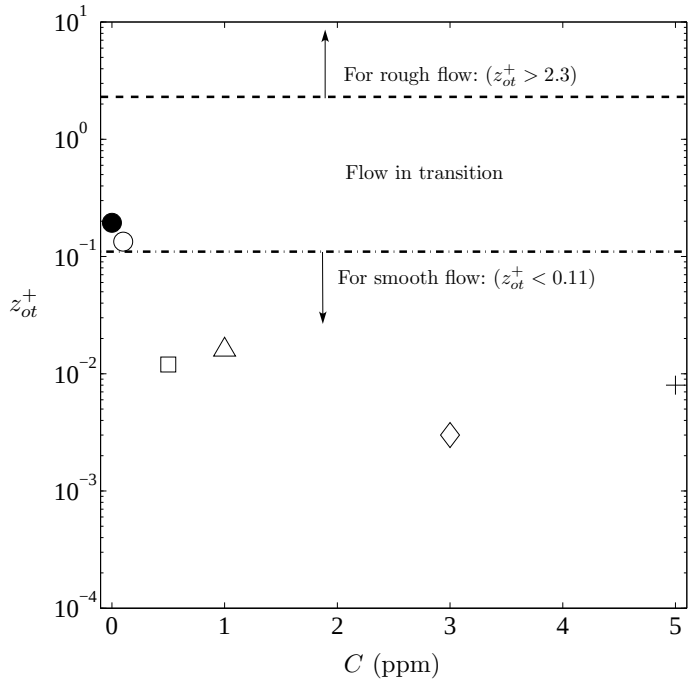

Figure 6.4: A plot of hydrodynamic roughness Reynolds number, z_{ot}^+ versus the concentration, C. For clean experiment, C: ●,= 0 ppm. For surfactant-influenced experiments, C (ppm): ○,= 0.1; □,= 0.5; △,= 1.0; ◊,= 3.0; +,= 5.0. Experiments were conducted at a wind speed of 7.9 m s^{-1} and a fetch of 4.8 m.

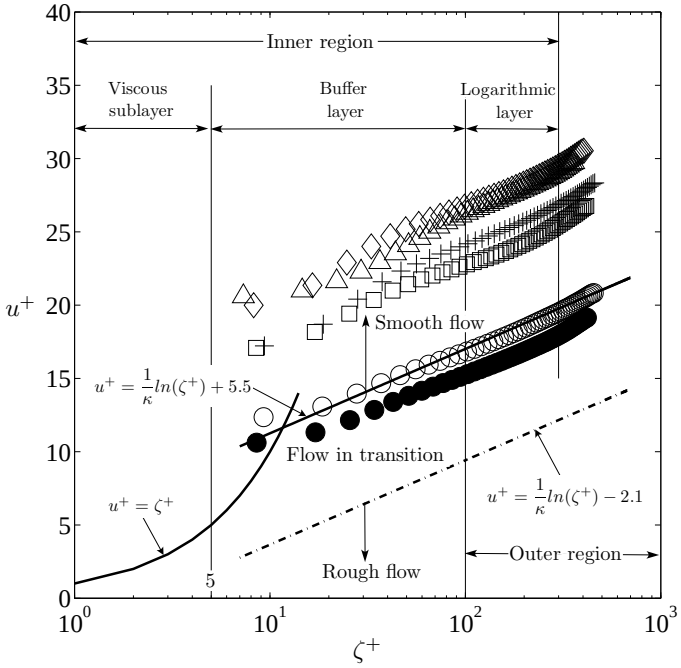

Figure 6.5: The streamwise mean velocity plotted in the form of a velocity defect law in wall coordinates. $u^+ = (U_s - U)/u_{*t}$ and $\zeta^+ = \zeta u_{*t}/\nu_w$. For clean experiment, C: ●,= 0 ppm. For surfactant-influenced experiments, C (ppm): ○,= 0.1; □,= 0.5; △,= 1.0; ◊,= 3.0; +,= 5.0. Experiments were conducted at a wind speed of 7.9 m s^{-1} and a fetch of 4.8 m.

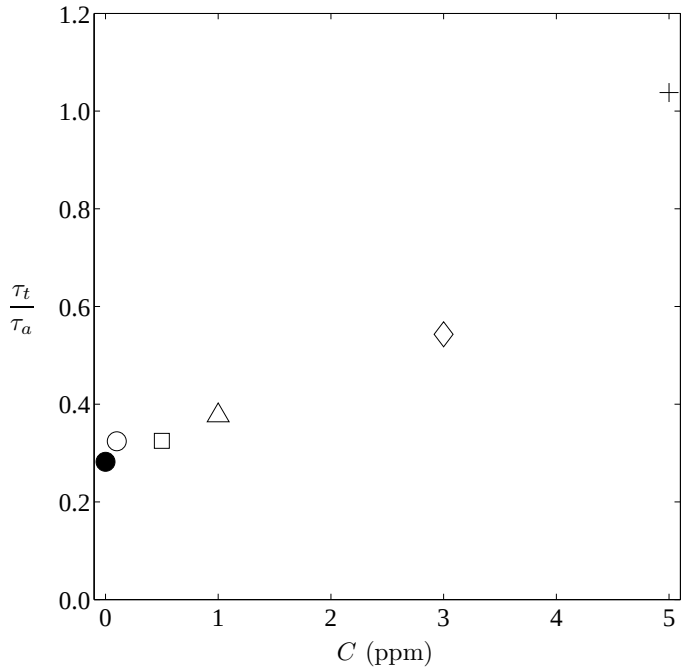

Figure 6.6: Stress ratio, τ_t/τ_a, versus surfactant concentration, C, for clean and surfactant-influenced experiments. For clean experiment, C: ●,= 0 ppm. For surfactant-influenced experiments, C (ppm): ○,= 0.1; □,= 0.5; △,= 1.0; ♢,= 3.0; +,= 5.0. Experiments were conducted at a constant wind speed of 7.9 m s^{-1} and a fetch of 4.8 m.

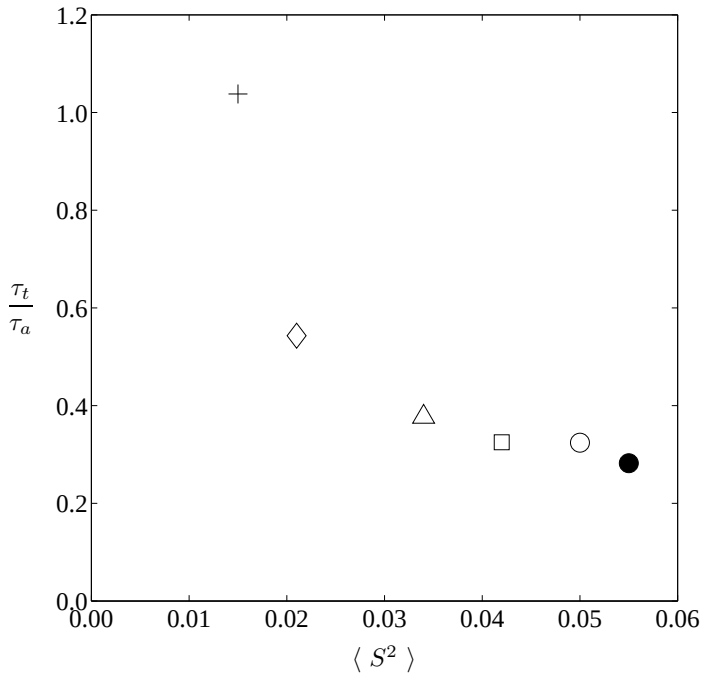

Figure 6.7: Stress ratio, τ_t/τ_a, versus mean square wave slope, $\langle S^2 \rangle$, for clean and surfactant-influenced experiments. For clean experiment, C: ●,= 0 ppm. For surfactant-influenced experiments, C (ppm): ○,= 0.1; □,= 0.5; △,= 1.0; ◇,= 3.0; +,= 5.0. Experiments were conducted at a wind speed of 7.9 m s^{-1} and a fetch of 4.8 m.

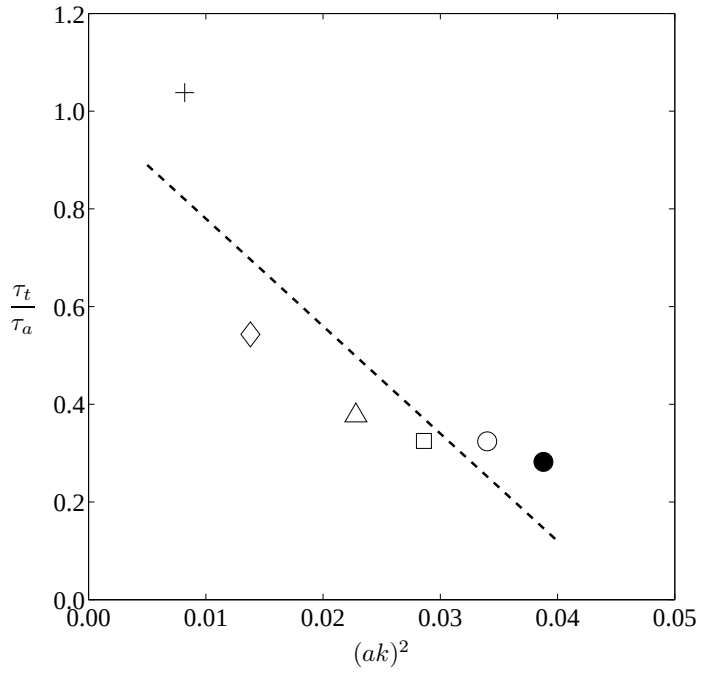

Figure 6.8: Stress ratio, τ_t/τ_a, versus wave steepness, ak, for clean and surfactant-influenced experiments, where a is the r.m.s. wave amplitude (cm) and k is the dominant wavenumber (rad cm^{-1}). For clean experiment, C: ●,= 0 ppm. For surfactant-influenced experiments, C (ppm): ○,= 0.1; □,= 0.5; △,= 1.0; ◊,= 3.0; +,= 5.0. Experiments were conducted at a constant wind speed of 7.9 m s^{-1} and a fetch of 4.8 m. The dashed line represents Mitsuyasu's (1985) equation.

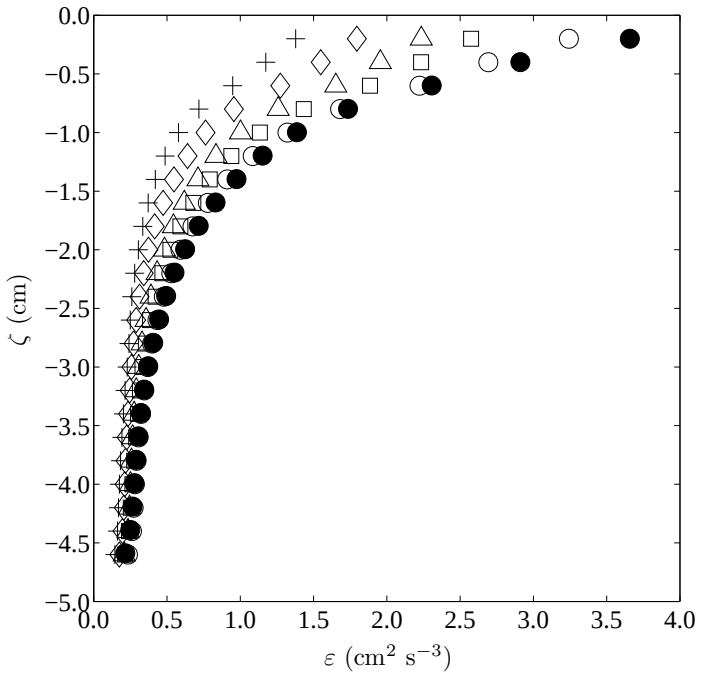

Figure 6.9: Energy dissipation profiles, ε, along the depth from the interface, ζ, for clean and surfactant-influenced experiments. For clean experiment, C: ●,= 0 ppm. For surfactant-influenced experiments, C (ppm): ○,= 0.1; □,= 0.5; △,= 1.0; ◊,= 3.0; +,= 5.0. Experiments were conducted at a constant wind speed of 7.9 m s^{-1} and a fetch of 4.8 m.

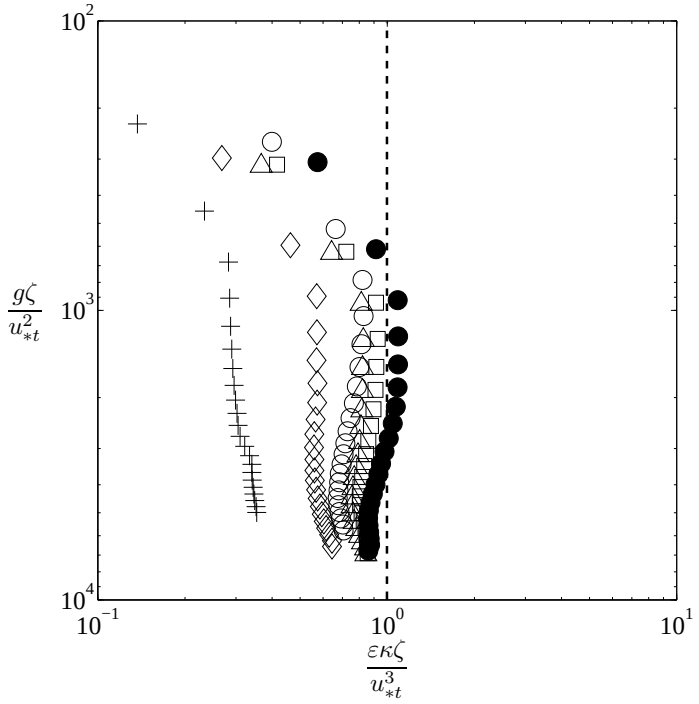

Figure 6.10: Dimensionless energy dissipation profiles, $\varepsilon\kappa\zeta/u_{*t}^3$, as a function of dimensionless depth, $g\zeta/u_{*t}^2$. The constant stress layer is represented by the vertical dashed line at $\varepsilon\kappa\zeta/u_{*t}^3 = 1$. For clean experiment, C: ●,= 0 ppm. For surfactant-influenced experiments, C (ppm): ○,= 0.1; □,= 0.5; △,= 1.0; ◊,= 3.0; +,= 5.0. Experiments were conducted at a wind speed of 7.9 m s^{-1} and a fetch of 4.8 m.

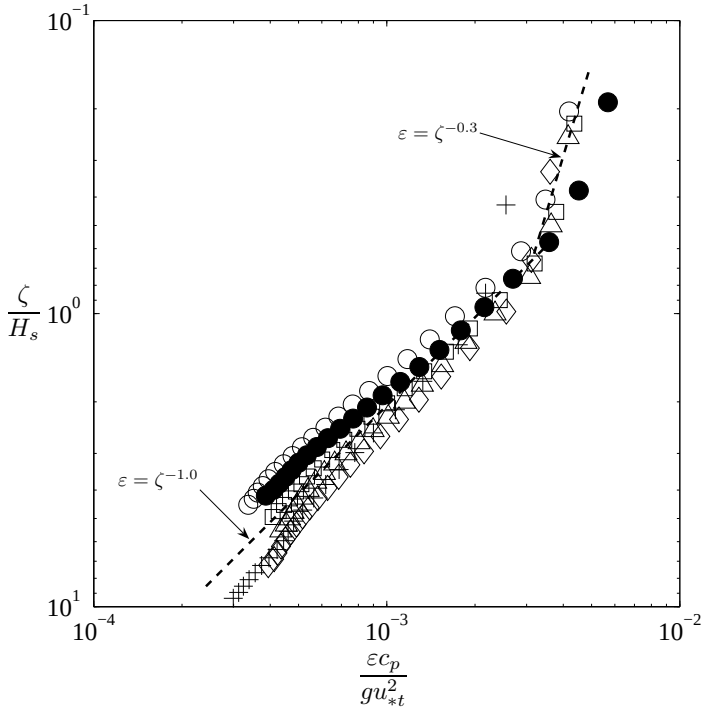

Figure 6.11: A plot of normalized energy dissipation profiles, $\varepsilon c_p / g u_{*t}^2$ versus normalized depth, ζ / H_s for all six experiments. For clean experiment, C: ●,= 0 ppm. For surfactant-influenced experiments, C (ppm): ○,= 0.1; □,= 0.5; △,= 1.0; ◇,= 3.0; +,= 5.0. Experiments were conducted at a wind speed of 7.9 m s^{-1} and a fetch of 4.8 m.

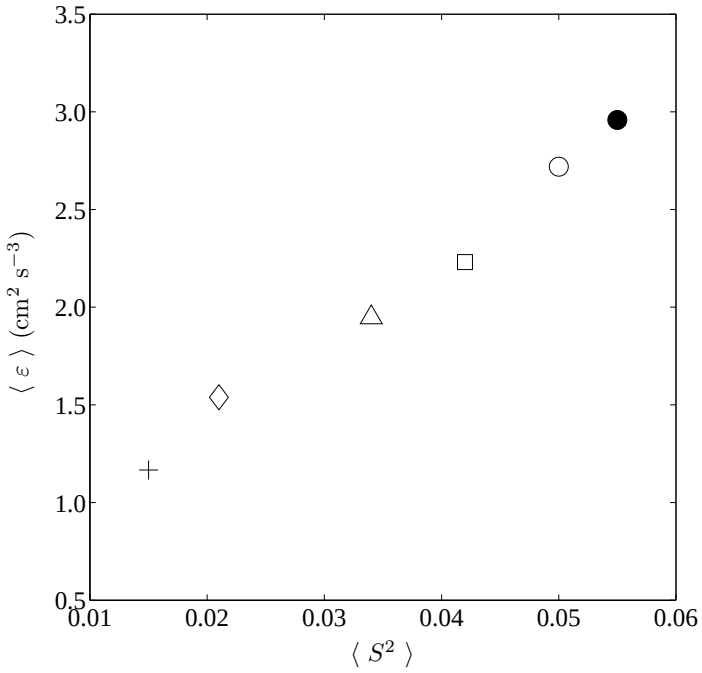

Figure 6.12: Rate of energy dissipation, ε, (averaged over top $0.6H_s$ layer) versus mean square wave slope, $\langle S^2 \rangle$ for all six experiments. For clean experiment, C: ●,= 0 ppm. For surfactant-influenced experiments, C (ppm): ○,= 0.1; □,= 0.5; △,= 1.0; ◇,= 3.0; +,= 5.0. Experiments were conducted at a wind speed of 7.9 m s^{-1} and a fetch of 4.8 m.

Chapter 7

Turbulence Beneath Microscale Breaking Waves

7.1 Introduction

Microscale breaking waves are short wind waves that break without entraining air (Banner & Phillips, 1974). These waves generate turbulence beneath the water surface and enhance mass, momentum and energy transfer across the air-water interface (Siddiqui *et al.*, 2004; Zappa *et al.*, 2004; Siddiqui & Loewen, 2007). Moreover, mixing in the water-side boundary layer, the dispersion of buoyant pollutants and modeling of mixed layer processes are all influenced by the turbulence generated due to wave breaking (Melville, 1996; Terray *et al.*, 1996; Drennan *et al.*, 1996; Peirson & Banner, 2003; Siddiqui & Loewen, 2007). Microscale wave breaking is one of the key mechanisms that determine the structure of near-surface turbulence beneath the water surface at low to moderate wind speeds (Siddiqui & Loewen, 2007). The strength of turbulence generated due to wave breaking can be measured by studying the rate of dissipation of turbulent kinetic energy (TKE), ε. The structure of near-surface turbulence can be described by the vertical extent and decay of ε in the water column (Terray *et al.*, 1996; Drennan *et al.*, 1996; Siddiqui & Loewen, 2007).

The objective of this study was to investigate the structure of near-surface

turbulence beneath microscale breaking waves using laboratory wind wave measurements. According to Siddiqui & Loewen (2007), the dominant energy input to the turbulence beneath microscale breaking waves comes from the wave-induced motions and shear currents. Therefore, the specific focus of this study was oriented around the determination of the influence of the wave-induced motions and shear currents to describe the vertical extent and decay of ε beneath microscale breaking waves. A wave-dependent scaling method proposed by Terray *et al.* (1996) was modified to describe the structure of near-surface turbulence beneath microscale breaking waves.

This study is organized as follows. Following the introduction in §7.1 and literature review in §7.2, the characteristics of the near-surface turbulence beneath short wind waves are presented in §7.3. A scheme describing the detection of microscale breaking waves is presented in §7.4, following the characteristics of the microscale breaking waves in §7.5. The influence of microscale wave breaking on the structure of the near-surface turbulence is discussed next in §7.6. Finally, conclusions are summarized in §7.7.

7.2 Literature Review

7.2.1 Microscale Breaking Waves

Micro-breaking occurs at low to moderate wind speeds (i.e. 4 to 12 m s^{-1}). Microscale breaking waves are typically $O(0.1 - 1)$ m in length, a few centimeters in amplitude and have a bore-like crest directly preceded by parasitic capillary waves riding along the forward face (Jessup *et al.*, 1997). A number of methods are available to detect the occurrence of microscale breaking waves. These include methods based on infrared (IR) imagery (Jessup *et al.*, 1997; Jessup & Phadnis, 2005), wave slope (Banner, 1990), and DPIV vorticity (Siddiqui *et al.*, 2001; Loewen & Siddiqui, 2006).

Jessup *et al.* (1997) studied microscale breaking waves using IR imagery. They observed that the warm turbulent wakes generated by microscale breaking waves disrupted the cool skin layer and were visible in the IR images. An excellent discussion on the infrared signature of microscale breaking waves that described the cool skin layer and warm turbulent wake was presented in Jessup *et al.* (1997). Jessup *et al.* (1997) used these infrared signatures to detect microscale breaking waves by applying a simple temperature based thresholding technique. The temperature threshold was set based on the mean surface temperature and the bulk-skin temperature difference for the entire run. At a wind speed of 5.0 m s^{-1} and a fetch of 5 m, they estimated that the breaking percentage was 33%. They demonstrated that infrared imagery provides the quantitative measurements necessary to incorporate microscale wave breaking into heat and gas transfer models. Moreover, they argued that not all microscale breaking waves produced the downward "bursting" phenomena.

Banner (1990) and Banner & Peirson (1998) used a local wave slope based method to detect microscale breaking waves. In their method a microscale breaking wave was defined as any wave that exceeded a slope threshold of 0.5 on the downwind faces of the waves. At a fetch of 4.35 m, Banner & Peirson (1998) estimated the percentage of breaking waves as 53%, 70% and 89% at wind speeds of 4.8, 6.3 and 8.1 m s^{-1}, respectively. Peirson & Banner (2003) examined the flow beneath microscale breaking waves using high-resolution digital particle image velocimetry (DPIV) measurements. They detected microscale breaking waves using a local wave slope based detection scheme similar to Banner (1990) and Banner & Peirson (1998). They observed high values of vorticity and surface convergence at the leading edge of the spilling region. They argued that these regions of localized convergence were produced by subduction of the fluid beneath the spilling region.

Zappa *et al.* (2001) examined the influence of microscale breaking waves on air-water gas transfer and heat transfer using simultaneously sampled IR and wave slope imagery in a laboratory wind wave tank. In their experiment, microscale breaking waves were detected using IR imagery similar to Jessup *et al.* (1997). They found that the fractional area coverage of the wakes (A_B) generated by microscale breaking waves was correlated with the air-water gas and heat transfer velocities. They also observed that the disruption of the skin layer coincided with waves that have a dimpled bore-like crest and steep forward face. Zappa *et al.* (2004) measured the local heat transfer velocities inside and outside the wakes generated by microscale breaking waves and found that on average, the transfer velocity was enhanced by a factor of 3.5 inside the wakes.

Jessup & Phadnis (2005) used image processing algorithms to detect microscale breaking waves and investigated the kinematics and dynamics of breaking waves in IR images. They provided estimates of the distribution of breaking crest lengths as a function of crest speed, in a laboratory wind-wave tank.

Siddiqui *et al.* (2001) reported on a series of laboratory wind wave experiments beneath microscale breaking waves using simultaneously sampled DPIV measurements and IR imagery. They observed strong persistent vortices in the wave crests and warm turbulent wakes beneath the microscale breaking waves using the simultaneously sampled data. They observed strong correlations between the near-surface vorticity and both A_B and the local heat transfer velocity.

Loewen & Siddiqui (2006) developed a DPIV based detection method using the variance of vorticity as a threshold to detect microscale breaking waves. They compared their method with a wave slope and IR imagery detection methods and concluded that the vorticity method was the most accurate

in detecting microscale breaking waves. At a fetch of 5.5 m, their method predicted that the percentage of microscale breaking waves was 9%, 78% and 90% at wind speeds of 4.5, 7.4 and 11 m s^{-1}, respectively.

Siddiqui & Loewen (2007) studied the characteristics of the wind drift layer and turbulence beneath microscale breaking waves. They detected microscale breaking waves using the method developed by Loewen & Siddiqui (2006). They used simultaneously sampled DPIV measurements and IR imagery to investigate the near-surface flows at a fetch of 5.5 m and wind speeds ranging from 4.5 to 11 m s^{-1} and concluded that the enhanced near-surface turbulence was the result of microscale breaking waves.

7.2.2 Turbulence Beneath Breaking Waves

Agrawal *et al.* (1992) presented dissipation estimates obtained during the WAVES (Water-Air Vertical Exchange Study) experiment in Lake Ontario. Near-surface water velocities were measured using three different types of velocimeters: an acoustic current meter array (BASS), drag-sphere velocimeters and laser Doppler velocimeter (LDV) under strong breaking wave conditions. They reported that rates of dissipation of turbulent kinetic energy were one to two orders of magnitude higher than values predicted by wall layer theory. In addition, using time-dependent dissipation estimates at a wind speed of 12 m s^{-1}, they showed that the occurrence of enhanced ε was highly intermittent compared to a wall layer. They argued that the breaking of larger waves (i.e. whitecaps) was the source of this enhanced intermittent turbulence.

Anis & Moum (1995) measured velocity profiles using microstructure profilers in the upper oceanic boundary layer under various atmospheric and sea conditions. Depending on the forcing conditions, they found that sometimes ε followed the wall-layer theory, while, at other times ε was larger

in magnitude and decayed exponentially with depth, z. They proposed two different mechanisms to explain the enhanced ε values near the surface. First they proposed that enhanced turbulence kinetic energy was generated by wave breaking at the surface, which was transported downward by the motion of the swell and then balanced by dissipation. Second, they postulated that energy was drawn from the rotational wave field into the mean flow via wave stresses, and then it was drawn from the mean flow into the turbulent flow and then balanced by dissipation.

Terray *et al.* (1996) proposed a wave-dependent scale model for the near-surface dissipation rate based on the significant wave height, H_s and the rate of energy input from the wind to the waves, F_w. Their observations were from the same WAVES experiment reported by Agrawal *et al.* (1992) where data were obtained under strongly forced fetch-limited young waves for wave ages ranging from 4 to 7. They collected an extensive set of tower-based data using acoustic, mechanical and laser Doppler velocimeters during the WAVES experiments in Lake Ontario and found that ε was significantly larger compared to the values predicted by wall layer theory. Moreover, they proposed that the wave stirred near-surface zone was comprised of three layers. They argued that the extent of the topmost layer was approximately equal to the significant wave height and that in this layer ε was approximately constant. Below this an intermediate layer existed where ε decayed as z^{-2} such that,

$$\frac{\varepsilon H_s}{F_w} = 0.3 \left(\frac{z}{H_s} \right)^{-2} \tag{7.1}$$

where, H_s is the significant wave height and F_w is the rate of energy input from the wind to waves per unit mass. Below the intermediate layer, the values of ε asymptote to wall-layer values.

Drennan *et al.* (1996) reported measurements of ε made in the North Atlantic Ocean from a SWATH ship during the Surface WAves Dynamics

Experiment (SWADE). Their data were collected in the open ocean and the wave ages ranged from 13 to 29. The open ocean data collected during the SWADE experiment yielded dissipation rates in the near-surface region that are one to two orders of magnitude higher than wall layer prediction. The SWADE data satisfied the same scaling proposed using the WAVES data in the intermediate region supporting the validity of the scale model of Terray *et al.* (1996) for more developed waves typical of the open ocean. In addition, they proposed another wave-dependent scale model to normalize near-surface dissipation rates in which they used k_d as an alternate scaling variable as opposed to H_s proposed by Terray *et al.* (1996). In their model, ε in the upper ocean was normalized as follows,

$$\frac{\varepsilon}{k_d F_w} = 0.1\,(zk_d)^{-2} \tag{7.2}$$

where, k_d is the dominant wavenumber defined as $k_d = 2\pi/\lambda_d$, in which λ_d is the dominant wavelength. Moreover, they argued that there is an advantage of using their model over the model of Terray *et al.* (1996) because of easy computation of k_d from the wave spectrum compared to H_s which is particularly difficult to estimate when swell and wind sea coexists.

Soloviev & Lukas (2003) made near-surface measurements of turbulence in the western equatorial Pacific during the TOGA Coupled Ocean-Atmosphere Response Experiment (COARE) under a variety of wind forcing conditions. For wind speeds greater than 7 m s^{-1} (measured at a 15 m height), they observed enhanced values of ε which were up to one order of magnitude higher than wall layer predictions.

Gemmrich & Farmer (2004) made measurements of the turbulent velocity and entrained air bubble field as part of the Fluxes, Air-sea Interaction and Remote Sensing (FAIRS) experiment in the open ocean 150 km offshore of Monterey, California. They also observed enhanced values of dissipation that

were one order of magnitude higher than wall layer predictions. Moreover, they found that ε measured beneath the crests of breaking waves was approximately 1.6 times larger than beneath the troughs. In addition, in the wave crests above the mean water line, ε varied as $z^{-2.3}$ but below the wave troughs ε was approximate constant.

Thais & Magnaudet (1996) examined the turbulent structure of the flow generated due to wind waves and wind-ruffled mechanical waves using LDA measurements in a wind wave tank. Three components of the instantaneous velocity below the wave troughs at a fetch of 26 m and at wind speeds up to 7.8 m s^{-1} were measured in their study. Thais & Magnaudet (1996) separated the wave and turbulent components of the instantaneous velocities using a nonlinear triple decomposition method described in Thais & Magnaudet (1995). They investigated the similarity between the turbulent flow generated beneath wind-driven water surfaces and wall-layer flows. It was found that the turbulent kinetic energy and associated dissipation rate were significantly enhanced compared to wall-layer values. They suggested that the high values of the near-surface turbulence beneath the crests of the dominant wave could be attributed to vorticity generation by capillary ripples or wave breaking.

Siddiqui & Loewen (2007) provided evidence using laboratory measurements that enhanced near-surface dissipation was caused by microscale wave breaking. Moreover, they showed that the enhanced dissipation due to microscale wave breaking could be scaled non-dimensionally based on wind and wave parameters as proposed by Terray *et al.* (1996). Using vertical profiles of ε they found that two distinct layers existed beneath microscale breaking waves. They found that ε decayed as $\zeta^{-0.7}$ immediately beneath the surface and below this layer it decayed as ζ^{-2}, where ζ is the distance from the interface in a wave-following coordinate system.

Craig & Banner (1994) developed a model employing a "level $2\frac{1}{2}$" turbulence closure scheme in which the action of wave breaking was modeled by a turbulent kinetic energy input at the surface. They predicted that ε decayed as $z^{-3.4}$.

7.3 Turbulence Beneath Short Wind Waves

Estimates of turbulent kinetic energy dissipation rates were made using the 'direct' method (Doron *et al.*, 2001) described in Chapter 6 (see §6.6 on page 173). One important issue was to examine whether the spatial resolution of the DPIV measurements was sufficient to resolve the velocity gradients responsible for the dissipation of the turbulent kinetic energy (Siddiqui & Loewen, 2007). An estimate of the size of the smallest turbulent motions is the Kolmogorov length scale, $\eta = (\nu_w^3/\varepsilon)^{1/4}$, where, ν_w is the kinematic viscosity of water. The smallest spatial scale that was resolved in this study by the DPIV measurements was 2.0 mm, corresponding to a wavenumber, k=3140 rad m^{-1}, and the Kolmogorov length scale, η, varied between 165 and 695 μm. Cowen & Monismith (1997) argued that it is not necessary to resolve the Kolmogorov length scale to obtain reliable estimates of ε. They showed that 99% of the dissipation takes place for $k\eta < 5.5$ and that the maximum dissipation occurs at $k\eta = 0.1$. In this study, the range of $k\eta$ varied from 0.52 to 2.18. Based on the dissipation spectrum shown in Cowen & Monismith (1997), it was estimated that the calculated values of ε captured 80% to 99% of the total dissipation with an average value of 90%. It was concluded that the spatial resolution of the DPIV measurements was sufficient to obtain reliable estimates of ε.

The vertical profiles of ε for various wind speeds at three fetches of 4.8, 8.8 and 12.4 m are plotted in Figures 7.1 to 7.3. These profiles show that ε was enhanced significantly near the surface and that ε did not vary significantly

below depths of 40 to 60 mm. Below this depth, ε was approximately constant. In Figure 7.1, the rate of dissipation of TKE is plotted for six wind speeds ranging from 4.1 to 9.0 m s^{-1} at a fetch of 4.8 m. This plot shows that at all wind speeds the magnitude of ε, on average, decreased by a factor of approximately 10 at a depth of 40 mm compared to the values at a depth of 6 mm. In Figure 7.2, the rate of dissipation of TKE is plotted for five wind speeds ranging from 4.2 to 7.9 m s^{-1} at a fetch of 8.8 m. It was observed that at three wind speeds (except 6.1 and 7.2 m s^{-1}), the magnitude of ε, on average, decreased by a factor of approximately 12 from a depth of 6 mm to 40 mm. For the two wind speeds of 6.1 and 7.2 m s^{-1}, reliable estimates of near-surface values of ε were not available due to the so-called trough effect (see Chapter 5, §5.4.4 on page 115). In Figure 7.3, the rate of dissipation of TKE is plotted for four wind speeds ranging from 4.0 to 6.9 m s^{-1} at a fetch of 12.4 m. This plot shows that at all four wind speeds the magnitude of ε, on average, decreased by a factor of approximately 10 from a depth of 6 mm to 40 mm.

Soloviev *et al.* (1988) proposed the following dimensionless relationship for fully developed wind-waves,

$$\frac{\varepsilon\kappa\zeta}{u_{*t}^3} = \chi\left(\frac{g\zeta}{u_{*t}^2}\right) \tag{7.3}$$

where, κ is the von Kármán constant ($\kappa = 0.4 - 0.41$), u_{*t} is the tangential friction velocity, g is the acceleration due to gravity, ζ is the wave following vertical coordinate referenced to the water surface and χ is a universal function of the argument $g\zeta/u_{*t}^2$. Using this scaling, the normalized rate of energy dissipation for a constant stress layer would be unity at all depths (Agrawal *et al.*, 1992). In Figures 7.4 to 7.6, the normalized rate of energy dissipation is plotted versus the normalized depth using the scaling given in Equation (7.3) for various wind speeds at three fetches. In these figures, a vertical dashed line

is drawn at $\varepsilon\kappa\zeta/u_{*t}^3 = 1$ that represents an unstratified constant stress shear flow near a rigid wall (Lumley & Panofsky, 1964). The only notable finding from these profiles was that the normalized dissipation rates were higher (by a factor of 1.3 to 4.5) than the wall layer prediction at all normalized depths except for four experiments (i.e. 5.3 and 6.1 m s^{-1} at a fetch of 4.8 m, and 4.2 and 5.4 m s^{-1} at a fetch of 8.8 m). In Figure 7.4, at a fetch of 4.8 m, the normalized ε seemed to collapse according to the wall layer scaling only at two wind speeds (i.e. at 5.3 and 6.1 m s^{-1}) and for the remaining four wind speeds the normalized ε was increased by a factor of approximately 1.3 to 4.0 compared to wall layer prediction. Likewise, in Figure 7.5, at a fetch of 8.8 m, the normalized ε was increased by a factor of approximately 2.0 to 3.0 except for the two lowest wind speeds. In Figure 7.6, at a fetch of 12.4 m and for all wind speeds, the normalized ε was increased by a factor of approximately 2.0 to 4.5 compared to the wall layer prediction.

7.4 Detection of Microscale Breaking Waves

There is a considerable experimental evidence that microscale breaking waves generate warm turbulent wakes that disrupt the cool skin layer (Jessup *et al.*, 1997; Siddiqui *et al.*, 2001; Jessup & Phadnis, 2005) and produce strong vortices in their crests (Siddiqui *et al.*, 2001; Loewen & Siddiqui, 2006). Jessup *et al.* (1997) first showed that microscale breaking waves disrupt the cool skin layer and generate the warm turbulent wake that are detectable as thermal signatures using IR imagery. Using simultaneously sampled DPIV measurements and IR imagery, Siddiqui *et al.* (2001) showed that the presence of strong vortices in the crests of the microscale breaking waves coincides with the warm turbulent wakes observed in the IR images. Loewen & Siddiqui (2006) used the variance of these strong vortices as a characteristic signature to detect the microscale breaking waves.

In this study, sequences of simultaneously sampled IR images and DPIV data were utilized to detect microscale breaking waves similar to Loewen & Siddiqui (2006). Figures 7.7 to 7.9 show three successive IR images sampled 1/15 s apart and the contour plots of the turbulent vorticity fields obtained from the DPIV measurements at a wind speed of 6.2 m s^{-1} and at a fetch of 12.4 m. Figures 7.7 to 7.9 show a typical microscale breaking wave generating strong vortices in its crest and these vortices disrupt the cool skin layer and generate a warm turbulent wake that is visible in the IR image (Siddiqui *et al.*, 2001). Figures 7.7(a) to 7.9(a) show three sequences of a IR image where a microscale breaking wave is propagating from top to bottom. In these figures, the DPIV field of view is shown as a solid black line in which the location of the peak of the wave crest is identified as a circle. In Figures 7.7(b) to 7.9(b), the corresponding DPIV vorticity contour plots are shown for the same breaking wave. Figure 7.7(a) shows that the breaking wave has entered the upwind end of the DPIV field of view. A warm turbulent wake is visible as a bright white patch in the IR image. In Figure 7.7(b), strong vortices in the range of 10 to 20 s^{-1} are visible in the leading edge of the breaking crest beneath the water surface. In Figure 7.8(a), the leading edge of the breaker has propagated to the middle half of the DPIV field of view. Strong vortices in the range of 10 to 20 s^{-1} are observed to propagate with the wave crest as shown in the corresponding vorticity contour plot (see Figure 7.8(b)). In Figure 7.9(a), the leading edge of the breaking crest is still visible in the IR image and within the DPIV field of view, and, in Figure 7.9(b), the strong vortices are left behind in the wake as the leading edge of the breaking crest propagates downwind. Figures 7.7(b) to 7.9(b) suggest that a vorticity threshold based microscale breaking wave detection method as developed by Loewen & Siddiqui (2006) can be used in this study to distinguish between the microscale breaking and non-breaking waves.

Figure 7.10 shows an example of a typical non-breaking wave. In this figure weak wakes are visible in the IR image (see Figure 7.10(a)) and corresponding weak vortices in the range of 5 s^{-1} are visible in the vorticity contour plot (see Figure 7.10(b)). This figure shows that a typical non-breaking wave generates weak vortices that are not strong enough to disrupt the cool skin layer.

7.4.1 Vorticity Threshold Based Detection

A vorticity threshold based detection method as described by Loewen & Siddiqui (2006) was adapted in this study to detect microscale breaking waves. Their method can be summarized in four simple steps. First, wave crests were identified within the DPIV field of view. Second, a region-of-interest within each wave crest was set. Third, the variance of the vorticity within the region-of-interest was computed and recorded. Fourth, a wave was detected as a microscale breaking wave if the maximum of the variance of the vorticity, Ω, exceeded a pre-defined vorticity threshold, Ω_{th}.

In order to identify wave crests within the DPIV field of view, surface wave profiles were used. In a typical 10-minute experiment, 18000 surface wave profile images were recorded simultaneously with the DPIV measurements. Two surface wave profile images were collected for each pair of DPIV images. These profile images were almost identical because they were gathered only a few millisecond apart and therefore, only one profile image was used, which reduced the total number of profile images to half (i.e. 9000 profile images) for further analysis. The surface wave profiles were detected within the profile images and scaled to the DPIV field of view. These profiles were then digitally filtered with a cutoff wavenumber of 4369 rad m^{-1} to eliminate noise from the detected wave profiles since the shortest detected wave had a wavelength of 1.44 mm. The mean water level and the rms wave amplitude were computed using these wave profiles. Location of zero crossings within each wave profile were

identified by subtracting the mean water level from the surface displacement. If the surface displacement was positive between two successive zero crossings then that portion of the wave profile was identified as a wave crest, and vice-versa for a wave trough. However, wave crests that had amplitudes less than one-quarter of the r.m.s. wave amplitude were ignored. The number of waves that appeared within the DPIV field of view depended on the wind speed and fetch. At the shortest fetch and lowest wind speed, a maximum of three waves appeared within a DPIV field of view, while at longer fetches and moderate to high wind speeds, only a partial wave appeared.

The next step was to set a region-of-interest within each wave crest. The length of the region-of-interest was set equal to a quarter of the dominant wavelength (see Table 7.1) and its depth was set to 1 cm following Loewen & Siddiqui (2006). This depth was chosen because Siddiqui *et al.* (2001) found that the size of the strong vortices generated by microscale breaking wave was $O(1$ cm). The region-of-interest was centered at the peak of each wave amplitude, (i.e. η_{max}) and the top of the region-of-interest was aligned with the third grid point (i.e. 6 mm below the surface) to avoid the so-called "trough effect". Lowering the crest region prevented inclusion of the inaccurate velocity data that would otherwise affect the detection of the microscale breaking waves. In some cases η_{max} was located closer than one-eighth of a wavelength to the edge of the DPIV field of view and in these cases the region-of-interest was placed at the edge of the DPIV field of view.

In Figure 7.8(b), the contour plot of the vorticity field beneath the water surface is shown plotted at a wind speed of 6.2 m s^{-1} and at a fetch of 12.4 m, and the region-of-interest is shown as a dotted box in the figure. When a wave crest appeared within the DPIV field of view, the variance of the vorticity, Ω, within the region-of-interest was computed.

In the final step, each wave crest was tracked as it moved through the DPIV

field of view. The tracking became challenging when more than one wave crests appeared within a DPIV field of view. To facilitate tracking of each wave, the location of the peak of each wave crest was recorded in each DPIV field. In addition, the values of Ω were also recorded for each wave and the maximum value of the variance of the vorticity, Ω_{max}, was then computed for a given wave as it passed through the DPIV field of view. If the value of Ω_{max} exceeded a pre-defined vorticity threshold, Ω_{th}, that wave was identified as a microscale breaking wave. Otherwise, the wave was identified as a non-breaking wave. The optimum value of Ω_{th} was selected by comparing the number of breaking waves detected visually in the sequences of simultaneously sampled IR images and those detected by the vorticity threshold based detection method.

7.4.2 IR Imagery Based Detection

Visual detection of microscale breaking waves in the IR images was relatively straight forward although laborious. Figures 7.7(a) to 7.9(a) show a typical infrared signature of a warm turbulent wake generated by a microscale breaking wave. This characteristic infrared signature was used in this study to visually detect microscale breaking waves in the IR images. The IR image based detection consisted of the following simple steps. First, the DPIV field of view was delineated within the IR image. Then the peak of one or more wave crests were plotted on the line marking the DPIV field of view in the IR image. Typically, one to three wave crests appeared within the DPIV field of view in the IR image. A wave in the IR image was visually detected as a microscale breaking wave when the leading edge of an infrared signature travel across the DPIV field of view as shown in Figures 7.7(a) to 7.9(a). Waves typically appeared in three to four consecutive IR images. At the higher wind speeds, visual detection of microscale breaking waves was relatively easy because of the size and clarity of the warm turbulent wakes. However, at lower wind

speeds, it was difficult to visually identify the warm turbulent wakes because of their relatively weak thermal signatures.

7.4.3 Selection of Optimum Vorticity Threshold

To facilitate the selection of an optimum vorticity threshold for all experimental run, a total of 1800 simultaneously sampled IR images and DPIV vorticity fields (i.e. 120 s of data at 15 Hz) at a wind speed of 7.9 m s^{-1} and at a fetch of 8.8 m were used in this study similar to Loewen & Siddiqui (2006). Microscale breaking waves in 1800 IR images were first visually detected. Then the vorticity threshold based detection method was applied to the corresponding 1800 DPIV vorticity fields by setting the vorticity threshold, Ω_{th} equal to 10, 20 and 30 s^{-2}. The identity and number of microscale breaking waves were recorded for both methods. The value of Ω_{th} at which a maximum number of microscale breaking waves were matched between the IR imagery based and vorticity threshold based detection methods was chosen as the optimum threshold. The outcome of this analysis is summarized in Table 7.2.

Table 7.2 lists the number of microscale breaking waves detected using the vorticity threshold based detection method (i.e. N_{DS}), the number visually detected in the IR images (i.e. N_V) and the number detected simultaneously in both methods (i.e. N_C) for three vorticity thresholds of 10, 20 and 30 s^{-2} at a wind speed of 7.9 m and at a fetch of 8.8 m. For example, 451 microscale breaking waves were detected visually in the IR images and the vorticity threshold based detection method detected 453 waves using a vorticity threshold of 20 s^{-2}. Moreover, 417 breaking waves were simultaneously detected by both methods. That is, 36 waves that were detected by the vorticity threshold based detection method, were not detected visually in the IR images. These waves were referred to as false positives (N_{FP}) because the

vorticity threshold based detection method falsely identified them as breaking waves. In addition, the vorticity threshold based detection method did not detect 34 waves out of the 451 visually detected waves and these waves are referred to as false negatives (N_{FN}). The values of N_{FP} and N_{FN} are also listed in Table 7.2. Table 7.2 shows that the values of N_{FP} decreased and the values of N_{FN} increased as the Ω_{th} was increased from 10 to 30 s^{-2}. Therefore, the optimum value for Ω_{th} was chosen when the sum of false positives and false negatives was a minimum. Using Table 7.2, the optimum value of Ω_{th} was found to be 20 s^{-2} because at this value the total number of false positives and false negatives was a minimum. Therefore, a threshold value of $\Omega_{th} = 20$ s^{-2} was used for detecting microscale breaking waves using the vorticity threshold based detection method.

The vorticity threshold based detection method was then applied at various wind speeds at all three fetches to detect microscale breaking waves. The velocity fields associated with the breaking and non-breaking waves were then conditionally sampled. For each wave, the velocity field in which the maximum value of the variance of the vorticity occurred was designated as the representative field. Non-breaking velocity fields were also conditionally sampled in the same manner. This conditional sampling allowed the comparison of the characteristics and structure of the turbulent flow beneath microscale breaking and non-breaking waves.

7.5 Characteristics of Microscale Breaking Waves

The percentage of microscale breaking waves, P_b, is plotted as a function of wind speed at three fetches in Figure 7.11. The breaking percentage found by Siddiqui & Loewen (2007) at wind speed ranging from 4.5 to 11.0 m s^{-1} and at a fetch of 5.5 m is also plotted in Figure 7.11. The percentage of

microscale breaking waves was defined as the number of breaking waves divided by the sum of the number of breaking and non-breaking waves expressed as a percentage. Figure 7.11 shows that P_b increased with wind speed at all fetches, however, the variation of P_b with fetch was not systematic. This plot also shows that P_b is equal to approximately 4% at a wind speed of 4.1 m s^{-1} and P_b jumped to over 90% for wind speeds higher than 7.9 m s^{-1} at a fetch of 4.8 m. At a fetch of 8.8 m, P_b was equal to approximately 1% at a wind speed of 4.2 m s^{-1} and increased to over 85% at a wind speed of 7.9 m s^{-1}. At a fetch of 12.4 m, P_b was equal to approximately 3% at a wind speed of 4.0 m s^{-1} and reached over 70% at wind speed of 6.9 m s^{-1}. These percentages were comparable to the findings of Siddiqui & Loewen (2007). A regression line fitted to the data presented in Figure 7.11 for the wind speed range of $4 \leq U_z \leq 8$ m s^{-1} gives the following relationship,

$$P_b = 22.51 \times U_z - 96.44 \qquad r = 0.87 \tag{7.4}$$

where, r is the Pearson product-moment correlation coefficient (Rodgers & Nicewander, 1988). This plot shows that $P_b \simeq 0\%$ at $U_z \leq 4$ m s^{-1} and then P_b increases linearly with U_z for $4 \leq U_z \leq 8$ m s^{-1}. The percentage of breaking waves remains almost constant ($P_b \simeq 90\%$) for $U_z > 8$ m s^{-1}. It should be noted that at higher wind speeds significant air entrainment will occur.

The average values of the maximum wave amplitude, $\langle \eta_{max} \rangle$; and maximum wave slope on the forward face, $\langle S_{max} \rangle$ were computed for both breaking and non-breaking waves and are listed in Table 7.3. In order to compute the maximum wave slope (S_{max}), slopes on the forward face of a wave over an interval of 16 pixels (approximately 2 mm) were computed and then the maximum value of the slopes provided an estimate of S_{max}. For microscale breaking waves, it is evident that $\langle \eta_{max} \rangle$ increased with wind speed at all three fetches. At a fetch of 4.8 m, as wind speed increased from 4.1 to 9.0 m s^{-1},

$\langle \eta_{max} \rangle$ increased from 0.10 to 0.64 cm. At a fetch of 8.8 m, as wind speed increased from 4.2 to 7.9 m s^{-1}, $\langle \eta_{max} \rangle$ increased from 0.28 to 0.88 cm. At a fetch of 12.4 m, as wind speed increased from 4.0 to 6.9 m s^{-1}, $\langle \eta_{max} \rangle$ increased from 0.58 to 1.11 cm. The increase in $\langle S_{max} \rangle$ with wind speed is evident at the short (4.8 m) and intermediate (8.8 m) fetch but not at the long (12.4 m) fetch. At a fetch of 4.8 m, $\langle S_{max} \rangle$ increased from 0.06 to 0.33 as wind speed increased from 4.1 to 9.0 m s^{-1}. At a fetch of 8.8 m, $\langle S_{max} \rangle$ increased from 0.20 to 0.35 as wind speed increasing from 4.2 to 7.2 m s^{-1} and then remained constant. At the longest fetch of 12.4 m, $\langle S_{max} \rangle$ remained almost constant between the values 0.33 and 0.35 for all four wind speeds. For non-breaking waves, the variations in $\langle \eta_{max} \rangle$ and $\langle S_{max} \rangle$ were not systematic with increasing wind speed at different fetches. These results show that microscale breaking waves were on average, 61% larger in amplitude, and 43% steeper on the forward face compared to the non-breaking waves. Siddiqui & Loewen (2007) found that microscale breaking waves were on average, 60% larger in amplitude and 45% steeper than non-breaking waves. Data at the lowest wind speeds (i.e. 4.0 to 4.2 m s^{-1}) and three fetches were not used in the further analysis since over 95% of the waves were non-breaking waves.

7.6 Turbulence Beneath Microscale Breaking Waves

7.6.1 Energy Dissipation

The energy dissipation rates beneath microscale breaking and non-breaking waves are denoted by ε_{msb} and ε_{non}, respectively (Siddiqui & Loewen, 2007). In order to estimate ε_{msb} and ε_{non}, the 'direct' method presented by Doron *et al.* (2001) was applied to the conditionally sampled (i.e. breaking and non-breaking) wave-turbulent component of the DPIV velocity data.

Vertical profiles of ε_{msb} and ε_{non} are shown plotted in Figures 7.12 to 7.14 for various wind speeds at three fetches. Figures 7.12(a) to 7.14(a) show that the magnitudes of ε_{msb} varied significantly up to a depth of 4.0 cm and below this depth the variation of the rate of dissipation of TKE was not significant. In Figure 7.12(a), the rate of dissipation of TKE is plotted for five wind speeds ranging from 5.3 to 9.0 m s^{-1} at a fetch of 4.8 m. Figure 7.12(a) shows that the magnitude of ε_{msb} 6 mm below the surface varied between 2.5 and 6.0 cm^2 s^{-3} for wind speeds less than 7.0 m s^{-1} and for wind speeds higher than 7.0 m s^{-1}, ε_{msb} jumped abruptly to values between 16.0 and 17.9 cm^2 s^{-3}. The abrupt jump in ε_{msb} was likely caused by the fact that the percentage of breaking waves, P_b, increased from less than 55% at $U_z < 7.0$ m/s, more than 90% at $U_z > 7.0$ m/s,. Figure 7.12(b) shows that the magnitude of ε_{non} at the two highest wind speeds was slightly higher than at the three lower wind speeds. Remnants of the strong vortices left behind by the large numbers of microscale breaking waves ($P_b > 90\%$) may have caused these increases in ε_{non}. The data in Figure 7.12 reveal that the magnitude of ε_{msb} increased by a factor of 1.9 to 3.8 compared to the magnitude of ε_{non} as wind speed increased from 5.3 to 9.0 m s^{-1} at a depth of 6 mm. The magnitude of ε_{msb} and ε_{non}, on average, increased by a factor of approximately 15 and 6, respectively going from a depth of 40 mm to 6 mm.

At a fetch of 8.8 m, estimates of ε_{msb} and ε_{non} were available for four wind speeds ranging from 5.4 to 7.9 m s^{-1}. However, reliable estimates of the near-surface values of ε_{msb} and ε_{non} were not available for two intermediate wind speeds of 6.1 and 7.2 m s^{-1} due to trough effect. The data in Figure 7.13 shows that the magnitude of ε_{msb} was 2.3 times higher than the magnitude of ε_{non} at the lowest wind speed of 5.4 m s^{-1}, whereas, the magnitude of ε_{msb} was 5.4 times higher than the magnitude of ε_{non} at the highest wind speed of 7.9 m s^{-1}. The magnitude of ε_{msb} and ε_{non}, on average, increased by a factor of

approximately 17 and 7, respectively going from a depth of 40 mm to 6 mm.

In Figure 7.14, estimates of ε_{msb} and ε_{non} were plotted for three wind speeds ranging from 5.3 to 6.9 m s^{-1} at a fetch 12.4 m. For all three wind speeds, the magnitude of ε_{msb} increased by a factor of approximately 4 compared to the magnitude of ε_{non} as the wind speed increased from 5.3 to 6.9 m s^{-1}. The magnitude of ε_{msb} and ε_{non}, on average, increased by a factor of approximately 20 and 7, respectively going from a depth of 40 mm to 6 mm.

In order to quantify the relative strength of turbulence beneath the microscale breaking waves over the non-breaking waves, the ratio of the depth-averaged rate of dissipation of TKE beneath the breaking and non-breaking waves were computed. To facilitate the comparison, the depth-averaged rate of dissipation of TKE for microscale breaking, $\langle\varepsilon_{msb}\rangle$, and non-breaking waves, $\langle\varepsilon_{non}\rangle$, were computed over the upper 40 mm in the water column. The ratio of $\langle\varepsilon_{msb}\rangle/\langle\varepsilon_{non}\rangle$ is plotted as a function of wind speed at three fetches in Figure 7.15. In general, it was found that $\langle\varepsilon_{msb}\rangle/\langle\varepsilon_{non}\rangle$ increased with wind speed at all three fetches. At a fetch of 4.8 m, $\langle\varepsilon_{msb}\rangle/\langle\varepsilon_{non}\rangle$ increased from 1.5 to 2.4 as the wind speed increased from 5.3 to 9.0 m s^{-1} . At a fetch of 8.8 m, $\langle\varepsilon_{msb}\rangle/\langle\varepsilon_{non}\rangle$ increased from 1.9 to 3.5 as the wind speed increased from 5.4 m s^{-1} to 7.9 m s^{-1}. At a fetch of 12.4 m, $\langle\varepsilon_{msb}\rangle/\langle\varepsilon_{non}\rangle$ increased from 2.6 to 3.4 as the wind speed increased from 5.3 m s^{-1} to 6.9 m s^{-1}. At a given wind speed, $\langle\varepsilon_{msb}\rangle/\langle\varepsilon_{non}\rangle$ tended to increase with fetch.

A direct measure of the strength of turbulence solely due to wave breaking can be obtained by computing ε_b as follows,

$$\varepsilon_b = \varepsilon_{msb} - \varepsilon_{non} \tag{7.5}$$

where, ε_b is the dissipation rate solely due to microscale breaking (Siddiqui & Loewen, 2007). Siddiqui & Loewen (2007) argued that the ratio $\varepsilon_b/\varepsilon_{non}$ is a reasonable first-order estimate of the influence of wave breaking on the

near-surface turbulence. In Figures 7.16 to 7.18, $\varepsilon_b/\varepsilon_{non}$ is plotted versus the normalized depth, ζ/H_s, for various wind speeds at three fetches. It is evident in Figures 7.16 to 7.18 that the influence of wave breaking on the turbulence extends up to a depth of approximately one significant wave height. Figure 7.16 shows that the ratio $\varepsilon_b/\varepsilon_{non}$ at $\zeta/H_s \simeq 1.0$ increased from 1.2 to 3.2 as wind speed increased from 5.3 to 9.0 m s^{-1} at a fetch of 4.8 m. For $\zeta/H_s > 1.0$, the relative contribution of wave breaking to the turbulence has dropped to $\varepsilon_b/\varepsilon_{non} \leq 1.2$, and for $\zeta/H_s > 5.0$ the contribution is less than 10%. In Figure 7.17, the ratio $\varepsilon_b/\varepsilon_{non}$ at $\zeta/H_s \simeq 1.0$ increased from 1.2 to approximately 5.0 as wind speed increased from 5.4 to 7.9 m s^{-1} at a fetch of 8.8 m. For $\zeta/H_s > 1.0$, the ratio of $\varepsilon_b/\varepsilon_{non}$ varied between 0 and 1.2. In Figure 7.18, the ratio $\varepsilon_b/\varepsilon_{non}$ at $\zeta/H_s \simeq 1.0$ increased from 1.2 to approximately 4.0 as wind speed increased from 5.3 to 6.9 m s^{-1} at a fetch of 12.4 m. For $\zeta/H_s > 1.0$, the ratio of $\varepsilon_b/\varepsilon_{non}$ varied between 0 and 1.2. Figures 7.16 to 7.18 provide quantitative evidence that the near-surface dissipation is enhanced due to wave breaking. Siddiqui & Loewen (2007) also found similar evidence that near-surface dissipation rate was enhanced due to microscale wave breaking. They found that immediately beneath the water surface the ratio of $\varepsilon_b/\varepsilon_{non}$ increased from 0.7 to 2.2 as wind speed increased from 4.5 to 11 m s^{-1} at a fetch of 5.5 m.

7.6.2 Dissipation Rate Scaling

Terray *et al.* (1996) proposed that the rate of dissipation beneath breaking waves should scale with the friction velocity, significant wave height, phase speed and depth. Moreover, they suggested that ε decayed at three different rates depending on the depth. They assumed that ε is approximately constant immediately beneath the breaking wave and the vertical extent of this layer is approximately $0.6H_s$. Below this layer they proposed a transition layer in

which ε decays as z^{-2}, where z is the depth below the mean water level. They estimated that the vertical extent of the transition layer varied from 8.3 to $13H_s$ for their field data. They also argued that below the transition layer ε should decay as z^{-1} to match with a traditional wall-layer behavior.

Following Terray *et al.* (1996), it was also assumed in this study that three distinct layers exist in the water column beneath microscale breaking waves to describe the structure of near-surface turbulence. The topmost layer is defined as the 'wave-induced layer' and the extent of this region is assumed to be equal to $0.6H_s$. Below this layer, a 'transition layer' of thickness approximately $9H_s$ is assumed. The lower layer is defined as the 'shear-induced layer'.

Siddiqui & Loewen (2007) normalized ε_b using the scaling of Terray *et al.* (1996) and showed that this scaling is appropriate for ε_b. In addition, Siddiqui & Loewen (2007) used u_{*t} as friction velocity to normalize ε_b instead of u_{*w} that was used by Terray *et al.* (1996), where, u_{*w} is the water-side friction velocity converted from the wind friction velocity, u_{*a}, such that $u_{*w} = \sqrt{\rho_a/\rho_w}u_{*a}$, where, ρ_a and ρ_w are the density of air and water, respectively. The use of an appropriate friction velocity to normalize ε_b using the scaling of Terray *et al.* (1996) was explored in the following paragraphs.

The rate of total dissipation of TKE, ε, in wind generated turbulence can be written as the sum of three components,

$$\varepsilon = \varepsilon_c + \varepsilon_w + \varepsilon_u \tag{7.6}$$

where, ε_c, ε_w and ε_u are the dissipation rates due to convection, wave and shear, respectively (Soloviev *et al.*, 2007). Accordingly, the rate of total dissipation of TKE occurring beneath microscale breaking waves (ε_{msb}) and non-breaking waves (ε_{non}) can be written as,

$$\varepsilon_{msb} = \varepsilon_{c\_msb} + \varepsilon_{w\_msb} + \varepsilon_{u\_msb} \tag{7.7}$$

$$\varepsilon_{non} = \varepsilon_{c\_non} + \varepsilon_{w\_non} + \varepsilon_{u\_non} \tag{7.8}$$

where, the subscripts '*msb*' and '*non*' represent breaking and non-breaking waves. Assuming that ε_{non} is the background dissipation rate, the rate of dissipation of TKE solely due to wave breaking, ε_b is given by,

$$\begin{aligned} \varepsilon_b &= \varepsilon_{msb} - \varepsilon_{non} \\ &= \varepsilon_{w\_b} + \varepsilon_{u\_b} \end{aligned} \tag{7.9}$$

where, $\varepsilon_{w\_b} = \varepsilon_{w\_msb} - \varepsilon_{w\_non}$ and $\varepsilon_{u\_b} = \varepsilon_{u\_msb} - \varepsilon_{u\_non}$. In Equation (7.9), it was assumed that the dissipation rates due to convection under breaking and non-breaking waves were approximately equal, i.e. $\varepsilon_{c\_msb} \approx \varepsilon_{c\_non}$. Therefore, ε_b is comprised only of the wave- and shear-induced dissipation terms.

The energy input for the wave related dissipation, ε_{w_b}, is the turbulent kinetic energy generated by breaking waves. The shear related dissipation term, ε_{u_b}, represents the rate of dissipation of TKE associated with shear currents (Rapp & Melville, 1990; Melville, 1996). It was hypothesized in this study that in the wave-induced layer, ε_{w_b} will dominate over ε_{u_b} and therefore, ε_b should be scaled with u_{*wv}, where, u_{*wv} is the wave-induced friction velocity. The wave-induced friction velocity, u_{*wv}, was computed assuming the fact that the wind stress, $\tau_a = \rho_a u_{*a}^2$, was partitioned into wave-induced stress, $\tau_w = \rho_w u_{*wv}^2$ and tangential stress, $\tau_t = \rho_w u_{*t}^2$ such that $\tau_a = \tau_w + \tau_t$ at the air-water interface. Therefore, u_{*wv} was computed using the following equation,

$$u_{*wv} = \sqrt{u_{*w}^2 - u_{*t}^2} \tag{7.10}$$

In the transition layer, both ε_{w_b} and ε_{u_b} are thought to be equally important, and therefore, ε_b should be scaled with both u_{*wv} and u_{*t}. In the shear-induced layer, ε_{u_b} is assumed to dominate over ε_{u_w}, and therefore, ε_b should be scaled only with u_{*t}. A schematic illustrating this hypothesis is presented in Figure 7.19.

A simple analogy is presented in Figure 7.20 that support the use of

layer based friction velocity to normalize ε_b. In Figure 7.20(a), ε_b was normalized using u_{*wv} and in Figure 7.20(b) ε_b was normalized using u_{*t}. Figure 7.20(a) shows that the normalized ε_b collapsed quite well up to a depth of approximately $0.6H_s$ and below this, for $\zeta/H_s > 0.6$, the normalized data was scattered. In Figure 7.20(b) the normalized ε_b is shown to collapse into a narrow band for $\zeta/H_s > 10.0$ and partly for $0.6 < \zeta/H_s < 10.0$ but for $\zeta/H_s < 0.6$ the normalized data is scattered. This simple analogy shows that the scaling of Terray *et al.* (1996) does not perform well in all layers of the water column only if a single friction velocity is used to normalize ε_b. Therefore, it was hypothesized that the water column beneath microscale breaking waves should be divided into three layers and different friction velocities should be used to normalize ε_b in each layer using the scaling of Terray *et al.* (1996).

The validity of this three layer hypothesis was investigated using the laboratory measurements made in this study. In Figures 7.21 to 7.23, ε_b was normalized based on the proposed hypothesis using the scaling method of Terray *et al.* (1996) for various wind speeds and three fetches of 4.8, 8.8 and 12.4 m. Figure 7.21 shows that ε_b decays with depth at three different rates in three layers at a fetch of 4.8 m. In the wave-induced layer for $\zeta/H_s < 0.6$, ε_b decays as $\zeta^{-0.2}$ which is not significantly different than the approximation of constant dissipation assumption made by Terray *et al.* (1996). The vertical extent of this layer was found to vary from the water surface up to a depth of approximately $0.6H_s$ as shown in Figure 7.21, which is comparable to the findings of Terray *et al.* (1996) and Siddiqui & Loewen (2007). In the transition layer, ε_b decays as $\zeta^{-2.0}$, which is similar to the depth dependent turbulent structure found by Terray *et al.* (1996) and Siddiqui & Loewen (2007). The vertical extent of this layer was found to vary from 0.6 to $10H_s$ as shown in Figure 7.21. In the lower layer, ε_b decays as ζ^{-1} similar to the traditional wall-layer behavior, which is consistent with the argument of Terray *et al.*

(1996). In Figures 7.22 and 7.23, the normalized data did not extend to sufficient depth to support three layer hypothesis. However, two distinct layers were clearly observed in the figures. In Figures 7.22 and 7.23, and in the wave-induced layer at the fetches of 8.8 and 12.4 m, ε_b decays as $\zeta^{-0.2}$ which is similar to the finding of this study at the short fetch and the findings of Terray *et al.* (1996) and Siddiqui & Loewen (2007). The vertical extent of this layer is again up to $0.6H_s$. In the transition layer, two distinct decay rates are observed which is different from the observation made in the short fetch. In the upper region of the transition layer, ε_b decays as $\zeta^{-2.0}$, which is similar to the findings at the short fetch however, with a different vertical extent. In Figures 7.22 and 7.23, the vertical extent of this region was found to vary from 0.6 to $3H_s$. In the lower region of the transition layer, ε_b decays as $\zeta^{-4.0}$, which is similar to the turbulent structure found by Gargett (1989) in the northeast Pacific Ocean. The vertical extent of this region was found to vary from 3 to $10H_s$ for the intermediate region in Figure 7.22 and 3 to $7H_s$ for the longest fetch in Figure 7.23.

7.7 Conclusions

The main focus of this chapter is to develop a better understanding of the structure of near-surface turbulence beneath microscale breaking waves. A DPIV vorticity threshold based detection scheme similar to Loewen & Siddiqui (2006) was adapted in this study to detect the microscale breaking waves. The structure of the near-surface turbulence beneath microscale breaking waves beneath a clean water surface was also examined. It was observed that the short wind waves started to break at wind speeds higher than 4 m s^{-1} and that the percentage of breaking waves increased linearly with wind speed up to 90% for wind speed less than or equal to 8 m s^{-1}. The percentage of breaking waves remained almost constant at 90% for wind speed greater than 8 m s^{-1}.

No systematic variation in the % of microscale breaking waves was observed with fetch.

The rate of dissipation of turbulent kinetic energy was used as a measure of strength of turbulence beneath the microscale breaking waves. The ratio of depth-averaged dissipation rates beneath microscale breaking and non-breaking waves were used as a measure of influence of microscale breaking waves over non-breaking waves. It was found that depth-averaged dissipation rates beneath microscale breaking waves were always higher than the corresponding dissipation rates beneath non-breaking waves at a given fetch and wind speed. Moreover, the ratio of the depth-averaged dissipation rates beneath microscale breaking and non-breaking waves increased with wind speed at a given fetch. In addition, at a given wind speed, the ratio of the depth-averaged dissipation rates beneath microscale breaking and non-breaking waves increased as the fetch increased.

The structure of near-surface turbulence beneath microscale breaking waves was investigated using the wave-dependent scaling method proposed by Terray *et al.* (1996). It was determined that the scaling proposed by Terray *et al.* (1996) could be used to describe the structure of turbulence beneath microscale breaking waves if layer based friction velocities are used in the different layers to scale energy dissipation rates. Three distinct layers were observed beneath microscale breaking waves. A wave-induced layer was identified from the surface (6 mm below the air-water interface) to a depth of 0.6 times the significant wave height where turbulence was generated by wave-induced motions. A transition layer was identified from a depth of 0.6 to 10 times the significant wave height where turbulence was generated by both wave-induced motions and shear currents. A shear-induced layer was identified at a lower depth that extend beyond 10 times the significant wave height to a deeper depth where turbulence was produced by shear currents.

At a fetch of 4.8 m, it was found that energy dissipation rates solely due to breaking decayed as $\zeta^{-0.2}$ in the wave-induced layer, which was similar to the approximation of constant dissipation made by Terray *et al.* (1996). In the transition layer, energy dissipation rates decayed as $\zeta^{-2.0}$, which is similar to the findings of Terray *et al.* (1996) and Siddiqui & Loewen (2007). At lower layer, energy dissipation rates decayed as $\zeta^{-1.0}$, which was similar to the traditional wall-layer. At fetches 8.8 and 12.4 m, energy dissipation rates also decayed as $\zeta^{-0.2}$ in the wave-induced layer. In the transition layer, dissipation rates decayed at two different rates depending on the depth. In the upper region of the transition layer, dissipation rates decayed as $\zeta^{-2.0}$. In the lower region of the transition layer, dissipation rates decayed as $\zeta^{-4.0}$. However, energy dissipation rates were not available to describe the lower layer.

F (m)	U_z (m s^{-1})	H_s (cm)	H_{rms} (cm)	λ_d (cm)	k_d (rad cm^{-1})	$\langle S^2 \rangle$	c_p (cm s^{-1})	T_{air} ($^\circ$C)	T_{water} ($^\circ$C)
	5.3	0.35	0.23	5.6	1.12	0.039	29.6	20.6	23.3
	6.1	0.52	0.35	7.2	0.87	0.046	33.5	19.8	22.8
4.8	6.8	0.69	0.47	8.6	0.73	0.047	36.6	22.8	24.4
	7.9	0.97	0.66	10.8	0.58	0.054	41.1	21.5	23.8
	9.0	1.18	0.80	12.5	0.50	0.060	44.2	20.2	22.5
	5.4	0.78	0.53	10.0	0.63	0.044	39.5	21.8	22.1
	6.1	1.11	0.75	12.8	0.49	0.048	44.6	15.6	21.7
8.8	7.2	1.41	0.96	15.3	0.41	0.054	48.8	19.7	21.0
	7.9	1.59	1.08	16.7	0.38	0.061	51.0	21.9	22.2
	9.6	2.04	1.38	19.1	0.33	0.078	54.6	19.9	21.1
	5.3	1.41	0.95	16.4	0.38	0.041	50.5	18.9	23.0
	6.2	1.70	1.15	18.7	0.34	0.048	54.1	18.9	22.0
12.4	6.9	1.97	1.33	19.9	0.32	0.056	55.8	20.1	22.5
	7.9	2.38	1.61	22.1	0.28	0.070	58.7	19.9	22.6
	9.2	2.81	1.91	23.7	0.27	0.092	60.8	19.8	21.8

Table 7.1: Summary of wind-wave characteristics at different experimental conditions. U_z, wind speed in the wave tank; H_s, the significant wave height; H_{rms}, the r.m.s. wave height; λ_d, the dominant wavelength; k_d, the dominant wavenumber; $\langle S^2 \rangle$, the mean-square wave slope; (c_p), the wave phase speed; T_{air}, the bulk air temperature; T_{water}, the bulk water temperature.

$F(m)$	U_z (m s^{-1})	Ω_{th} (s^{-2})	N_{DS}	N_V	N_C	N_{FP}	N_{FN}	$\lvert N_{FP} + N_{FN} \rvert$
		10	473	451	427	46	-24	22
8.8	7.9	20	453	451	417	36	-34	2
		30	417	451	387	30	-64	34

Table 7.2: Values of Ω_{th}, the vorticity threshold; N_{DS}, the number of microscale breaking waves identified by the vorticity threshold based detection method; N_V, the number of microscale breaking waves detected visually in the IR images; N_C, the number of microscale breaking waves identified by both methods; N_{FP}, the number of false positive waves, $N_{FP} = N_{DS} - N_C$; N_{FN}, the number of false negative waves, $N_{FN} = N_C - N_V$. The results are based on 1800 DPIV vorticity fields and IR images for three vorticity thresholds at a wind speed of 7.9 m s^{-1} and a fetch of 8.8 m.

F (m)	U_z (m s^{-1})	P_b (%)	$\langle \eta_{max} \rangle$ (cm)		$\langle S_{max} \rangle$	
			Breaking	Non-breaking	Breaking	Non-breaking
4.8	4.1	4	0.10	0.10	0.06	0.06
	5.3	8	0.21	0.18	0.15	0.13
	6.1	28	0.32	0.25	0.23	0.18
	6.8	53	0.40	0.29	0.26	0.21
	7.9	93	0.55	0.27	0.30	0.23
	9.0	91	0.64	0.31	0.33	0.20
8.8	4.2	1	0.28	0.21	0.20	0.15
	5.4	14	0.49	0.38	0.30	0.23
	6.1	23	0.68	0.51	0.33	0.26
	7.2	56	0.85	0.53	0.35	0.25
	7.9	87	0.88	0.37	0.34	0.19
12.4	4.0	3	0.58	0.40	0.33	0.20
	5.3	33	0.91	0.59	0.34	0.22
	6.2	51	1.05	0.63	0.35	0.21
	6.9	73	1.11	0.56	0.34	0.21

Table 7.3: Values of $\langle \eta_{max} \rangle$, the average maximum wave amplitude; and, $\langle S_{max} \rangle$, the average maximum wave slope on the forward face for microscale breaking and non-breaking waves at wind speed, U_z, fetch, F and breaking percentage, P_b.

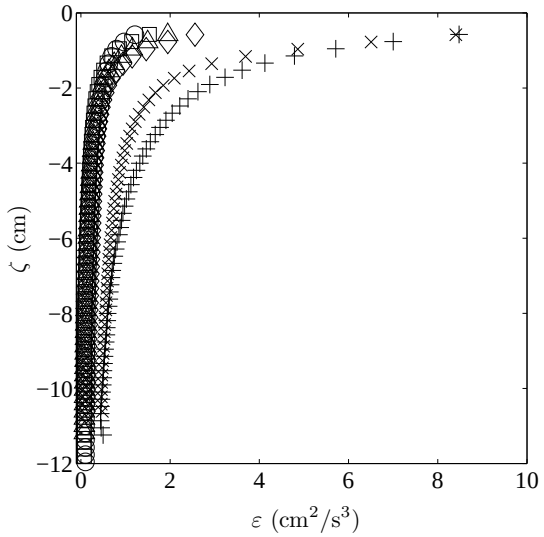

Figure 7.1: Vertical profiles of the rate of energy dissipation, ε, at a fetch of 4.8 m and for wind speed, U_z (m s^{-1}): ○,= 4.1; □,= 5.3; △,= 6.1; ◊,= 6.8; +,= 7.9; ×,= 9.0. ζ is the wave following vertical coordinate referenced to the water surface. The values of ε at a given depth were time-averaged over 10-minutes and spatially averaged over the width of the DPIV field of view.

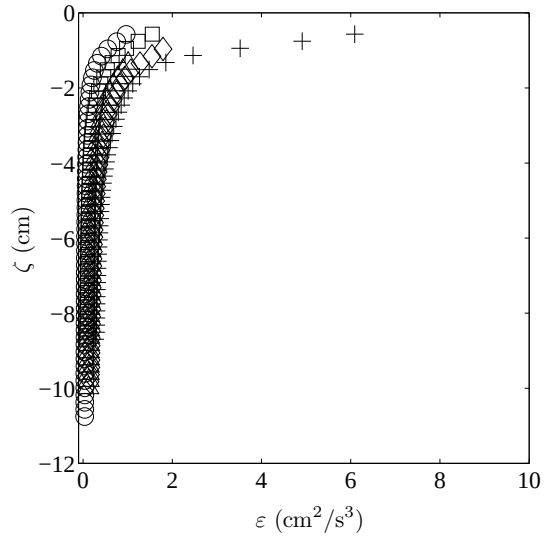

Figure 7.2: Vertical profiles of the rate of energy dissipation, ε, at a fetch of 8.8 m and for wind speed, U_z (m s^{-1}): ○,= 4.2; □,= 5.4; △,= 6.1; ◊,= 7.2; +,= 7.9. ζ is the wave following vertical coordinate referenced to the water surface. The values of ε at a given depth were time-averaged over 10-minutes and spatially averaged over the width of the DPIV field of view.

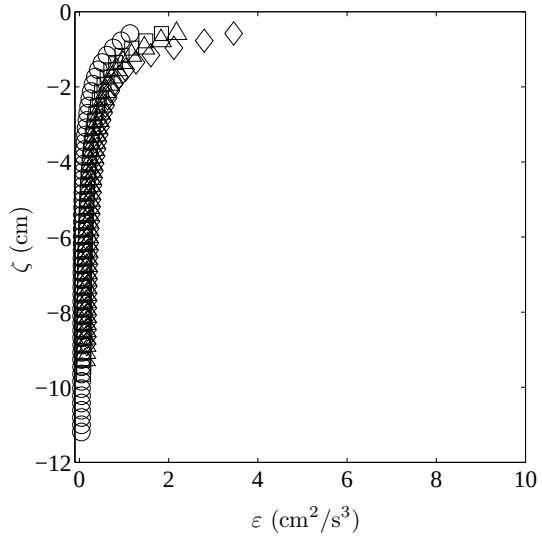

Figure 7.3: Vertical profiles of the rate of energy dissipation, ε, at a fetch of 12.4 m and for wind speed, U_z (m s^{-1}): ○,= 4.0; □,= 5.3; △,= 6.2; ◊,= 6.9. ζ is the wave following vertical coordinate referenced to the water surface. The values of ε at a given depth were time-averaged over 10-minutes and spatially averaged over the width of the DPIV field of view.

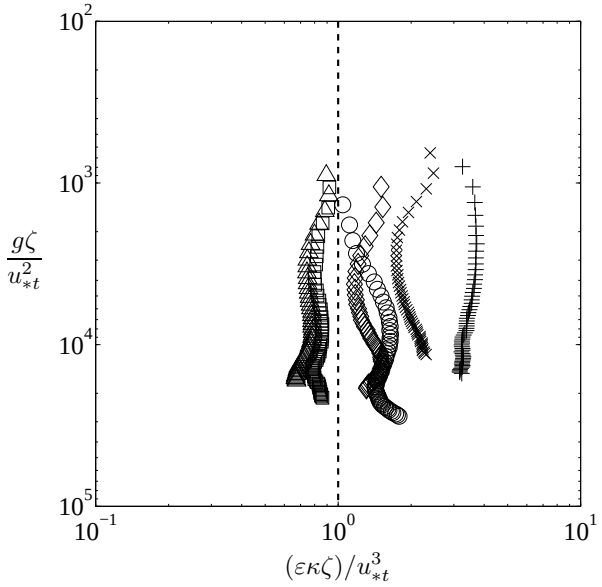

Figure 7.4: The normalized rate of energy dissipation, $(\varepsilon\kappa\zeta)/u_{*t}^3$ plotted versus the normalized depth, $g\zeta/u_{*t}^2$ at fetch of 4.8 m for wind speed, U_z (m s^{-1}): ○,= 4.1; □,= 5.3; △,= 6.1; ◊,= 6.8; +,= 7.9; ×,= 9.0. The dashed vertical line at $(\varepsilon\kappa\zeta)/u_{*t}^3 = 1$ shows the wall layer prediction.

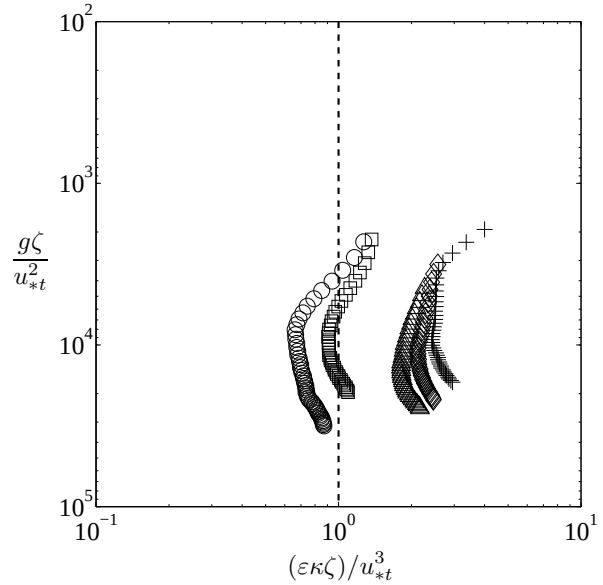

Figure 7.5: The normalized rate of energy dissipation, $(\varepsilon\kappa\zeta)/u_{*t}^3$ plotted versus the normalized depth, $g\zeta/u_{*t}^2$ at fetch of 8.8 m for wind speed, U_z (m s^{-1}): ○,= 4.2; □,= 5.4; △,= 6.1; ◊,= 7.2; +,= 7.9. The dashed vertical line at $(\varepsilon\kappa\zeta)/u_{*t}^3 = 1$ shows the wall layer prediction.

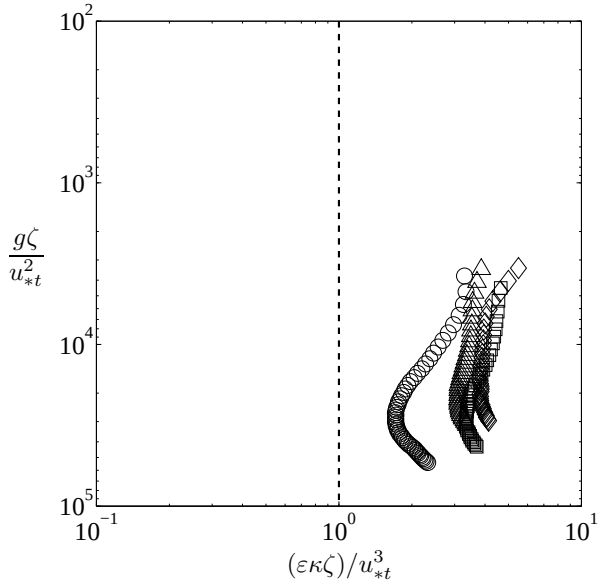

Figure 7.6: The normalized rate of energy dissipation, $(\varepsilon\kappa\zeta)/u_{*t}^3$ plotted versus the normalized depth, $g\zeta/u_{*t}^2$ at fetch of 12.4 m for wind speed, U_z (m s^{-1}): ○,= 4.0; □,= 5.3; △,= 6.2; ◊,= 6.9. The dashed vertical line at $(\varepsilon\kappa\zeta)/u_{*t}^3 = 1$ shows the wall layer prediction.

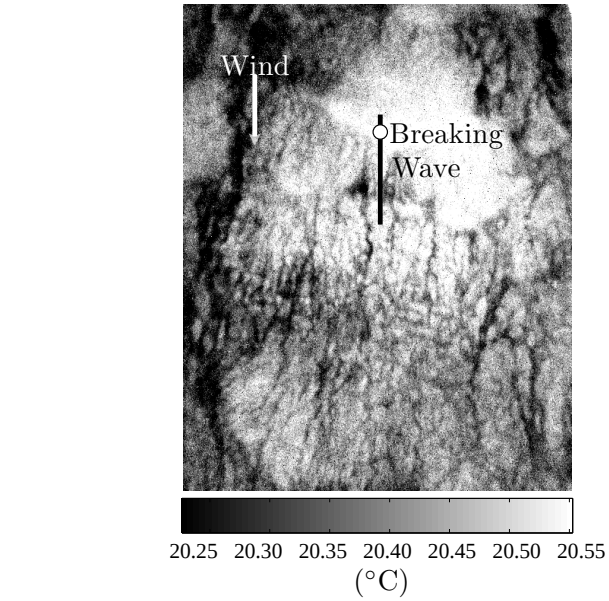

(a)

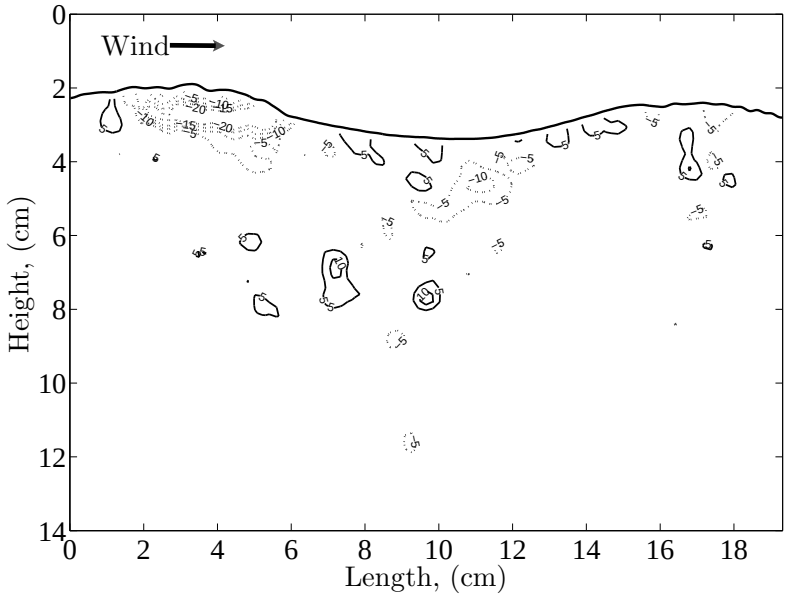

(b)

Figure 7.7: Plots of an IR image (top) and DPIV vorticity field (bottom) at a wind speed of 6.2 m s^{-1} and at a fetch 12.4 m. In (a), a microscale breaking wave entered into the DPIV field of view (marked by the solid black line) from the top. In (b), the same breaking wave entered into the DPIV field of view from the left. The solid contours corresponded to clockwise vorticity and dotted contours corresponded to counter-clockwise vorticity.

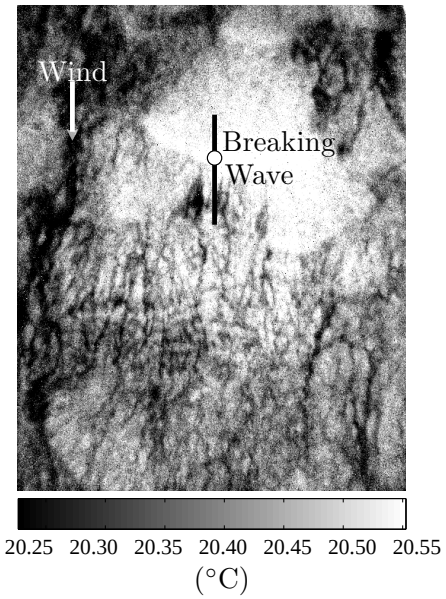

(a)

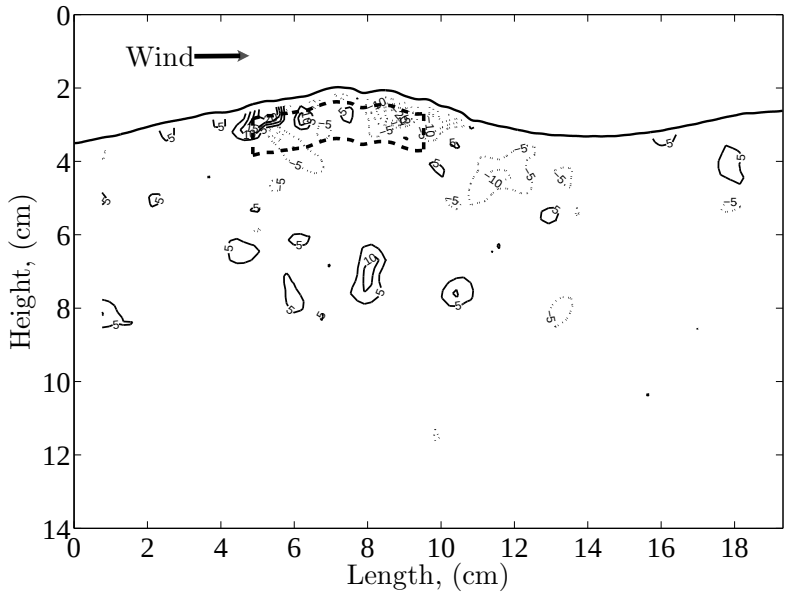

(b)

Figure 7.8: Plots of an IR image (top) and DPIV vorticity field (bottom) at a wind speed of 6.2 m s^{-1} and a fetch of 12.4 m. In (a), a microscale breaking wave was passing the middle half of the DPIV field of view (marked by a solid black line) from top. In (b), the same breaking wave was shown traveling towards the right and the region-of-interest was marked with a dotted box. Solid contours corresponded to clockwise vorticity and dotted contours corresponded to counter-clockwise vorticity.

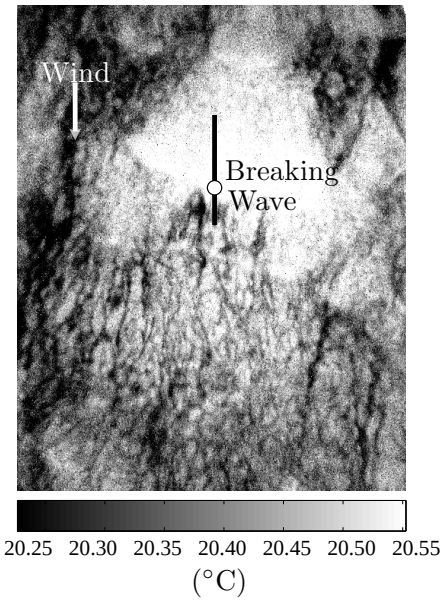

(a)

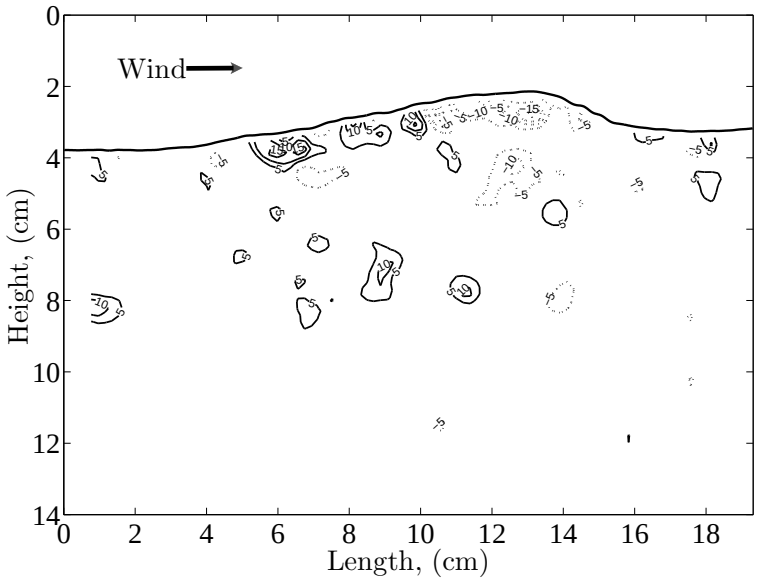

(b)

Figure 7.9: Plots of an IR image (top) and DPIV vorticity field (bottom) at a wind speed of 6.2 m s^{-1} and at a fetch of 12.4 m. In (a), a microscale breaking wave propagated to the end of the DPIV field of view (marked by the solid black line) from the top. In (b), the same wave was shown traveling to the right and solid contours corresponded to clockwise vorticity and dotted contours corresponded to counter-clockwise vorticity.

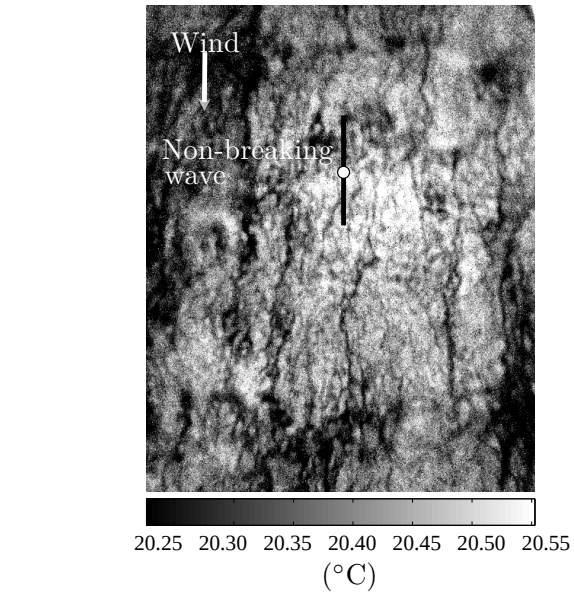

(a)

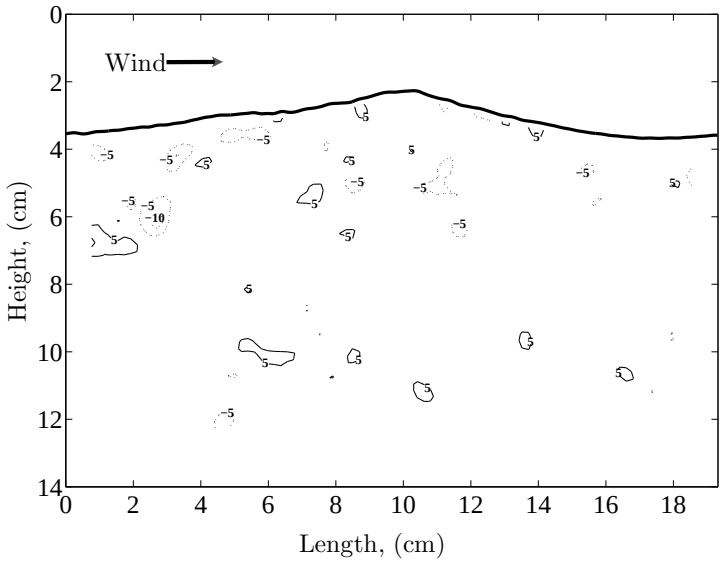

(b)

Figure 7.10: Plots of IR image (top) and DPIV vorticity field (bottom). In (a) a non-breaking wave was passing through the middle half of the DPIV field of view (marked by the solid black line) at a wind speed of 6.2 m s^{-1} and at a fetch of 12.4 m. In (b), the same wave was shown plotted where the solid contours corresponded to clockwise vorticity and dotted contours corresponded to counter-clockwise vorticity.

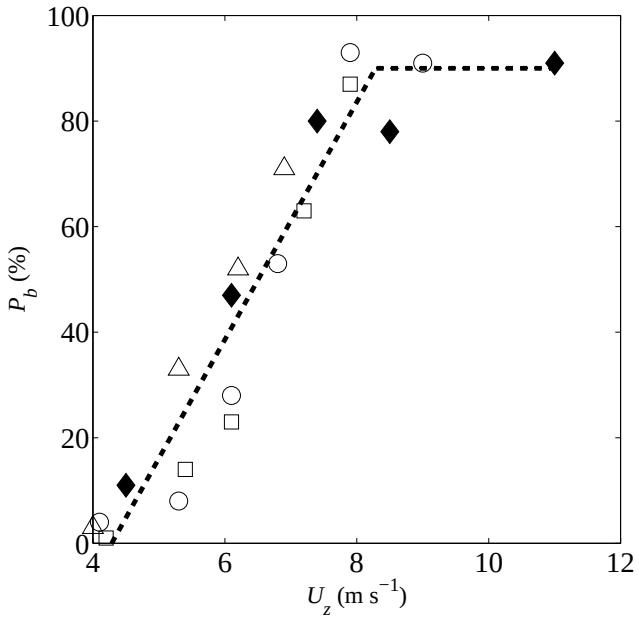

Figure 7.11: The percentage of microscale breaking waves (P_b) versus wind speed, U_z. Wave fetch, F: ○ = 4.8 (m); □ = 8.8 (m); △ = 12.4 (m); and ♦ = 5.5 (m) Siddiqui & Loewen (2007).

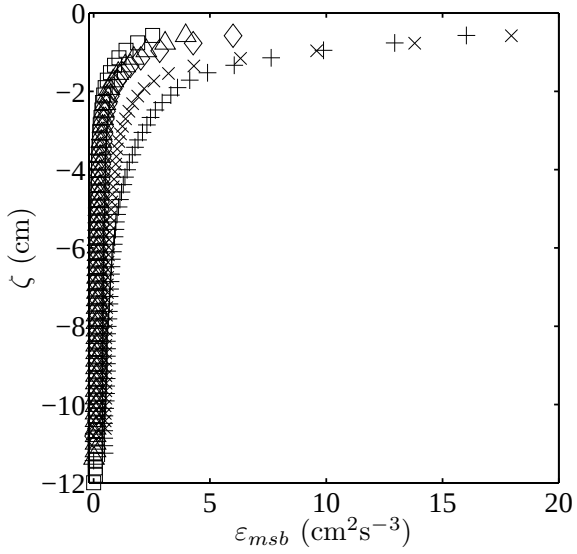

(a)

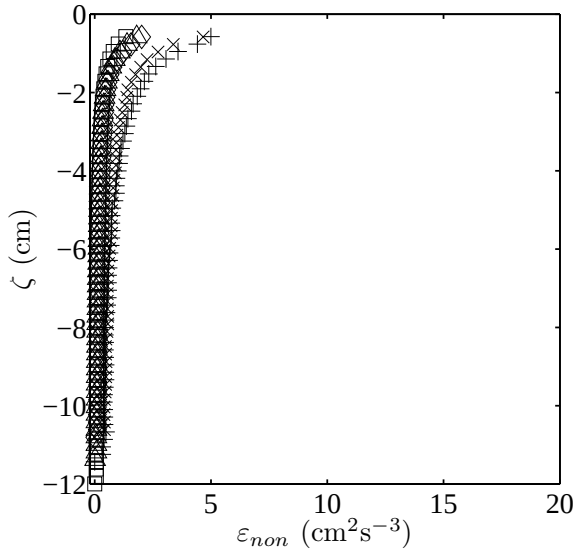

(b)

Figure 7.12: Vertical profiles of the rate of energy dissipation beneath (a) microscale breaking waves (ε_{msb}) and (b) non-breaking waves (ε_{non}) at a fetch of 4.8 m and for wind speed, U_z (m s^{-1}): □,= 5.3; △,= 6.1; ◊,= 6.8; +,= 7.9; ×,= 9.0. ζ is the wave following vertical coordinate referenced to the water surface. The values of energy dissipation rates at a given depth in both plots were ensemble-averaged beneath (a) microscale breaking waves, and (b) non-breaking waves and were spatially-averaged over the width of the DPIV field of view.

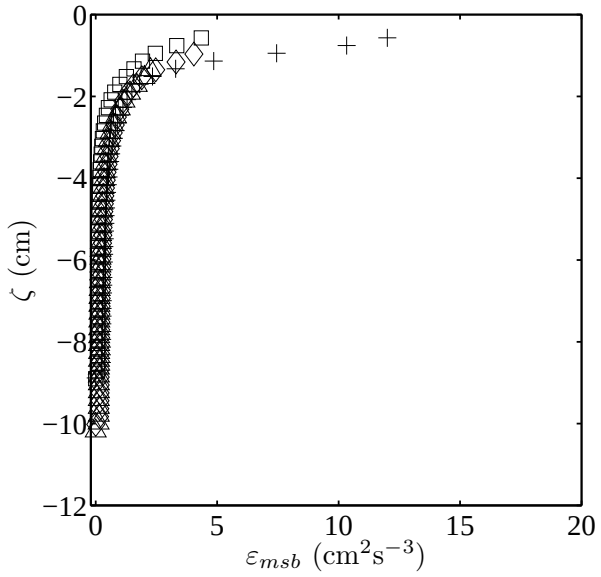

(a)

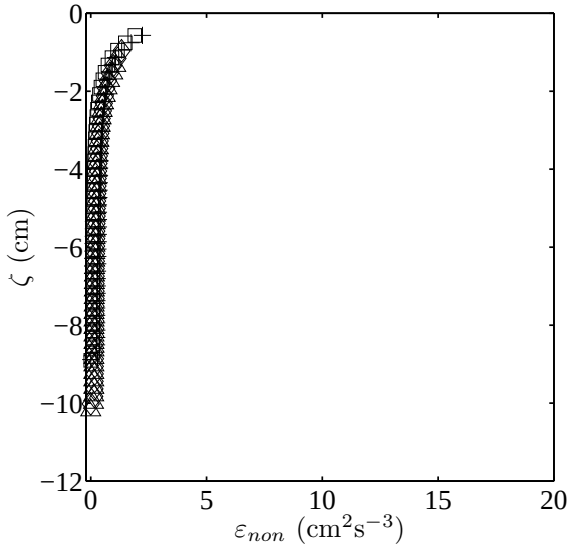

(b)

Figure 7.13: Vertical profiles of the rate of energy dissipation beneath (a) microscale breaking waves (ε_{msb}) and (b) non-breaking waves (ε_{non}) at a fetch of 8.8 m and for wind speed, U_z (m s^{-1}): □,= 5.4; △,= 6.1; ◊,= 7.2; +,= 7.9. ζ is the wave following vertical coordinate referenced to the water surface. The values of energy dissipation rates at a given depth in both plots were ensemble-averaged beneath (a) microscale breaking waves, and (b) non-breaking waves and were spatially-averaged over the width of the DPIV field of view.

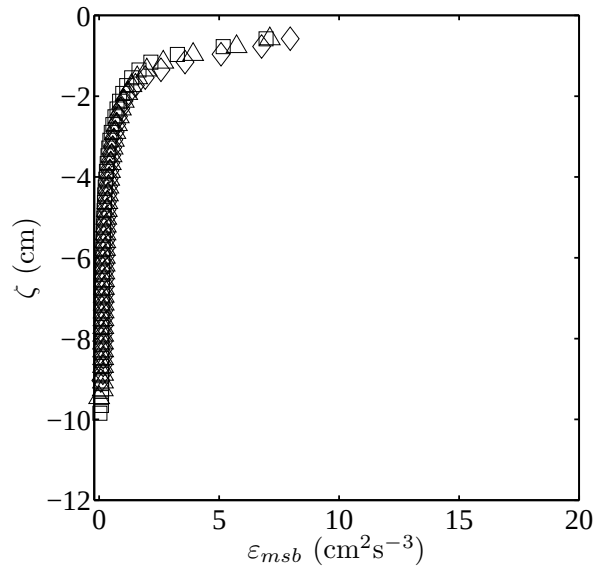

(a)

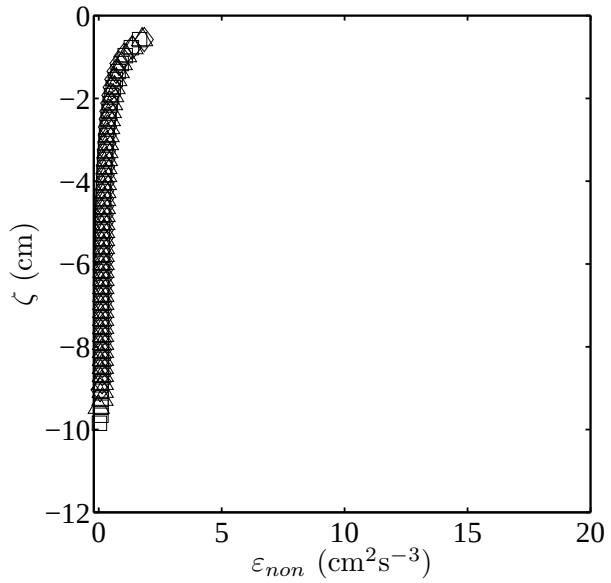

(b)

Figure 7.14: Vertical profiles of the rate of energy dissipation beneath (a) microscale breaking waves (ε_{msb}) and (b) non-breaking waves (ε_{non}) at a fetch of 12.4 m and for wind speed, U_z (m s^{-1}): □,= 5.3; △,= 6.2; ◊,= 6.9. ζ is the wave following vertical coordinate referenced to the water surface. The values of energy dissipation rates at a given depth in both plots were ensemble-averaged beneath (a) microscale breaking waves, and (b) non-breaking waves and were spatially-averaged over the width of the DPIV field of view.

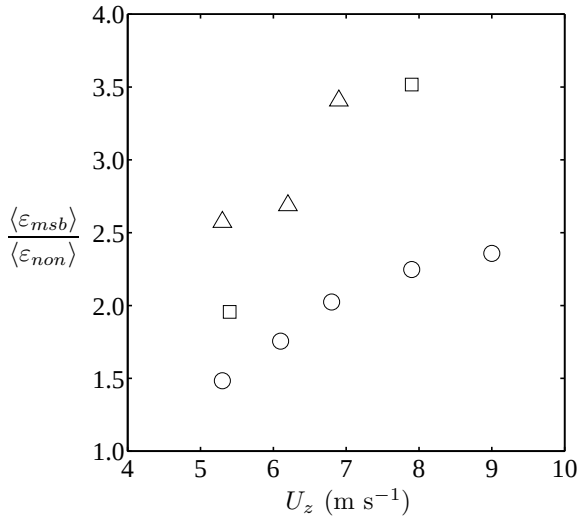

Figure 7.15: The ratio of energy dissipation rates, $\langle \varepsilon_{mab} \rangle / \langle \varepsilon_{non} \rangle$, versus wind speed, U_z, plotted at three fetches of 4.8 (○), 8.8 (□) and 12.4 m (△). $\langle \varepsilon_{msb} \rangle$ and $\langle \varepsilon_{non} \rangle$ were the average rates of energy dissipation beneath breaking and non-breaking waves, respectively. Dissipation rates were depth-averaged over the top 4 cm of the water column.

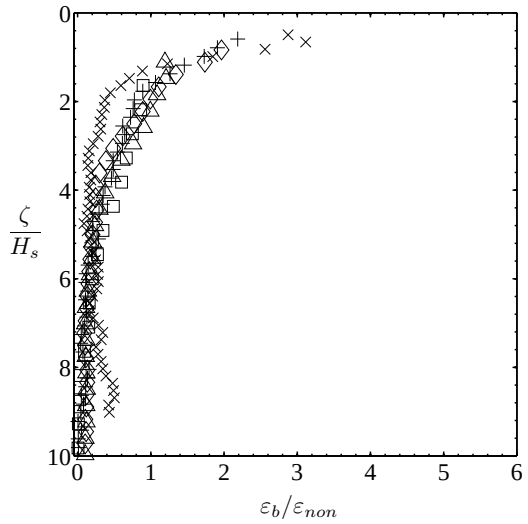

Figure 7.16: The ratio of the rate of energy dissipation, $\varepsilon_b/\varepsilon_{non}$, versus normalized depth, ζ/H_s, plotted at a fetch of 4.8 m and for wind speed, U_z (m s^{-1}): □,= 5.3; △,= 6.1; ◇,= 6.8; +,= 7.9; ×,= 9.0.

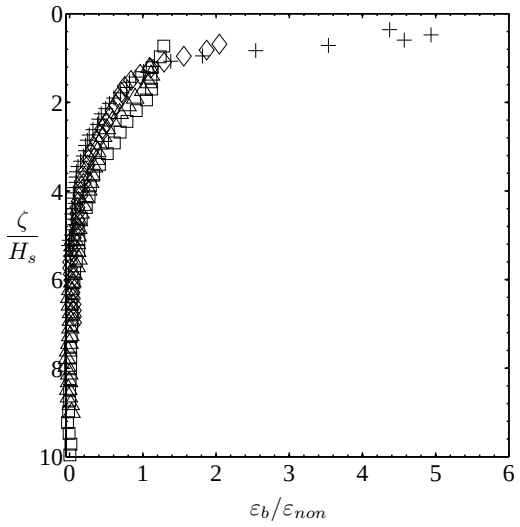

Figure 7.17: The ratio of the rate of energy dissipation, $\varepsilon_b/\varepsilon_{non}$, versus normalized depth, ζ/H_s, plotted at a fetch of 8.8 m and for wind speed, U_z (m s^{-1}): $\square$,= 5.4; $\triangle$,= 6.1; $\Diamond$,= 7.2; $+$,= 7.9.

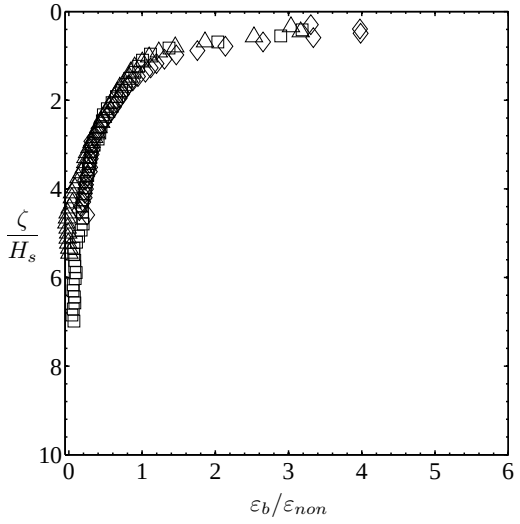

Figure 7.18: The ratio of the rate of energy dissipation, $\varepsilon_b/\varepsilon_{non}$, versus normalized depth, ζ/H_s, plotted at a fetch of 12.4 m and for wind speed, U_z (m s^{-1}): $\square$,= 5.3; $\triangle$,= 6.2; $\Diamond$,= 6.9.

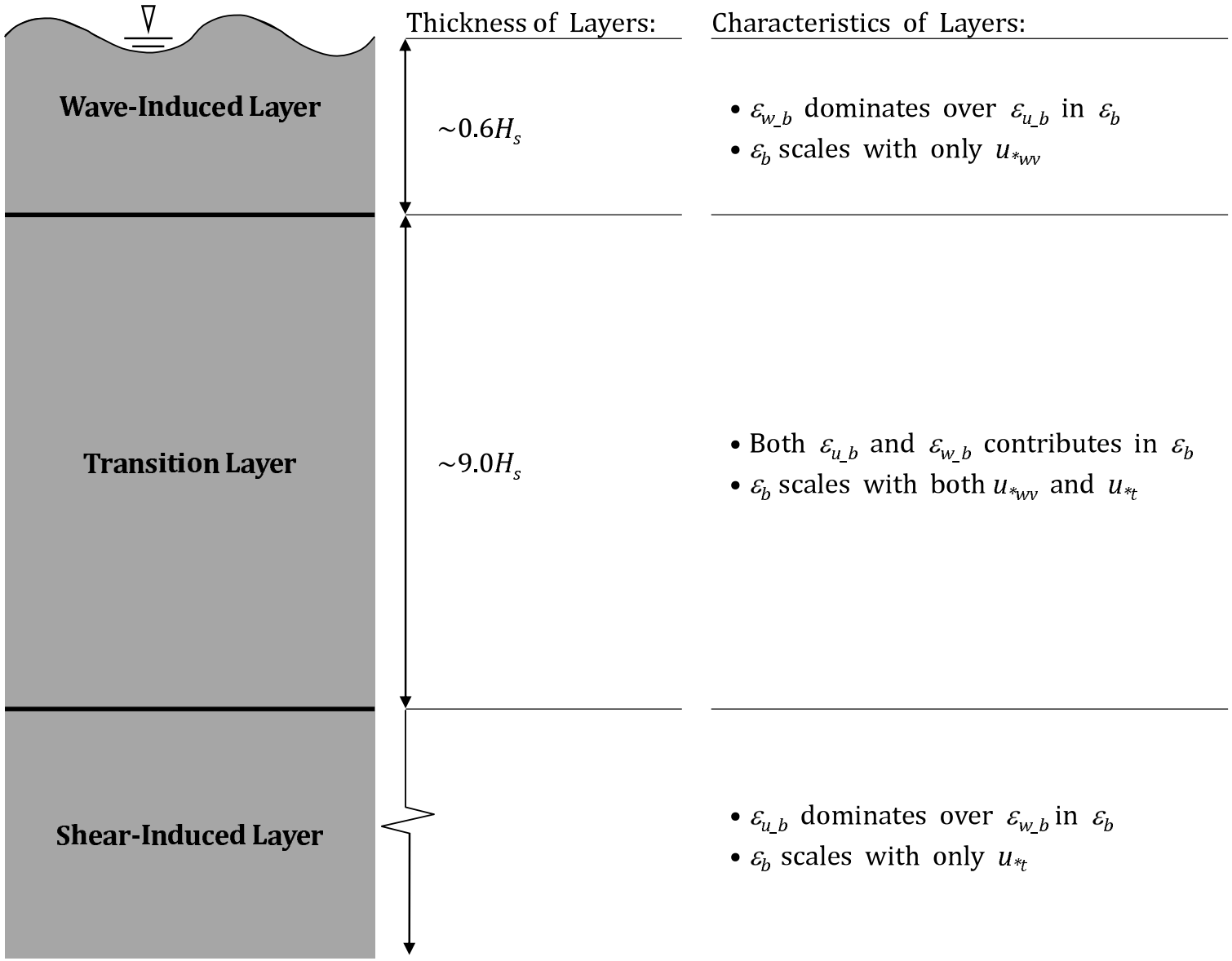

Figure 7.19: Schematic of the vertical distribution of dissipation rate.

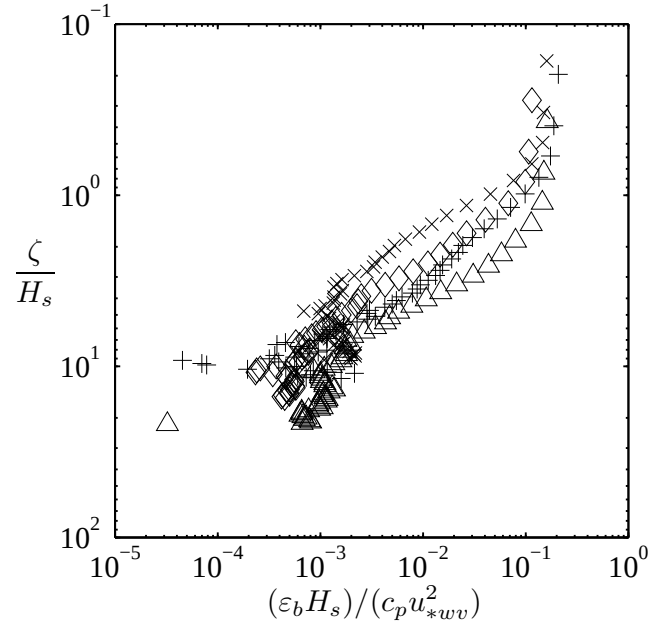

(a)

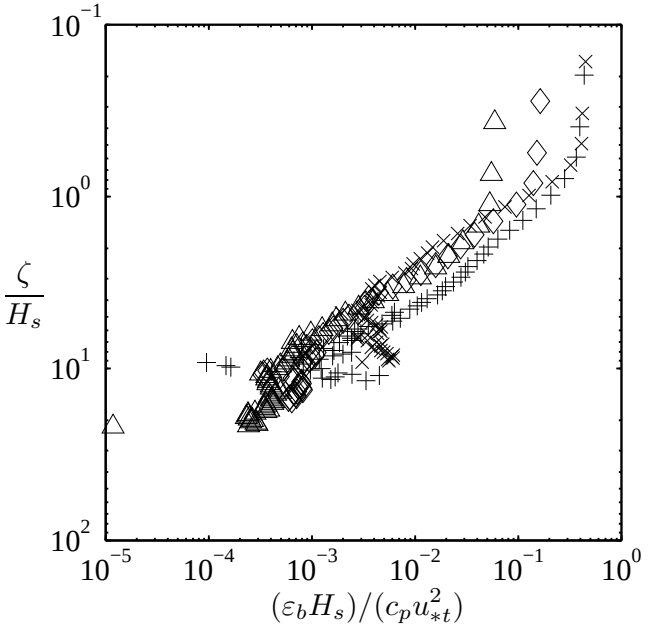

(b)

Figure 7.20: The normalized rate of energy dissipation, $(\varepsilon_b H_s)/F_w$, versus the normalized depth, ζ/H_s, at a fetch of 4.8 m plotted for four wind speeds, U_z (m s^{-1}): $\triangle$,= 6.1; $\Diamond$,= 6.8; $+$,= 7.9; $\times$,= 9.0, according to the scaling method of Terray *et al.* (1996) where, (a) F_w was estimated from u_{*wv} such that $F_w = c_p u_{*wv}^2$, and (b) F_w was estimated from u_{*t} such that $F_w = c_p u_{*t}^2$.

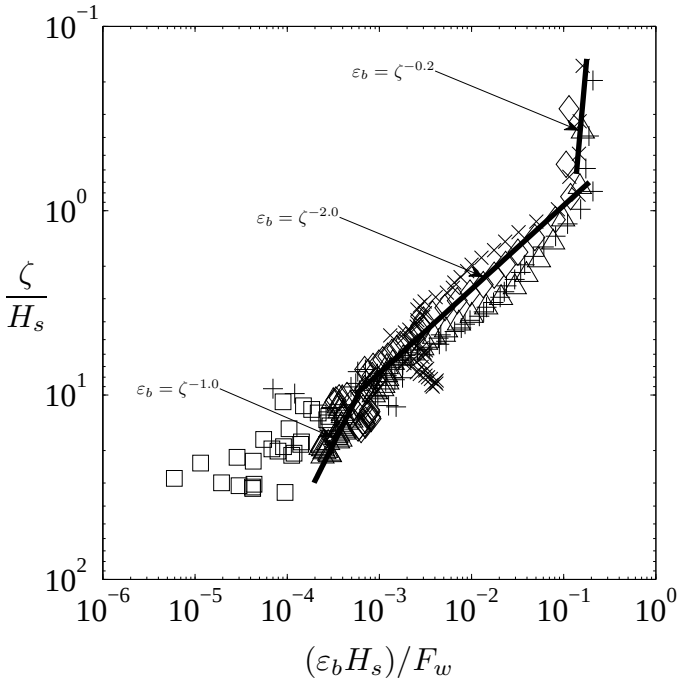

Figure 7.21: The normalized rate of energy dissipation, $(\varepsilon_b H_s)/F_w$, versus the normalized depth, ζ/H_s, plotted at a fetch of 4.8 m and at five wind speeds, U_z (m s^{-1}): $\square$,= 5.3; $\triangle$,= 6.1; $\Diamond$,= 6.8; $+$,= 7.9; $\times$,= 9.0, according to the scale model of Terray *et al.* (1996). For $\zeta/H_s < 0.6$, $F_w = c_p u_{*wv}^2$; for $0.6 < \zeta/H_s < 10$, $F_w = 0.5 c_p (u_{*wv}^2 + u_{*t}^2)$; and for $\zeta/H_s > 10$, $F_w = c_p u_{*t}^2$.

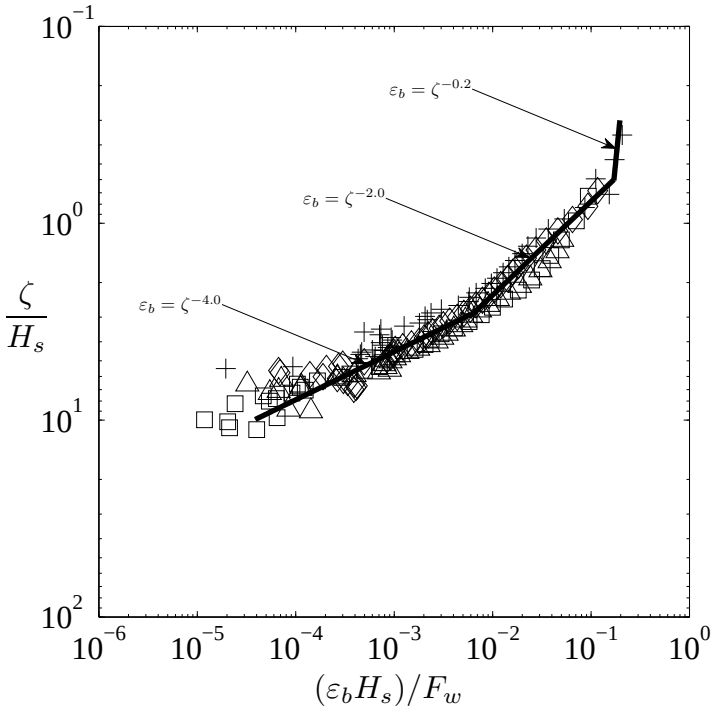

Figure 7.22: The normalized rate of energy dissipation, $(\varepsilon_b H_s)/F_w$, versus the normalized depth, ζ/H_s, plotted at a fetch of 8.8 m and at four wind speeds, U_z (m s^{-1}): □,= 5.4; △,= 6.1; ◊,= 7.2; +,= 7.9, according to the scale model of Terray *et al.* (1996). For $\zeta/H_s < 0.6$, $F_w = c_p u^2_{*wv}$; for $0.6 < \zeta/H_s < 10$, $F_w = 0.5 c_p (u^2_{*wv} + u^2_{*t})$; and for $\zeta/H_s > 10$, $F_w = c_p u^2_{*t}$.

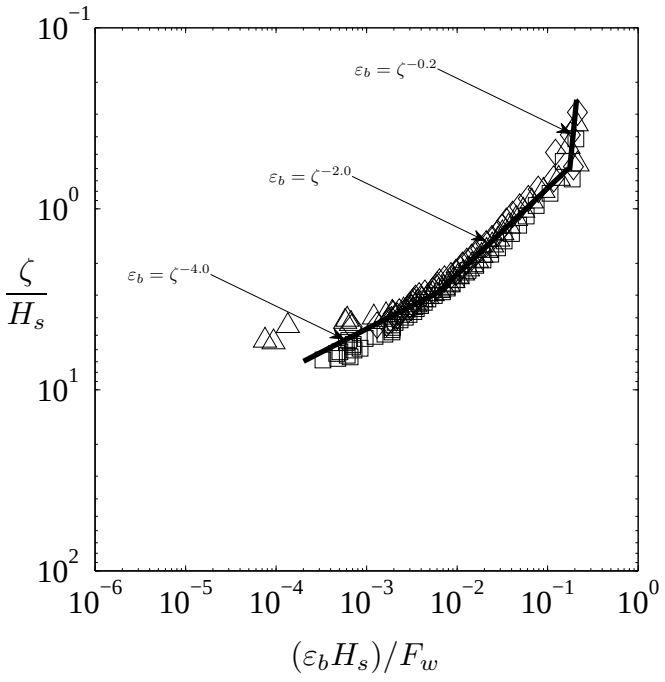

Figure 7.23: The normalized rate of energy dissipation, $(\varepsilon_b H_s)/F_w$, versus the normalized depth, ζ/H_s, plotted at a fetch of 12.4 m and at three wind speeds, U_z (m s^{-1}): $\square$,= 5.3; $\triangle$,= 6.2; $\Diamond$,= 6.9, according to the scale model of Terray *et al.* (1996). For $\zeta/H_s < 0.6$, $F_w = c_p u^2_{*wv}$; for $0.6 < \zeta/H_s < 10$, $F_w = 0.5 c_p (u^2_{*wv} + u^2_{*t})$; and for $\zeta/H_s > 10$, $F_w = c_p u^2_{*t}$.

Chapter 8

Dependence of Air-Water Gas Transfer on Short Wind Waves

8.1 Introduction

Gas transfer across the air-water interface is one of the important processes in the global climate system (Wanninkhof, 1992; Asher *et al.*, 1996). The prediction of net global carbon dioxide (CO_2) uptake by the ocean or the estimate of aeration in lakes and rivers are significantly uncertain (Takahashi *et al.*, 2002; Richey *et al.*, 2002). One reason for this uncertainty lies in the inaccuracy and difficulty in measuring gas fluxes directly in the field (Zappa *et al.*, 2007).

The flux, F_G, of a sparingly soluble, aqueous-phase controlled gas such as carbon dioxide (CO_2) can be parameterized as the product of a gas transfer rate, k_G, and a chemical potential gradient of the gas between the air and water, $\Delta\mu$, as follows,

$$F_G = k_G \Delta\mu \tag{8.1}$$

where, the gas transfer rate characterizes the kinetic rate of exchange across the air-water interface (Zappa *et al.*, 2004). It is common practice in the gas transfer literature to express gas flux as the product of its air-water concentration difference instead of the chemical potential gradient such that

(Wanninkhof, 1992; Zappa *et al.*, 2007),

$$F_G = k_G(C_w - sC_a) \tag{8.2}$$

where, s is the Ostwald solubility coefficient, and C_w and C_a are the gas concentrations in the bulk water and air near the interface, respectively. The accurate prediction of gas flux is generally limited by the accuracy in resolving the gas transfer rate, since, measurements of the concentration difference are straightforward (Zappa *et al.*, 2007).

Researchers have developed various empirical relationships for k_G to estimate gas flux using concentration difference. Wind forcing has long been known to significantly influence gas exchange in reservoirs, lakes and oceans. As a result, numerous empirical relationships between k_G and wind speed measured at 10-m height, U_{10} have been developed (Liss & Merlivat, 1986; Wanninkhof, 1992; Wanninkhof & McGillis, 1999; Nightingale *et al.*, 2000; McGillis *et al.*, 2001*a*; Frew *et al.*, 2004). Moreover, various other specific factors such as short wind waves (Jahne *et al.*, 1987; Bock *et al.*, 1999; Frew *et al.*, 2004), surfactants (Frew, 1997; Frew *et al.*, 2004), tidal currents (Zappa *et al.*, 2007) and rain (Zappa *et al.*, 2009) have been determined to influence gas transfer across the air-water interface.

A series of laboratory experiments were conducted in a large wind-wave-current research facility at three fetches of 4.8, 8.8 and 12.4 m. Simultaneous measurements were made of wind speed, wind friction velocity, surface wave slope, near-surface turbulence and gas transfer rate. These direct and simultaneous measurements facilitated direct comparison of various empirical relationships commonly used to parameterize gas transfer rate. It should be noted that this study was limited to a data set obtained at low to moderate wind conditions where wind speed varied from 4.0 to 9.6 m s^{-1}.

8.2 Literature Review

The prediction of gas fluxes in climate models rely on parameterizing the gas transfer rate based on the empirical relationship between the wind speed measured at 10 m height, U_{10}, and the gas transfer rate (Liss & Merlivat, 1986; Wanninkhof, 1992; Takahashi *et al.*, 2002). Liss & Merlivat (1986) developed an empirical relationship for k_G based on the experimental results of a deliberate tracer gas exchange experiment conducted by Wanninkhof *et al.* (1985) and wind wave tank experiments conducted by Broecker *et al.* (1978) and Broecker & Siems (1984). Their relationship consisted of three linear segments with breaks at $U_{10} = 3.6$ m s^{-1}, which was the onset of capillary waves and at $U_{10} = 13$ m s^{-1}, when breaking waves and bubble entrainment enhanced gas transfer. Wanninkhof (1992) found a quadratic wind speed dependent relationship for k_G based on the natural-^{14}C disequilibrium and the bomb-^{14}C inventory methods. He proposed the following relationship between the gas transfer rate and wind speed,

$$k_G = \alpha_1 U_{10}^2 \tag{8.3}$$

where, α_1 is a constant, and $\alpha_1 = 0.39$ when long-term averaged wind is used to estimate the long-term average transfer rate and $\alpha_1 = 0.31$ when short-term wind or steady wind similar to the wind in wind-wave tunnel experiments is used to parameterize gas transfer rate. The gas transfer rate is a function of the kinematic viscosity of the water, ν_w, and the diffusion coefficient of the gas in question, D (Wanninkhof, 1992). Therefore, the dependence of k_G on ν_w and D is expressed as the Schmidt number, $Sc = \nu_w/D$. Ledwell (1984) found that for an interface with waves k_G is proportional to $Sc^{-1/2}$. To include the Schmidt number dependency of gas transfer rate in Equation(8.3), the estimated gas transfer rates are multiplied with $(Sc/660)^{-0.5}$. Where, 660 is the Schmidt number of CO_2 in seawater at 20 °C, as compared to a Schmidt

number of CO_2 of 600 at 20°C in fresh water.

Although, the wind speed has been widely used to parameterize gas transfer rate because of its global availability, it was found to be a poor estimator of gas transfer rate in various environmental systems, specifically, when surfactants were present on the water surface (Bock *et al.*, 1999; Frew *et al.*, 2004) or when gas exchange was driven by tidal currents and rain (Zappa *et al.*, 2007, 2009). Bock *et al.* (1999) showed that the gas transfer rate decreased by as much as 80% at a given wind speed when a surfactant was introduced. Frew *et al.* (2004) found that gas transfer rates estimated using a quadratic relationship with wind speed over predicted the transfer rate in the presence of surfactants. Zappa *et al.* (2007) observed that the wind speed based parameterization of gas transfer rate accounted for only 7% of the observed variance in their measured data where other processes such as tidal currents and rain dominated the gas exchange process rather than wind.

Another wind related parameter, the wind friction velocity, u_{*a}, has been used to parameterize k_G. The gas transfer rate was found to correlate better with the wind friction velocity than with the wind speed, particularly when the water surface was contaminated by surfactants (Jahne *et al.*, 1987; Bock *et al.*, 1999). The reason for this improved correlation was that the wind friction velocity decreased in the presence of a surfactant whereas the wind speed remained unchanged. Jahne *et al.* (1987) carried out laboratory gas transfer measurements in two circular tunnels and in a large wind wave facility (Jahne *et al.*, 1985) using six different tracers. They argued that the gas transfer rate was related to the wind friction velocity since near-surface turbulence was driven by the momentum transfer across the interface produced by wind shear. They proposed that,

$$k_G = \beta^{-1} Sc^{-n} u_{*w} \tag{8.4}$$

where, u_{*w} is the wind friction velocity converted to water-side such that

$u_{*w} = \sqrt{\rho_a/\rho_w}u_{*a}$, in which, ρ_a and ρ_w are the density of air and water, respectively. The constant, β, is a dimensionless transfer resistance for momentum transfer across the water-side viscous boundary layer (Jahne *et al.*, 1987). The Schmidt number exponent n varies between 1/2 (clean wavy surface) and 2/3 (highly contaminated surface or rigid wall) depending on the surface boundary conditions of the subsurface turbulence (Jahne *et al.*, 1987). Jahne *et al.* (1987) found that $\beta = 8.9$ and $n = 1/2$ for a clean wavy surface based on experiments in wind wave tanks. Munnich & Flothmann (1975) also developed an expression for a free wavy surface similar to Equation(8.4) based on a surface renewal model (Danckwerts, 1970) and predicted that $\beta = 16$ and $n = 1/2$.

A wave related parameterization such as the total mean square slope of short wind waves, $\langle S^2 \rangle$, was found to correlate better with k_G than wind speed or wind friction velocity. Jahne *et al.* (1984) first suggested that $\langle S^2 \rangle$ should correlate strongly with the gas transfer rate. This conclusion was based on experimental measurements made in three wind wave tanks. Hara *et al.* (1995) reported gas exchange measurements from a set of experiments conducted in two annular laboratory wind wave tanks. They found that k_G increased linearly with $\langle S^2 \rangle$ in both experiments and concluded that the enhancement of k_G was related to the small-scale waves. Bock *et al.* (1999) observed that the total mean square slope showed a reasonable linear correlation with the gas transfer rate regardless of the surface boundary condition, consistent with Jahne *et al.* (1987) and Hara *et al.* (1995). Bock *et al.* (1999) also observed that the mean square slope of very short wind waves (wavenumber range greater than 200 rad m^{-1}) correlated better with k_G than the mean square slope of larger waves (wavenumber range less than 200 rad m^{-1}). Frew *et al.* (2004) investigated the influence of wind speed, wind friction velocity and mean square slope of small-scale waves on k_G at wind speeds less than 10 m s^{-1}.

Their gas transfer rates were extrapolated from water-side heat transfer rates derived from infrared imagery, direct covariance and bulk heat flux estimates. They found that their estimates of k_G followed a quadratic relationship with U_{10} and explained approximately 75 to 77% of the observed variance with respect to wind. However, they found considerable scatter and a non-linear dependence of gas transfer rate on wind friction velocity. In contrast, they observed that gas transfer rate varied linearly with mean square slope obtained over a wavenumber range of 40 to 800 rad m^{-1}. Frew *et al.* (2004) proposed the following empirical relationship between k_G and $\langle S^2 \rangle$,

$$k_G = \alpha_2 + \alpha_3 \langle S^2 \rangle \tag{8.5}$$

where, α_2 and α_3 constants equal to 1.1 and 7.3E02, respectively. The Schmidt number dependency of gas transfer rate could be included in the above equation by multiplying the estimated gas transfer rate by $(Sc/660)^{-0.5}$ since they made gas transfer measurements in coastal and offshore seawaters. Frew *et al.* (2004) concluded that the mean square slope could be a better candidate to parameterize k_G compared to U_{10} or u_{*a} since it explained approximately 89 to 95% of the observed variance in k_G and did not over predict k_G in the presence of surfactants.

Bock *et al.* (1999) suggested that turbulence unrelated to wind or surface waves might also be important for gas exchange. Zappa *et al.* (2007, 2009) showed that tidal currents and rain generated near-surface turbulence regulated gas exchange even in the absence of wind. Hence, U_{10}, u_{*a} or $\langle S^2 \rangle$ could not be used alone to parameterize k_G in these environmental systems. Alternatively, near-surface turbulence in the water-side boundary layer (WBL) was demonstrated to regulate gas transfer rate across the air-water interface in a wide variety of environmental systems such as wind, waves, tidal currents and rain.

Turbulent kinetic energy (TKE) dissipation rate, ε was first proposed by Lamont & Scott (1970) as a suitable turbulence driven scaling parameter based on surface renewal theory to parameterize k_G since ε is a direct measure of the strength of turbulence in the WBL. An empirical relationship to parameterize gas transfer rate was proposed as follows,

$$k_G = \alpha_4(\varepsilon\nu_w)^{1/4}Sc^{-n} \tag{8.6}$$

where, α_4 is a constant. Kitaigorodskii (1984) put forward a boundary layer model considering the vertical structure of three-dimensional turbulence in turbulent patches, generated by wave breaking and derived the same expression. Recently, this relationship was also suggested by Lorke & Peeters (2006) as a unified relationship for interfacial fluxes at both the benthic and air-water boundary layers. They derived this relationship using dimensional arguments based on mass diffusion across a layer of the thickness of the Batchelor (1959) scale $\delta_B = Sc^{-1/2}\eta$, where $\eta = (\nu_w^3/\varepsilon)^{1/4}$ is the Kolmogorov, or dissipative, microscale. This scaling had been tested successfully in laboratory grid-mixing tanks for varying surface conditions (Dickey *et al.*, 1984) and was also found to work in a variety of environmental systems such as tidal currents and rain (Zappa *et al.*, 2007, 2009). The constant of proportionality was found to vary between ∼0.2 (Calderbank & Moo-Young, 1961; Kitaigorodskii, 1984; Lorke & Peeters, 2006) and ∼0.4 (Lamont & Scott, 1970; Zappa *et al.*, 2007, 2009).

8.3 Results

The digital particle image velocimetry (DPIV) measurements were made at three fetches of 4.8, 8.8 and 12.4 m, and at wind speed varying from 4.0 to 9.6 m s^{-1}. The measured wind speeds were referenced to 10-m height (i.e. U_{10}) using a method proposed by Smith (1988) and U_{10} was found to vary from 5.3

to 13.7 m s^{-1}. The wind friction velocity for each experiment was estimated using a widely used velocity profile method that was described in Chapter 5 (see §5.4.3 on page 113).

It should be noted that 4.8 and 8.8 m fetches were established by covering 7.6 and 3.6 m length of the open water surface, respectively on the upwind end of the tank with bubble wrap similar to Jahne *et al.* (1989). The PIV and other instruments were always kept at a fetch of 12.4 m. The total length of the tank was 18.29 m, therefore, the length of the open water surface was 10.69, 14.69 and 18.29 m for three fetches of 4.8, 8.8 and 12.4 m, respectively during the gas transfer measurements. The tank-averaged or bulk gas transfer rates were measured by applying a conservative mass balance method using Helium (^3He) and Sulfur Hexafluoride (SF_6) as dual tracers for CO_2. The details of the method can be found in Asher *et al.* (1996) and Zappa *et al.* (2004). Accuracy of the gas transfer measurement for each experiment was determined based on the standard deviation of the gas transfer rate obtained from three sampling stations and presented in Table 8.1. The gas transfer measurements were found to be repeatable with a standard error of the mean of 0.7 cm hr^{-1}. All gas transfer measurements were performed in bulk fresh water that had been skimmed to create a clean water surface. The rates were scaled to a Schmidt number of 600 ($Sc = 600$ for CO_2 in freshwater at 20 °C) using the following relationship,

$$k_{600} = k_G \left(\frac{600}{Sc} \right)^{-n} \tag{8.7}$$

The Schmidt number exponent, n, for each experiment was determined using dual tracers, ^3He and SF_6 as outlined below,

$$n = \frac{\ln(k_{G1}/k_{G2})}{\ln(Sc_2/Sc_1)} \tag{8.8}$$

where, the subscripts 1 and 2 correspond to ^3He and SF_6, respectively. The Schmidt number exponent, n, was found to vary between 0.34 and 0.55 in

this study. These results are consistent with previous studies. For example, Wanninkhof & Bliven (1991) investigated the relationship between air-water gas transfer velocities with wind speed, friction velocity, and radar backscatter from the surface in a large wind-wave tank. The exchange rates of dual tracers, sulfur hexafluoride and nitrous oxide, were measured at wind speeds ranging from 3.5 m s^{-1} to 20 m s^{-1}. They found that the Schmidt number exponent, n, varied between 0.30 and 0.70 for wind speed less than 10 m s^{-1}, and between 0.12 and 0.40 for wind speeds greater than 10 m s^{-1}.

Estimates of turbulent kinetic energy dissipation rates were made using the 'direct' method (Doron *et al.*, 2001) that was described in Chapter 6 (see §6.6 on page 173). Table 8.1 lists the measurements used in this study.

8.3.1 Dependence of Gas Transfer Rate on Wind Speed and Fetch

In Figure 8.1, estimates of k_{600} are plotted as a function of wind speed, U_{10}, for three fetches. At a fetch of 4.8 m, k_{600} increased from 8.8 to 21.1 cm hr^{-1} as U_{10} increased from 6.1 to 13.7 m s^{-1}. At a fetch of 8.8 m, k_{600} increased from 6.2 to 24.9 cm hr^{-1} as U_{10} increased from 5.8 to 13.7 m s^{-1}. At a fetch of 12.4 m, k_{600} increased from 7.7 to 32.1 cm hr^{-1} as U_{10} increased from 5.3 to 13.3 m s^{-1}. It was found that k_{600} increased at all fetches with U_{10}.

The dependency of gas transfer rate on fetch was not apparent from Figure 8.1. It can be argued that the gas transfer rate increased with fetch at the highest wind speed, although, the fetch dependency of gas transfer rate was not pronounced at the lower wind speeds. Jahne *et al.* (1989) made gas transfer measurements at four fetches varying from 2 to 8 m to investigate the fetch dependency of gas transfer rate. They argued that fetch dependency of gas transfer rate was associated with wave field development since they observed that the gas transfer rate at two lower wind speeds of 4.2 and 5.6

m s^{-1} increased 34% as the fetch increased from 2 to 8 m. While, the gas transfer rates were almost constant at a highest wind speed of 7.7 m s^{-1} at all four fetches. Wanninkhof & Bliven (1991) made gas transfer measurements in a large wind-wave tank for U_{10} ranging from 3.5 to 20 m s^{-1}. They argued that the gas transfer rate increased with fetch since they observed a fetch dependence on gas transfer rate at intermediate and high wind speeds.

Several empirical relationships proposed by the researchers between the gas transfer rate and U_{10} are also plotted in Figure 8.1 for comparison purpose. Figure 8.1 shows that the majority of the estimates of k_{600} lied outside the envelope defined by the empirical relationships. It is evident from Figure 8.1 that the majority of the estimated gas transfer rates were significantly over predicted by the empirical relationships. However, it was not surprising to observe a weaker dependence of gas transfer rate on wind speed since U_{10} affects k_{600} only indirectly. Wanninkhof (1992) argued that the gas transfer rate might exhibit weaker dependence on wind speed if wind speeds were obtained in a fetch-limited system similar to a linear wind-wave tank used in this study

8.3.2 Dependence of Gas Transfer Rate on Wind Friction Velocity

In Figure 8.2, estimates of k_{600} are plotted as a function of u_{*w} and compared to Equation(8.4) using the proportionality factors proposed by Munnich & Flothmann (1975) and Jahne *et al.* (1987). Figure 8.2 shows that k_{600} increased with u_{*w} at all three fetches. It was evident from Figure 8.2 that the observed data collapsed within the envelope defined by both the empirical relationships. The empirical relationship proposed by Jahne *et al.* (1987) was found to be the upper bound, while, the empirical relationship proposed by Munnich & Flothmann (1975) was found to be the lower bound for the gas transfer

measurements made in this study.

8.3.3 Dependence of Gas Transfer Rate on Wave Slope

In Figure 8.3, estimates of k_{600} are plotted versus the total mean square wave slope, $\langle S^2 \rangle$, from this study as well as from previous studies. Note that in this study the total mean square wave slopes were computed over all wavenumbers. Table 8.1 lists the dominant wavenumber for each experiment. Figure 8.3 shows that k_{600} increased with $\langle S^2 \rangle$ at all three fetches. It was evident from this study that the gas transfer rates collapsed well at all three fetches with the total mean square slope. Bock *et al.* (1999) and Frew *et al.* (2004) argued that larger waves (wavenumber less than 50 rad m^{-1}) were not directly related to the gas transfer process since they observed a poor correlation between the mean square slope of these larger waves and the gas transfer rate. They concluded that the gas transfer rate correlated better with the slope of shorter waves (wavenumber range of 200 to 800 rad m^{-1}) than the slope of medium waves (wavenumber range of 50 to 200 rad m^{-1}). Bock *et al.* (1999) argued that the gas transfer rate exhibited a weaker dependence on the mean square slope of relatively longer surface waves since laboratory wave fields over the wavenumber range of 50 to 200 rad m^{-1} were strongly influenced by the tank geometry.

The measurements made by Bock *et al.* (1999) in a large circular tank and the empirical relationship proposed by Frew *et al.* (2004) using field data are also plotted in Figure 8.3 for comparison purpose. The differences observed between the measurements made by Bock *et al.* (1999) and this study, and the empirical relationship proposed by Frew *et al.* (2004) and this study were mainly due to the differences in magnitude of mean square wave slopes. The empirical relationship proposed by Frew *et al.* (2004) was derived based on the mean square wave slope varying up to 0.025 computed over a wavenumber

range from 40 to 800 rad m^{-1}. Moreover, their data included measurements mostly from the surfactant-influenced seawater. Whereas, estimates of gas transfer rate in this study were obtained for clean wavy water surface with a total mean square wave slope varying from 0.029 to 0.092. In addition, the difference between the measurements made by Bock *et al.* (1999) and this study could be attributed to the fact that Bock *et al.* (1999) made measurements in a large circular wave tank mostly beneath surfactant-influenced water surface and the measurements in this study were made in a fetch-limited linear wind-wave-current research facility beneath clean water surface. The wave fields in the circular tanks were significantly different from those in the linear wind-wave tank due to the absence of narrow-banded fetch limited gravity waves in a circular tank.

8.3.4 Dependence of Gas Transfer Rate on Near-Surface Turbulence

Although, the gas exchange had long been speculated to be controlled by the near-surface turbulence generated by wind, waves and other forcing (Lamont & Scott, 1970; Kitaigorodskii, 1984; Jahne *et al.*, 1987; Bock *et al.*, 1999; Frew *et al.*, 2004), only limited observational evidence supported this hypothesis (Dickey *et al.*, 1984; Zappa *et al.*, 2007, 2009). In Figure 8.4, estimates of k_{600} are plotted as a function of ε_o, where, ε_o is the turbulent kinetic energy dissipation rate estimated 6 mm below the interface within the WBL. Figure 8.4 shows that the gas transfer rate correlated reasonably well with ε_o over a range of wind speeds and fetches. The empirical relationships as determined by Equation(8.6) using constants of 0.2 and 0.4 are also plotted in Figure 8.4 for comparison. Figure 8.4 shows that the majority of the gas transfer measurements fell within the envelope defined by the empirical relationships.

8.4 Discussion

Figure 8.5 shows measured k_{600} versus predicted gas transfer rates determined using a quadratic relationship with wind speed similar to Wanninkhof (1992). The proportionality factor, α_1 in Equation(8.3) was found to be 0.15. This factor was determined by minimizing the root mean square difference ($\pm$ 4.2 cm hr^{-1}) between the measured gas transfer rates and the right-hand side of Equation(8.3). Wanninkhof (1992) found a proportionality factor of 0.31 when short-term wind or steady wind similar to the wind in wind-wave tunnel experiments was used to estimate gas transfer rate. The coefficient of determination between the measured and modeled gas transfer rates was found to be 0.78.

Figure 8.6 shows the same measured k_{600} versus predicted gas transfer rates determined using Equation(8.4) similar to Munnich & Flothmann (1975) and Jahne *et al.* (1987). The proportionality factor, β, in Equation(8.4) was found to be 10.6. This factor was determined by minimizing the root mean square difference ($\pm$ 3.2 cm hr^{-1}) between the measured gas transfer rates and the right-hand side of Equation(8.4). The proportionality factor estimated in this study was found to be within the range proposed by Jahne *et al.* (1987) and Munnich & Flothmann (1975). The coefficient of determination between the measured and modeled gas transfer rates was found to be 0.79.

Figure 8.7 shows the same measured k_{600} versus predicted gas transfer rates determined using Equation(8.5) similar to Frew *et al.* (2004). The proportionality factors α_2 and α_3 in Equation(8.5) were found to be -4.675 and 397.97, respectively. These factors were determined by minimizing the root mean square difference ($\pm$ 2.0 cm hr^{-1}) between the measured gas transfer rates and the right-hand side of Equation(8.5). The coefficient of determination between the measured and modeled gas transfer rates was found

to be 0.92.

Figures 8.8 and 8.9 show the same measured k_{600} versus predicted gas transfer rates determined using Equation(8.6) with ε_o estimated at a depth of 6 mm below the surface and $\langle \varepsilon_o \rangle$ averaged over a depth of 4 cm in the water column, respectively. The constant, α_4, in Equation(8.6) was found to be 0.24 and 0.33. These factors were determined by minimizing the root mean square difference ($\pm$ 2.9 cm hr^{-1} for both cases) between the measured gas transfer rates and the right-hand side of Equation(8.6). Therefore, either ε_o or $\langle \varepsilon_o \rangle$ could be used as a turbulence driven parameter to parameterize the gas transfer rate. One conclusion from this analysis was that α_4 increased from 0.24 to 0.33 since the magnitudes of $\langle \varepsilon_o \rangle$ were much smaller than the near surface values of ε_o. These values were within the range proposed in several previous studies. Kitaigorodskii (1984) used near-surface dissipation rates obtained from the laboratory experiments of Dickey *et al.* (1984) and found $\alpha_4 = 0.17$. Zappa *et al.* (2007) used dissipation rates measured at variable depths (depth varied from 0.1 m to 3 m) from the surface and estimated that $\alpha_4 = 0.42$. The coefficients of determination between the measured and modeled gas transfer rates using surface dissipation and average dissipation were found to be equal to 0.76 and 0.75, respectively.

It was clear from above discussion that the slope is the best parameterization since 92% of the variance was explained. The other four parameterizations worked equally well since they explained 75% to 79% of the variance. It was very surprising to observe that the wind speed parameterization explained 78% of the variance because this value is much higher than what other researchers have found in the field. The primary explanation for the high value (78%) was that in this wind wave tank study only a small subset of the parameters were investigated that were known to influence gas transfer. So, under these idealized conditions the wind speed

parameterization looked promising, although it did not work well in the field. The same argument can also be made about the slope parameterization that it only worked well in wind wave tanks. However, other studies (e.g. Jahne *et al.* (1987), Bock *et al.* (1999) and Frew *et al.* (2004)) also supported our finding that slope parameterization works well.

8.5 Conclusions

A series of laboratory experiments were conducted where gas transfer measurements of a sparingly soluble, aqueous-phased controlled, non-reactive gas were made using dual tracers for low to moderate wind speeds at three fetches of 4.8, 8.8 and 12.4 m beneath clean water surface. Simultaneous measurements of wind speed, wind friction velocity, surface wave slope, surface wave driven near-surface turbulence and gas transfer rate facilitated the investigation of several empirical relationships commonly used in the gas transfer literature to parameterize gas transfer rates.

Comparison of four empirical relationships revealed that slope is the best parameterization since 92% of the variance was explained. The gas transfer rate was found to vary linearly with total mean square wave slope and correlated better than the other three parameterizations. This finding is similar to the results of Jahne *et al.* (1987), Bock *et al.* (1999) and Frew *et al.* (2004). However, wind speed, wind friction velocity, and energy dissipation based parameterizations of the gas transfer rate were also performed reasonably well since they explained 75% to 79% of the variance, respectively.

F (m)	k_{600} (cm hr^{-1})	U_z (m s^{-1})	U_{10} (m s^{-1})	u_{*a} (cm s^{-1})	$\langle S^2 \rangle$	k_d (rad m^{-1})	ε_o (cm^2 s^{-3})	$\langle \varepsilon_o \rangle$ (cm^2 s^{-3})
4.8	8.8±1.0	5.3	6.1	19.7	0.039	112	1.53	0.42
	11.3±0.3	6.1	7.9	26.8	0.046	87	1.95	0.55
	14.0±0.7	6.8	9.3	33.0	0.047	73	2.56	0.69
	19.1±2.3	7.9	11.6	42.8	0.054	58	8.48	2.97
	21.1±1.0	9.0	13.7	52.6	0.060	50	8.41	2.16
8.8	6.2±1.5	4.2	5.8	18.4	0.029	90	0.97	0.22
	11.1±0.7	5.4	8.7	30.2	0.044	63	1.55	0.42
	20.2±0.8	7.9	12.0	44.9	0.061	38	6.09	1.36
	24.9±2.3	9.6	13.7	52.8	0.078	33	-	-
12.4	7.7±1.5	4.0	5.3	16.7	0.033	53	1.13	0.33
	13.8±0.7	5.3	8.1	27.9	0.041	38	1.84	0.57
	19.2±2.2	6.2	8.6	30.1	0.048	34	2.18	0.71
	15.2±0.4	6.9	9.8	35.0	0.056	32	3.46	0.92
	22.4±1.0	7.9	10.3	37.2	0.070	28	-	-
	32.1±0.9	9.2	13.3	50.6	0.092	27	-	-

Table 8.1: Summary of experimental measurements made on three fetches (F) of 4.8, 8.8 and 12.4 m. k_{600}, gas transfer rate referenced to $Sc = 600$; U_z, wind speed in the wave tank; U_{10}, wind speed referenced to 10-m height; u_{*a}, wind friction velocity; $\langle S^2 \rangle$, the mean square wave slope (total); k_d, the dominant wavenumber; ε_o, turbulent kinetic energy dissipation rate 6 mm below the water surface and $\langle \varepsilon_o \rangle$, turbulent kinetic energy dissipation rate averaged over a depth of 4 cm in the water column below the water surface.

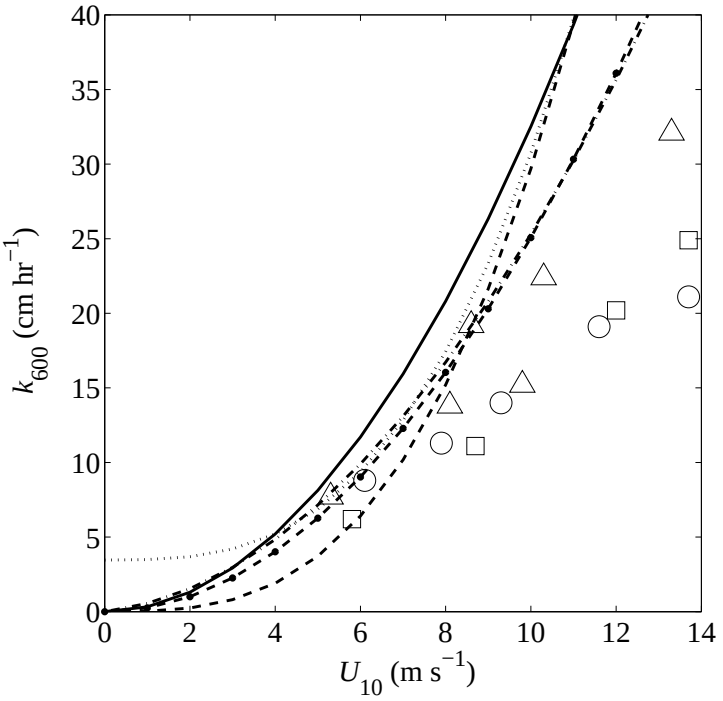

Figure 8.1: Gas transfer rate, k_{600} plotted as a function of wind speed at 10-m height, U_{10}. Gas transfer measurements were made on three fetches, F: ○, = 4.8 m; □, = 8.8 m and △, = 12.4 m. Several empirical relationships between the gas transfer rate and wind speed were also plotted for reference. These empirical relationships were proposed by Wanninkhof (1992) (solid line); Wanninkhof & McGillis (1999) (dashed line); Nightingale *et al.* (2000) (dash-dotted line); McGillis *et al.* (2001*a*) (dotted line); and Frew *et al.* (2004) (dashed line with solid circle symbol).

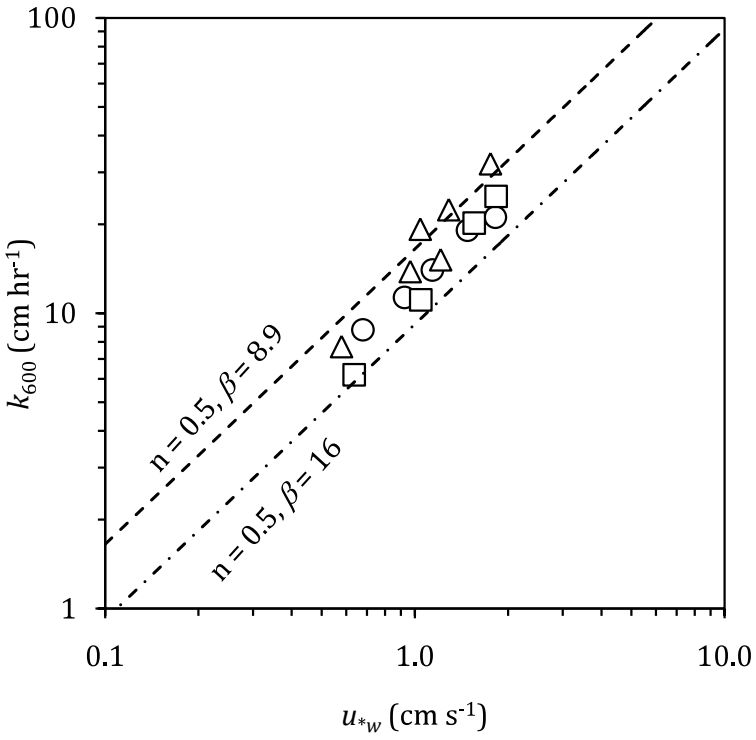

Figure 8.2: Gas transfer rate, k_{600} versus wind friction velocity converted to water-side, u_{*w}. Gas transfer measurements were made on three fetches, F: ○, = 4.8 m; □, = 8.8 m and △, = 12.4 m. Empirical relationships proposed by Munnich & Flothmann (1975) (dash-dotted) and Jahne *et al.* (1987) (dashed) were also plotted for reference.

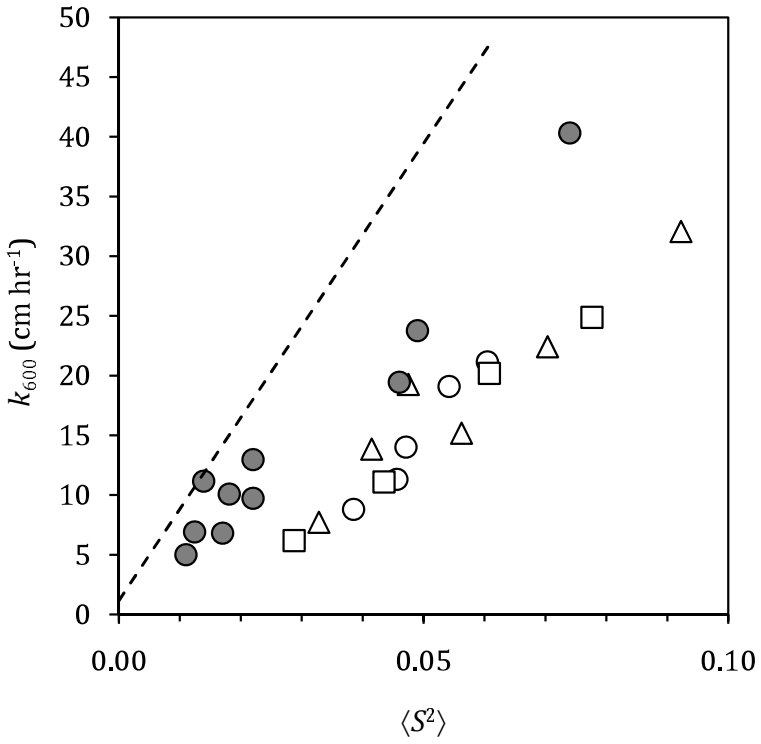

Figure 8.3: Gas transfer rate, k_{600} versus total mean square wave slope, $\langle S^2 \rangle$. Gas transfer measurements were made on three fetches, F: ○, = 4.8 m; □, = 8.8 m and △, = 12.4 m. Empirical relationship proposed by Frew *et al.* (2004) (dashed) was plotted for reference. The measurements made by Bock *et al.* (1999) in a large circular tank was also plotted as solid circle.

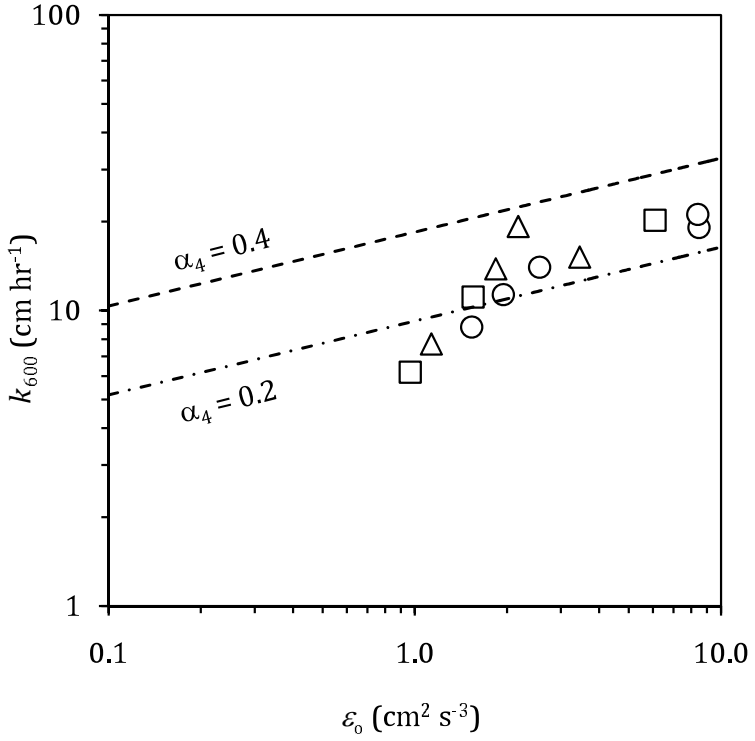

Figure 8.4: Gas transfer rate, k_{600} versus turbulent kinetic energy dissipation rate, ε_o. Gas transfer measurements were made on three fetches, F: ○, = 4.8 m; □, = 8.8 m and △, = 12.4 m. Empirical relationships as determined from Equation(8.6) using proportionality factors of 0.2 (dot-dashed) and 0.4 (dashed) were plotted for reference. Dissipation rates (ε_o) were estimated at a depth of 6 mm below the water surface.

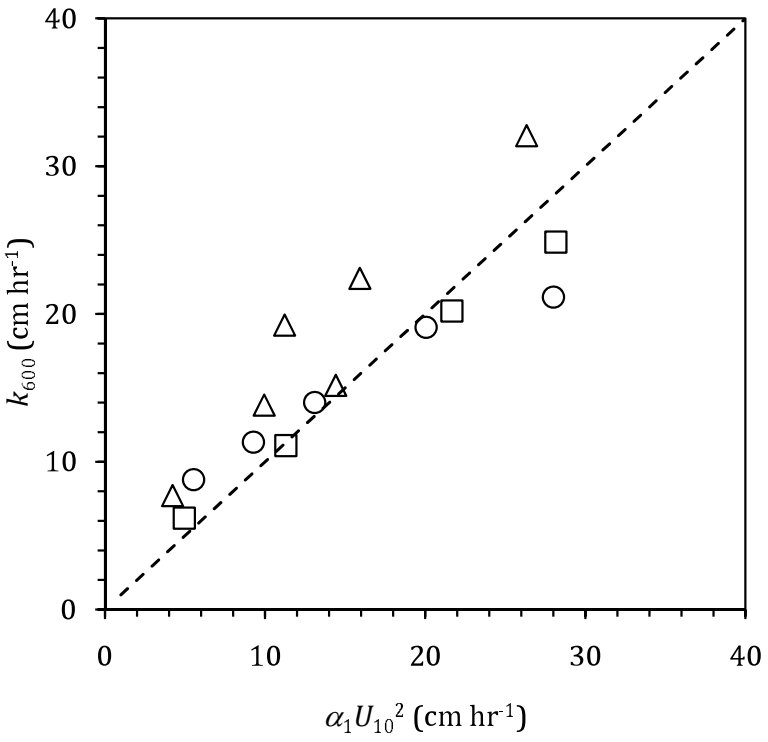

Figure 8.5: Gas transfer rate, k_{600} versus modeled k_G as determined from Equation(8.3) using a proportionality factor of $\alpha_1 = 0.15$. Gas transfer measurements were made on three fetches, F: ○, = 4.8 m; □, = 8.8 m and △, = 12.4 m.

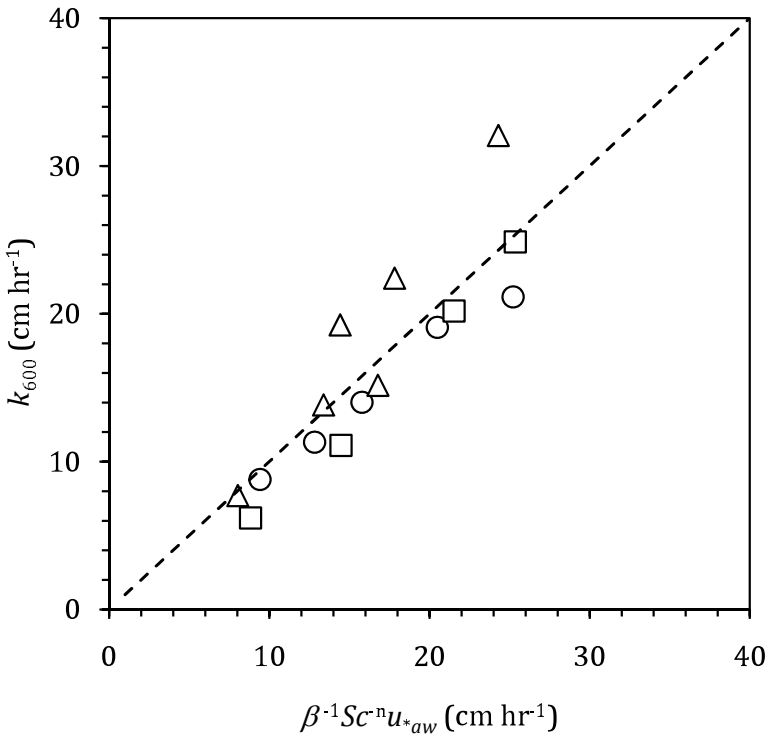

Figure 8.6: Gas transfer rate, k_{600} versus modeled k_G as determined from Equation(8.4) using a proportionality factor of $\beta = 10.6$, $Sc = 600$ and $n = -1/2$. Gas transfer measurements were made on three fetches, F: ○, = 4.8 m; □, = 8.8 m and △, = 12.4 m.

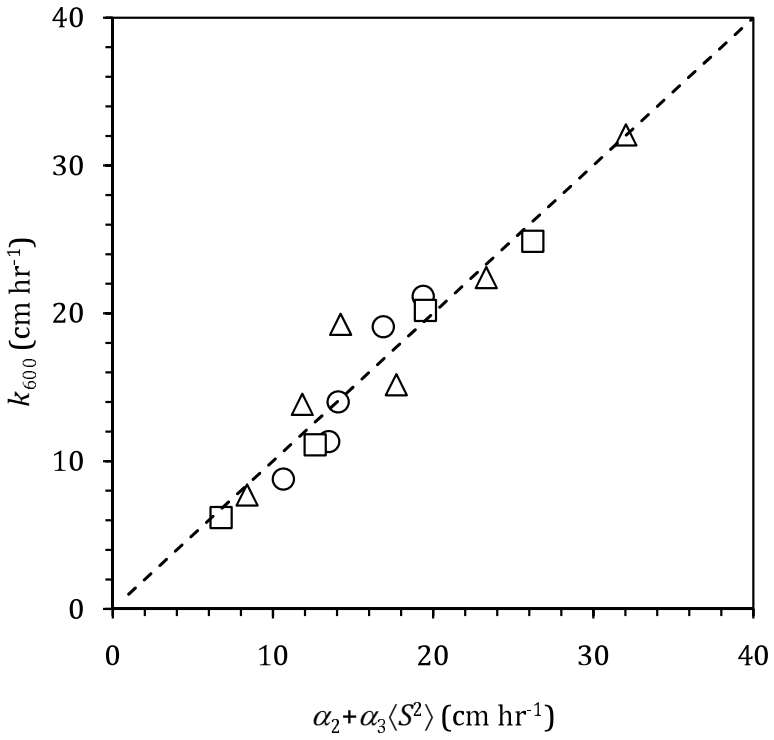

Figure 8.7: Gas transfer rate, k_{600} versus modeled k_G as determined from Equation(8.5) using proportionality factors of $\alpha_2 = -4.675$ and $\alpha_3 = 397.97$. Gas transfer measurements were made on three fetches, F: ○, = 4.8 m; □, = 8.8 m and △, = 12.4 m.

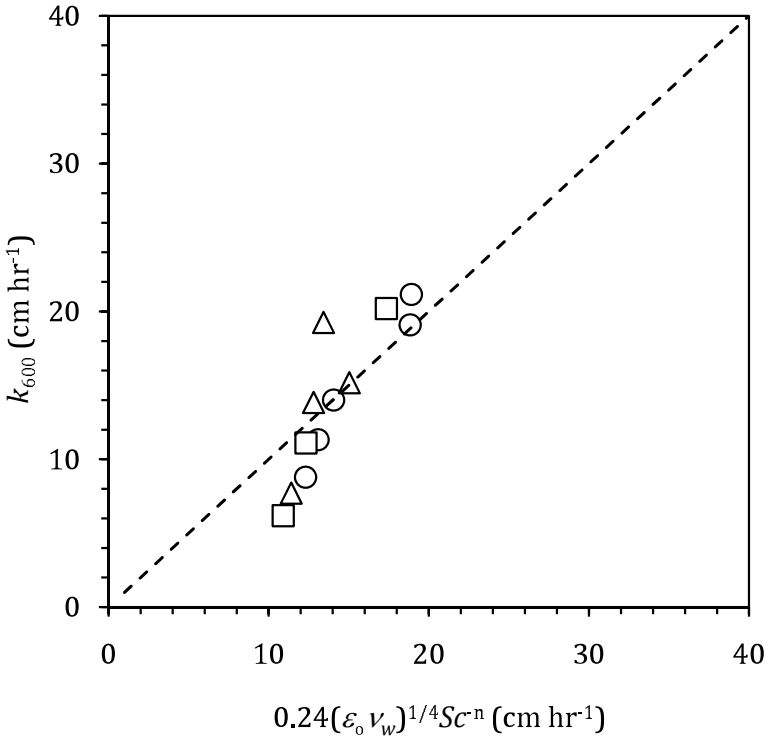

Figure 8.8: Gas transfer rate, k_{600} versus modeled k_G as determined from Equation(8.6) using a proportionality factor of $\alpha_4 = 0.24$, $Sc = 600$ and $n = -1/2$. Gas transfer measurements were made at three fetches, F: ○, = 4.8 m; □, = 8.8 m and △, = 12.4 m and dissipation rates (ε_o) were estimated at a depth of 6 mm below the water surface.

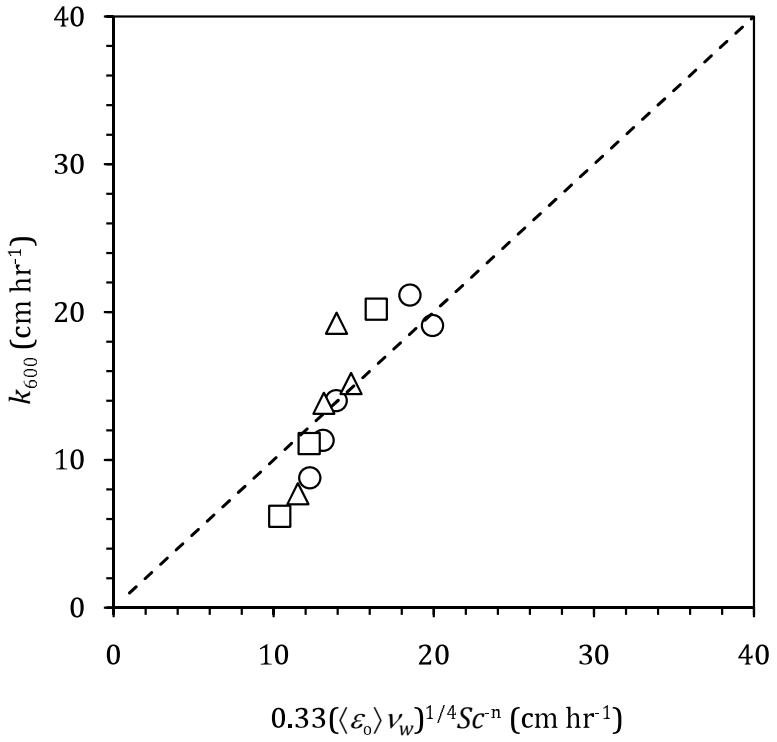

Figure 8.9: Gas transfer rate, k_{600} versus modeled k_G as determined from Equation(8.6) using a proportionality factor of $\alpha_4 = 0.33$, $Sc = 600$ and $n = -1/2$. Gas transfer measurements were made at three fetches, F: ○, = 4.8 m; □, = 8.8 m and △, = 12.4 m and dissipation rates ($\langle\varepsilon_o\rangle$) were averaged over a depth of 4 cm in the water column below the water surface.

Chapter 9

Conclusions and Recommendations

9.1 Summary and Conclusions

A series of experiments were conducted in the Wind-Wave-Current Research Facility at the Air-Sea Interaction Laboratory, Observational Science Branch, NASA Goddard Space Flight Center/Wallops Flight Facility, VA, in April-May 2004. Measurements were made at varying wind speeds ranging from 4.1 to 9.6 m s^{-1} and at three fetches of 4.8, 8.8 and 12.4 m. A particle-image based wave profile measurement technique was used to obtain accurate surface wave profiles. Digital Particle Image Velocimetry (DPIV) technique was used to measure two-dimensional velocity fields beneath the wind waves in a plane parallel to the wind and bisecting the water surface. In addition, water surface (skin layer) temperature, local heat transfer velocity, bulk gas transfer velocity, bulk air and water temperatures, relative humidity, surface tension, and mean wind speed were also measured in this study as a part of a collaborative effort.

The experimental setup and procedures of above measurements were quite complicated and described in Chapter 2. Thirty one (31) laboratory experiments were conducted in this study. These experiments were separated into two groups based on water surface cleanliness. The first group, referred to as clean experiments, included twenty-four experiments

conducted using filtered tap water and the second group, referred to as surfactant-influenced experiments, included seven experiments conducted using surfactant-influenced water. Surface tension measurements were made only for the surfactant-influenced experiments. Gas transfer measurements were made only during the clean experiments.

In Chapter 3, a particle-image based wave profile measurement technique that was developed to measure surface wave profiles in digital monochrome video images was described. The algorithm presented here, referred to as the variable threshold method, corrects for non-uniform illumination and the non-uniform distribution of near-surface seed particles. The technique accurately detects wind generated waves as short as 10 pixels (1.44 mm) in wavelength. The true r.m.s. error associated with the variable threshold method varied from approximately ± 0.7 (± 0.1 mm) to ± 1.1 (± 0.16 mm) pixels.

The measurement of two-dimensional instantaneous velocity fields using a digital particle image velocimetry (DPIV) technique was described in Chapter 4. In this study, it was necessary to make velocity measurements very close to the water surface. These measurements were very challenging due to the fact that the measurements were made beneath short wind waves and these waves generate a complex air-water interface when they break. Therefore, the surface wave profiles were used to locate the complex air-water interface in the DPIV images. A multi-pass multi-grid DPIV algorithm was developed to estimate the near-surface instantaneous velocity fields beneath complex air-water interface in a wave-following Eulerian coordinate system.

The accuracy of the DPIV algorithm was assessed by comparing the estimated velocity vectors with the ground truth velocity vectors and with the published results of Thomas *et al.* (2005). The accuracy of the DPIV algorithm was found to be comparable to that of Thomas *et al.* (2005). In the absence

of a free surface the predicted velocities agreed with the ground truth data 85%-95% of the time. Moreover, it was found that the wave-following Eulerian coordinate DPIV algorithm produced near-surface velocity estimates that were up to a factor of 6.6 times more accurate than a fixed Eulerian coordinate DPIV algorithm. In addition, the near-surface accuracy of the DPIV algorithm was found to agree closely (approximately 94% to 95% agreement) with the ground truth vectors, when a triangular wave form was used to model an air-water interface in a wave-following Eulerian coordinate system.

In Chapter 5, the dependence of surface roughness on wind-wave properties and the momentum transfer at the air-water interface were investigated. Air and water-side roughnesses of the coupled boundary layers were represented by the aerodynamic and hydrodynamic Charnock parameters. It was found that the aerodynamic Charnock parameter increases with increasing wave age. Similar trends have been observed in previous laboratory wind-wave experiments by Keller *et al.* (1992) and the model predictions of Makin & Kudryavtsev (2002). The aerodynamic Charnock parameter was found to be only weakly correlated with wave steepness. The hydrodynamic Charnock parameter decreased with increasing wave steepness although the correlation was rather weak and it did not correlate significantly with wave age. The aerodynamic roughness Reynolds number was closely correlated with the wave steepness but the hydrodynamic roughness Reynolds number was only weakly correlated with wave steepness.

Momentum transfer at the air-water interface was studied by examining the partitioning of the wind stress into its component viscous tangential stress. It was determined that the momentum transfer across the air-water interface depends on the wind speed, fetch, and wind-wave properties. It was found that the wave age and wave steepness are the two most important wind-wave properties that control the momentum transfer in the coupled boundary layers.

It was observed that the ratio of the tangential stress to wind stress is strongly correlated with wave steepness and the ratio of roughness lengths. Based on our measurements of interfacial stresses and roughness lengths in the coupled boundary layers, and model studies by Caulliez *et al.* (2008) it was argued that the airflow separation from the crests of breaking waves may be responsible for making the air-side boundary layer rougher and water-side boundary layer smoother. It was concluded that airflow above wind-waves was in the rough regime at moderate to high wind speed. The flow in the water-side boundary layer was found to be in the transitional regime and then became smooth as wind speed increased. In addition, it was established that the water-side friction velocity calculated using Clauser's method is an accurate estimate of the tangential or viscous friction velocity. Moreover, it was argued that the non-dimensional viscous sub-layer thickness is approximately a factor of two thicker than the conventional wall layer estimate.

In Chapter 6, the influence of surfactant concentration on the momentum transfer at the air-water interface and on the structure of the near-surface turbulence were investigated. The synthetic surfactant Triton X-100 in concentrations from 0 to 5 ppm was added to filtered tap water to model surfactant-influenced water surfaces. All experiments were conducted at a wind speed of 7.9 m s^{-1} and fetch of 4.8 m. As expected, the presence of a surfactant made the waves significantly smaller in amplitude and less steep. The significant wave height and mean square wave slope were reduced by a factor of 2.2 and 3.7, respectively as the concentration was increased from 0 to 5 ppm. However, the effect of the surfactant on the wavelength was insignificant. The wind stress was found to decrease by a factor of 2.7 as concentration increased from 0 to 5 ppm. This is clear evidence that the wind stress is reduced significantly as the surface contamination increases although the wind speed remains constant. The air-side boundary layer was found to be

aerodynamically rough at all concentrations, although, it became less rough as the surfactant concentration increased. The water-side boundary layer was found to be in the transition regime at concentrations less than or equal to 0.1 ppm and then became hydrodynamically smooth at concentrations greater than or equal to 0.5 ppm. The roughness lengths in both the air-side boundary layer and water-side boundary layer were found to decrease as the surfactant concentration was increased. The surface drift velocity was increased by a factor of 1.3 as the concentration increased from 0 to 5 ppm.

Momentum transfer at the air-water interface was studied by examining the partitioning of the wind stress into its component viscous tangential stress similar to the clean water experiments. The ratio of the viscous tangential stress to the wind stress increased from approximately 0.3 to 1 as the surfactant concentration increased from 0 to 5 ppm. The stress partitioning ratio was observed to increase with decreasing wave slope or wave steepness as the surfactant concentration was increased. The rate of dissipation of turbulent kinetic energy decreased monotonically as concentration increased and the reduction was most significant near the surface. At a concentration of 5 ppm the surfactant reduced the dissipation rate by a factor of 2.7 compared to clean water. A new wave-dependent dissipation scaling model was proposed based on the observed dissipation data. The dissipation rate is normalized using the gravitational acceleration, the wave phase speed, water-side friction velocity, the significant wave height and the depth. The near-surface turbulence had two distinct layers in the presence of a surfactant beneath these short wind waves. An upper layer in which the dissipation rate decays as $\zeta^{-0.3}$ and a lower layer in which dissipation rate decays as ζ^{-1}. The rate of dissipation of turbulent kinetic energy beneath the surface up to a depth of approximately 0.6 times the significant wave height was found to be significantly smaller than would occur in a comparable wall-layer. However, at larger depths, the

dissipation rates were comparable to wall-layer theory. The depth-averaged energy dissipation rate decreased as the mean square wave slope decreased and as the surfactant concentration increased. In addition, the depth-averaged dissipation rate was reduced by approximately a factor of three at the highest concentration compared to the clean experiment.

The structure of the near-surface turbulence beneath microscale breaking waves in clean water was examined in Chapter 7. The specific focus of this chapter was to determine the influence of the wave-induced motions and shear currents on the vertical extent and depth dependence of dissipation rate beneath microscale breaking waves.

A DPIV vorticity threshold based detection scheme similar to Loewen & Siddiqui (2006) was adapted in this study to detect the microscale breaking waves. It was observed that the short wind waves started to break at wind speeds higher than 4 m s^{-1} and that the percentage of breaking waves increased linearly with wind speed up to 90% for wind speed less than or equal to 8 m s^{-1}. The percentage of breaking waves remained almost constant at 90% for wind speed higher than 8 m s^{-1}. No systematic variation in the percentage of microscale breaking waves was observed with fetch.

The structure of the near-surface turbulence showed three distinct layers in clean water. In the top layer, the near-surface turbulence was dominated by the wave-induced motions associated with microscale breaking waves. Below this layer, turbulence was generated by both wave-induced motions and shear currents. In the lower layer, turbulence was produced predominantly by shear currents. It was determined that the energy dissipation rate could be scaled using the depth, friction velocity, wave height and phase speed as proposed by Terray *et al.* (1996) provided that layer based friction velocities are used. At a fetch of 4.8 m, it was found that the dissipation rates solely due to breaking decayed as $\zeta^{-0.2}$ in the wave-induced layer, which was similar to the

approximation of constant dissipation assumed by Terray *et al.* (1996). In the transition layer, the dissipation rates decayed as $\zeta^{-2.0}$, in agreement with the findings of Terray *et al.* (1996) and Siddiqui & Loewen (2007). In the lower layer, dissipation rates decayed as $\zeta^{-1.0}$, similar to a traditional wall-layer. At fetches of 8.8 and 12.4 m, the dissipation rates also decayed as $\zeta^{-0.2}$ in the wave-induced layer. However, in the transition layer, dissipation rates decayed at two different rates depending on the depth. In the upper region of the transition layer, dissipation rates decayed as $\zeta^{-2.0}$. In the lower region of the transition layer, dissipation rates decayed as $\zeta^{-4.0}$. However, energy dissipation data did not extend into the lower layer at fetches of 8.8 and 12.4 m.

In Chapter 8, the dependence of air-water gas transfer rates on wind-wave properties and on near-surface turbulence was investigated in clean water surface. Simultaneous measurements of wind speed, wind friction velocity, surface wave slope, surface wave driven near-surface turbulence and gas transfer rate facilitated the investigation. Comparison of four empirical relationships revealed that slope is the best parameterization since 92% of the variance was explained. The gas transfer rate was found to vary linearly with total mean square wave slope and correlated better than the other three parameterizations. This finding is similar to the results of Jahne *et al.* (1987), Bock *et al.* (1999) and Frew *et al.* (2004). However, wind speed, wind friction velocity, and energy dissipation based parameterizations of the gas transfer rate also performed reasonably well since they explained 75% to 79% of the variance, respectively.

9.2 Recommendations for future work

The findings presented in this research have improved our understanding of the role played by short wind waves including microscale breaking waves in

generating near-surface turbulence and enhancing momentum transfer and air-water gas transfer at the interface. However, the key physical mechanisms that lead to the breaking of these short steep waves are not fully understood. Longuet-Higgins (1992) suggested that the intense vorticity generated beneath the capillary waves that appear on the forward face of these waves could be responsible for triggering breaking. In order to investigate the behavior of these parasitic capillary waves and their role in breaking, significantly high resolution DPIV and profile measurements would be required. Measurements with both higher temporal and spatial resolution might confirm the hypothesis presented by Longuet-Higgins (1992).

Makin & Kudryavtsev (2002) developed a wind-over-waves coupled model to investigate the impact of airflow separation from the dominant breaking waves. This model could be validated using the findings presented in this study. Of particular interest would be to use of the findings of this study to calibrate and validate numerical models of momentum transfer, air-water gas transfer and energy dissipation processes due to microscale breaking waves. Moreover, numerical models representing the effect of surfactant on momentum transfer and energy dissipation rate can also be calibrated and validated using the findings of this study.

Bibliography

Adrian, R. J. 1988 *Statistical properties of particle image velocimetry measurements in turbulent flow*, laser anemometry in fluid mechanics - iii edn., pp. 115–129. Lisbon: LADOAN Instituto Superior Technico.

Adrian, R. J. 1991 Particle-imaging techniques for experimental fluid mechanics. *Annu. Rev. Fluid Mech.* **23**, 261–304.

Agrawal, Y. C., Terray, E. A., Donelan, M. A., Hwang, P. A., III, A. J. Williams, Drennan, W. M., Kahma, K. K. & Kitaigorodskii, S. A. 1992 Enhanced dissipation of kinetic energy beneath surface waves. *Nature* **359**, 219–220.

Agui, J. C. & Jimenez, J. 1987 On the performance of particle tracking. *J. Fluid Mech.* **185**, 447–468.

Aitken, J. 1883; cited by Miles, 1966 *Proc. Roy. Soc. Edinb.* **12**.

Anctil, F. & Donelan, M. A. 1996 Air-water momentum flux observations over shoaling waves. *J. Phys. Oceanogr.* **26**, 1344–1353.

Anis, A. & Moum, J. N. 1995 Surface wave-turbulence interactions: Scaling ε(z) near the sea surface. *J. Phys. Oceanogr.* **25**, 2025–2045.

Asher, W. E., Karle, L. M., Higgins, B. J., Farley, P. J., Monahan, E. C. & Leifer, I. S. 1996 The influence of bubble plumes on air-seawater gas transfer velocities. *J. Geophys. Res.* **101(C5)**, 12027–12041.

Atmane, M. A., Asher, W. E. & Jessup, A. T. 2004 On the use of the active infrared technique to infer heat and gas transfer velocities at the air-water free surface. *J. Geophys. Res.* **109**.

Banner, M. L. 1990 The influence of wave breaking on the surface pressure distribution in wind-wave interactions. *J. Fluid Mech.* **211**, 463–495.

Banner, M. L. & Peirson, W. L. 1998 Tangential stress beneath wind-driven air-water interfaces. *J. Fluid Mech.* **364**, 115–145.

Banner, M L & Peregrine, D H 1993 Wave breaking in deep water. *Annu. Rev. Fluid Mech.* **25**, 373–397.

Banner, M. L. & Phillips, O. M. 1974 On the incipient breaking of small scale waves. *J. Fluid Mech.* **65**, 647–656.

Batchelor, G. K. 1959 Small-scale variation of convected quantities like temperature in turbulent fluid. Part 1. general discussion and the case of small conductivity. *J. Fluid Mech.* **5**, 113–133.

Benilov, A. Y., Kouznetsov, O. A. & Panin, G. N. 1974 On the analysis of wind-induced disturbances in the atmospheric turbulent surface layer. *Bound.-Layer Meteor.* **6**, 269–285.

Bock, E. J., Hara, T., Frew, N. M. & McGillis, W. R. 1999 Relationship between air-sea gas transfer and short wind waves. *J. Geophys. Res.* **104(C11)**, 25821–25831.

Botte, V. & Mansutti, D. 2005 Numerical modelling of the marangoni effects induced by plankton-generated surfactants. *J. Mar. Sys.* **57**, 55–69.

Bourassa, M. A. 2000 Shear stress model for the aqueous boundary layer near the air-sea interface. *J. Geophys. Res.* **105(C1)**, 1167–1176.

Broecker, H. C., Peterman, J. & Siems, W. 1978 The influence of wind on CO_2 exchange in a wind-wave tunnel, including the effects of mono layers. *J. Mar. Res.* **36**, 595–610.

Broecker, H. C. & Siems, W. 1984 The role of bubbles for gas transfer from water to air at higher windspeeds: Experiments in the wind-wave facility in Hamburg. In *Gas Transfer at Water Surfaces* (ed. W. Brutsaert & G. H. Jirka), pp. 229–238. D. Reidel, Hingham, Mass.: Springer.

Bye, J. A. T. 1965 Wind-driven circulation in unstratified lakes. *Limnology and Oceanography* **10**, 451–458.

Bye, J. A. T. 1967 The wave-drift current. *J. of Mar. Res.* **25**, 95–102.

Bye, J. A. T. 1988 The coupling of wave drift and wind velocity profiles. *J. Mar. Res.* **46**, 457–472.

Calderbank, P. H. & Moo-Young, M. B. 1961 The continuous phase heat and masstransfer properties of dispersions. *Chem. Eng. Sci.* **16**, 39–54.

Cane, M. A., Clement, A. C., Kaplan, A., Kushnir, Y., Pozdnyakov, D., Seager, R., Zebiak, S. E. & Murtugudde, R. 1997 Twentieth-century sea surface temperature trends. *Science* **275**, 957–960.

Caulliez, G., Makin, V. & Kudryavtsev, V. 2008 Drag of the water surface at very short fetches: observations and modeling. *J. Phys. Oceanogr.* **38**, 2038–2055.

Charnock, H. 1955 Wind stress on a water surface. *Quart. J. Roy. Meteor. Soc.* **81**, 639–640.

Charnock, H. 1958 A note on empirical wind-wave formulae. *Quart. J. Roy. Meteor. Soc.* **84**, 443–447.

Cheung, T. K. & Street, R. L. 1988 The turbulent layer in the water at an air-water interface. *J. Fluid Mech.* **194**, 133–151.

Churchill, J. H. & Pade, B. H. 1980 Measurement of near-surface current in Cape Cod Bay using sighted drogues. Tech. Rep. WHOI-80-8. Woods Hole Oceanogr. Inst., Woods Hole, Mass.

Churchill, J. H. & Pade, B. H. 1981 Acoustically and visually tracked drogue measurements of near-surface water velocities in Lake Huron, plus observations of a coastal upwelling. Tech. Rep. WHOI-81-91. Woods Hole Oceanogr. Inst., Woods Hole, Mass.

Clauser, F. H., ed. 1956 *Advances in Applied Mechanics*, , vol. IV. New York: Academic Press.

Cowen, E. A. & Monismith, S. G. 1997 A hybrid digital particle tracking velocimetry technique. *Exp. in Fluids* **22**, 199–211.

Craig, P. D. & Banner, M. L. 1994 Modeling wave-enhanced turbulence in the ocean surface layer. *J. Phys. Oceanogr.* **24**, 2546–2559.

Csanady, G. T. 1984 The free surface turbulent shear layer. *J. Phys. Oceanogr.* **14**, 402–411.

Danckwerts, P. V. 1970 *Gas-Liquid Reaction*. New York: McGraw-Hill.

Davies, J. T. & Rideal, E. K., ed. 1963 *Interfacial Phenomena*, 2nd edn. New York: Academic Press.

Dickey, T. D., Hartman, B., Hammond, D. & Hurst, E. 1984 A laboratory technique for investigating the relationship between gas transfer and fluid turbulence. In *Gas Transfer at Water Surfaces* (ed. W. Brutsaert & G. H. Jirka), pp. 93–100. Germany: Springer.

Donelan, M. A. 1979 On the fraction of wind momentum retained by waves. In *Marine Forecasting, Predictability and Modelling in Ocean Hydrodynamics* (ed. J. C. Nihoul). Amsterdam: Elsevier.

Donelan, M. A. 1982 The dependence of the aerodynamic drag coefficient on wave parameters. In *First Int. Conf. on Meteorological and Air/Sea Interaction of the Coastal Zone*, pp. 381–387. Boston, Mass.: Amer. Meteor. Soc.

Donelan, M. A. 1990 *Air-Sea Interaction*, , vol. 9. New York: John Wiley and Sons, Inc.

Donelan, M. A., Dobson, F. W., Smith, S. D. & Anderson, R. J. 1993 On the dependence of sea surface roughness on wave development. *J. Phys. Oceanogr.* **23**, 2143–2149.

Doron, P., Bertuccioli, L., Katz, J. & Osborn, T. R. 2001 Turbulence characteristics and dissipation estimates in the coastal ocean bottom boundary layer from PIV data. *J. Phys. Oceanogr.* **31**, 2108–2134.

Drennan, W. M., Donelan, M. A., Terray, E. A. & Katsaros, K. B. 1996 Oceanic turbulence dissipation measurements in SWADE. *J. Phys. Oceanogr.* **26**, 808–815.

Drennan, W. M., Graber, H. C., Hauser, D. & Quentin, C. 2003 On the wave age dependence of wind stress over pure wind seas. *J. Geophys. Res.* **108(C3)**, 8062.

Drennan, W. M., Taylor, P. K. & Yelland, M. J. 2005 Parameterizing the sea surface roughness. *J. Phys. Oceanogr.* **35**, 835–848.

Elkamash, M. K. 2005 The effect of surfactants on microscale wave breaking and the aqueous boundary layer. PhD thesis, University of Alberta, Edmonton, Canada.

Fincham, A. M. & Spedding, G. R. 1997 Low cost, high resolution DPIV for measurement of turbulent fluid flow. *Exp. in Fluids* **23**, 449–462.

Fitzgerald, L. M. 1964 The effect of wave-damping on the surface velocity of water in a wind tunnel. *Aust. J. Phys.* **17**, 184–188.

Foss, J. F., Tropea, C., Panton, R., McKeon, B., Merzkirch, W., Dreizler, A., Schulz, C., Katz, J., Nobach, H. & Jhne, B. 2007 *Handbook of experimental fluid mechanics*, 1st edn., *Engineering*, vol. XXVIII. Berlin, Heidelberg: Springer.

Franklin, B. 1774; cited by Miles, 1966 On the stilling of waves by means of an oil. *Phil. Trans. Roy. Soc.* **64**.

Frew, N. M. 1997 The role of organic films in air-sea gas exchange. In *The Sea Surface and Global Change* (ed. P. S. Liss & R. A. Duce), pp. 121–172. New York: Cambridge Univ. Press.

Frew, N. M., Bock, E. J., McGillis, W. R., Kara-chintsev, A. V., Hara, T., Munsterer, T. & Jahne, B. 1995 Variation of air-water gas transfer with wind stress and surface viscoelasticity. In *Air-Water Gas Transfer* (ed. B. Jahne & E. C. Monahan), pp. 529–541. Germany: AEON Verlag and Studio.

Frew, N. M., Bock, E. J., Schimpf, U., Hara, T., Haubecker, H., Edson, J. B., McGillis, W. R., Nelson, R. K., McKenna, S. P., Uz, B. M. & Jahne, B. 2004 Air-sea gas transfer: Its dependence on wind stress, small-scale roughness, and surface films. *J. Geophys. Res.* **109**.

Gargett, A. E. 1989 Ocean turbulence. *Annu. Rev. Fluid Mech.* **21**, 419–451.

Gemmrich, J. R. & Farmer, D. M. 2004 Near-surface turbulence in the presence of breaking waves. *J. Phys. Oceanogr.* **34**, 1067–1086.

Gottifredi, J. C. & Jameson, G. J. 1970 The growth of short waves on liguid surfaces under the action of a wind. *Proc. Roy. Soc. Lond.* **319**, 373–397.

Groen, P. & Dorrestein, R. 1958 report no. 11. Zeegolven, Kon. Ned. Met. Inst.

Gui, L., Longo, J. & Stern, F. 2001 Biases of PIV measurement of turbulent flow and the masked correlation-based interrogation algorithm. *Exp. in Fluids* **30**, 27–35.

Gui, L., Merzkirch, W. & Fei, R. 2000 A digital mask technique for reducing the bias error of the correlation-based PIV interrogation algorithm. *Exp. in Fluids* **29**, 30–35.

Hall, E. L. 1979 *Computer image processing and recognition*. New York: Academic Press.

Hara, T., Bock, E. J., Frew, N. M. & McGillis, W. R. 1995 Relationship between air-sea gas transfer velocity and surface roughness. In *Air-Water Gas Transfer* (ed. B. Jahne & E. C. Monahan), pp. 611–616. Germany: AEON Verlag and Studio.

Honkanen, M. & Nobach, H. 2005 Background extraction from double-frame PIV images. *Exp. in Fluids* **38(3)**, 348–362.

Hsu, C. T., Hsu, E. Y. & Street, R. L. 1981 On the structure of turbulent flow over a progressive water wave: theory and experiment in a transformed, wave-following coordinate system. *J. Fluid Mech.* **105**, 87–117.

Hsu, C. T., Wu, H. Y., Hsu, E. Y. & Street, R. L. 1982 Momentum and energy transfer in wind generation of waves. *J. Phys. Oceanogr.* **12**, 929–951.

Hsu, S. A. 1974 A dynamic roughness equation and its application to wind stress determination at the air-sea interface. *J. Phys. Oceanogr.* **4**, 116–120.

Jahne, B. 1997 *Digital image processing concepts, algorithms, and scientific applications*, 4th edn. Berlin, Heidelberg, New York: Springer.

Jahne, B., Huber, W., Dutzi, A., Wais, T. & Ilmberger, J. 1984 Wind/wave-tunnel experiment on the schmidt number and wave field dependence of air/water gas exchange. In *Gas Transfer at Water Surfaces* (ed. W. Brutsaert & G. H. Jirka), pp. 303–309. Germany: Springer.

Jahne, B., Libner, P., Fischer, R., Billen, T. & Plate, E. J. 1989 Investigating the transfer process across the free aqueous viscous boundary layer by the controlled flux method. *Tellus* **41B**, 177–189.

Jahne, B., Munnich, K. O., Bosinger, R., Dutzi, A., Huber, W. & Libner, P. 1987 On the parameters influencing air-water gas exchange. *J. Geophys. Res.* **92(C2)**, 1937–1949.

Jahne, B., Wais, T., Memery, L., Caulliez, G., Merlivat, L., Munnich, K. O. & Coantic, M. 1985 He and Rn gas exchange experiments in the large wind-wave facility of IMST. *J. Geophys. Res.* **90**, 11989–11997.

Janssen, P. A. E. M. 1989 Wave induced stress and the drag of air flow over sea waves. *J. Phys. Oceanogr.* **19**, 745–754.

Janssen, P. A. E. M. 1999 On the effect of ocean waves on the kinetic energy balance and consequences for the inertial dissipation technique. *J. Phys. Oceanogr.* **29**, 530–534.

Jessup, A. T. & Phadnis, K. R. 2005 Measurement of the geometric and kinematic properties of microscale breaking waves from infrared imagery using a PIV algorithm. *Meas. Sci. Technol.* **16**, 1961–1969.

Jessup, A. T., Zappa, C. J. & Yeh, H. 1997 Defining and quantifying microscale wave breaking with infrared imagery. *J. Geophys. Res.* **102**, 23145–23153.

Jiang, J. Y., Street, R. L. & Klotz, S. P. 1990 A study of wave-turbulence interaction by use of a nonlinear water wave decomposition technique. *J. Geophys. Res.* **95**, 16037–16054.

Johnson, H. K., Hoejstrup, J., Vested, H. J. & Larsen, S. E. 1998 On the dependence of sea surfce roughness on wind waves. *J. Phys. Oceanogr.* **28**, 1702–1716.

Keane, R. D. & Adrian, R. J. 1990 Optimization of particle image velocimeters. Part 1: double pulsed system. *Meas. Sci. Technol.* **1**, 1202–1215.

Keller, M. R., Keller, W. C. & Plant, W. J. 1992 A wave tank study of the dependence of X band cross sections on wind speed and water temperature. *J. Geophys. Res.* **97**, 5771–5792.

Kennedy, J. B. & Neville, A. M. 1976 *Basic statistical methods for engineers and scientists*. New York: Harper and Row.

Kenyon, K. 1969 Stokes drift from random gravity waves. *J. Geophys. Res.* **74**, 6991–6994.

Keulegan, G. H. 1951 Wind tides in small closed channels. *J. Res. Nat. Bur. Stnd* .

Kitaigorodskii, S. A. 1973 The physics of air-sea interaction. p. 237. Jerusalem: Israel Program for Scientific Translations.

Kitaigorodskii, S. A. 1984 On the fluid dynamical theory of turbulent gas transfer across an air-sea interface in the presence of breaking wind-waves. *J. Phys. Oceanogr.* **14**, 960–972.

Kitaigorodskii, S. A., Donelan, M. A., Lumley, J. L. & Terray, E. A. 1983 Wave-turbulence interactions in the upper ocean. Part II: Statistical characteristics of wave and turbulent components of the random velocity field in the marine surface layer. *J. Phys. Oceanogr.* **13**, 1988–1999.

Kitaikorodskii, S. A. & Volkov, Y. A. 1965 On the roughness parameter of the sea surface and the calculation of momentum flux in the near-water layer of the atmosphere. *Izv. Acad. Sci. USSR Atmos. Oceanic Phys. Engl. Transl.* **1**, 973–988.

Kundu, P. K. & Cohen, I. M., ed. 2002 *Fluid mechanics*, 2nd edn. California: Academic Press.

Lamont, J. C. & Scott, D. S. 1970 An eddy cell model of mass transfer into the surface of a turbulent liquid. *AIChE Journal* **16** (4), 513–519.

Lang, A. W. & Gharib, M. 2000 Experimental study of the wake behind a surface piercing cylinder for a clean and contaminated free surface. *J. Fluid Mech.* **402**, 109–136.

Lange, B., Johnson, H. K., Larsen, S., Hoejstrup, J., Kofoed-Hansen, H. & Yelland, M. J. 2004 On detection of a wave age dependency for the sea surface roughness. *J. Phys. Oceanogr.* **34**, 1441–1458.

Lapham, G. S., Dowling, D. R. & Schultz, W. W. 2001 Linear and nonlinear gravity-capillary water waves with a soluble surfactant. *Exp. in Fluids* **30**.

Law, C. N. S., Khoo, B. C. & Chew, T. C. 1999 Turbulence structures in the immediate vicinity of the shear-free air-water interface induced by a deeply submerged jet. *Exp. in Fluids* **27**, 321–331.

Ledwell, J. J. 1984 The variation of the gas transfer coefficient with molecular diffusivity pp. 293–302.

Levich, V. G., ed. 1962, first Russian edition was published in 1952 *Physicochemical Hydrodynamics*. Englewood Cliffs, NJ: Prentice-Hall.

Lin, H.J. & Perlin, M. 1998 Improved methods for thin, surface boundary layer investigations. *Exp. in Fluids* **25**, 431–444.

Liss, P. S. & Merlivat, L. 1986 Air-sea gas exchange rates: Introduction and synthesis. In *The role of air-sea exchange in geochemical cycling* (ed. P. Buat-Menard), pp. 113–129. D. Reidel, Hingham, Mass, USA.

Liu, X., Duncan, J. H., nd, G. M. Korenowski & Kelly, J. S. 2007 A laboratory study of longitudinal waves in surfactant films in a water wave tank. *J. Geophys. Res.* **112**, 3337–3352.

Loewen, M. R. & Siddiqui, M. H. K. 2006 Detecting microscale breaking waves. *Meas. Sci. Technol.* **17**, 771–780.

Longuet-Higgins, M. S. 1992 Capillary rollers and bores. *J. Fluid Mech.* **240**, 659–679.

Lorke, A. & Peeters, F. 2006 Toward a unified scaling relation for interfacial fluxes. *J. Phys. Oceanogr.* **36**, 955–961.

Lumley, J. L. & Panofsky, H. A. 1964 *The structure of atmospheric turbulence*. New York: Intersci.

Maat, N., Kraan, C. & Oost, W. A. 1991 The roughness of wind waves. *Bound.-Layer Meteor.* **54**, 89–103.

Makin, V. K. & Kudryavtsev, V. N. 2002 Impact of dominant waves on sea drag. *Bound.-Layer Meteor.* **103**, 83–99.

Manton, M. J. 1971 Wave generation on the air-sea interface. *Bound.-Layer Meteor* **2**, 152–160.

Mass, J. T. & Milgram, J. H. 1998 Dynamic behaviour of natural sea surfactant films. *J. Geophys. Res.* **103**, 15695–15715.

McGillis, W. R., Edson, J. B., Hare, J. E. & Fairall, C. W. 2001*a* Direct covariance air-sea CO_2 fluxes. *J. Geophys. Res.* **106**, 16729–16745.

McGillis, W. R., Edson, J. B., Ware, J. D., Dacey, J. W. H., Hare, J. E., Fairall, C. W. & Wanninkhof, R. 2001*b* Carbon dioxide flux techniques performed during GasEx-98. *Mar. Chem.* **75**, 267–280.

Melville, W. K. 1996 The role of surface-wave breaking in air-sea interaction. *Annu. Rev. Fluid Mech.* **28**, 279–321.

Melville, W. K., Veron, F. & Whitey, C. J. 2002 The velocity field under breaking waves: coherent structures and turbulence. *J. Fluid Mech.* **454**, 203–233.

Miles, J. W. 1966 Surface-wave damping in closed basins. *Proc. Roy. Soc. London* **297**.

Milgram, J. H. 1998 Short wave damping in the simultaneous presence of a surface film and turbulence. *J. Geophys. Res.* **103**, 15717–15727.

Mitsuyasu, H. 1985 A note on the momentum transfer from wind to waves. *J. Geophys. Res.* **90(C4)**, 3343–3346.

Mitsuyasu, H. & Honda, T. 1982 Wind induced growth of water waves. *J. Fluid Mech.* **123**, 425–442.

Moon, I.-J., Hara, T., Ginis, I., Belcher, S. E. & Tolman, H. L. 2004 Effect of surface waves on air-sea momentum exchange. Part I: Effect of mature and growing seas. *Bound.-Layer Meteor.* **61**, 2321–2333.

Mukto, M. A., Atmane, M. A. & Loewen, M. R. 2007 A particle-image based wave profile measurement technique. *Exp. in Fluids* **42(1)**, 131–142.

Munnich, K. O. & Flothmann, D. 1975 Gas exchange in relation to other air-sea interaction phenomena. In *Air-Sea Interaction Phenomena*. Miami, Fla.

Niblack, W. 1986 *An introduction to digital image processing*. Englewood Cliffs, NJ: Prentice-Hall.

Nightingale, P. D., Malin, G., Law, C. S., Watson, A. J., Liss, P. S., Liddicoat, M. L., Boutin, J. & Upstill-Goddard, R. C. 2000 In situ evaluation of air-sea gas exchange parameterizations using novel conservative and volatile tracers. *Global Biogeochem. Cycles* **14**, 373–387.

Nordeng, T. E. 1991 On the wave age dependent drag coefficient and roughness length at sea. *J. Geophys. Res.* **96**, 7167–7174.

Okamoto, K., Nishio, S., Saga, T. & Kobayashi, T. 2000 Standard images for particle image velocimetry. *Meas. Sci. Technol.* **11(6)**, 685–691.

Peirson, W. L. 1997 Measurement of surface velocities and shears at a wavy air-water interface using particle image velocimetry. *Exp. in Fluids* **23**, 427–437.

Peirson, W. L. & Banner, M. L. 2003 Aqueous surface layer flows induced by microscale breaking wind waves. *J. Fluid Mech.* **479**, 1–38.

Phillips, O. M., ed. 1977 *The dynamics of the upper ocean*, 2nd edn. New York: Cambridge Univ. Press.

Quenot, G. & Okamoto, K. 2000 A standard protocol for quantitative performance evaluation of PIV systems. In *9th International Symposium on Flow Visualisation*.

Raffel, M., Willert, C., Wereley, S. & Kompenhans, J., ed. 2007 *Particle image velocimetry - a practical guide*, 2nd edn. Heidelberg, Germany: Springer.

Rapp, R. J. & Melville, W. K. 1990 Laboratory measurements of deep-water breaking waves. *Philos. Trans. Roy. Soc. London* **A331**, 735–800.

Reynolds, O. 1880; cited by Miles, 1966 On the effect of oil destroying waves on the surface of water. *Brit. Assoc. Rept.; Papers* **1**.

Richey, J. E., Melack, J. M., Aufdenkampe, A. K., Ballester, V. M. & Hess, L. L. 2002 Outgassing from amazonian rivers and wetlands as a large tropical source of atmospheric CO_2. *Nature* **416** (6881), 617–620.

Rodgers, J. L. & Nicewander, W. A. 1988 Thirteen ways to look at the correlation coefficient. *The American Statistician* **42(1)**, 59–66.

Ross, S. M. 2003 Peirce's criterion for the elimination of suspect experimental data. *J. of Eng. Tech.* **20(2)**, 38–41.

Saylor, J. R., Szeri, A. J. & Foulks, G. P. 2000 Measurement of surfactant properties using a circular capillary wave field. *Exp. in Fluids* **29**, 509–518.

Scarano, F. 2002 Iterative image deformation methods in PIV. *Meas. Sci. Technol.* **13**, R1–R19.

Scarano, F. & Riethmuller, M. L. 1999 Iterative multigrid approach in PIV image processing. *Exp. in Fluids* **26**, 513–523.

Scarano, F. & Riethmuller, M. L. 2000 Advances in iterative multigrid PIV image processing. *Exp. in Fluids* **29(7)**, S51–S60.

Schlichting & Gersten 2000 Turbulent flow. In *Applications of Bifurcation Theory* (ed. P. H. Rabinovich), pp. 359–384. Academic.

Siddiqui, M. H. K. & Loewen, M. R. 2007 Characteristics of the wind drift layer and microscale breaking waves. *J. Fluid Mech.* **573**, 417–456.

Siddiqui, M. H. K., Loewen, M. R., Asher, W. E. & Jessup, A. T. 2004 Coherent structures beneath wind waves and their influence on air-water gas transfer. *J. Geophys. Res.* **109**.

Siddiqui, M. H. K., Loewen, M. R., Richardson, C., Asher, W. E. & Jessup, A. T. 2001 Simultaneous particle image velocimetry and infrared imagery of microscale breaking waves. *Phys. Fluids* **13**, 1891–1903.

Smith, S. D. 1980 Wind stress and heat flux over the ocean in gale force winds. *J. Phys. Oceanogr.* **10**, 709–726.

Smith, S. D. 1988 Coefficients for sea surface wind stress, heat flux and wind profiles as a function of wind speed and temperature. *J. Geophys. Res.* **93**, 15467–15472.

Smith, S. D., Anderson, R. J., Oost, W. A., Kraan, C., Maat, N., DeCosmo, J., Katsaros, K. B., Davidson, K. L., Bumke, K., Hasse, L. & Chadwick, H. M. 1992 Sea surface wind stress and drag coefficients: The HEXOS results. *Bound.-Layer Meteor.* **60**, 109–142.

Snyder, R. L., Dobson, F. W., Elliot, J. A. & Long, R. B. 1981 Array measurements of atmospheric pressure fluctuations above gravity waves. *J. Fluid Mech.* **102**, 1–59.

Soloviev, A., Donelan, M., Graber, H., Haus, B. & Schlussel, P. 2007 An approach to estimation of near-surface turbulence and CO_2 transfer velocity from remote sensing data. *J. Mar. Syst.* **66**, 182–194.

Soloviev, A. & Lukas, R. 2003 Observation of wave-enhanced turbulence in the near-surface layer of the ocean during TOGA COARE. *Deep-Sea Res. I* **50**, 371–395.

Soloviev, A. V., Vershinsky, N. V. & Bezverchnii, V. A. 1988 Small-scale turbulence measurements in the thin surface layer of the ocean. *Deep-Sea Res.* **35**, 1859–1874.

Stanislas, M., Okamoto, K. & Kaehler, C. 2003 Main results of the first international PIV challenge. *Meas. Sci. Technol.* **14**, R63–R89.

Stanislas, M., Okamoto, K., Kahler, C. J. & Westerweel, J. 2005 Main results of the second international PIV challenge. *Exp. in Fluids* **39**, 170–191.

Stanislas, M., Okamoto, K., Kahler, C. J., Westerweel, J. & Scarano, F. 2008 Main results of the third international PIV challenge. *Exp. in Fluids* **45(1)**, 27–71.

Stansell, P. & Macfarlane, C. 2002 Experimental investigation of wave breaking criteria based on phase speeds. *J. Phys. Oceanogr.* **32**, 1269–1283.

Stewart, R. W. 1961 The wave drag of wind over water. *J. Fluid Mech.* **10**, 189–194.

Takahashi, T., Sutherland, S. C., Sweeney, C., Poisson, A., Metzl, N., Tilbrook, B., Bates, N., Wanninkhof, R., Feely, R. A., Sabine, C., Olafsson, J. & Nojiri, Y. 2002 Global sea-air CO_2 flux based on climatological surface ocean pCO_2, and seasonal biological and temperature effects. *Deep Sea Research Part II: Topical Studies in Oceanography* **49** (9-10), 1601–1622.

Taylor, P. K. & Yelland, M. J. 2001 The dependence of sea surface roughness on the height and steepness of the waves. *J. Phys. Oceanogr.* **31**, 572–590.

Terray, E. A., Donelan, M. A., Agrawal, Y. C., Drennan, W. M., Kahama, K. K., III, A. J. Williams, Hwang, P. A. & Kitaigorodskii, S. A. 1996 Estimates of kinetic energy dissipation under breaking waves. *J. Phys. Oceanogr.* **26**, 792–807.

Thais, L. & Magnaudet, J. 1995 A triple decomposition of the fluctuating motion below laboratory wind water-waves. *J. Geophys. Res.* **100(C1)**, 741–755.

Thais, L. & Magnaudet, J. 1996 Turbulent structure beneath surface gravity waves sheared by the wind. *J. Fluid Mech.* **328**, 313–344.

Thomas, M., Misra, S., Kambhamettu, C. & Kirby, J. T. 2005 A robust motion estimation algorithm for PIV. *Meas. Sci. Technol.* **16**, 865–877.

Toba, Y., Iida, H., Kawamura, H., Ebuchi, N. & Jones, I. S. F. 1990 Wave dependence of sea-surface wind stress. *J. Phys. Oceanogr.* **20**, 705–721.

Toryanik, A. I. & Pogrebnyak, V. G. 1976 Surface tension of aqueous solutions of acetone. *Translated from Zhurnal Struktutnoi Khimii* **17(3)**, 536–537.

Tseng, R.-S., Hsu, Y.-H. L. & Wu, J. 1992 Methods of measuring wind stress over a water surface - discussions of displacement height and von karman constant. *Bound.-Layer Meteor.* **58**, 51–68.

Tsubokura, M., Kobayashi, T. & Taniguchi, N. 1997 In *FLUCOME 97*, , vol. 2, p. 875.

Van-Dorn, W. G. 1953 Wind stress on an artificial pond. *J. Mar. Res.* **12(3)**.

Veron, F., Saxena, G. & Misra, S. K. 2007 Measurements of the viscous tangential stress in the airflow above wind waves. *Geophys. Res. Lett.* **34**, L19603 (1–5).

Wanninkhof, R. 1992 Relationship between wind speed and gas exchange over the ocean. *J. Geophys. Res.* **97(C5)**, 7373–7382.

Wanninkhof, R. & Bliven, L. 1991 Relationship between gas exchange, wind speed and radar backscatter in a large wind-wave tank. *J. Geophys. Res.* **96(C2)**, 2785–2796.

Wanninkhof, R., Ledwell, J. R. & Broecker, W. S. 1985 Gas exchangewind speed relationship measured with sulfur hexafluoride on a lake. *Science* **227**, 1224–1226.

Wanninkhof, R. & McGillis, W. R. 1999 A cubic relationship between air-sea CO_2 exchange and wind speed. *J. Geophys. Res.* **26(13)**, 1889–1892.

Westerweel, J. 1997 Fundamentals of digital particle image velocimetry. *Meas. Sci. Technol.* **8**, 1379–1392.

Westerweel, J. 2000 Theoretical analysis of the measurement precision in particle image velocimetry. *Exp. in Fluids* **29**, S3–S12.

Westerweel, J. & Scarano, F. 2005 Universal outlier detection for PIV data. *Exp. in Fluids* **39**, 1096–1100.

Willert, C. E. & Gharib, M. 1991 Digital particle image velocimetry. *Exp. in Fluids* **10**, 181–193.

Wilmott, C. J., Ackleson, S. G., Davis, R. E., Feddema, J. J., Klink, K. M., Legates, D. R., O'Donnell, J. & Rowe, C. M. 1985 Statistics for the evaluation and comparison of models. *J. Geophys. Res.* **90**, 8995–9005.

Wilson, W. B. & Collier, A. 1972 The production of surface-active material by marine phytoplankton cultures. *J. Mar. Res.* **30**, 15–26.

Wu, J. 1968 Laboratory studies of wind-wave interactions. *J. Fluid Mech.* **34**, 91–111.

Wu, J. 1975 Wind-induced drift currents. *J. Fluid Mech.* **68**, 49–70.

Wu, J. 1980 Wind-stress coefficient over sea surface near neutral conditions - a revisit. *J. Phys. Oceanogr.* **10**, 727–740.

Wu, J. 1987 Momentum flux from wind to aqueous flows at various wind velocities and fetches. *J. Phys. Oceanogr.* **18**, 140–144.

Zappa, C. J., Asher, W. E. & Jessup, A. T. 2001 Microscale wave breaking and air-water gas transfer. *J. Geophys. Res.* **106**, 9385–9391.

Zappa, C. J., Asher, W. E., Jessup, A. T., Klinke, J. & Long, S. R. 2004 Microbreaking and the enhancement of air-water gas transfer velocities. *J. Geophys. Res.* **109**.

Zappa, C. J., Ho, D. T., McGillis, W. R., Banner, M. L., Dacey, J. W. H., Bliven, L. F., Ma, B. & Nystuen, J. 2009 Rain-induced turbulence and air-sea gas transfer. *J. Geophys. Res.* **114**, C07009 (1–17).

Zappa, C. J., McGillis, W. R., Raymond, P. A., Edson, J. B., Hintsa, E. J., Zemmelink, H. J., Dacey, J. W. H. & Ho, D. T. 2007 Environmental turbulent mixing controls on air-water gas exchange in marine and aquatic systems. *Geophys. Res. Lett.* **34**, L10601 (1–6).

Zappa, C. J., Raymond, P. A., Terray, E. A. & McGillis, W. R. 2003 Variation in surface turbulence and the gas transfer velocity over a tidal vycle in a macro-tidal estuary. *Estuaries* **26(6)**, 1401–1415.

Zarruk, G. A. 2005 Measurement of free surface deformation in PIV images. *Meas. Sci. Technol.* **16**, 1970–1975.

Zutic, V., Cosovic, B., Marcenko, E., Bihari, N. & Krsinic, F. 1981 Surfactant production by marine phytoplankton. *Marine Chemistry* **10**, 505–520.

Appendices

Appendix A

Measurement Uncertainty

A.1 Statistical Formulae

A.1.1 The Mean, The Standard Deviation and The Standard Error of the Mean

The uncertainties in the measurements were determined by calculating the mean, the standard deviation and the standard error of the mean. Let us assume that x is the variable being measured and x_1, x_2, x_3, ..., x_N were obtained for a sample of size N. Then the mean or average value (μ_x) of the sample is given by (Kennedy & Neville, 1976),

$$\mu_x = \frac{\sum_{i=1}^{N} x_i}{N} \tag{A.1}$$

The standard deviation (σ_x) of the measured variable that describes the scatter of measurements about the average is given by (Kennedy & Neville, 1976),

$$\sigma_x = \sqrt{\frac{\sum_{i=1}^{N}(x_i - \mu_x)^2}{N-1}} \tag{A.2}$$

The variance (ν_x) is defined as the square of the standard deviation of this variable such that $\nu_x = \sigma_x^2$. The coefficient of variation (c_v) can be expressed as a percentage as follows: $c_v = (\sigma_x/\mu_x) \times 100$ (Kennedy & Neville, 1976). The standard error of the mean (δ_x) is defined as (Kennedy & Neville, 1976),

$$\delta_x = \frac{\sigma_x}{\sqrt{N}} \tag{A.3}$$

A.1.2 Propagation of Error

In many cases, the parameters presented in this study were derived from several measured variables. For example, if y is a derived parameter that depends on several measured variables x, z and w then y can be represented as,

$$y = f(x, z, w) \tag{A.4}$$

The formula for propagation of error for y in terms of variance (σ_y^2) can be written as follows (Kennedy & Neville, 1976),

$$\sigma_y^2 = \left(\frac{\partial f}{\partial x}\sigma_x\right)^2 + \left(\frac{\partial f}{\partial z}\sigma_z\right)^2 + \left(\frac{\partial f}{\partial w}\sigma_w\right)^2 \tag{A.5}$$

where, σ_x, σ_z and σ_w are the standard deviations of the variables x, z and w.

A.2 Measurement Uncertainty in Wind-Wave Properties

The measurement uncertainties in wave properties were estimated using the surface wave profile data measured at the highest wind speed of 9.2 m s^{-1} and at the longest fetch of 12.4 m. It was assumed that the maximum measurement uncertainty would occur at the highest wind speed and at the longest fetch. Surface wave profile data were sampled at a rate of 30 Hz for a duration of 10 minutes and the total number of profiles collected in each experiment were 18000. In addition, the length of the vector of surface wave profile data was 1600 pixels.

The mean, the standard deviation, the coefficient of variation and the standard error of the mean of the significant wave height (H_s), the r.m.s wave height (H_{rms}), the dominant wave length (λ_d) and mean-square wave slope ($\langle S^2 \rangle$) were computed using statistical formulae presented in §A.1.1 and are listed in Table A.1. For example, the standard deviation, the coefficient of variation and the standard error of the mean of H_s were computed as

follows. First, 1600 time series, each with a duration of 10 minutes, were extracted from the surface wave profile data. The odd and even numbered wave profiles were then separated from each time series since two consecutive surface wave profiles were almost identical as they were acquired only by a few millisecond apart. The average of the highest one-third of the wave heights in each time series was computed that gave an estimate of H_s. Next, a total of 1600 samples of H_s were used to estimate the standard deviation of H_s. The final estimate of the standard deviation of H_s ($\pm$0.027 cm) was obtained as the average of the standard deviations estimated for the odd and even time series. The significant wave height at the highest wind speed of 9.2 m s^{-1} and at the longest fetch of 12.4 m was estimated to be 2.81 cm. Therefore, the coefficient of variation in computing H_s was determined to be equal to $\pm$1% (i.e. $\pm 0.027/2.81 \times 100$). The standard error of the mean was then computed as $\pm$0.0007 cm (i.e. $\pm 0.027/\sqrt{1600}$).

A.3 Measurement Uncertainty in Mean Flow Properties

The measurement uncertainties in both air-side and water-side mean flow properties were estimated using the air-side and water-side velocity measurements. The air-side mean flow properties included wind speed (U_z), wind friction velocity (u_{*a}) and aerodynamic roughness length (z_{oa}). The water-side mean flow properties included the Lagrangian surface drift velocity (U_{SL}), the Stokes drift velocity (U_{Stokes}), tangential friction velocity (u_{*t}) and hydrodynamic roughness length (z_{ot}). Table A.2 lists the measurement uncertainties for both air-side and water-side mean flow properties.

The measurement uncertainties in U_z, and u_{*a} were estimated using the vertical profile of mean wind speed data measured at the highest wind speed of 9.2 m s^{-1} and at the longest fetch of 12.4 m. It was assumed that the

maximum measurement uncertainty would occur at the highest wind speed and at the longest fetch. For this experiment, five vertical profiles of mean wind speed data were obtained that were sampled at a rate of 50 Hz over a time period of 1.7 hours. The mean wind speed and u_{*a} were then computed from each profile and the associated measurement uncertainties were estimated. For example, the mean and the standard deviation of U_z were estimated to be 9.2 m s^{-1} and $\pm$0.012 m s^{-1}, respectively using the five profiles. The coefficient of variation of U_z was determined to be equal to $\pm$0.1% (i.e. $\pm 0.012/9.2 \times 100$). The standard error of the mean was then computed as $\pm$0.005 m s^{-1} (i.e. $\pm 0.012/\sqrt{5}$).

The measurement uncertainties in U_{SL}, U_{Stokes}, u_{*t}, z_{ot} and z_{oa} were estimated using 10 repeated experiments, two repeats at each wind speed, for five wind speeds at a fetch of 4.8 m. The percentage error, ϵ_i, (where, i varies from 1 to 5 as an index for five wind speeds) in a measured variable at each wind speed was first computed as,

$$\epsilon_i = \left(\frac{\Delta x_i}{\frac{(x_1 + x_2)}{2}} \right) \times 100 \tag{A.6}$$

where, $\Delta x_i = |x_1 - x_2|$ is the difference in magnitude between two estimates (x_1 and x_2) of a variable obtained from two repeated experiment at a given wind speed. The mean percentage error ($\overline{\epsilon}$) and the standard deviation of the percentage error (σ_ϵ) were then computed. Next, the standard deviation of a measured variable in percentage, which was also an estimate of the coefficient of variation (c_v) was computed as follows,

$$c_v = \overline{\epsilon} + \sigma_\epsilon \tag{A.7}$$

Finally, the standard deviation of a measured variable (σ_x) was computed as given below,

$$\sigma_x = \mu_x \times \left(\frac{c_v}{100} \right) \tag{A.8}$$

where, μ_x was computed from the data of 10 repeated experiments.

For example, the percentage error in U_{SL} was computed from 10 repeated experiments using Equation(A.6) and found to vary from 0.8% to 3.2%. Then, the mean percentage error and the standard deviation of the percentage error were computed and were found to be 1.62% and ±0.94%, respectively. So, the coefficient of variation in U_{SL}, using Equation(A.7), was determined to be ±2.56%. Now, the mean value of U_{SL} using 10 repeated experiments was found to be 26.8 cm s^{-1}. Therefore, the standard deviation of U_{SL}, using Equation(A.8), was estimated to be ±0.68 cm s^{-1} (i.e. ±26.8×2.56/100). Finally, the standard error of the mean was computed as ±0.306 cm s^{-1} (i.e. $\pm 0.68/\sqrt{5}$).

A.4 Measurement Uncertainty in Rate of Dissipation of Turbulent Kinetic Energy

The measurement uncertainty in the rate of dissipation of turbulent kinetic energy (ε) was estimated using the dissipation measurements made at a depth of 6 mm from the surface at the highest wind speed of 9.0 m s^{-1} at the short fetch of 4.8 m. The standard deviation, the coefficient of variation and the standard error of the mean of the dissipation rate at a depth of 6 mm were estimated to be ±0.723 cm^2 s^{-3}, ±11%, and ±0.229 cm^2 s^{-3}, respectively.

To compute the standard deviation of the dissipation rate at a depth of 6 mm, ten estimates of the dissipation rate were first computed by time averaging the velocity gradients over one minute interval using the 'Direct' method for the above 10-minutes experimental run. Then the standard deviation of these ten estimates of the dissipation rate was computed as ±0.723 cm^2 s^{-3}. The average of these ten estimates of the dissipation rate was determined to be 6.5 cm^2 s^{-3}. Therefore, the coefficient of variation in computing ε was determined to be equal to ±11% (i.e. ±0.723/6.5×100). The standard error of the mean

was then computed as ± 0.229 cm^2 s^{-3} (i.e. $\pm 0.723/\sqrt{10}$). It was assumed that the rate of energy dissipation beneath microscale breaking waves (ε_{msb}) and non-breaking waves (ε_{non}) would produce similar measurement uncertainty.

A.5 Measurement Uncertainty in Derived Parameters

A.5.1 Uncertainty in Derived Wind-Wave Properties

The uncertainties in the derived wind-wave properties such as the dominant wavenumber (k_d), the dominant wave frequency (f_d), and the wave phase speed (c_p) were estimated using the propagation of error formula given by Equation(A.5). It should be noted that k_d, f_d and c_p were computed from λ_d using the deep-water linear dispersion relationship.

For example, k_d was derived from λ_d using the formula; $k_d = 2\pi/\lambda_d$. Now, using the propagation of error formula the expression for the standard deviation of k_d (i.e. σ_{kd}) can be derived as; $\sigma_{kd} = (2\pi/\lambda_d)(\sigma_{\lambda d}/\lambda_d)$. Therefore, using $\lambda_d = 23.7$ cm and $\sigma_{\lambda d} = \pm 0.199$ cm, the standard deviation of k_d was computed as $\sigma_{kd} = \pm 0.222$ rad m^{-1}. Using $k_d = 26.5$ rad m^{-1}, the coefficient of variation was then computed as $\pm 0.8\%$ (i.e. $\pm 0.222/26.5 \times 100$). Similarly, the standard deviations of f_d and c_p were estimated to be ± 0.011 Hz, and ± 0.003 cm s^{-1}, respectively. The coefficient of variations in computing f_d and c_p were estimated to be $\pm 0.4\%$ and $\pm 0.004\%$, respectively.

Two other dimensionless wind-wave properties were the dominant wave steepness (H_s/λ_d) and wave age (c_p/u_{*a}). The standard deviations of H_s/λ_d and c_p/u_{*a} were estimated to be ± 0.0015 and ± 0.071, respectively. The coefficient of variations in computing H_s/λ_d and c_p/u_{*a} were estimated to be $\pm 1.3\%$ and $\pm 5.9\%$, respectively. Table A.3 lists the measurement uncertainties for all derived wind-wave properties.

A.5.2 Uncertainty in Derived Mean Flow Properties

The derived mean flow properties included the surface drift velocity (U_s), the aerodynamic roughness Reynolds number ($z_{oa}^{+} = z_{oa}u_{*a}/\nu_a$), the hydrodynamic roughness Reynolds number ($z_{ot}^{+} = z_{ot}u_{*t}/\nu_w$), the aerodynamic Charnock parameter ($\alpha_{Ch}^{a} = gz_{oa}/u_{*a}^2$), the hydrodynamic Charnock parameter ($\alpha_{Ch}^{w} = gz_{ot}/u_{*t}^2$), and roughness length ratio (z_{ot}/z_{oa}). The uncertainties in these derived mean flow properties were estimated using the propagation of error formula given by Equation(A.5). Table A.4 lists all the measurement uncertainties for the derived mean flow properties.

A.5.3 Uncertainty in Derived Turbulent Flow Properties

The derived turbulent flow properties included the rate of dissipation of turbulent kinetic energy solely due to wave breaking (ε_b) and three normalized rates of energy dissipation; $(\varepsilon\kappa\zeta)/u_{*t}^3$, $(\varepsilon c_p)/(gu_{*t}^2)$, and $(\varepsilon_b H_s)/(c_p u_{*t}^2)$. The uncertainties in these derived turbulent properties were estimated using the propagation of error formula given by Equation(A.5). Table A.5 lists all the measurement uncertainties for the derived turbulent flow properties.

A.5.4 Uncertainty in Other Derived Dimensionless Parameters

Other derived dimensionless parameters that were used in this study included dimensionless aerodynamic roughness lengths (z_{oa}/H_{rms} and z_{oa}/H_s), dimensionless hydrodynamic roughness length (z_{ot}/H_s), the dimensionless depth ($g\zeta/u_{*t}^2$), and the stress ratio (τ_t/τ_a). The uncertainties in these derived dimensionless parameters were estimated using the propagation of error formula given by Equation(A.5). Table A.6 lists the measurement uncertainties for all other derived dimensionless parameters.

Uncertainty Parameter	H_s	H_{rms}	λ_d	$\langle S^2 \rangle$
Mean (cm, cm, cm, cm.cm^{-1})	2.81	1.91	23.7	0.09
Standard Deviation (cm, cm, cm, cm.cm^{-1})	±0.027	±0.018	±0.199	±0.002
Coefficient of Variation (%)	±1	±0.9	±0.8	±2.4
Standard Error of the Mean (cm, cm, cm, cm.cm^{-1})	±0.0007	±0.0004	±0.0795	±0.0016

Table A.1: The measurement uncertainties in wind-wave properties. H_s, the significant wave height; H_{rms}, the r.m.s. wave height; λ_d, the dominant wavelength; $\langle S^2 \rangle$, the mean-square wave slope.

Uncertainty Parameter	U_z	u_{*a}	z_{oa}	U_{SL}	U_{Stokes}	u_{*t}	z_{ot}
Mean (m s^{-1}, cm s^{-1}, μm, cm s^{-1}, cm s^{-1}, cm s^{-1}, μm)	9.2	50.6	369	26.8	1.21	0.811	53
Standard Deviation (m s^{-1}, cm s^{-1}, μm, cm s^{-1}, cm s^{-1}, cm s^{-1}, μm)	±0.012	±3.01	±76.6	±0.68	±0.12	±0.061	±33.6
Coefficient of Variation (%)	±0.1	±5.9	±20.8	±2.56	±9.9	±7.5	±63
Standard Error of the Mean (m s^{-1}, cm s^{-1}, μm, cm s^{-1}, cm s^{-1}, cm s^{-1}, μm)	±0.005	±1.35	±34.3	±0.306	±0.053	±0.027	±15

Table A.2: The measurement uncertainties in air-side and water-side mean flow properties. U_z, wind speed in the wave tank; u_{*a}, wind friction velocity; z_{oa}, aerodynamic roughness length; U_{SL}, the Lagrangian surface drift velocity; U_{Stokes}, the Stokes drift velocity; u_{*t}, water-side or tangential friction velocity; z_{ot}, hydrodynamic roughness length.

Uncertainty Parameter	k_d	f_d	c_p	H_s/λ_d	c_p/u_{*a}
Mean (rad m^{-1} for k_d, Hz for f_d, cm s^{-1} for c_p)	26.5	2.6	60.8	0.12	1.2
Standard Deviation (rad m^{-1} for k_d, Hz for f_d, cm s^{-1} for c_p)	±0.222	±0.011	±0.003	±0.0015	±0.071
Coefficient of Variation (%)	±0.8	±0.4	±0.004	±1.3	±5.9

Table A.3: The measurement uncertainties in derived wind-wave properties. k_d, the dominant wavenumber; f_d, the dominant wave frequency; c_p, the wave phase speed; H_s/λ_d, the dominant apparent wave steepness; and, c_p/u_{*a}, the wave age.

Uncertainty Parameter	U_s	z_{oa}^+	z_{ot}^+	α_{Ch}^a	α_{Ch}^w	z_{ot}/z_{oa}
Mean ($cm\ s^{-1}$ for U_s)	25.5	12.4	0.46	0.014	7.95	0.145
Standard Deviation ($cm\ s^{-1}$ for U_s)	±0.695	±2.69	±0.294	±0.0034	±5.15	±0.096
Coefficient of Variation (%)	±2.7	±21.8	±63.5	±23.9	±65.2	±66.7

Table A.4: The measurement uncertainties in derived mean flow properties. U_s, the surface drift velocity; z_{oa}^+, aerodynamic roughness Reynolds number; z_{ot}^+, hydrodynamic roughness Reynolds number; α_{Ch}^a, aerodynamic Charnock parameter; α_{Ch}^w, hydrodynamic Charnock parameter; z_{ot}/z_{oa}, roughness length ratio.

Uncertainty Parameter	ε_b	$(\varepsilon\kappa\zeta)/(u_{*t}^3)$	$(\varepsilon c_p)/(g u_{*t}^2)$	$(\varepsilon_b H_s)/(c_p u_{*t}^2)$
Mean ($cm^2\ s^{-3}$ for ε_b)	13.1	2.927	0.613	0.921
Standard Deviation ($cm^2\ s^{-3}$ for ε_b)	±2.06	±0.747	±0.115	±0.201
Coefficient of Variation (%)	±15.7	±25.5	±18.7	±21.8

Table A.5: The measurement uncertainties in derived turbulent flow properties. ε_b, rate of dissipation of turbulent kinetic energy solely due to wave breaking; and, three normalized rates of energy dissipation; $(\varepsilon\kappa\zeta)/u_{*t}^3$, $(\varepsilon c_p)/(g u_{*t}^2)$, and $(\varepsilon_b H_s)/(c_p u_{*t}^2)$.

Uncertainty Parameter	z_{oa}/H_{rms}	z_{oa}/H_s	z_{ot}/H_s	$g\zeta/u_{*t}^2$	τ_t/τ_a
Mean	0.0193	0.0131	0.0019	895	0.215
Standard Deviation	±0.004	±0.0027	±0.0012	±140	±0.041
Coefficient of Variation (%)	±20.8	±20.8	±63.4	±15.6	±19.2

Table A.6: The measurement uncertainties in other derived dimensionless parameters. z_{oa}/H_{rms} and z_{oa}/H_s, dimensionless aerodynamic roughness lengths; z_{ot}/H_s, dimensionless hydrodynamic roughness length; $g\zeta/u_{*t}^2$, dimensionless depth; and τ_t/τ_a, stress ratio.